

**INAUGURAL - DISSERTATION**  
zur Erlangung der Doktorwürde der  
Naturwissenschaftlich-Mathematischen Gesamtfakultät der  
Ruprecht-Karls-Universität  
Heidelberg

**Intramolecular Charge Transfer in Solvated  
Organic Molecules:  
A Quantum Chemical Study**

vorgelegt von  
Mercedes Vanessa Bohnwagner  
aus Duisburg

14.12.2017

**Gutachter:**

Prof. Dr. Andreas Dreuw

Prof. Dr. Peter Comba

Datum der mündlichen Prüfung: 22.02.2018



*Für die Wissenschaft*



*“Denn es mag wohl eben keiner von uns beiden etwas Tüchtiges oder Sonderliches wissen; allein dieser doch meint zu wissen, da er nicht weiß, ich aber, wie ich eben nicht weiß, so meine ich es auch nicht. Ich scheine also um dieses wenige doch weiser zu sein als er, daß ich, was ich nicht weiß, auch nicht glaube zu wissen”*  
*- Ich weiß, dass ich nichts weiß -*

Sokrates



# Abstract

Photochemical reactions are ubiquitous in nature. Furthermore, they play an important role in organic and inorganic synthesis. In such reactions, light energy is used to induce chemical transformations. Two prime examples of such reactions are photosynthesis – the conversion of light energy to chemical energy, and the cis-trans isomerization reaction in the retina which enables vision. Upon absorption of light, the electrons in a molecule are promoted to higher energy levels; the molecule is elevated from its electronic ground state to an electronically excited state. Once in the excited state, different processes may take place such as the emission of light, interactions with the environment, or chemical reactions. One class of processes often involved in photochemical reactions and of particular importance are charge-transfer processes. A charge transfer can occur intermolecularly i.e., between different molecules or within a molecular complex from a ligand to the center and vice versa. These intermolecular charge-transfer processes, for example, occur in organometal complexes and play a crucial role in numerous catalytic reactions. In intramolecular charge-transfer processes, charge is transferred from one part of a molecule, the donor moiety, to a different part of the molecule, the acceptor moiety. Among those, so-called twisted intramolecular charge-transfer (TICT) processes and the corresponding TICT states are of particular interest. TICT molecules are characterized by the fact that they undergo a rotation about a single bond connecting the donor and acceptor moiety in the excited state. This twisting is accompanied by a charge transfer from the donor to the acceptor, resulting in a highly polar CT state exhibiting a mutually perpendicular orientation of donor and acceptor subsystems. Due to this process, TICT compounds show a very interesting unusual fluorescence behavior, named dual fluorescence, in medium polar and polar solvents. Dual fluorescence means that there are two fluorescence bands observable: one corresponding to the transition from the TICT state and the other from the transition from a planar excited state. In this dissertation, photochemical reactions of different small- and medium-sized organic molecules have been investigated with a particular focus on intramolecular charge-transfer. The well-known and experimentally well-investigated small donor-acceptor TICT compound N-pyrrolobenzonitrile (PBN) and its thiophene derivative 5-(1H-pyrrole-1-yl)thiophenecarbonitrile (TCN) are studied, among others. For this purpose, different quantum chemical electronic structure methods are employed. Especially when used along with spectroscopy, these *ab initio* methods are powerful tools to study the molecular structure and photochemical reactions. Quantum chemical methods can provide reliable excitation energies, excited state properties, and absorption strengths and allow for the computation of deactivation pathways. In this work, it is shown that the chosen quantum chemical methodology is well suited to describe the photochemical behavior of the considered organic compounds and new insights into the photochemistry of these systems are provided.



# Zusammenfassung

Photochemische Reaktionen stellen eine sehr wichtige Klasse an chemischen Reaktionen dar. Sie sind zahlreich in der Natur zu finden und spielen eine wichtige Rolle in der organischen und anorganischen Synthese. Die wohl wichtigste und bekannteste photochemische Reaktion ist die Photosynthese. Hier wird Lichtenergie photosynthetisch in chemische Energie umgewandelt. Somit bildet die Photosynthese die Hauptenergiequelle für nahezu alle Organismen auf der Erde. In einer photochemischen Reaktion wird die für die Reaktion benötigte Energie durch Absorption von Lichtenergie gewonnen. Das molekulare System wird dabei in einen elektronisch angeregten Zustand überführt. Im angeregten Zustand können unterschiedliche Prozesse stattfinden, über die das System die überschüssige Energie abführt und in seinen Grundzustand, den Zustand niedrigster Energie, zurückkehrt. Diese Prozesse werden auch Deaktivierungsprozesse genannt. Die Energie kann z.B. durch Stöße mit anderen Molekülen teilweise oder ganz in Wärme umgewandelt oder für eine chemische Reaktion genutzt werden. Alternativ kann die überschüssige Energie durch Emission von Licht abgegeben werden.

In zahlreichen photochemischen Reaktionen treten sogenannte Ladungstransfer Prozesse und Ladungstransfer Zustände auf. Eine besonders interessante Klasse an Ladungstransfer Zuständen sind sogenannte TICT (*twisted intramolecular charge-transfer*) Zustände. Bei der Bildung eines TICT Zustandes findet der Ladungstransfer, intramolekular, von einem Part des Moleküls, dem Donor, zu einem anderen Part des Moleküls, dem Akzeptor, statt. Donor und Akzeptor sind durch eine Einfachbindung miteinander verbunden. Während dieses Prozesses kommt es zu einer Drehung um die Einfachbindung. Es resultiert eine Geometrie in der Donor und Akzeptor, mehr oder weniger, orthogonal zueinander orientiert sind, was in einer starken räumlichen Ladungstrennung resultiert. Aus diesem Grund weisen TICT Zustände auch typischerweise große elektrische Dipolmomente auf und somit eine hohe Polarität. TICT Zustände wurden vor allem durch das mit ihnen verbundene Auftreten von dualer Fluoreszenz bekannt. Duale Fluoreszenz bedeutet, dass neben der in der Gasphase und in unpolaren Lösungsmitteln auftretenden "normalen" Emission, in polaren Lösungsmitteln zusätzlich eine zweite, stark rotverschobene "anomale" Emission beobachtbar wird. Mit der Entdeckung der dualen Fluoreszenz des kleinen Donor-Akzeptor Moleküls 5-cyano-N,N,-dimethylanilin (DMABN) im Jahre 1959, begann eine intensive Erforschung von Ladungstransfer Zuständen und Ladungstransfer Prozessen.

Die Untersuchung photochemischer Reaktionen und Prozesse kann entweder spektroskopisch oder theoretisch erfolgen oder durch Kombination beider Analyseverfahren. Für eine theoretische Untersuchung stehen zahlreiche quantenchemischen *ab initio* Methoden zur Verfügung. Mit Hilfe dieser Methoden können allein aus der Struktur eines Moleküls, ohne weitere Annahmen, verschiedene Eigenschaften, wie z.B. Energie, Übergangsstärke und Schwingungsverhalten und Deaktivierungspfade berechnet werden.

Das zentrale Thema dieser Dissertation ist die theoretische Untersuchung photochemischer Eigenschaften und Reaktionen kleiner und mittelgroßer organischen Moleküle. Ein besonderer Augenmerk liegt dabei auf der Rolle von TICT Zuständen. Für die Untersuchungen werden unterschiedliche quantenchemische *ab initio* Methoden verwendet.

Zunächst werden in Kapitel 2 TICT Zustände eingeführt und näher beschrieben. In Kapitel 3 werden grundlegende quantenchemische Konzepte, wichtige Näherungen und die verwendeten

Methoden vorgestellt und diskutiert. In den anschließenden Kapiteln 4-7 werden schließlich die zuvor eingeführten Methoden angewandt, um photochemische Prozesse in einer Anzahl an molekularen Systemen zu untersuchen.

Bei den in Kapiteln 4-6 untersuchten Systemen, P-pyrrolbenzotrifluorid (PBN), 5-(1H-pyrrol-1-yl)thiophencarbonitril (TCN) und 4-Fluoro-*N,N*-dimethylanilin (FDMA) handelt es sich um kleine Donor-Akzeptor Moleküle, die dem bekannten, in polarem Lösungsmittel dual fluoreszierenden DMABN Molekül strukturell sehr ähnlich sind. Die vier in Kapitel 7 untersuchten Systeme sind Derivate des Hemithioindigo-Hemistilben (HTI) Moleküls. HTI ist ein sogenannter Photoschalter. Unter Bestrahlung mit Licht verändert HTI seine Struktur und rotiert dabei um seine zentrale Kohlenstoff-Kohlenstoff Doppelbindung. Das letzte Kapitel umfasst eine Grundzustands Studie. Hier werden intermolekulare Wechselwirkungen in vier verschiedenen Dimer Systemen untersucht um Aufschlüsse über ein auffälliges Kristallstrukturmotiv zu gewinnen.

In dieser Arbeit wird gezeigt, dass sich die verwendeten quantenchemischen Methoden gut für die Untersuchung der Photochemie der betrachteten organischen Moleküle eignen und sie experimentelle Daten gut reproduzieren können. Des Weiteren werden neue Erkenntnisse und Einsichten über die photochemischen Eigenschaften und Deaktivierungsmechanismen der behandelten organischen Moleküle präsentiert.

---

## CONTENTS

---

<b>Abstract</b>	<b>I</b>
<b>Zusammenfassung</b>	<b>III</b>
<b>Abbreviations</b>	<b>IX</b>
<b>1 Preface</b>	<b>1</b>
1.1 Quantum Chemistry . . . . .	1
1.2 Photochemistry . . . . .	2
<b>2 Introduction</b>	<b>7</b>
2.1 Twisted Intramolecular Charge-Transfer . . . . .	8
<b>3 Theoretical Background and Methodology</b>	<b>13</b>
3.1 The Schrödinger Equation . . . . .	14
3.2 Born-Oppenheimer Approximation and Franck-Condon Principle . . . . .	16
3.3 Ground State Self-Consistent Field Methods . . . . .	20
3.3.1 Hartree-Fock Theory . . . . .	22
3.4 Density Functional Theory . . . . .	28
3.4.0.1 Self-Interaction Error . . . . .	34
3.4.0.2 Dispersion Corrections: DFT-D . . . . .	35
3.5 Electron Correlation and Post-Hartree-Fock Methods . . . . .	37
3.5.1 Møller-Plesset Perturbation Theory . . . . .	38
3.5.2 Coupled Cluster Theory . . . . .	41
3.6 Excited State Methods . . . . .	43
3.6.1 Configuration Interaction Singles . . . . .	44
3.6.2 Linear Response CC2 . . . . .	47
3.6.3 Algebraic Diagrammatic Construction Scheme . . . . .	48
3.6.4 Linear Response Time-Dependent Density Functional Theory . . . . .	50
3.6.4.1 Charge-Transfer Failure . . . . .	54
3.7 Spin-Flip Approach . . . . .	55
3.8 Solvation Effects . . . . .	56
3.8.1 Continuum Solvation Models . . . . .	57
3.8.2 Ground State Equilibrium Solvation . . . . .	61
3.8.3 Considerations for Excited States . . . . .	62

3.9	Characterization of Electronic States . . . . .	70
<b>4</b>	<b>The Photochemistry of PBN</b>	<b>73</b>
4.1	Motivation and Background . . . . .	74
4.1.1	Previous experimental studies . . . . .	75
4.1.2	Previous theoretical studies . . . . .	76
4.2	Computational Methods . . . . .	79
4.3	Results . . . . .	80
4.3.1	Ground state properties of PBN . . . . .	80
4.3.2	Vertical excited states of PBN . . . . .	82
4.3.3	Structural relaxation in the excited states . . . . .	86
4.3.3.1	The dark 1B (LE) state: . . . . .	88
4.3.3.2	The bright 2A ( $\pi\pi^*$ ) state: . . . . .	89
4.3.3.3	The 2B (CT) state: . . . . .	92
4.3.4	TICT formation mechanism . . . . .	95
4.4	Summary and Conclusion . . . . .	100
<b>5</b>	<b>The Photochemistry of TCN</b>	<b>105</b>
5.1	Motivation and Background . . . . .	106
5.2	Computational Methods . . . . .	107
5.3	Results . . . . .	108
5.3.1	Ground state properties of TCN . . . . .	108
5.3.2	The gas phase photochemistry of TCN . . . . .	109
5.3.3	Nonradiative decay in the gas phase . . . . .	114
5.3.4	The photochemistry of TCN in solution . . . . .	117
5.4	Summary and Conclusion . . . . .	120
<b>6</b>	<b>The Photochemistry of FDMA</b>	<b>123</b>
6.1	Motivation and Background . . . . .	123
6.1.1	Experimental and theoretical findings by Fujiwara et al.: the observation of dual fluorescence . . . . .	125
6.1.2	Experimental findings by Zachariasse et al.: the observation of single fluorescence . . . . .	126
6.1.3	Computational details . . . . .	126
6.2	Results . . . . .	128
6.2.1	Simulated absorption spectra of FDMA . . . . .	130
6.3	Summary and Conclusion . . . . .	138
<b>7</b>	<b>The Photochemistry of Donor Substituted Hemithioindigo (HTI) Derivatives</b>	<b>141</b>
7.1	Motivation and Background . . . . .	142
7.2	Computational Methods . . . . .	144
7.3	Results . . . . .	148
7.3.1	Ground state properties and static absorption spectra . . . . .	148
7.3.2	Excited state properties and fluorescence spectra of HTIs Z1-Z4 . . . . .	155
7.3.3	Mechanism of the Z/E photoisomerization of HTIs Z1-Z4 . . . . .	159
7.3.4	TICT formation in HTIs Z1-Z3 . . . . .	164

7.4	Summary and Conclusion . . . . .	168
<b>8</b>	<b>Intermolecular Interactions in Quinoxalinophenanthrophenazine Dimers</b>	<b>171</b>
8.1	Motivation and Background . . . . .	172
8.2	Computational Methods . . . . .	174
8.3	Results . . . . .	175
8.3.1	Structural study . . . . .	175
8.3.2	Energetic study . . . . .	178
8.3.2.1	Total binding energies and dispersion energy contribution . .	179
8.4	Conclusion . . . . .	180
<b>9</b>	<b>Global Summary &amp; Outlook</b>	<b>183</b>
9.1	Global Summary . . . . .	183
9.2	Outlook . . . . .	188
	<b>Appendices</b>	<b>191</b>
<b>A</b>	<b>Appendix for Chapter 5</b>	<b>191</b>
A.1	The Photochemistry of TCN . . . . .	191
<b>B</b>	<b>Appendix for Chapter 6</b>	<b>195</b>
B.1	The Photochemistry of FDMA . . . . .	195
<b>C</b>	<b>Appendix for Chapter 7</b>	<b>201</b>
C.1	Z/E Photoisomerization of Hemithioindigo Derivatives Z1-Z4 . . . . .	201
<b>D</b>	<b>Appendix for Chapter 8</b>	<b>209</b>
D.1	Intermolecular Interactions in Quinoxalinophenanthrophenazine (QPP) Dimers . . . . .	209
	<b>Bibliography</b>	<b>211</b>
	<b>Publication List</b>	<b>241</b>
	<b>List of Figures</b>	<b>243</b>
	<b>List of Tables</b>	<b>251</b>
	<b>Danksagung</b>	<b>253</b>
	<b>Eidesstattliche Versicherung</b>	<b>255</b>



---

## ABBREVIATIONS

---

<b>ADC</b>	Algebraic Diagrammatic Construction
<b>ASC</b>	Apparent Surface Charges
<b>BO</b>	Born-Oppenheimer
<b>CC</b>	Coupled-Cluster
<b>CI</b>	Configuration Interaction
<b>CIS</b>	Configuration Interaction Singles
<b>COSMO</b>	Conductor like Screening Model
<b>C-PCM</b>	Conductor like Polarization Continuum Model
<b>CS</b>	Crystal Structure
<b>CSM</b>	Continuum Solvation Model
<b>CT</b>	Charge-Transfer
<b>D</b>	Debye
<b>DFT</b>	Density Functional Theory
<b>DMABN</b>	N-dimethylaminobenzonitrile
<b>EA</b>	Electron Affinity
<b>eV</b>	Electron Volt
<b>FDMA</b>	4-fluoro-N,N-dimethylaniline
<b>FC</b>	Franck-Condon
<b>GTO</b>	Gaussian type orbital
<b>HF</b>	Hartree-Fock
<b>HOMO</b>	Highest Occupied Molecular Orbital
<b>HTI</b>	Hemithioindigo-Hemistilbene
<b>IVR</b>	Internal Vibrational Relaxation
<b>IC</b>	Internal Conversion

<b>IP</b>	Ionization Potential
<b>ISC</b>	Inter System Crossing
<b>ISR</b>	Intermediate State Representation
<b>KS</b>	Kohn-Sham
<b>LR</b>	Linear Response
<b>LUMO</b>	Lowest Unoccupied Molecular Orbital
<b>MP</b>	Møller-Plesset
<b>MO</b>	Molecular Orbital
<b>PBN</b>	N-pyrrolobenzonitrile
<b>PCM</b>	Polarizable Continuum Model
<b>PES</b>	Potential Energy Surface
<b>QPP</b>	Quinoxalinophenanthrophenazines
<b>RI</b>	Resolution of the Identity
<b>SCF</b>	Self-Consistent Field
<b>SIE</b>	Self-Interaction Error
<b>SS</b>	State Specific
<b>SOC</b>	Spin-Orbit Coupling
<b>TCN</b>	5-(1H-pyrrole-1-yl)thiophenecarbonitrile

## PREFACE

---

### 1.1 QUANTUM CHEMISTRY

*“If quantum mechanics hasn’t profoundly shocked you,  
you haven’t understood it yet.”*

Nils Bohr

It is the work by the physicist Erwin Schrödinger on the formulation of the famous Schrödinger equation in 1926<sup>[1,2]</sup> and the subsequent work by physicists Walter Heitler and Fritz London in 1927<sup>[3]</sup> on the first application of the Schrödinger equation for the hydrogen molecule that might be considered as the historical beginning of quantum chemistry. Ever since quantum chemistry has become a constantly evolving field of science and industry. Along with the rapidly developing computer technology, it is still growing and becoming more and more important. As the name suggests, quantum chemistry is a field of chemistry whose focus is on the application of quantum mechanics to study electronic properties of molecular systems, chemical and physical processes and reactions. A current google scholar search with keywords ‘quantum chemical study’ produced 2,530,000 results showing the significance of this research field. For comparison, the keywords ‘global warming’ resulted in 3,040,000 hits.

Ever since the advent of quantum mechanics in the early 20th century, which caused a revolution in natural sciences, it has become more and more evident that quantum mechanical laws govern matter. Thus, it also became clear that many chemical, and physical processes and reactions can only be substantially understood and adequately described within a quantum mechanical

framework. Some important examples are: i) photosynthesis,<sup>[4-8]</sup> i.e. the cyclic sequence of reactions in which light energy is converted into chemical energy by a number of different pigment molecules, ii) light-induced DNA damage and repair mechanism(s)<sup>[9-12]</sup> occurring in a variety of organisms, iii) the process of visual perception involving a light-induced isomerization reaction of the retinal pigment molecule<sup>[13-15]</sup> and charge-transfer in semiconductor materials<sup>[16-20]</sup>. Apart from its relevance in fundamental research in natural science, the study of quantum chemical processes and reactions is also important for industry, especially high-tech industry. This is mainly because such processes and reactions strongly determine the properties of the employed materials (typically semiconductors) and thus the performance and efficiency of the corresponding devices.

## 1.2 PHOTOCHEMISTRY

The primary focus of the thesis lies in the investigation of the photochemistry of small- and medium-sized organic molecules using different quantum chemical electronic structure methods. Here, a particular emphasis is on the role of so-called *charge-transfer* states.

However, before I introduce charge-transfer states and elucidate their role in photochemical reactions, their influence on electronic properties of organic semiconducting materials and especially their relation to the phenomenon of *dual fluorescence*, I will briefly present some basic concepts of photochemistry.

For a chemical reaction to occur, energy is required in two ways. On the one hand as activation energy and on the other hand as reaction enthalpy. Activation energy is needed because the two charge distributions of the reacting molecules repel each other. Hence, the reactants must have sufficient energy to overcome this energy barrier. The reaction enthalpy, in turn, results from the change in energy due to bond breaking and reformation leading to the products.<sup>[21]</sup> Besides thermal reactions, which need heat energy to be activated and take place in the ground state of the chemical system, there exist numerous other reactions in which the activation energy barrier is bypassed due to electronic excitation by absorption of light energy. These so-called *photochemical* reactions, in contrast, proceed in the excited state.

Typically, if not perturbed by an external force, a chemical system, e.g., a single molecule resides in its energetically lowest state, the *electronic ground state*. Interaction with light may promote an

electron from an occupied molecular orbital to an energetically higher-lying unoccupied molecular orbital leading to the population of an energetically higher-lying so-called *electronically excited state*. This process, called photoexcitation, is very fast on the femtosecond (fs) time scale, and orders of magnitude faster than nuclear motion. Therefore, it is also termed vertical or Franck-Condon excitation, based on the *Franck-Condon principle*<sup>[22–24]</sup>, which will be discussed in more detail in **chapter 3** of this thesis.

Usually, the molecule is not only excited electronically but also vibrationally, meaning that the atoms in the molecules start to move. In the excited state, many different photochemical processes can ensue (see Fig. 1.1). Due to the energy conservation law, the acquired excess energy is directly dissipated or ‘quenched’, and the molecule decays back to its electronic ground state. The decay may happen radiatively, e.g., through fluorescence or phosphorescence, or it can proceed nonradiatively, e.g., through internal vibrational relaxation, interaction with an environment, geometry relaxation, or conversion into chemical energy by some photochemical reaction.<sup>[25]</sup>

These processes are not mutually exclusive and may even compete with one another.

Internal vibrational relaxation (IVR) (see Fig. 1.1) is the most rapid decay process, occurring on the femtosecond to picosecond (ps) time scale and thus the most likely process. During IVR the molecule relaxes from a higher vibrational level of an electronically excited state towards the vibrational ground state level of the excited state. In this case, the molecule stays in the same electronic state. However, when vibrational levels of two excited states overlap, another mode of relaxation, named internal conversion (IC) (see Fig. 1.1), becomes available. Here, the transition proceeds to a higher vibrational level of an energetically lower excited state potential energy surface, i.e., the electronic state is changed. However, the spin multiplicity is the same for the initial and final state. The time scale of IC typically is of the same order as for IVR. However, it can also fall in the sub-nanosecond (ns) range, depending on the character of the involved states. The nonradiative transition between a singlet and a triplet state named intersystem crossing (ISC) is spin-forbidden (forbidden by selection rules<sup>[26]</sup>). The rate of ISC is dependent on a few different factors, i.a., the energy separation of the involved electronic states and a relativistic effect named spin-orbit coupling (SOC)<sup>[27,28]</sup>. In this context, relativistic means that extremely fast motions, at speeds approaching that of light, are involved. SOC results from interaction (coupling) of the magnetic moments of electron spin and electron orbital angular momentum. Roughly speaking, a strong SOC between energetically close-lying electronic states enables efficient ISC.

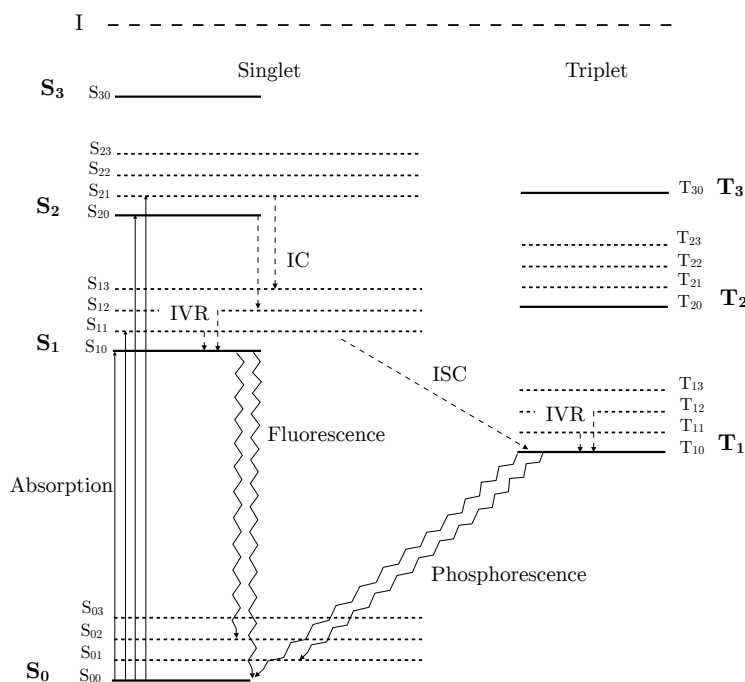


FIGURE 1.1: Jablonski-diagram illustrating possible decay processes occurring after vertical excitation at the Franck-Condon geometry. Spin singlet (S) and triplet (T) states are separated for clarity. The ionization level  $I$  is shown at the top. Ground state ( $S_0$ ) and the first three lowest lying excited singlet states ( $S_1$ - $S_3$ ) together with the three lowest lying excited triplet states ( $T_1$ - $T_3$ ) are shown in bold lines while vibrational sub-levels are represented by dashed horizontal lines. Typical nonradiative relaxation processes such as internal vibrational relaxation (IVR), internal conversion (IC) and intersystem crossing (ISC) and radiative decay processes like fluorescence and phosphorescence are shown.

According to Kasha's rule<sup>[29]</sup> spontaneous emission (fluorescence or phosphorescence) commonly occurs from the lowest vibrational level of the lowest lying electronically excited state. Fluorescence emission results from a spin-allowed transition between two states with the same spin and has short lifetimes typically in the order of a few nanoseconds. Phosphorescence emission, in contrast, results from a spin-forbidden transition from an excited triplet to the singlet ground state. The lifetime of phosphorescence can vary from sub-picoseconds to several seconds. In solution some, additional effects emerge which can strongly affect the photochemical behavior. After IVR and IC the excess vibrationally energy can be dissipated to the solvent molecules. This can either lead to wavelength shifts in absorption and emission spectra, reduce fluorescence emission or quench it completely. The induced shift in the absorption or emission spectrum of the molecule in response to interactions with the solvent is known as solvatochromism.<sup>[30]</sup> The extent of the effect on the photochemistry of a molecule can vary significantly from solvent to solvent. If the spectral bands are shifted to larger wavelengths (lower energies) one speaks of a

bathochromic or red shift. A shift of the bands to shorter wavelengths (higher energies) is called a hypsochromic or blue shift.

One central concept in computational photochemistry is the so-called *potential energy surface* (PES) of an electronic state. A PES (see Fig. 3.1) is a mathematical function that gives the relationship between the potential energy of a molecular system and its geometry. It is a very powerful and convenient tool for aiding analysis of photochemical reactions. This concept assumes that each molecular geometry has its unique energy. Thus, geometric changes create a smooth energy "landscape". Each electronic state has its own PES. After excitation to an excited state, the molecule can take different paths on the energy landscape. It can either stay on the PES of the initially excited state and relax to a nearby minimum. It can also change the PES through a so-called *conical intersection*. A conical intersection (CI)<sup>[31,32]</sup> is a particular molecular configuration for which the energies of two (or more) PESs of the same symmetry are degenerate (see Fig. 3.1). At this particular point in the nuclear configuration space the two PESs intersect. CIs are very important regions of the molecular energy landscape because their position, relative to the Franck-Condon point, determines the photostability of a molecule. Generally, the larger the molecular system, the more complex the topology of the PESs, and thus the more variable the photochemistry of the molecular system.

Experimentally, photochemical processes and reactions can be studied using stationary and time-resolved spectroscopy. Two widely used spectroscopic techniques are absorption and fluorescence spectroscopy. Stationary absorption and fluorescence experiments yield sample properties, such as concentrations and photophysical properties. While information on optically allowed *bright* electronic states can be easily obtained from absorption or fluorescence spectra, this is not the case for forbidden *dark* states. The reason for this is that due to the small transition strength of forbidden transitions, coupling to the electromagnetic field is small, and thus signals are very weak and can hardly be detected. Information on excited-state dynamics, e.g., decay rates and life times, can be obtained by using time-resolved transient absorption and fluorescence up-conversion spectroscopy<sup>[33]</sup>, with which one can achieve very high temporal resolution of a few tens of femtoseconds<sup>[34,35]</sup>. For more details of these methods, the reader is referred to the book "Ultrafast Dynamics of Chemical Systems " by J.D. Simon<sup>[33]</sup>. With transient absorption spectroscopy, not only ultrafast processes like IC and ISC, but also the evolution of dark states can be investigated due to their high sensitivity. These methods are based on the pump-probe technique. Here, the sample is excited by an ultrashort laser pulse (the pump pulse) at a given

frequency. After a certain adjustable delay time, a probe pulse is applied, of which transmission is measured by a detector. The probe signal is monitored as a function of the time delay yielding information on the decay dynamics of the different excited state species.

Besides many advantages, these spectroscopic methods also present some severe limitations. They are usually not able to provide information on the nature of the excited states involved in a photochemical reaction. Furthermore, experimental setup related effects, such as noisy optical signals, background scattering and broadening of spectral lines often encumber the interpretation of experimental data. For instance, it is possible that two or more energetically close lying excited states are hidden behind one broad absorption band. However, to obtain fundamental insights into reaction mechanisms or structure-property relationships, it is substantial to receive detailed information on all excited states, including forbidden dark states. This information can be obtained from quantum chemical electronic structure calculations. For this reason, many photochemical studies involve both experimental and computational methods which complement each other well.

A profound understanding of photochemical processes and reactions can help to further improve and refine current ideas, principles, and theories in the research area of chemistry and related fields and can also be profitable for industry. Accurate information on excitation energies, transition probabilities and possible reaction pathways is needed to gain such a profound understanding. This information is provided by quantum chemical electronic structure methods.

---

## INTRODUCTION

---

*“Anybody who has been seriously engaged in scientific work of any kind realizes that over the entrance to the gates of the temple of science are written the words: Ye must have faith. It is a quality which the scientist cannot dispense with”*

Max Planck

Charge-transfer (CT) states are ubiquitous in chemistry and biology.<sup>[36–40]</sup> They participate in many photochemical reactions and processes and can strongly influence reaction dynamics and the photophysical behavior of a molecular system.<sup>[41–44]</sup> In general, CT states involve a pronounced electron density transfer, and thus typically exhibit strikingly large electric dipole moments. This property, in most cases, distinguishes them from the other photochemically relevant excited state types like optically allowed bright  $\pi\pi^*$ , local  $\pi\pi^*$ ,  $n\pi^*$  or Rydberg states. The charge transfer can occur within a molecule (*intramolecular CT*) or between different molecules (*intermolecular CT*). In an intramolecular CT transition electron density is transferred from one part of the molecule, the donor moiety, to a different part of the molecule, the acceptor moiety. An example for a typical intramolecular CT state is shown in Fig. 2.1. In an intermolecular CT transition an electron is transferred from one molecule to another molecule or in a molecular complex, e.g., dimers, oligomers, polymers or inorganic metal complexes, from one molecular entity to another.

Inter- and intramolecular CT states, for instance, play a crucial role in organic semiconducting materials applied in photovoltaics.<sup>[43,45]</sup> Here, commonly electron donor compounds like conjugated polymers are combined with electron acceptors, e.g., fullerenes to form charge-transfer

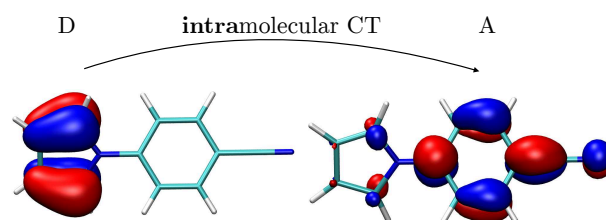


FIGURE 2.1: Schematic illustration of the energetically lowest intramolecular charge-transfer state of the donor- (D) acceptor (A) molecule N-pyrrolobenzonitrile (PBN) at its ground state equilibrium (or Franck-Condon) geometry. The surface plots correspond to molecular orbitals.

complexes.<sup>[45–47]</sup> Upon photoexcitation of the donor, an electron is transferred to the acceptor and subsequently the charges (hole and electron) get either separated or the electron-hole pair recombines. In order to generate an electrical current efficient charge separation and thus stable CT states are needed. Intermolecular CT states also play an important role in photoredox catalysis<sup>[48,49]</sup>, a powerful tool in synthetic organic chemistry, namely in form of metal-to-ligand charge-transfer (MLCT) states. In a MLCT state, charge is transferred from the ligands to the metal center and vice versa. The spatial separation of charge within the molecular complex is the underlying reason for the redox activity of the excited state.

## 2.1 TWISTED INTRAMOLECULAR CHARGE-TRANSFER

A particularly interesting class of intramolecular CT states are *twisted intramolecular charge-transfer* (TICT) states.<sup>[40,50–55]</sup> It has been found that when a molecule has an electron donor group and an acceptor group, joined by a flexible single bond, after photoexcitation to a bright optically allowed excited state often an electron is transferred from the donor to the acceptor, thereby undergoing a torsional motion about the flexible connecting single bond. This process results in the formation of a highly polar TICT state in which the electronic  $\pi$ -system is decoupled. In the molecular orbital (MO) picture this means that the involved  $\pi$  MOs are (almost) completely decoupled. In this state, typically, the molecule has a conformation in which donor and acceptor groups are twisted against each other by  $\approx 90^\circ$ . The energies of TICT state are strongly solvent polarity dependent. This is because TICT states typically exhibit unusual large electric dipole moments. Generally TICT states are stabilized in polar solvents; thus, their energies are lowered. TICT compounds find a wide range of applications in chemistry and biology<sup>[51,56,57]</sup>, e.g., as fluorescent “molecular rotors” for probing microenvironmental viscosity, the stability of biomembranes or conformational changes in macromolecules.<sup>[40,58]</sup> TICT compounds can also be used

as polarity probes and as optically controllable molecular switches<sup>[59,60]</sup>. Moreover, they find application in the field of optoelectronics, e.g., in organic light emitting diodes (OLEDs) in which their hybridized local and charge-transfer (HLCT) states enhance the electroluminescence efficiencies of OLEDs.<sup>[40,61]</sup>

Furthermore, TICT state formation is often accompanied by an unusual fluorescence behavior called *dual fluorescence*.<sup>[54,62–68]</sup> This particular fluorescence behavior was the reason why TICT got into the focus of research about 50 years ago.<sup>[69]</sup> Dual fluorescence can be described as an anomalous photophysical phenomenon, observed in certain donor-acceptor compounds exhibiting two-color emission that involve two distinct excited state species: an optically allowed locally excited (LE) and a polar CT state (see Fig. 2.2). Thus, in case of dual fluorescence, the emission spectrum shows two bands, a “normal” short-wavelength band, corresponding to the LE state, and a red-shifted “anomalous” band, corresponding to the polar CT state. While the energy of the LE band is rather insensitive with respect to solvent polarity, the energy of the anomalous CT band is dependent on solvent polarity. Usually, the more polar the solvent, the more intense the anomalous band and the stronger the red shift. Dual fluorescence was first observed in the early 60’s for the small organic donor-acceptor molecule N-dimethylaminobenzonitrile (DMABN) in polar solution<sup>[70,71]</sup>. The structure of DMABN and a schematic illustration of its fluorescence spectrum are depicted in Fig. 2.2. Since the discovery of dual fluorescence, a lot

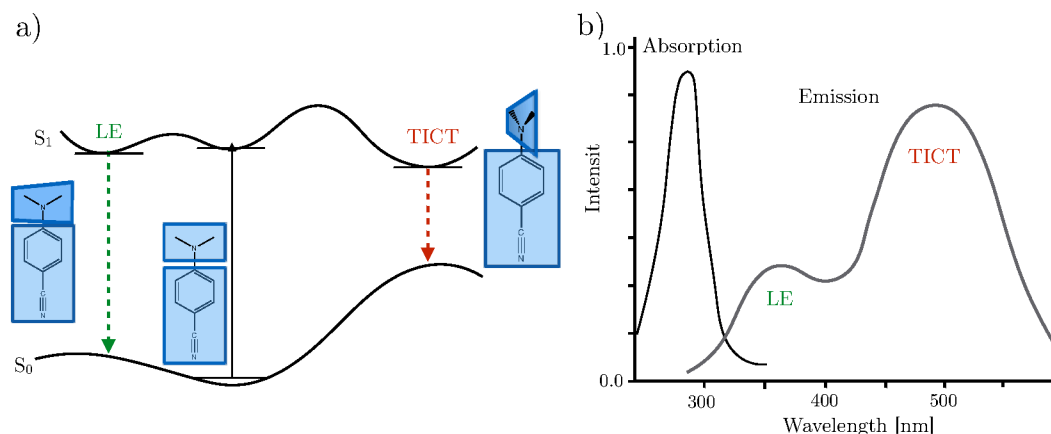


FIGURE 2.2: a) Sketch of experimental absorption and emission spectra of the TICT compound DMABN in polar acetonitrile solution. The emission spectrum shows dual fluorescence. (The spectra are adapted from refs<sup>[72,73]</sup>) b) Schematic illustration of the TICT mechanism. After vertical excitation two minima on the  $S_1$  state PES may be populated. The almost planar LE state minimum and the TICT state minimum.

of research, both experimentally and theoretically, has been done to understand the underlying photochemical mechanism, and to determine the nature of the highly polar state. This is true

for DMABN<sup>[54,74–79]</sup>, but also for numerous other donor-acceptor systems.<sup>[80–86]</sup> Corresponding to the TICT model<sup>[87,88]</sup>, which, today is the most generally accepted one and also effective in DMABN<sup>[54,89]</sup>, the polar CT state corresponds to a TICT state (see Fig. 2.2 a)). In contrast, the alternative PICT model<sup>[75,90]</sup> postulates a planar structure of the CT state. A direct measurement of the structure of the emitting excited states is experimentally challenging.

Here, *ab initio* quantum chemical electronic structure calculations come into play, since they provide stable excited state geometries, so-called equilibrium geometries, energies and also information on the nature of the excited states.

The major part of this thesis is concerned with the application of quantum chemical electronic structure methods to study the photochemistry of some small- and medium-sized organic donor-acceptor compounds with a focus on intramolecular CT states.

The subsequent part of this thesis is organized as follows. A short introduction and discussion of the employed methods is given in **chapter 3**. Here, the focus is on the key concepts of these methods. **Chapter 4** considers the fluorescence behavior of the small donor-acceptor molecule N-pyrrolobenzonitrile (PBN). New insights concerning its dual fluorescence and the underlying TICT mechanism are presented. In **chapter 5** the photochemistry of thiophene analogues of PBN is investigated; notably the two isomers 5-(1H-pyrrole-1-yl)thiophene-2-carbonitrile (2-TCN) and 5-(1H-pyrrole-1-yl)thiophene-3-carbonitrile (3-TCN). This study reveals the interesting and somewhat unexpected fact that TCN exhibits a different photochemistry compared to the dual fluorescent molecules DMABN and PBN even though it is structurally closely related to those molecules. Here, *ab initio* computations show that TICT formation is efficiently quenched by internal modes of thiophene.

**Chapter 6** deals with the question whether 4-Fluoro-N,N-dimethylaniline (FDMA), the fluorinated derivative of DMABN, like DMABN exhibits dual fluorescence or not. It is shown that FDMA most likely shows only single fluorescence. In **chapter 7** the photochemical cis-trans isomerization of four different donor substituted hemistilbene-hemithioindigo (HTI) derivatives is investigated. Hereby, special emphasis is put on the role of TICT state formation as competing deactivation mechanism in polar solvents.

The content of **chapter 8** concerns a unique crystal packing motif found in a particular  $\pi$ -extended pyraacene based molecule named tris(quinoxalinophenanthrophenazine (tQPP) and the influence of attractive dispersion interactions on the molecular structure and the crystal packing. In **chapter 9** the primary results of this work are summarized and a brief outlook on possible further

steps and future projects are given.

Overall, this work aims to provide new insights into the photochemistry of several organic donor-acceptor molecules and thus to make a small contribution to the field of quantum chemistry.

Some of the results presented and discussed in this dissertation have already been published by myself and by my coauthors. These publications are listed below in chronological order:

- **Solvent Polarity Tunes the Barrier Height for Twisted Intramolecular Charge Transfer in N-pyrrolobenzonitrile (PBN)**, Bohnwagner MV, Burghardt I, Dreuw A, *Journal of Physical Chemistry A*, **2016**, *120*(1), pages 14-27.
- **Attractive Dispersion Interactions Versus Steric Repulsion of tert-Butyl groups in the Crystal Packing of a  $D_{3h}$ -Symmetric Tris(quinoxalinophenanthrophenazine)** Kohl B, Bohnwagner MV, Rominger F, Wadepl H, Dreuw A, Mastalerz M, *Chemistry-A European Journal*, **2016**, *22*, pages 646-655.
- **Regular and red-shifted fluorescence of the donor-acceptor compound 5-(1H-pyrrole-1-yl)thiophenecarbonitrile (TCN) is efficiently quenched by internal modes of thiophene**, Bohnwagner MV, Burghardt I, Dreuw A, *Physical Chemistry Chemical Physics*, **2017**, *19*(21), pages 13951-13959.
- **Regular Fluorescence of 4-Fluoro-N,N-dimethylaniline: No Charge Transfer and No Twisting**, Bohnwagner MV, Dreuw A, *Journal of Physical Chemistry A*, **2017**, *121*(31), pages 5834-5841.



---

## THEORETICAL BACKGROUND AND METHODOLOGY

---

This chapter aims to provide the theoretical background on which the quantum chemical studies presented in the subsequent chapters are based. It is organized into two parts: Since quantum chemical investigations always involve the solution of the Schrödinger equation, at first I will introduce both the time-independent and time-dependent versions of the Schrödinger equation. In this context also some important quantum mechanical concepts, approximations and tools which were developed to reduce the complexity of the mathematical problem of solving the Schrödinger equation are presented and discussed. In the second part, an overview of some conventional *ab initio* methods is given, which are based on those concepts and approximations and aim to approximately solve the Schrödinger equation. To keep the whole work as compact and concise as possible, the focus thereby lies on the basic ideas of these methods, relations between them and their advantages and limitations. From a detailed mathematical derivation is refrained here and the reader is referred to the cited literature.

At first, I will present and discuss ground state methods. For this purpose, I will begin with the Hartree-Fock (HF) method since firstly, it is one of the early *ab initio* methods and secondly, because, even though conceptually very simple, it is highly relevant because it forms the basis for a variety of more sophisticated, so-called post HF methods. After this, I will proceed to Density Functional Theory (DFT) which was developed shortly after the HF method and the development of which was honored with the Nobel Prize in Chemistry 1998. At next, two more advanced, post HF methods will be presented namely second-order Møller Plesset perturbation theory (MP2) and second-order approximate coupled cluster singles and doubles theory (CC2). At the end, the employed excited state methods are discussed such as time-dependent variants

of DFT, i.e. TD-DFT and CC2 i.e. linear response CC2 and the Algebraic Diagrammatic Construction (ADC) scheme of the polarization propagator methods. One method I want to mention here, a version of which has been used in **chapter 8** to compute the total intermolecular interaction energy of a number of dimers, which, however, will not be further discussed, is symmetry-adapted perturbation theory (SAPT)<sup>[91-94]</sup>. Due to technical reasons, instead of the original, computationally very demanding SAPT method (with scaling of  $O(N^7)$  with  $N$  being the number of electrons) a hybrid approach including empirical dispersion corrections named XSAPT(KS)+D<sup>[95-97]</sup> has been employed. Some details about this method are given in the context of the respective study. More information can be found in the paper by J. Herbert et al.<sup>[97]</sup> Concerning the notation used in the equations given in this chapter, I adopt the convention to use lower-case italic letters  $i, j$  to refer to general orbitals. The letters  $a, b$  refer to occupied and  $r, s$  to unoccupied (virtual) orbitals. Capital letters are used to index nuclei. Lower-case Greek letters are used for basis set functions. Matrices and vectors are written in bold letters.

### 3.1 THE SCHRÖDINGER EQUATION

In 1926 Erwin Schrödinger<sup>[1]</sup> formulated a differential equation of which solution produces eigenfunctions in the form of spherical harmonics multiplied by polynomials in the radius and eigenvalues yielding the correct emission spectrum of the hydrogen atom. This work was motivated by the idea of finding a quantum mechanical atomic model able to describe the emission spectrum of the hydrogen atom by extending Niels Bohr's original atomic model from 1913<sup>[98]</sup>. In this model, Bohr assumed electrons to behave like particles moving in circular quantized orbits around the nucleus as in classical mechanics. The crucial advantage of Schrödingers work on this problem which probably is also the reason why it became so popular is that the whole derivation and discussion is well comprehensible. This wave equation which is one of the fundamental equations in quantum mechanics and which was of great importance for the development of quantum chemistry, is named, after its inventor, Schrödinger equation. The time-independent nonrelativistic molecular Schrödinger equation as an eigenvalue problem may be formulated as:

$$\hat{\mathcal{H}} \Psi = E \Psi \quad (3.1)$$

where  $\hat{\mathcal{H}}$  is the systems Hamilton operator, or Hamiltonian,  $\Psi$  the wave function (an eigenfunction of  $\hat{\mathcal{H}}$ ) containing all information about the quantum state of the system and  $E$  (an eigenvalue of  $\hat{\mathcal{H}}$ ) its total energy. The molecular Hamiltonian eq. (3.2)<sup>[99]</sup> contains five energy contributions, i.e., the kinetic energy of the nuclei  $\hat{T}_N$ , the kinetic energy of the electrons  $\hat{T}_e$ , the Coulomb attraction between nuclei and electrons  $\hat{V}_{Ne}$ , the Coulomb repulsion between the electrons  $\hat{V}_{ee}$  and the Coulomb repulsion between the nuclei  $\hat{V}_{NN}$  and can be expressed as follows (using atomic units for simplicity: Planck-constant  $\hbar$ , the elementary charge  $e$ , the electron mass  $m_e$ , and the speed of light  $c$  are set to 1):

$$\hat{\mathcal{H}} = - \underbrace{\sum_I \frac{1}{2M_I} \nabla_I^2}_{\hat{T}_N} - \underbrace{\sum_i \frac{1}{2} \nabla_i^2}_{\hat{T}_e} - \underbrace{\sum_i \sum_I \frac{Z_I}{|\mathbf{r}_i - \mathbf{R}_I|}}_{\hat{V}_{Ne}} + \underbrace{\sum_{j>i} \frac{1}{|\mathbf{r}_i - \mathbf{r}_j|}}_{\hat{V}_{ee}} + \underbrace{\sum_{J>I} \frac{Z_I Z_J}{|\mathbf{R}_I - \mathbf{R}_J|}}_{\hat{V}_{NN}} \quad (3.2a)$$

with

$$\nabla^2 \equiv \frac{\partial^2}{\partial x^2} + \frac{\partial^2}{\partial y^2} + \frac{\partial^2}{\partial z^2},$$

where  $Z$  is the nuclear charge and  $M$  the atomic mass. The time-dependent variant of the Schrödinger equation may be expressed in the following form:

$$i\hbar \frac{d}{dt} \Psi(t) = \hat{\mathcal{H}}(t) \Psi(t) \quad (3.3)$$

In general, for computation of the ground state energy the time-independent Schrödinger equation has to be solved for the lowest eigenvalue  $E_0$  and associated eigenfunction. To obtain excitation energies, transition moments and other properties like electric dipole moments the time-dependent Schrödinger equation has to be solved. This, however, is an extremely challenging or rather impossible endeavor, since, for the exact solution of the Schrödinger equation, the exact wave function has to be known. The exact wave function contains all information about the system, e.g., number and position of electrons and nuclei and their mutual interactions, the mathematical problem quickly becomes too complex to be solved exactly, at least at the current state of computer technology. The largest molecular systems for which exact solutions can be obtained consist of maximal two atoms the famous ones being the hydrogen atom and the hydrogen molecule  $\text{H}_2$ .

### 3.2 BORN-OPPENHEIMER APPROXIMATION AND FRANCK-CONDON PRINCIPLE

Fortunately, only one year after publication of the time-independent Schrödinger equation, Max Born and J. Robert Oppenheimer<sup>[100]</sup> presented a brilliant idea how to simplify it. Roughly speaking, they showed that the motion of nuclei and electrons can be separated, resulting in a separate nuclear  $\hat{H}_{nuc}$  and electronic  $\hat{H}_{elec}$  Hamiltonian and thus also in an electronic and a nuclear part of the Schrödinger equation, which can be solved separately.<sup>[100]</sup> This approach is today known as the *Born-Oppenheimer approximation* or *adiabatic approximation* and is the heart of almost any quantum chemical treatment. Born and Oppenheimer assumed, that such a separability of the total energy is possible since atomic nuclei are much more heavy than electrons, and thus stay still while the electrons move. This means that the correlation between the movements of electrons and nuclei is neglected. It is assumed that electrons adiabatically follow geometry changes in the molecule. Consequently, it can be assumed that the electronic wave function  $\Psi_{elec}$  depends on the electronic coordinates  $\mathbf{r}_i$  and only parametrically on the nuclear coordinates  $\mathbf{R}_I$  and the electronic Schrödinger equation can be expressed as:

$$\underbrace{\left[ -\sum_I \frac{1}{2M_I} \nabla_I^2 - \sum_i \sum_J \frac{Z_I}{|\mathbf{r}_i - \mathbf{R}_I|} + \sum_{j>i} \frac{1}{|\mathbf{r}_i - \mathbf{r}_j|} \right]}_{\hat{H}_{elec}} \Psi_{elec}(\mathbf{r}_i; \mathbf{R}_I) = E_{elec}(\mathbf{R}_I) \Psi_{elec}(\mathbf{r}_i; \mathbf{R}_I) \quad (3.4)$$

Parametric dependence means that for a different arrangement of nuclei,  $\Psi_{elec}$  is a different function of the electronic coordinates. The total energy  $E_{tot}$  also includes the constant nuclear repulsion  $V_{NN}(\mathbf{R}_I)$  and is thus given as:

$$E_{tot}(\mathbf{R}_I) = E_{elec}(\mathbf{R}_I) + V_{NN}(\mathbf{R}_I) \quad (3.5)$$

When  $E_{tot}(\mathbf{R})$  is computed for different nuclear configurations a potential energy surface (PES) is obtained. An example for two simple one-dimensional PESs along an arbitrary reaction coordinate, e.g., a bond length, is depicted in Figure 3.1. These one-dimensional PESs represent cuts through the multidimensional energy landscape of the molecule along the excited nuclear motion coordinate. Local minima on a PES correspond to equilibrium geometries, meaning stable molecular configurations with minimal energy. Since all quantum chemical investigations presented in this work involved solution of the electronic Schrödinger equation only, I will omit

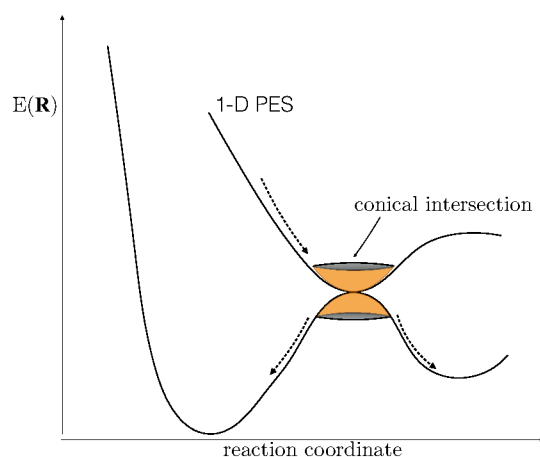


FIGURE 3.1: Schematic representation of two different one-dimensional potential energy surfaces of an arbitrary polyatomic molecule as a function of the reaction coordinate. Furthermore, a conical intersection of the two potential energy surfaces is shown.

discussion of the nuclear Schrödinger equation and focus solely on the electronic problem eq. (3.4 and 3.5) in the rest of this chapter.

Even though the Born-Oppenheimer (BO) approximation is a rather severe approximation, it is valid for many quantum chemical problems. It holds as long as the PESs of the electronic states are energetically well separated and relativistic effects (e.g., spin-orbit coupling or vibronic coupling)<sup>[101]</sup> do not play a role. However, in regions of nuclear coordinate space where two electronic states approach one another closely energetically and nonadiabatic coupling<sup>[102]</sup> becomes important, e.g. at avoided crossings or conical intersections<sup>[102]</sup> (see Fig. 3.1) the approximation breaks down. This is because the nonadiabatic coupling terms contained in the coupled nuclear Schrödinger equations, which describe the dynamical interaction between the electronic and nuclear motion, are assumed to be zero within the BO approximation. This is why it is also named adiabatic approximation. Adiabatic, from the Greek word *adiabatos* for “impassable” means that adiabatic PESs are not allowed to cross one another. In other words, the transition from one adiabatic PES to another is “not allowed”.

The *Franck-Condon principle* (see Fig. 3.2) for electronic transitions introduced in 1926-28<sup>[23,103,104]</sup> by James Franck and Edward U. Condon is closely related to the BO approximation and of equal importance. This rule is not only used in computational quantum chemistry, but also in spectroscopy connecting both fields. It was introduced to explain the intensity distribution of transitions between vibrational states of two electronic states, the vibronic transitions. On the one hand, the Franck-Condon (FC) principle states that an electronic transition which usually also

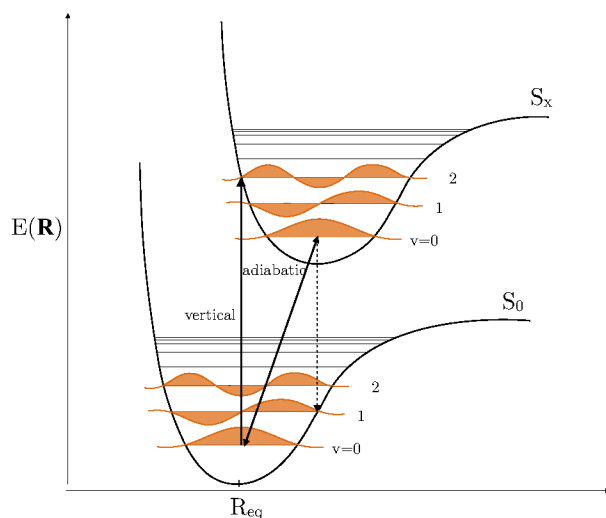


FIGURE 3.2: Illustration of the Franck-Condon principle. After photon absorption a vertical transition (bold arrow) from the lowest lying vibrational state ( $v = 0$ , indicated in orange) of the ground state  $S_0$  to a vibrational state of an excited state  $S_x$  occurs. If the overlap of initial and final vibrational wave function is large, the transition is intense and a strong absorption band will be observable in experiment. The dotted arrow indicates the vertical emission.

involves a vibrational transition is more likely to occur if initial and final vibrational wave functions ( $\vartheta_i$ , and  $\vartheta_f$ ) exhibit large overlap integrals or a large Franck-Condon factor  $|\langle \vartheta_i | \vartheta_f \rangle|^2$ .<sup>[105]</sup> As a consequence, the band shape corresponding to an electronic transition (this only holds for symmetry allowed transitions) depends on the displacement of the excited electronic state with respect to that of the ground state.<sup>[105]</sup> If the geometries of final excited state and ground state are similar, i.e., the displacement small, then the overlap between vibrational levels  $v = 0$  of ground and excited state is largest and the 0-0 transition is the most intense one. The corresponding energy  $E_{0-0}$  can be measured for most molecules, however, usually does not correspond, and thus should not be directly compared, to the computed vertical excitation energy.

On the other hand, the FC principle also states that electronic transition occurs instantaneously, i.e., *vertically*, why it is also called vertical or nonadiabatic transition (see Fig. 3.2).<sup>[105]</sup> The resulting excited state is referred to as Franck-Condon state. Analogous to the BO approximation the FC principle stipulates that only the light electrons will move during the ultrafast vertical transition while the heavy nuclei have no time to readjust themselves, such that the molecule can be assumed to remain in the same geometry during this process.<sup>[105]</sup> A concept, which to some extent follows from the FC principle, is vibrational selection rules. Those rules determine how likely, hence, how intense a vibrational transition is. In other words, they determine if the transition is forbidden or allowed. If, for instance, the overlap of vibrational wave functions is small than the transition is considered to be FC forbidden, and the corresponding optical band

will only have a small intensity, if observable at all.

The FC principle is also related to another famous rule named *Fermi's Golden Rule*<sup>[106]</sup>. Based on time-dependent perturbation theory it yields an expression for the transition rate  $k_{fi}$  eq. (3.6) of a transition between two electronic states of a molecule induced by an oscillating electromagnetic field and can be expressed as:

$$k_{fi} = \frac{2\pi}{\hbar} |\langle f | \mathcal{V} | i \rangle|^2 \varrho \quad (3.6)$$

where  $\langle f | \mathcal{V} | i \rangle$  is the transition dipole matrix element of the perturbation determining the coupling strength between electrons and electromagnetic field and  $\varrho$  is the state density. For a quantum chemical investigation of absorption and emission processes, the corresponding computable quantity is the transition dipole moment matrix element  $D_{fi} = \langle \Psi_f | \hat{\mu}_{tot} | \Psi_i \rangle$  with  $\hat{\mu}_{tot}$  being the molecular dipole operator including an electronic and a nuclear part. However, within the BO approximation the total wave function  $\Psi$  and also the dipole moment operator can be separated into electronic and nuclear parts yielding the following expression for  $D_{fi}$ :

$$D_{fi} = \langle \psi_f | \mu_{elec} | \psi_i \rangle \langle \vartheta_{f,v_f} | \vartheta_{i,v_0} \rangle \quad (3.7)$$

where  $\langle \psi_f | \mu_{elec} | \psi_i \rangle$  being the electronic transition dipole moment  $\mu_{fi}$  and  $\langle \vartheta_{f,v_f} | \vartheta_{i,v_0} \rangle$  the overlap integral of the two vibrational wave functions of final and initial states. While, as pointed out above, the FC factor  $|\langle \vartheta_{f,v_f} | \vartheta_{i,v_0} \rangle|^2$  determines the intensity of the vibrational transitions the square of electronic transition dipole moment  $|\mu_{fi}|^2$ , also called dipole strength determines the magnitude of the pure electronic transition. The dipole strength, in turn, is related to the quantum chemical quantity determining the strength of a vertical electronic transition referred to as oscillator strength  $f$ . The oscillator strength<sup>[107]</sup> is proportional to the square of the electronic transition dipole moment  $\mu_{fi}$  and can be expressed as:

$$f = K |\mu_{fi}|^2 \cong 10^{-5} \tilde{\nu} |e \mathbf{r}_{fi}|^2 \quad (3.8a)$$

with K given as

$$K = \frac{8\pi m_e \tilde{\nu}}{3\hbar e^2}, \quad (3.8b)$$

where  $m_e$  is the electron mass,  $\tilde{\nu}$  the energy of the transition (in  $cm^{-1}$ ),  $\hbar$  the Planck constant and  $\mathbf{r}_{fi}$  the length (in cm) of the transition dipole.  $f$  is a unit-less value and is used throughout this work as a measure of the strengths of the considered electronic transitions.

Even though the BO approximation significantly reduces the complexity of the molecular Schrödinger equation, the remaining electronic problem is still too complex to be solved exactly for molecules having more than three atoms. The reason for this lies in the Coulomb repulsion term  $V_{ee} = \sum_{j>i} \frac{1}{|r_i - r_j|}$  which describes the electron-electron interaction between each pair of electrons of the system. It means that the behavior of each electron affects that of all others. Due to this correlated behavior, it is not possible to simply solve the electronic Schrödinger equation one electron at a time. This effect is also called *electron correlation* that, obviously, is a very crucial effect. For this reason, many different approaches have been developed to treat electron correlation at least in an approximate manner.

### 3.3 GROUND STATE SELF-CONSISTENT FIELD METHODS

The following chapter strongly follows the books "Modern Quantum Chemistry" by Szabo et al.<sup>[108]</sup> and "Essentials of Computation Chemistry Theories and Models" by C. J. Cramer<sup>[99]</sup>.

A very convenient way to approximately solve the electronic Schrödinger equation is given by the *self-consistent field* (SCF) method which is the basis of many other ground and excited state methods. Here, an approximate trial wave function and an approximate Hamiltonian are employed to iteratively solve the Schrödinger equation to obtain a more accurate solution which is then used for the next iteration step to solve the equation again until the results converge. The trick of this method is, to transform the Schrödinger equation of an  $N$ -electron system into a set of easily solvable equations, one for each electron. As the name suggests, it in some way involves a field. In the following two subsections, I will present and discuss two basic and widely used SCF methods namely Hartree-Fock (HF) and Kohn-Sham density functional theory (KS-DFT) and in this context, I will also elaborate on the nature of the field mentioned above. For this purpose, first, some important mathematical concepts will be introduced like the Slater determinant.

#### The Slater Determinant

A very convenient mathematical tool with particularly advantageous properties is the Slater determinant<sup>[109]</sup>, a determinant of one-particle orbitals eq. (3.10). In connection with the development of the Hartree-Fock method, Fock and Slater were looking for a way to express

the many-electron wave function  $\Psi(\mathbf{r})$  such that the electron spin being an essential quantum mechanical property is considered and the *Pauli exclusion principle*<sup>[110]</sup> is satisfied. This principle states that no two electrons in an atom or molecule can be in the same quantum state. In other words, this requires that the wave function must be antisymmetric with respect to the simultaneous interchange of both the spatial and spin coordinates of two electrons.<sup>[108]</sup> They found that a determinant build up of single-electron wave functions (or single-particle orbitals), is well suited for such a description since it naturally satisfies the Pauli exclusion principle namely by changing sign when two rows (columns) are interchanged. For the construction of the Slater determinant commonly, *spin orbitals*  $\chi(\mathbf{x})$  are used which are defined as products of a *spatial*  $\psi(\mathbf{r})$  and a spin  $\alpha(\omega)$  (spin up) or  $\beta(\omega)$  (spin down) function i.e.,  $\chi(\mathbf{x}) = \psi(\mathbf{r})\alpha(\omega)$  and  $\chi(\mathbf{x}) = \psi(\mathbf{r})\beta(\omega)$  with  $\mathbf{x}$  indicating both space and spin coordinates. For mathematical convenience, spatial orbitals  $\psi(\mathbf{r})$  which are also called molecular orbitals (MOs) are expressed in terms of a (finite) basis set, i.e. as linear combinations of known spatial basis functions. This ansatz is also called linear combination of atomic orbitals (LCAO). For this purpose, typically Gaussian functions are used, since they have the great advantage that they are easy to integrate, both analytically and numerically. However, Gaussian functions are not optimal basis functions as their functional behavior deviates from the known functional behavior of MOs. Thus, in practice, a number of so-called primitive Gaussian functions is linearly combined (contracted) in a way, such that the resulting contracted Gaussian functions (or Gaussian type orbitals GTOs) approximate the functional form of the spherical harmonic solutions of the hydrogen atom (which represent optimal basis functions for MOs).<sup>[99]</sup> The resulting Gaussian basis sets can be categorized according to the number of contracted GTOs used to describe a single orbital. A double- $\zeta$  (DZ) basis set e.g., would have two contracted GTOs per single orbital. Optionally, the default basis sets of which most of them already include some diffuse and polarization functions can be extended with additional diffuse or polarization functions or both which can be advantageous or also necessary in certain situations. By adding extra diffuse function, for instance, the charge distribution of heavy atoms like sulfur is better described. Thus, a set of MOs  $\{\psi_i(\mathbf{r})\}$  may be obtained by the following expansion:

$$\psi_i(\mathbf{r}) = \sum_{\mu=1}^K c_{\mu i} \phi_{\mu}(\mathbf{r}) \quad (3.9)$$

where  $\{\phi_{\mu}(\mathbf{r})\}$  are the known spatial basis functions. An SCF calculation aims to optimize the expansion coefficients  $c_{\mu i}$  with respect to the ground state energy. The details about this procedure will be given further below.

A further important feature of the Slater determinant is that it introduces exchange-correlation effects which means that the motion of electrons with parallel spin ( $\uparrow\uparrow$  or  $\downarrow\downarrow$ ) is correlated, or in other words, electrons with the same spin naturally avoid each other. exchange-correlation, however, only arise in the case of parallel spin. For electrons with opposite spin, the motion remains uncorrelated. For an  $N$ -electron system with corresponding  $N$  spin orbitals ( $\chi_i, \dots, \chi_k$ , or any other one-electron orbital) the antisymmetric wave function can expressed as follows (using a generalized form):

$$\Psi(\mathbf{x}_1, \mathbf{x}_2, \dots, \mathbf{x}_N) = (N!)^{-\frac{1}{2}} \begin{vmatrix} \chi_i(\mathbf{x}_1) & \chi_j(\mathbf{x}_1) & \cdots & \chi_k(\mathbf{x}_1) \\ \chi_i(\mathbf{x}_2) & \chi_j(\mathbf{x}_2) & \cdots & \chi_k(\mathbf{x}_2) \\ \vdots & \vdots & \ddots & \vdots \\ \chi_i(\mathbf{x}_N) & \chi_j(\mathbf{x}_N) & \cdots & \chi_k(\mathbf{x}_N) \end{vmatrix} \quad (3.10a)$$

or alternatively

$$\Psi(\mathbf{x}_1, \mathbf{x}_2, \dots, \mathbf{x}_N) = |\chi_i \chi_j \cdots \chi_k\rangle$$

Every electron appears in every spin orbital somewhere in the expansion accounting for the indistinguishability of electrons.

### 3.3.1 Hartree-Fock Theory

One reason why the *Hartree-Fock method* or HF approximation is so essential is that its result namely the variationally-optimized HF wave function serves as starting point for various other more advanced *ab initio* methods like Møller Plesset perturbation theory which will be discussed in the next sections.

The central ideas of the HF method are the following: Firstly, a single Slater determinant  $|\Psi_0\rangle$  is used as approximate ground state wave function of the  $N$  electron system described by the electronic Hamiltonian  $\mathcal{H}$ .  $\mathcal{H}$  is replaced by the one-electron *Fock* operator  $f(i)$  eq. (3.11) containing the so-called HF potential  $v^{HF}(i)$ .

$$f(i) = -\frac{1}{2}\nabla_i^2 - \sum_I^{nuc} \frac{Z_I}{|r_i - R_I|} + v^{HF}(i) \quad (3.11)$$

Note here, that there is a key distinction between the Hamiltonian  $\mathcal{H}$  and the Fock operator  $f(i)$ .  $\mathcal{H}$  returns the electronic energy of the many-electron system. The Fock operator, however, is the

one-electron operator used to find the optimal HF one-electron MOs from which the HF wave function (Slater determinant) is constructed.

Thirdly, instead of solving the exact electronic Schrödinger equation, the variational principle is used to derive HF equations which yield the best possible (variational) ground state wave function and the best possible ground state energy  $E_0^{HF}$  which can be expressed as:

$$E_0^{HF} = \sum_a^{occ} h_{aa} + \frac{1}{2} \sum_{ab}^{occ} (\langle ab|ab \rangle - \langle ab|ba \rangle) = \sum_a^{occ} \varepsilon_a - \frac{1}{2} \sum_a^{occ} \sum_b^{occ} \langle ab||ab \rangle = E_0^{(0)} + E_0^{(1)} \neq \sum_a \varepsilon_a \quad (3.12)$$

using the following shorthand notation for two-electron integrals:

$$\langle ij||ij \rangle = \int \frac{\psi_i^*(\mathbf{r}_1)\psi_j^*(\mathbf{r}_2)\psi_i(\mathbf{r}_1)\psi_j(\mathbf{r}_1)}{|\mathbf{r}_1 - \mathbf{r}_2|} d\mathbf{r}_1 d\mathbf{r}_2 - \int \frac{\psi_i^*(\mathbf{r}_1)\psi_j^*(\mathbf{r}_2)\psi_j(\mathbf{r}_1)\psi_i(\mathbf{r}_2)}{|\mathbf{r}_1 - \mathbf{r}_2|} d\mathbf{r}_1 d\mathbf{r}_2$$

The term  $a = b$  does not make any contribution to the sum because the two terms  $\langle aa|aa \rangle - \langle aa|aa \rangle$  exactly cancel in this case. Hence, in HF theory self-interaction is corrected. This is one major difference between HF theory and DFT which will be discussed in more detail further below.

The variational theorem assures that the HF energy  $E_0^{HF}$  is an upper bound to the exact ground state energy  $E_0$ . It is noteworthy here, that  $E_0^{HF}$  is not the sum of one-electron energies (or eigenenergies of  $f(i)$ )  $\varepsilon_i$ , unlike the case of truly independent electrons. This discrepancy stems from the description of a true many-electron system in terms of single-electron functions. If one simply adds up all orbital energies, the electron-electron interaction is counted twice. This is because  $\varepsilon_a$  includes Coulomb and exchange interactions between the electron in orbital  $\phi_a$  (or  $\chi_a$ ) and electrons in all other occupied orbitals, hence, also with the electron in  $\phi_b$ . The same, however, is true for  $\varepsilon_b$ . The term  $-\frac{1}{2} \sum_a \sum_b \langle ab||ab \rangle$  corrects for the double counting. This term is important and will reappear in the section on second-order Møller-Plesset perturbation theory (MP), namely in form of the first order energy  $E_0^{(1)}$  given as  $\langle \Psi_0^{(0)} | V | \Psi_0^{(0)} \rangle = -\frac{1}{2} \sum_a \sum_b \langle ab||ab \rangle$

The essence of the HF method is to simplify the whole electronic problem by replacing the explicit electron-electron repulsion term in the Hamiltonian by the single particle potential  $v^{HF}(i)$  (see Fig. 3.3). The trick hereby is to treat electron correlation in an average way. The HF potential  $v^{HF}(i)$  can be viewed as the “field” seen by the  $i$ th electron which is generated by all other electrons on average. For this reason the HF method it is also often referred to as *mean field* approach. The general form of the HF equations eq. (3.13) is obtained by minimizing the energy expression  $E_0[\Psi_0] = \langle \Psi_0 | \mathcal{H} | \Psi_0 \rangle$ . In the spin-orbital basis they have the following form (where

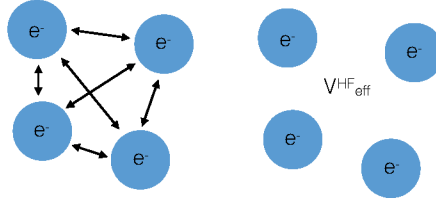


FIGURE 3.3: Schematic representation of the basic idea of the HF approximation. Electron correlation (left) is treated in an average way by introducing an effective potential called HF potential (right).

(1) indicates electron 1):

$$h(1)\chi_i(1) + \underbrace{\sum_{j \neq i} \left[ \int |\chi_j(2)|^2 \frac{1}{|r_1 - r_2|} d\mathbf{x}_2 \right]}_{\mathcal{J}} \chi_i(1) - \underbrace{\sum_{j \neq i} \left[ \int \chi_j^*(2) \chi_i(2) \frac{1}{|r_1 - r_2|} d\mathbf{x}_2 \right]}_{\mathcal{K}} \chi_j(1) \quad (3.13a)$$

$$= \varepsilon_i \chi_i(1)$$

where the one-electron operator  $h(1)$  is defined as:

$$h(1) = -\frac{1}{2} \nabla_1^2 - \sum_l \frac{Z_l}{|r_1 - r_l|}$$

where  $\varepsilon_i$  is the energy eigenvalue associated with spin orbital  $\chi_i$ .  $\mathcal{J}$  and  $\mathcal{K}$  are the *Coulomb* and *exchange* operator, respectively. The restriction  $j \neq i$  on the summation in the HF equations eq. (3.13) can be eliminated since  $[\mathcal{J}_i(1) - \mathcal{K}_i(1)] \chi_i(1) = 0$  resulting in the eigenvalue equations:

$$f|\chi_j\rangle = \varepsilon_j |\chi_j\rangle \quad (3.14)$$

Multiplying this equation with  $\langle \chi_i |$  reveals that the matrix representation of  $f(i)$  in the basis of spin orbital eigenfunctions is diagonal with diagonal elements corresponding to orbital energies:

$$\varepsilon_i = \langle \chi_i | [h(1) + \sum_b (J_b - K_b)] | \chi_i \rangle = \langle i | h | i \rangle + \sum_b \langle i b | i b \rangle - \langle i b | b i \rangle \quad (3.15)$$

Accounting for self-interaction  $\langle aa||aa \rangle$ , the corresponding expressions for occupied and unoccupied orbital energies are<sup>[108]</sup>:

$$\varepsilon_a = \langle a|h|a \rangle + \sum_{b \neq a} \langle ab|ab \rangle - \langle ab|ba \rangle \quad (3.16a)$$

$$\varepsilon_r = \langle r|h|r \rangle + \sum_b \langle rb|rb \rangle - \langle rb|br \rangle \quad (3.16b)$$

Since the Fock operator  $f(i)$  contains the potential  $v^{HF}(i)$  depending on the orbitals of all electrons (but the  $i$ th) which means that  $f(i)$  depends on its own eigenfunctions, the eigenvalue problem must be solved iteratively. The corresponding iterative procedure is called *Hartree-Fock self consistent field* method.

The exchange term  $\mathcal{K}$  in the HF equation has no intuitive classical interpretation, it arises from the antisymmetric nature of the Slater determinant. The Coulomb term arises due to the fact that electron 1 occupying orbital  $\chi_i$  experiences the Coulomb potential  $v_i(1) = \sum_{j \neq i} \int |\chi_j|^2 \frac{1}{|r_1 - r_2|} d\mathbf{x}_2$  which since the summation runs over all  $j \neq i$  is the total averaged potential arising from the  $N - 1$  other spin orbitals. According to this classical interpretation the Coulomb operator can be expressed as:

$$\mathcal{J}_j(1) = \int |\chi_j(2)|^2 \frac{1}{|r_1 - r_2|} d\mathbf{x}_2 \quad (3.17)$$

or alternatively:

$$\mathcal{J}_{ij} = \langle ij|ji \rangle \quad (3.18)$$

In this way it represents the average *local* potential (the locality is important and should be kept in mind) at  $\mathbf{x}_1$  arising from an electron in  $\chi_j$ . A similar definition can be formulated for the exchange operator  $\mathcal{K}_b(1)$ , however, in an indirect way by defining it by its effect on an electron in spin orbital  $\chi_i(1)$ :

$$\mathcal{K}_j(1)\chi_i(1) = \left[ \int \chi_j^*(2) \frac{1}{|r_1 - r_2|} \chi_i(2) d\mathbf{x}_2 \right] \chi_j(1) \quad (3.19)$$

or alternatively:

$$\mathcal{K}_{ij} = \langle ij|ji \rangle \quad (3.20)$$

Hence,  $\mathcal{K}$  causes an exchange of electron 1 and electron 2.  $\mathcal{K}$ , in contrast to the Coulomb operator  $\mathcal{J}(1)$  eq. (3.17) is said to be *nonlocal* (again this is an important fact and should be kept in mind) because there is no potential  $\mathcal{K}(\mathbf{x}_1)$  defined at a single point in space  $\mathbf{x}_1$ .

Instead of using spin orbitals, a computationally more convenient alternative approach to solve

the HF equations introduced by Clemens C. J. Roothaan<sup>[111]</sup> is to use a set of simple and easily integrable basis functions. In this context, it should be taken into account that there exists two types of spin orbitals: restricted ones which are constrained to have the same spacial functional for  $\alpha$  and  $\beta$  spin functions and unrestricted ones which have different spatial functions for the two spins, which leads to two different formalisms. Namely the restricted HF and the unrestricted HF formalism. For the sake of simplicity a restricted closed-shell systems will be assumed for the following derivation and discussion of the Roothaan equation eq. (3.21). This means, that it will be assumed that the ground state has an even number  $N$  of electrons all being spin-paired such that  $\frac{N}{2}$  spatial orbitals are occupied by two electrons with different spin. This formalism is called restricted closed-shell HF. It is well suited for systems which do not have a radical or open-shell character. For such systems alternative approaches are available such as restricted open-shell HF, multideterminantal methods (both are not discussed here) or the spin-flip approach which is presented further below. In order to convert the general spin orbital HF equation to a spatial eigenvalue equation, the spin orbitals have to be converted into spatial orbitals. This is achieved by integrating out the spin functions.

By introducing a set of  $K$  known basis functions  $\{\phi_\mu(\mathbf{r}) \mid \mu = 1, \dots, K\}$  and using the expansion  $\psi_i = \sum_{\mu=1}^K C_{\mu i} \phi_\mu$  for the spatial orbitals the HF equations are converted into the following matrix eigenvalue problem, i.e. the Roothaan equation:

$$\mathbf{FC} = \mathbf{SC}\boldsymbol{\varepsilon} \quad (3.21)$$

This equation is solved by the SCF method. The Fock matrix  $\mathbf{F}$  is a Hermitian matrix with elements  $F_{\mu\nu} = \langle \phi_\mu | f | \phi_\nu \rangle$ ,  $\mathbf{S}$  is named overlap matrix with elements  $S_{\mu\nu} = \langle \phi_\mu | \phi_\nu \rangle$ , being a measure for the overlap of the orbitals,  $\mathbf{C}$  is a square matrix containing the expansion coefficients and  $\boldsymbol{\varepsilon}$  is the diagonal matrix of the orbital energies  $\varepsilon_i$ . For orthonormal basis functions, the overlap becomes a delta function and the overlap, which induces inhomogeneity in the Roothaan equation, vanishes, and it becomes a simple eigenvalue equation. For this reason, an orthogonalization scheme e.g., the Gram-Schmidt scheme is sometimes employed in the SCF procedure in order to obtain orthonormal basis functions. Typically, the orbitals are already normalized from the beginning. One further important quantity connected to the Roothaan equation, which also represents a connection between HF and DFT is the density matrix  $\mathbf{P}$  which is guessed initially and then used during the following iterations to check for convergence of the expansion coefficients. This matrix with elements  $P_{\mu\nu}$  can be considered as a weight factor for the various

four-index integrals contained in the expression of  $F_{\mu\nu}$ . It describes to which extent individual basis functions contribute to the many-electron wave function. It is defined as

$$P_{\mu\nu} = 2 \sum_k^{\frac{N}{2}} C_{\mu k} C_{\nu k}^* \quad (3.22)$$

The factor 2 appears because the restricted closed-shell HF formalism is assumed which means that each MO is doubly occupied. Expanded in a set of basis functions  $\mathbf{P}$  yields the electron density  $\rho(\mathbf{r})$  as  $\rho(\mathbf{r}) = \sum_{\mu\nu} P_{\mu\nu} \phi_{\mu}(\mathbf{r}) \phi_{\nu}^*(\mathbf{r})$ .  $\rho(\mathbf{r})$  is the central quantity in DFT. When the SCF procedure has converged as results the density matrix  $\mathbf{P}$ , the orbital energies  $\varepsilon_i$  and the set of best possible orbital coefficients  $\{C_{\mu i}\}$  are obtained.

Concerning a physical interpretation of HF orbital energies the following interesting relation known as Koopmans' theorem<sup>[112]</sup> can be shown to exist between computed orbital energies  $\varepsilon_a$  (occupied) and  $\varepsilon_r$  (unoccupied) eq. (3.16) and the experimental observables ionization potential (IP) and electron affinity (EA). This theorem states that the IP, i.e., the energy required to remove an electron from an occupied orbital to create a (N-1) electron Slater determinant is just the negative of the energy of this orbital,  $-\varepsilon_a$ . While the EA, i.e., the energy required to generate a (N+1) electron Slater determinant is just  $-\varepsilon_r$ . Obviously, this relation has its origin in a different treatment of occupied and unoccupied orbitals. Analyzing the two expressions for the orbital energies eq. (3.16), it becomes apparent that the energy  $\varepsilon_a$  of an electron in an occupied orbital includes Coulomb and exchange interaction with each of the remaining (N-1) electrons in the other (N-1) orbitals where  $b \neq a$ . Its artificial interaction with itself cancels out.

In contrast, the energy  $\varepsilon_r$  of an electron in an unoccupied orbital includes Coulomb and exchange interaction with all  $N$  other electrons of the HF ground state  $|\Psi\rangle$  (all occupied orbitals), thus describes the energy of an  $(N + 1)$ th electron. On the contrary, in DFT, for instance, both occupied and unoccupied orbital energies are evaluated using the same N-electron potential.

Although HF theory exactly accounts for exchange correlation (which describes the correlated motion of parallel-spin electrons and prevents electrons with parallel spins to coincide) it assumes an average electron-electron interaction. Due to the mean field approximation, in the HF Slater determinant two electrons will never "see" each other, but only their charge clouds. Thus, *dynamic* correlation (which describes the correlated motion of electrons with opposite spin and prevents electrons with opposite spins to coincide) is neglected. As a consequence,  $E_0^{HF}$  deviates from the

exact ground state energy  $E_0$  by a contribution called correlation energy:

$$E_{corr} = E_0 - E_0^{HF} \quad (3.23)$$

In general, the contribution of  $E_{corr}$  to the total energy of a state is small, meaning less than about 1%.<sup>[113]</sup> Nevertheless, electron correlation is essential for a correct physical description of chemical properties, especially energy differences (such as activation energies or position of bands in a spectrum). Thus, alternative methods have been developed to consider electron correlation effects for both ground and excited state. Three of the most commonly used so-called correlated methods are Møller-Plesset perturbation theory (MP), configuration interaction (CI) and coupled cluster (CC) theory. Truncated variants of these methods namely MP2, CC2 and CIS are presented and discussed in the following subsections.

In the context of electron correlation, a further important strong correlation effect should be mentioned as well – namely *static*, or non-dynamic, correlation. It arises when occupied and virtual orbitals are energetically (nearly) degenerate and implicates that a single determinant description of the reference wave function is qualitatively wrong. In other words, in systems with strong static correlation effects the wave function differs qualitatively from the reference Slater determinant. Such systems are e.g., biradicals, twisted ethylene and electronic properties of linear acenes.

One way to estimate the relevance of static correlation in a molecular system is to use the D1 diagnostic<sup>[114]</sup> provided by an MP2 or CC2 ground state calculation. D1 values which are larger than 0.040 (MP2) and 0.050 (CC2) indicate that single reference methods are inadequate to describe the ground state of the system correctly.<sup>[114]</sup> Common approaches to account for static correlation are multideterminantal (or multireference) methods which employ linear combinations of one or more Slater determinant to describe the reference wave function instead of a single determinant or the Spin-Flip (SF) approach. The latter one will be discussed further below.

### 3.4 DENSITY FUNCTIONAL THEORY

Similar to the Hartree-Fock (HF) method density functional theory (DFT) can also be considered as a mean field approach. Likewise, it assumes that electrons move independently in an external potential. It also uses a Slater determinant to approximate the exact ground state wave function

and the SCF method for minimization of an energy functional.

Yet, DFT differs from HF in one significant respect: It uses a physical observable, namely the electron density  $\rho(\mathbf{r})$  to describe the ground state and to determine the energy of the electronic system, instead of the wave function. In short, DFT is based on the fact that the electron density  $\rho(\mathbf{r})$  completely characterizes the electronic system. This means that, if one could compute the electron density exactly, one could also obtain exact properties like the energy.

Since its advent in the 1970s DFT has developed into a very popular and widely used *ab initio* method. Its primary advantages are its efficiency, easy usage, comparably low computational costs, reasonable accuracy and, most importantly, applicability to large molecular systems (up to many hundreds of atoms). Additionally, an essential point is that DFT improves upon HF because it accounts for electron-correlation, however, cleverly not through increasing the complexity of the wave function (thus computational costs) but by introducing approximate exchange-correlation terms.

The majority of today's photochemical studies involve, at least to some extent, DFT (and TDDFT) methods. The award of the Nobel Prize for Chemistry in 1998 to J. A. Popel and W. Kohn<sup>[115]</sup> nicely demonstrates the vital role of DFT in the evolution of quantum chemistry.

The motivation behind this completely new approach to determine the ground state energy and other properties of a many-electron system can be explained as follows. On the one hand, the wave function  $\Psi(\mathbf{x})$  depending on four coordinates (spin and spatial) for every electron has a very high dimensionality for a many-electron system and is thus mathematically very difficult to handle. On the other hand, it has no intuitive physical interpretation and is not itself a measurable quantity. Most likely it can be considered as a probability amplitude in the sense that its square modulus  $|\Psi(r)|^2$  represents the measurable probability for electrons in specific states (Born interpretation).<sup>[116]</sup> The electron density  $\rho(\mathbf{r})$ , in turn, only depends on three spatial coordinates and is a physical observable, hence, directly measurable. Additionally,  $\rho(\mathbf{r})$  compared to  $\Psi(\mathbf{x})$  it is more tangible. A further huge advantage is that  $\rho(\mathbf{r})$  conveniently provides all information needed for the *a priori* construction of the Hamiltonian  $\mathcal{H}$ . For instance, integrated over all space it gives the total number of electrons  $N$  and it also gives the positions of nuclei since those correspond to local maxima (and also cusps) in the electron density, and the nuclear charges  $Z_I$ .

To evaluate the exact energy  $E_0$  using the electron density only, expressions for the different terms contributing to the total energy, i.e., for the potential energy components  $V_{ne}$  and  $V_{ee}$  and the kinetic energy  $T$  of the electrons are needed. First formulations of such expressions were

developed by E. Fermi, L. H. Thomas, J. C. Slater, M. F. Bloch and P. A. M. Dirac and are based on the uniform electron gas model.<sup>[117–123]</sup> Here, interacting electrons are assumed to move in a uniformly distributed positive charge which can be considered as an external potential. Furthermore, the  $V$  and  $T$  terms are defined as ‘density functionals’ (i.e., as functions of the electron density (function)). The resulting equations, together with an assumed variational principle can be considered as the first attempt to define a density functional theory. This theory, however, remained rather inaccurate for chemical applications because it is not able to describe chemical bonding and computed molecular energies are far too high.

The foundation of modern ground state DFT was laid by P. Hohenberg and W. Kohn<sup>[115,124]</sup> by proving two theorems which, on the one hand validate the use of  $\rho(\mathbf{r})$  to describe the ground state of a many-electron system instead of  $\Psi$ , and on the other hand show the existence of a variational principle for the energy functional that guarantees that the exact energy functional will be the ground state energy  $E_0$  for the exact ground state density  $\rho(\mathbf{r})_0$  and higher than  $E_0$  otherwise.<sup>[125]</sup> This means when a trial density is used instead of exact ground state density  $\rho(\mathbf{r})_0$  the energy obtained is an upper bound to the exact ground state energy  $E_0$ .

In short, the first Hohenberg-Kohn (HK) theorem states that a ground state density  $\rho(\mathbf{r})$  of a system of interacting electrons in some external potential  $V_{ext}(\mathbf{r})$  determines this potential uniquely (up to an additive constant).  $V_{ext}(\mathbf{r})$  in turn, gives, for a non-degenerate ground state, a unique ground state wave function  $\Psi_0$ . Consequently, both  $V_{ext}(\mathbf{r})$  and  $\Psi_0$  are functionals of  $\rho(\mathbf{r})$  and so are all expectation values of  $\Psi_0$ . The second HK theorem states that since  $\rho(\mathbf{r})$  determines  $\mathcal{H}$ , the exact ground state energy  $E_0$  can be determined by minimization of an energy functional  $E[\rho(\mathbf{r})]$  which depends on  $\rho(\mathbf{r})$  and  $V_{ext}(\mathbf{r})$  with respect to some trial density, whereby no explicit knowledge of  $V_{ext}(\mathbf{r})$  is required.

### **Kohn-Sham DFT**

An approximation fundamental for both ground state and time-dependent DFT was introduced by W. Kohn<sup>[115]</sup> and L. J. Sham.<sup>[126]</sup> Their approach lead to self-consistent one-electron equations analogous to the HF equations, called *Kohn-Sham equations*. The central idea of this approach is to map the physical (exact) system of interacting electrons onto a fictitious, non-interacting system of electrons moving in an effective potential for which  $\mathcal{H}$  can be expressed as a sum of

one-electron operators. This system is named *Kohn-Sham system*. One advantage is that the kinetic energy of such a non-interacting system  $T_{nie}$  is just the sum of the individual electronic kinetic energies and can be computed exactly. Kohn and Sham validated their approach by proving a theorem which states that two systems, specifically, the non-interaction and the interacting one, have exactly the same electron density  $\rho(\mathbf{r})$  but different external potentials.<sup>[115]</sup> The KS equations for non-interaction electrons moving in an effective external potential  $V_{eff}(\mathbf{r})$  instead of  $V_{ext}(\mathbf{r})$  reads as follows:

$$\sum_i^N h_i^{KS} \psi_i(\mathbf{r}) = \varepsilon_i \psi_i(\mathbf{r}) \quad (3.24)$$

where the KS one-electron Hamiltonian is defined as:

$$h_i^{KS} = \underbrace{-\frac{1}{2}\nabla_i^2}_{T_{nie}} + V_{eff}^{KS}(\mathbf{r}) \quad (3.25)$$

where  $T_{nie}$  refers to the kinetic energy of the noninteracting electrons and where  $V_{eff}^{KS}(\mathbf{r})$  is the effective KS potential defined as:

$$V_{eff}^{KS}(\mathbf{r}) = V_{ext}(\mathbf{r}) + \underbrace{\int \frac{\rho(\mathbf{r}')}{|\mathbf{r}_i - \mathbf{r}'|} d\mathbf{r}'}_{V_H} + V_{xc}(\mathbf{r})$$

with  $V_H$  or  $J_{ee}$  being the Hartree potential i.e., the classical electrostatic interaction of the electrons among themselves. The exact effective KS potential  $V_{eff}^{KS}(\mathbf{r})$  can be considered as the unique, fictitious external potential which leads, for the KS system, to the same physical electron density  $\rho(\mathbf{r})$  as that of the interacting electrons in the physical external potential  $V_{ext}(\mathbf{r})$ .

$V_{xc}$  is the functional derivative

$$V_{xc} = \frac{\partial E_{xc}}{\partial \rho}$$

of the local *exchange-correlation functional* (xc-functional)  $E_{xc}[\rho(\mathbf{r})]$ . The trick here is to lump together the correction to  $T_{nie}$  deriving from the interacting nature of the electrons, all non-classical corrections to the electron-electron repulsion energy and exchange effects by introducing  $E_{xc}[\rho(\mathbf{r})]$ . In contrast to HF theory, which by construction is approximate, when the exact  $E_{xc}[\rho(\mathbf{r})]$  and  $V_{xc}$  are employed DFT is an exact theory since all many-body effects are considered.

To obtain the KS equations, it is assumed that the electron density  $\rho(\mathbf{r})$  for the Slater determinant

$\Psi_0$  (which is an exact eigenfunction for the non-interaction (KS) Hamiltonian) is simply

$$\rho = \sum_i^N |\psi_i\rangle\langle\psi_i|$$

where, in the ground state, the sum runs over the  $N$  lowest eigenvalues. In order to convert the KS eigenvalue equations eq. (3.24) into a more easily computable secular equation (which is entirely analogous to that solved in the HF SCF method) the MOs  $\psi_i$  are expanded in a basis set  $\psi_i(\mathbf{r}) = \sum_{\mu}^K C_{\mu i} \phi_{\mu}(\mathbf{r})$ . In contrast to the HF method in which the SCF procedure yields the Fock matrix  $\mathbf{F}$  and HF MOs, the KS SCF procedure yields the KS matrix  $\mathbf{K}$  with elements  $K_{\mu\nu}$  given by:

$$K_{\mu\nu} = \left\langle \phi_{\mu} \left| -\frac{1}{2}\nabla_i^2 - \sum_I \frac{Z_I}{|\mathbf{r}_i - \mathbf{R}_I|} + \int \frac{\rho(\mathbf{r}')}{|\mathbf{r}_i - \mathbf{r}'|} d\mathbf{r}' + V_{xc} \right| \phi_{\nu} \right\rangle$$

and KS orbitals.

A further difference to the HF method in which the final ground state energy  $E_0^{HF}$  is computed as the expectation value of  $\mathcal{H}$  with respect to the HF Slater determinant is that in KS DFT the final ground state energy is obtained by plugging the converged density into the expression for the energy functional:

$$\begin{aligned} E[\rho(\mathbf{r})] &= \sum_i \langle \psi_i | -\frac{1}{2}\nabla_i^2 | \psi_i \rangle - \sum_I \langle \psi_i | \frac{Z_I}{|\mathbf{r}_i - \mathbf{R}_I|} | \psi_i \rangle + \sum_i \langle \psi_i | \frac{1}{2} \int \frac{\rho(\mathbf{r}')}{|\mathbf{r}_i - \mathbf{r}'|} d\mathbf{r}' | \psi_i \rangle + E_{xc}[\rho(\mathbf{r})] \\ &= T[\rho(\mathbf{r})] + V_{Ne}[\rho(\mathbf{r})] + J_{ee}[\rho(\mathbf{r})] + E_{xc}[\rho(\mathbf{r})] \end{aligned} \quad (3.26a)$$

The *exact* KS orbital energies  $\varepsilon_i$ , in contrast to their HF analogues (which obey Koopmann's theorem) have no known directly observable physical meaning, except for the fact that the energy of the highest occupied molecular orbital (HOMO)  $\varepsilon_a$  equals the negative of the exact first ionization potential. Instead, the difference of the KS orbital energies ( $\varepsilon_a - \varepsilon_r$ ) are usually excellent approximations for excitation energies. This is because, in contrast to the HF method, which evaluates the unoccupied orbitals for an  $N + 1$  electron system, all KS orbitals are subject to the same effective potential arising from an  $N$  electron system.

It should be mentioned, that today nearly all applications of DFT to chemical problems are undertaken within the KS formalism. This also applies to all DFT and TDDFT studies presented in the following chapters, thus, I will omit the abbreviation KS and only use the terms DFT and TDDFT throughout the rest of this work.

Since the exact form of  $E_{xc}[\rho(\mathbf{r})]$  is only known for the uniform electron gas, numerous approximate xc-functionals have been developed over time leading to different flavors of DFT. It should be noted here that many functionals contain empirically fitted parameters meaning that these functionals are no longer fully *ab initio* and that not every functional is equally well-suited for a particular chemical problem. In general, the choice of xc-functionals for a quantum chemical study should be made with great care.

As the name suggests, these functionals consist of an exchange and correlation part. Very popular, but rather crude approximate DFT functionals are the local density approximation (LDA) functionals. LDA functionals depend on the (spin-)density  $\rho(\mathbf{r})$  only. To improve LDA functionals, they were also made dependent on the gradient of the density, hence on the extent to which the density is locally changing. This approach is known as generalized gradient approximation (GGA). One famous correlation GGA functional is the LYP functional. Combined with Becke's three parameter GGA exchange functional<sup>[127]</sup>, the well-known BLYP (Becke-Lee-Yang-Parr) GGA xc-functional is obtained. Due to their supreme accuracy-to-numerical-costs ratio, the most widely used class of xc-functionals are hybrid functionals. They are called hybrid functionals because they incorporate both HF and DFT exchange. Their construction concept is based on the adiabatic connection method<sup>[128]</sup> which considers two limits: no electron-electron interaction and full interaction and thus connects the noninteracting KS system to the real interacting system. The idea is to obtain a functional in which the amount of incorporated nonlocal (exact) exchange can be varied by a number of adjustable parameters. B3LYP, the most popular and commonly used hybrid GGA functional has the following form<sup>[99]</sup>:

$$E_{xc}^{B3LYP} = (1 - a)E_x^{LSDA} + aE_x^{HF} + b\Delta E_x^B + (1 - c)E_c^{LSDA} + cE_c^{LYP}$$

It includes 80 % DFT and 20% nonlocal HF exchange.

A relatively recent class of hybrid functionals which gained increasing popularity in the last few years are range-separated hybrid functionals. The basic idea is to decompose the electron-electron interaction into a sum of short and long range terms by means of the error function  $f_{err}$ . DFT exchange interaction is included using the first term (short-range), and the long-range orbital-orbital exchange interaction is described with the HF exchange via the second term. One of the most widely used range-separated hybrid functionals is CAM-B3LYP<sup>[129]</sup>. Here, 'CAM' stands for Coulomb-attenuating method. In CAM-B3LYP, the Coulomb potential  $\frac{1}{r_{12}}$  is partitioned as

follows:

$$\frac{1}{r_{12}} = \frac{1 - [\alpha + \beta f_{err}(\mu r_{12})]}{r_{12}} + \frac{\alpha + \beta f_{err}(\mu r_{12})}{r_{12}} \quad (3.27)$$

where the adjustable parameter  $\alpha$  determines the amount of HF exchange over the whole range by a factor of  $\alpha$  and the adjustable parameter  $\beta$  determines the amount of DFT (Slater and Becke's) exchange over the whole range by a factor of  $1 - (\alpha + \beta)$ . The parameter  $\mu$  determines the balance of DFT to HF exchange over the whole range.

The reason for the great success of hybrid and especially range-separated hybrid functionals is because they ameliorate two severe limitations of DFT namely the *self-interaction error* inherent in most LDA and GGA xc-functionals and the resulting incorrect asymptotic behavior of the xc potential  $V_{xc}$ .<sup>[130]</sup> Yet, one problem remains. The optimal fraction of exact exchange is not known *a priori*. Hence, to obtain reliable DFT (and TDDFT) results different hybrid functionals with different amount of HF exchange should be used and analyzed regarding the effect of HF exchange.

### 3.4.0.1 Self-Interaction Error

A major drawback of DFT is that it does not correctly treat exchange-correlation. In DFT both dynamic correlation and exchange are treated approximately by employing approximate xc-functionals. As a consequence, the so-called one-electron *self-interaction error* (SIE) arises which as its name suggests is the spurious interaction of an electron with itself. It can be explained as follows. In HF theory exchange-correlation is treated exactly via the two electron exchange integrals  $K_{ij}$  and self-interaction contributions  $K_{ii}$  cancel out exactly with the Coulomb term  $J_{ii}$ . This becomes obvious by looking at the total energy which is given as:

$$E_0 = \sum_i^N h_{ii} + \frac{1}{2} \sum_i^N \sum_j^N (\mathcal{J}_{ij} - \mathcal{K}_{ij})$$

The Coulomb integral  $J_{ij}$  is the classical interaction energy between the charge density corresponding to electron  $i$  in orbital  $i$  and that corresponding to another electron in orbital  $j$ . The key point is that the double summation includes the terms where  $i = j$  which means that the energy includes the repulsion energy of each electron with itself. But  $J_{ii}$  is exactly equal to  $K_{ii}$  such that the self-interaction cancels out. On the contrary, in DFT, the final xc-functional  $E_{xc}$  eq. (3.26) which is used to obtain the total energy, contains the Hartree potential  $J_{ee}[\rho(\mathbf{r})]$  ( $V_H$ ) including

the same self-interaction as the HF energy, which should be compensated by the exchange term, however, since  $V_{xc}[\rho(\mathbf{r})]$  is approximate, this compensation happens only incompletely.

As a consequence, the orbital energies are also contaminated by the SIE since they are eigenvalues of the KS Hamiltonian  $h_i^{KS}$  eq. (3.25) which contains  $J_{ee}[\rho(\mathbf{r})]$  and  $V_{xc}[\rho(\mathbf{r})]$  and  $h_i^{KS}$  is the same for all orbitals. Furthermore, it is assumed that the SIE causes the xc-potential  $V_{xc}[\rho(\mathbf{r})]$  to decay exponentially in the asymptotic region, instead of decaying as  $-\frac{1}{r}$ . These problems of DFT are especially relevant when ionization processes or charge-transfer systems are studied. It was found that certain xc-functionals tend to overestimate intermolecular charge-transfer interactions.<sup>[99]</sup> In those cases, the DFT results should be carefully checked. Additionally, it may lead to an ‘overdelocalization’ of the electron density. This can result in erroneous predictions of higher symmetry geometries being preferred over lower symmetry ones and to poor or even wrong predictions along coordinates like bond dissociation and rotation about single bonds in conjugated systems.<sup>[99]</sup> Also in this case, range-separated functionals tend to show better performance than LDA, GGA and standard hybrid functionals.

Besides the problem of self-interaction, there are some further drawbacks of DFT methods. For example, there is no systematic way to improve the accuracy of the results. Moreover, DFT is not able to describe London dispersion interactions which derive entirely from electron correlation at long range.<sup>[99]</sup>

Nevertheless, commonly, DFT methods show a good performance for minimum energy structures of small neutral molecules. Accuracies in bond lengths and angles for instance for all kind of flavors are of similar accuracy as MP2, however, generally compare slightly less favorably with experiment than do HF and MP2.<sup>[99]</sup> A great advantage of DFT over HF and MP2, especially for computation of minimum energy structures is that it scales as  $O(N^3)$  ( $N$  being the number of basis functions) which is better than HF which scales as  $O(N^4)$  and a significantly better than MP2 which scales as  $O(N^5)$ .

### 3.4.0.2 Dispersion Corrections: DFT-D

London dispersion is a weak long range interaction, however, cumulative and therefore becomes increasingly important for larger systems. Dispersion interactions play a crucial role in noncovalently bound systems, e.g. dimers, supramolecular host-guest complexes molecular crystals. Furthermore, they are a key ingredient in the structure, stability, and response properties of

many molecular materials like porous materials for instance. They arise because the motions of electrons are correlated such that two nearby atoms simultaneously develop electrical moments that are oriented so as to be mutually attractive. Due to their nature, dispersion interactions are also often called induced dipole-induced dipole interactions. They have an inverse sixth power dependence on the separation between the atoms.

As mentioned above, conventional DFT methods including hybrid and range-separated xc-functionals do not contain the correct physics to describe dispersion interactions. Thus, over the last few years there have been many efforts to overcome this deficiency, i.a., by the development of simple empirical dispersion corrections. These corrections implemented within the conventional DFT formalism results in dispersion-corrected DFT (DFT-D) which can be considered as an "add-on" to standard DFT. The idea is to simply add damped, atom-atom pairwise empirical dispersion corrections  $E_{disp}$  of the form  $C_6 \cdot R^{-6}$ , to the employed xc-functional. The total energy is then given by:

$$E_{DFT-D} = E_{KS-DFT} + E_{disp} \quad (3.28)$$

Different versions of these  $D$  corrections are available the most common ones being S. Grimme's  $D$ ,  $D2$  and  $D3$  models. Some of the most widely used dispersion corrected xc-functionals are B97-D<sup>[131]</sup> and the more recent B97-D3<sup>[132]</sup>.  $E_{disp}$  in the B97-D functional is given by<sup>[131]</sup>:

$$E_{disp} = -s_6 \sum_I^N \sum_{J<I}^N \frac{C_6^{IJ}}{R_{IJ}^6} f_{damp}(R_{IJ}) \quad (3.29a)$$

$$C_6^{IJ} = (C_6^I C_6^J)^{\frac{1}{2}}$$

$$f_{damp}(R_{IJ}) = \frac{1}{1 + e^{-d(\frac{R_{IJ}}{R_{IJ}^0})^{-1}}}$$

Where  $N$  is the number of atoms in the system,  $s_6$  a scaling factor,  $C_6^{IJ}$  the dispersion coefficient for atom pair  $IJ$ ,  $R_{IJ}$  the interatomic distance,  $R^0$  is the sum of atomic van-der-Waals radii,  $f_{damp}$  the damping function which is needed to avoid near-singularities for small interatomic distances and double-counting correlations effects at intermediate distances and  $d$  has the value 20.

### 3.5 ELECTRON CORRELATION AND POST-HARTREE-FOCK METHODS

The error in the HF method lies in the use of one single Slater determinant  $|\Phi_0\rangle$  as many-electron wave function. Consequently, the central idea of correlated methods which aim at considering dynamic electron correlation (at least to some extent) and thus to improve the HF method is not to truncate the exact wave function  $|\Psi\rangle$  too drastically. They are all based on the general approach to include electron correlation by generating new terms in the total wave function via excitations of electrons from the HF determinant. In practice, this is achieved by replacing MOs which are occupied in the HF determinant by unoccupied MOs. Depending on how many-electrons are excited the new so-called excited determinants (or excited configurations)  $\Phi_\mu \in \{\Phi_{a^r}^r, \Phi_{ab}^{rs}, \dots\}$  are classified as *single* (S), *double* (D), *triple* (T) etc. excitations (see Fig. 3.4). Consequently, if all possible excited state determinants (in a given basis set) are included the complete correlation energy would be recovered. Approximate many-electron wave functions are then constructed

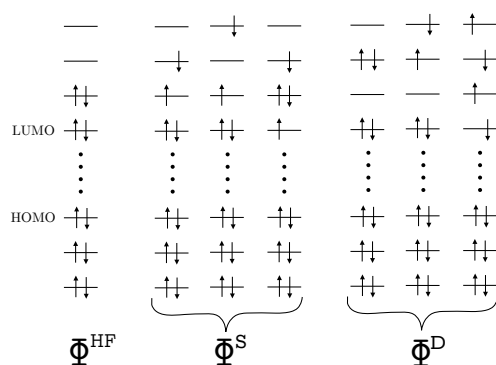


FIGURE 3.4: Schematic representation of the Hartree Fock reference determinant  $\Phi^{\text{HF}}$ , three possible single excitations resulting in three different singly excited determinants  $\Phi^{\text{S}}$  and three possible double excitations resulting in three different doubly excited determinants  $\Phi^{\text{D}}$ .

by expanding the wave function in terms of the HF determinant as leading term and different excited determinants. This, in turn, can be achieved in different ways. In configuration interaction theory, for instance, a linear expansion is used. Coupled cluster theory uses an exponential, and Møller-Plesset perturbation theory a perturbative expansion. Due to practical reasons, the particular expansion is truncated at some order.

### 3.5.1 Møller-Plesset Perturbation Theory

Second-order Møller-Plesset perturbation theory (MP2) is one of the most useful and most popular ground state methods beyond Hartree-Fock theory. The basic idea is to improve upon the HF approach by treating the effect of the correlated motion of electrons perturbatively. The general concept of Møller-Plesset perturbation theory (MP)<sup>[133]</sup> is a partitioning of the exact Hamiltonian  $\mathcal{H}$  into two parts, namely, an unperturbed  $H^{(0)}$  and a perturbed one  $V$ :

$$\mathcal{H} = H^{(0)} + \lambda V \quad (3.30)$$

where  $\lambda$  is an arbitrary real parameter determining the strength of the perturbation. Thus, the perturbed electronic Schrödinger equation which has to be solved is given by:

$$\mathcal{H}|\Phi_0\rangle = (H^{(0)} + \lambda V)|\Phi_0\rangle = E_0|\Phi_0\rangle \quad (3.31)$$

It is noteworthy hereby, that the perturbation  $V$  is assumed to be time-independent and small (which in most situations is true).

In MP theory the unperturbed Hamiltonian  $H^{(0)}$  is chosen to be the sum of Fock operators. This choice is mainly made because it fulfills the requirement of perturbation theory that the solutions to the unperturbed Schrödinger equation should be known.  $V$  is therefore given as the difference between the HF mean-field interaction and the exact Coulomb operator<sup>[108]</sup>:

$$V = \mathcal{H} - H^{(0)} = \sum_{i < j} \frac{1}{|\mathbf{r}_i - \mathbf{r}_j|} - \sum_i v^{HF}(i) \quad (3.32)$$

Starting point for the derivation of the expression for the second-order correction to the energy  $E_0^{(2)}$  is the exact HF solution i.e., the HF determinant  $\Phi_0$  as zeroth-order wave function  $|\Psi_0^{(0)}\rangle$ . Conveniently, the HF solutions form a complete orthonormal basis. The corresponding zeroth-order perturbation energy  $E_0^{(0)}$  or E(MP0) is given as the sum of MO energies:

$$E_0^{(0)} = \langle \Psi_0^{(0)} | H^{(0)} | \Psi_0^{(0)} \rangle = \sum_a \varepsilon_a \quad (3.33)$$

Note here, that the electron-electron repulsion is counted twice. Since the perturbation is increased from zero to a finite value, the new energy and wave function must also change continuously.

Thus,  $E_0$  and  $|\Phi_0\rangle$  can be written as a Taylor expansion<sup>[134]</sup>:

$$E_0 = \sum_n E_0^{(n)} = \lambda^0 E_0^{(0)} + \lambda^1 E_0^{(1)} + \lambda^2 E_0^{(2)} + \dots \quad (3.34a)$$

$$|\Phi_0\rangle = \sum_n |\Psi_0^{(n)}\rangle = \lambda^0 |\Psi_0^{(0)}\rangle + \lambda^1 |\Psi_0^{(1)}\rangle + \lambda^2 |\Psi_0^{(2)}\rangle + \dots \quad (3.34b)$$

In practice, intermediate normalization of the perturbed wave function is assumed i.e.:  $\langle \Psi_0^{(0)} | \Phi_0 \rangle = 1$  and thus  $\langle \Psi_0^{(0)} | \Psi_0^{(n)} \rangle$  has to be zero meaning that all correction terms are orthogonal to the HF reference wave function. When all correction terms are computed, the total wave function can be easily normalized.

Inserting the expansions eq. (3.34) into the exact Schrödinger equation eq. (3.31) and collecting terms with the same power of  $\lambda$  yield a set of perturbation equations:

$$\lambda^0 : H^{(0)} |\Psi_0^{(0)}\rangle = E_0^{(0)} |\Psi_0^{(0)}\rangle \quad (3.35a)$$

$$\lambda^1 : H^{(0)} |\Psi_0^{(1)}\rangle + V |\Psi_0^{(0)}\rangle = E_0^{(0)} |\Psi_0^{(1)}\rangle + E_0^{(1)} |\Psi_0^{(0)}\rangle \quad (3.35b)$$

$$\lambda^2 : H^{(0)} |\Psi_0^{(2)}\rangle + V |\Psi_0^{(1)}\rangle = E_0^{(0)} |\Psi_0^{(2)}\rangle + E_0^{(1)} |\Psi_0^{(1)}\rangle + E_0^{(2)} |\Psi_0^{(0)}\rangle \quad (3.35c)$$

⋮

By requiring the  $n$ th order correction to be orthogonal to  $|\Psi_0^{(0)}\rangle$ , i.e.  $\langle \Psi_0^{(0)} | \Psi_0^{(i)} \rangle$ , multiplying from the left by  $\langle \Psi_0^{(0)} |$  and integrating, the corresponding expressions for the energy corrections eq. (3.36)<sup>[108]</sup> are obtained. For the sake of compactness, only those expressions which are relevant for this work are given here.

$$\begin{aligned} E_0^{(1)} &= \langle \Psi_0^{(0)} | V | \Psi_0^{(0)} \rangle = \langle \Psi_0^{(0)} | \left( \sum_{i<j} \frac{1}{|\mathbf{r}_i - \mathbf{r}_j|} - \sum_i v^{HF}(i) \right) | \Psi_0^{(0)} \rangle \\ &= \frac{1}{2} \sum_{ab} \langle ab || ab \rangle - \sum_a \langle a | v^{HF} | a \rangle = -\frac{1}{2} \sum_{ab} \langle ab || ab \rangle \end{aligned} \quad (3.36a)$$

$$E_0^{(2)} = \langle \Psi_0^{(0)} | V | \Psi_0^{(1)} \rangle \quad (3.36b)$$

The first order energy correction  $E_0^{(1)}$  represents the difference between the expectation values of the Fock operator and exact Hamiltonian and yields a correction for the over-counting of electron-electron repulsion at zeroth-order (see  $E_0^{(0)}$  eq. (3.33)). Consequently, the HF energy  $E_0^{HF}$  (see eq. 3.12) is given by the sum of  $E_0^{(0)}$  and  $E_0^{(1)}$  which also means that the first correction to the HF energy occurs at the second-order in perturbation theory. By analyzing the expressions

for the energy corrections eq. (3.36) it can be seen that in MP theory the  $n$ th order energy correction can be obtained from the  $(n-1)$  order wave function.

For the computation of the second-order correction to the energy  $E_0^{(2)}$  eq. (3.36b) the first order wave function  $|\Psi_0^{(1)}\rangle$  is needed and products of the type  $\langle\Phi^j|V|\Phi^i\rangle\langle\Phi^i|V|\Phi_0\rangle$  where  $i$  and  $j$  represent different excitation levels of the excited determinants have to be evaluated. Since canonical HF orbitals are used (which are orthogonal to each other) and due to Brillouin's theorem<sup>[135]</sup> (which, in short, states that singly excited determinants do not mix with the HF ground state i.e.,  $\langle\Phi_a^r|\mathcal{H}|\Phi^{\text{HF}}\rangle = \langle\Phi^{\text{HF}}|\mathcal{H}|\Phi_a^r\rangle = 0$ ) matrix elements with single excited states are zero. Furthermore, since  $V$  is a two-electron operator, all matrix elements involving triple, quadruple, or higher excitations are zero as well. As a consequence the expression for  $E_0^{(2)}$  or  $E(\text{MP2})$  only includes a sum over doubly excited determinants  $\Phi^D$  (or  $|\Phi_{ab}^{rs}\rangle$ ) (see Fig. 3.4). Those determinants are generated by promoting two electrons from occupied HF orbitals  $a$  and  $b$  to unoccupied orbitals  $r$  and  $s$ . Thus, the second-order energy correction can be explicitly written as<sup>[108]</sup>:

$$E_0^{(2)} = \sum_{a<b}^{\text{occ}} \sum_{r<s}^{\text{unocc}} \frac{(\langle ab|rs\rangle - \langle ab|sr\rangle)}{\varepsilon_a + \varepsilon_b - \varepsilon_r - \varepsilon_s} \quad (3.37)$$

Since the two electron integrals are zero for  $a = b$  and  $r = s$  and because the result is invariant with respect to an interchange of  $ab$  and  $rs$  when real orbitals are used, the restriction in the summation can be dropped and the expression becomes<sup>[108]</sup>

$$E_0^{(2)} = E(\text{MP2}) = \frac{1}{2} \sum_{abrs} \frac{\langle ab|rs\rangle\langle rs|ab\rangle}{\varepsilon_a + \varepsilon_b - \varepsilon_r - \varepsilon_s} - \frac{1}{2} \sum_{abrs} \frac{\langle ab|rs\rangle\langle rs|ba\rangle}{\varepsilon_a + \varepsilon_b - \varepsilon_r - \varepsilon_s} \quad (3.38)$$

From eq. (3.38) it can be seen that MP2 improves the HF energy by including the energetic effect of a simultaneous excitation of two electrons.

MP2 theory is not variational, thus, the calculated energy may be lower than true ground state energy. This, however, is rarely a problem. But instead, MP theory is size-consistent at any order which is generally more important for practical application.

Due to its reasonable computational cost and the availability of highly efficient implementations (with which the formal scaling can be reduced to  $O(N^2)$ ), MP2 has become one of the workhorses of modern computational chemistry for the computation of structures, energies and other ground state properties. Commonly, the so-called resolution of the identity (RI) approximation<sup>[136,137]</sup> is applied to the MP2 correlation integrals to reduce the computation time and memory demands. The idea of the RI approximation is to express the correlation integrals in a so-called auxiliary or

fitting basis set.

### 3.5.2 Coupled Cluster Theory

The second-order approximate coupled cluster singles and doubles (CC2)<sup>[138]</sup> method is an approximate version of the well-known coupled cluster singles and doubles (CCSD) method, a truncated coupled cluster method including single and double excitations. The key point of the CC2 approach is that the singles equations which do not affect the energy to first order (but to second) are retained in their original form; whereas the doubles equations are retained only to first order. CC2 theory can be employed to treat both ground and excited states. For the generalization to excited states, usually, either the equation of motion (EOM)<sup>[139–141]</sup> or the linear response (LR)<sup>[141–143]</sup> formalism, are invoked. Using the LR formalism results in the LR-CC2 method which is discussed in subsection 3.6.2.

This section aims to briefly introduce the key concepts of coupled cluster (CC) theory.<sup>[144–146]</sup> A complete mathematical derivation and detailed discussion of CC theory and its variants would exceed the scope of this thesis. For more details, the reader is referred to the review articles by R. J. Bartlett<sup>[147]</sup> and Crawford and Schäfer<sup>[148]</sup>.

The central tenet of CC theory is the exponential expansion of the exact wave function  $\Psi$ :

$$\begin{aligned} |\Psi\rangle &= e^{\hat{\mathbf{T}}}| \Phi^{\text{HF}} \rangle \\ &= (1 + \hat{\mathbf{T}} + \frac{\hat{\mathbf{T}}^2}{2!} + \frac{\hat{\mathbf{T}}^3}{3!} + \dots) | \Phi^{\text{HF}} \rangle \end{aligned} \quad (3.39a)$$

where, again, the HF determinant  $| \Phi^{\text{HF}} \rangle$  serves as reference function.  $\hat{\mathbf{T}}$  is the so-called cluster operator. By using this ansatz, the wave function is always (at each truncation level) product separable and the energies are thus size extensive. The cluster operator  $\hat{\mathbf{T}}$  in eq. (3.39a) has the form:

$$\hat{\mathbf{T}} = \hat{\mathbf{T}}_1 + \hat{\mathbf{T}}_2 + \hat{\mathbf{T}}_3 + \dots + \hat{\mathbf{T}}_{N_{elec}}. \quad (3.40)$$

The various  $\hat{\mathbf{T}}_i$  operators generate all possible excited determinants, weighted by the corresponding cluster amplitudes  $t_{ab\dots}^{r's\dots}$ , by simultaneously exciting  $i$  electrons from occupied to unoccupied orbitals.  $\hat{\mathbf{T}}_1$ , for instance, generates singly excited determinants weighted by  $t_a^r$  and  $\hat{\mathbf{T}}_2$  generates

doubly excited determinants weighed by  $t_{ab}^{rs}$ . These two operators can be defined as<sup>[148]</sup>:

$$\hat{\mathbf{T}}_1|\Phi^{\text{HF}}\rangle = \sum_a \sum_r t_a^r |\Phi_a^r\rangle \quad (3.41a)$$

$$\hat{\mathbf{T}}_2|\Phi^{\text{HF}}\rangle = \frac{1}{4} \sum_{ab} \sum_{rs} t_{ab}^{rs} |\Phi_{ab}^{rs}\rangle \quad (3.41b)$$

Clearly, by operating on the HF determinant with  $\hat{\mathbf{T}}$  all possible excited determinants would be included in eq. (3.39a) and the wave function would be exact, and thus the exact energy within a given one-particle basis would be obtained. In configuration interaction (CI) theory, which is discussed further below, this is called ‘full CI’.

In practice, however,  $\hat{\mathbf{T}}$  is truncated at specific excitation levels resulting in a hierarchy of CC models. When only  $\hat{\mathbf{T}}_1$  and  $\hat{\mathbf{T}}_2$  are kept, the cluster operator reduces to  $\hat{\mathbf{T}} = \hat{\mathbf{T}}_1 + \hat{\mathbf{T}}_2$  and the aforementioned CCSD method is obtained. The advantage of the CCSD approximation is that it only lacks  $\hat{\mathbf{T}}_4$  and  $\hat{\mathbf{T}}_3\hat{\mathbf{T}}_1$  contributions to be complete through fourth-order of perturbation theory. Important higher-order excitations, in particular the quadruple-excitations are still quite accurately reproduced in CCSD. This is because the most important contribution to the quadruple-excitations are the  $\hat{\mathbf{T}}_2^2$  disconnected terms and those are included in the CCSD wave function. Thus, this truncation is a very reasonable approximation yielding very accurate energies.<sup>[149]</sup>

It is noteworthy here, that the  $\hat{\mathbf{T}}_2$  operator makes a direct contribution to the total energy, whereas the  $\hat{\mathbf{T}}_1$  operator does not contribute to first-order to the energy due to Brillouin’s theorem, but allows the MOs to relax from their HF reference form i.e., it accounts for orbital relaxations.

Due to the exponential ansatz, the CC amplitude equations eq. (3.43) cannot be conveniently solved in a variational approach. The reason for this is that due to the exponential ansatz of eq. (3.39a) the expectation value of the Hamiltonian would not truncate before the  $N_{elec}$  electron limit, even when the cluster operator  $\hat{\mathbf{T}}$  is truncated. This results in a computational effort similar to the one of full CI. Consequently, instead of solving the CC amplitude equations variationally, the so-called projection method is used. This means that the CC wave function eq. (3.39a) is inserted into the Schrödinger equation and multiplied by  $e^{-\hat{\mathbf{T}}}$  from the left to give the Schrödinger equation eq. (3.42a) of the so-called similarity transformed (non-Hermitian) Hamiltonian  $\bar{H}$

(3.42b).

$$\bar{H}|\Phi^{\text{HF}}\rangle = E|\Phi^{\text{HF}}\rangle \quad (3.42a)$$

with

$$\bar{H} = e^{-\mathbf{T}}\mathcal{H}e^{\mathbf{T}} \quad (3.42b)$$

where intermediate normalization  $\langle\Phi^{\text{HF}}|\Psi\rangle = 1$  is assumed. By projecting the Schrödinger equation (3.42a) onto  $|\Phi^{\text{HF}}\rangle$  and the excited determinants, expressions for the cluster amplitudes are obtained. Projection against all singles and doubles configurations, for instance, provides the amplitude equations (3.43) for  $t_a^r$  and  $t_{ab}^{rs}$ , respectively, which can be written as:

$$0 = \langle\Phi_a^r|\bar{H}|\Phi^{\text{HF}}\rangle \quad (3.43a)$$

$$0 = \langle\Phi_{ab}^{rs}|\bar{H}|\Phi^{\text{HF}}\rangle. \quad (3.43b)$$

Once the amplitudes are determined they can be used to compute the energy.

As mentioned before, CC methods are non-variational. However, they are size-consistent just like MP theory, which is one of the major advantages of CC and MP theory over CI.

Since the CCSD method is still very demanding in terms of computational costs and its formal scaling of  $\mathcal{O}(N^6)$  (with  $N$  being the number of basis functions), further approximate CC methods were developed. The most widely used one is CC2. The CC2 energy is correct to second-order of perturbation theory. For CC2 gradients and (numerical) Hessians are available for geometry optimizations and frequency analyses. CC2 scales formally as  $\mathcal{O}(N^5)^{[138]}$ , hence, slightly less favorable than MP2. Both ground state energies and equilibrium geometries obtained at CC2 level of theory are of comparable accuracy to those obtained using MP2.<sup>[138,149–152]</sup> In general both CC2 and MP2 methods outperform ground state DFT methods concerning energies. In practice commonly CC2 calculations, like MP2 ones, employ the RI<sup>[136,153]</sup> approximation to increase the efficiency of CC2.

### 3.6 EXCITED STATE METHODS

In this chapter a selection of *ab initio* excited state methods applied within the framework of this thesis are presented and discussed. In general, excited state methods are used to compute

geometries, energies and other properties of electronically excited states which are needed to investigate photochemical reactions. With respect to this, the computation of vertical excitation energies and oscillator strengths is of particular interest because they are needed to simulate absorption and emission spectra. Similar to ground state approaches, the description of dynamic electron correlation is also a central problem in the excited state methodology. For comparison with experimental data, e.g., absorption and emission spectra, the accuracy of the methods has to be sufficiently high.

I will start with one of the simplest and also most inaccurate wave function based excited state approach, namely configuration interaction singles (CIS). After this, linear response CC2 and linear response time-dependent density functional theory (LR-TDDFT) are presented and discussed.

### 3.6.1 Configuration Interaction Singles

Configuration interaction singles (CIS) can be considered as the excited state corollary of the ground state HF method. Thus, it similarly neglects electron correlation effects. It is a very simple and computationally efficient method which is why it is often used for excited state studies of large molecules ( $> 70$  atoms). Moreover, due to the variational nature of the employed CI wave function, gradients are available such that excited state geometry optimizations and frequency analyses can be performed at comparably low cost.

A major drawback of the CIS method is its poor performance concerning the computation of vertical excitation energies which mainly originates from the neglect of electron correlation. It was found that excitation energies are overestimated by up to 2 eV.<sup>[154,155]</sup> However, in contrast to conventional TDDFT, it yields reliable results for charge transfer transitions.

CIS is based on the well-known variational configuration interaction (CI) approach for the treatment of electron correlation. CI, analogous to MP and CC theory, is usually also based on the HF reference function  $|\Phi^{\text{HF}}\rangle$ . In CI the exact wave function  $\Psi$  method is formed as a linear combination of several Slater determinants. In the expansion  $|\Phi^{\text{HF}}\rangle$  appears as leading term. Since the HF determinant is obtained by variational optimization, it is the best single Slater determinant describing the wave function. Hence, its coefficient is by far the largest in the CI expansion (3.44). Like in CC theory the different excited determinants  $\Phi_{ab\dots}^{r,s\dots}$  included in the expansion are formed by exciting electrons from occupied orbitals  $a, b, \dots$  to unoccupied orbitals

$r, s, \dots$ . The CI wave function is given as:

$$\Psi = c_0 \Phi^{\text{HF}} + \sum_a^{\text{occ}} \sum_r^{\text{unocc}} c_a^r \Phi_a^r + \sum_{a<b}^{\text{occ}} \sum_{r<s}^{\text{unocc}} c_{ab}^{rs} \Phi_{ab}^{rs} + \dots \quad (3.44)$$

CI, if not truncated, is named full CI which, within the choice of basis set, is one of the most accurate methods for solving the Schrödinger equation available. Full CI within the BO approximation and a reasonable infinite basis set provides an exact solution to the time-independent electronic Schrödinger equation. However, due to its extremely high computational cost and its factorial scaling (with system size), full CI is unfeasible for all but the smallest systems. This is the reason why in practical calculations the linear expansion is typically truncated after a given number of excitations such as in CC theory. While full CI is size consistent, the truncated CI methods (except CIS) are not. The exception for CIS will be discussed in more detail further below.

The aim of the CI approach is to find the expansion coefficients  $c_{ab\dots}^{rs\dots}$  for each excited determinant which is included in the expansion (3.44). This is achieved by solution of the CI secular equation which is equivalent to diagonalizing the Hamiltonian (also called CI) matrix eq. (3.45) (i.e. the matrix collecting the matrix elements between the different Slater determinants)

$$H_{mn} = \langle \Phi_m | \mathcal{H} | \Phi_n \rangle \quad (3.45)$$

with  $\Phi_0 = \Phi^{\text{HF}}$ . The coefficients can then be determined from the eigenvectors and the energies (eigenvalues) from the roots. For this purpose the various matrix elements eq. (3.45) have to be evaluated. This in turn is achieved by exploiting some very useful rules named Slater-Condon rules<sup>[108]</sup> which significantly reduce the complexity of the mathematical problem. Since  $\mathcal{H}$  contains only one and two electron operators, if two excited state configurations differ in their occupied orbitals by three or more orbitals the corresponding matrix element will be zero (due to occurrence of orthogonal HF orbitals). The same holds for the remaining cases of configurations differing by two, one and zero orbitals. These rules, e.g. dictate that the matrix element between the HF determinant and a singly excited determinant

$$H_{0n} = \langle \Phi^{\text{HF}} | \mathcal{H} | \Phi_a^r \rangle = \langle \phi_r | f(i) | \phi_a \rangle \quad (3.46)$$

is equal to the product  $\varepsilon_a \delta_{ar}$ . To be singly excited,  $r$  must not be equal to  $a$ , thus, this matrix element is zero and thus all matrix elements between the HF determinant and singly excited

determinants are zero. This result for the Slater-Condon rules for the case of the HF reference determinant and a singly excited determinant is known as Brillouin's theorem<sup>[135]</sup>. Consequently, both Slater-Condon rules and Brillouin's theorem ensure that the CI matrix is reasonably sparse and thus more easy to handle.

As already mentioned before, the CI expansion eq. (3.44) is typically truncated at a certain excitation level. If only single configurations  $\Phi_a^r$  are included, the CIS method is obtained. The CIS matrix is block diagonal with one block corresponding to the HF energy  $H_{11}$  and the other being the singles/singles block. Since, the HF block is already diagonal, only the singles block has to be diagonalized.

Since singly excited determinants do not couple to the HF ground state due to Brillouin's theorem, the lowest energy root i.e., the ground state HF energy, is unaffected by inclusion of single excitations. Thus, unlike full CI and truncated CI methods, CIS does not improve the HF energy since it does not introduce any electron correlation. This is also the reason why CIS is not used as a ground state method.

Diagonalization of the CIS matrix takes place only in the excited state space, hence, it provides eigenvalues and associated eigenvectors corresponding to excited state energies and wave functions. The CIS wave function for an excited state  $k$  can be written as

$$\Psi_k = \sum_a^{\text{occ}} \sum_r^{\text{unocc}} c_{ark} \Phi_a^r \quad (3.47)$$

To obtain excitation energies  $\omega_{\text{CIS}}$ ,  $\mathcal{H}$  is shifted with respect to the HF ground state energy  $H = \mathcal{H} - E_0^{\text{HF}}$ . This Hamiltonian is then called the shifted Hamiltonian, and the following secular equation:

$$(\mathbf{A} - \omega)\mathbf{C} = 0 \quad (3.48)$$

has to be solved. In eq. (3.48)  $\mathbf{C}$  is the matrix of the expansion coefficients,  $\omega$  is the diagonal matrix of the excitation energies and  $\mathbf{A}$  is the matrix representation of the Hamiltonian in the space of the singly excited determinants with elements given as

$$A_{ar,bs} = (\varepsilon_s - \varepsilon_a)\delta_{ab}\delta_{rs} + \langle ar||sb \rangle. \quad (3.49)$$

In practice, the eigenvalue equation (3.48) is solved by diagonalization using the Davidson algorithm<sup>[156]</sup> which computes only the lowest eigenpairs (eigenvectors and eigenvalues).

While all other truncated CI methods suffer from size inconsistency, CIS is in fact size consistent

(like full CI) due to Brillouin's theorem. If the main target are excitation energies, the related CIS(D)<sup>[157,158]</sup> (a doubles correction to CIS) method should be used. Based on perturbation theory, CIS(D) introduces the effect of double excitations which are absent in CIS excited states. Excitation energies obtained in this way are still size consistent.

### 3.6.2 Linear Response CC2

Linear response CC2<sup>[138]</sup> is a powerful and widely used method for the computation of excited state geometries and properties. It is the excited state extension of the ground state CC2 method discussed before. One of the main advantages of this approach is that it does not require the explicit calculation of an excited-state wave function for the computation of excitation energies and other properties. Excitation energies are obtained as eigenvalues of the non-symmetric CC Jacobian  $\mathbf{A}$  matrix, the CC2 linear response function, which is defined as derivative of the vector function with respect to the cluster amplitudes (the explicit form is given in refs.<sup>[138,150]</sup>). For this purpose the eigenvalue equation

$$\mathbf{A}b_k = \omega_k b_k \quad (3.50)$$

has to be solved. In eq. (3.50)  $b_k$  are the eigenvectors (or Cholesky vectors)<sup>[159]</sup> and the  $\omega_k$  correspond to the excitation energy. In practice, this is achieved by employing both a modified Davidson<sup>[153]</sup> and a simple DIIS<sup>[153,160]</sup> (Direct Inversion of the Iterative Subspace) algorithm. Since  $\mathbf{A}$  is non-symmetric, left and right eigenvectors are not simply each other's adjoints and to obtain excited-state properties such as oscillator strengths and electric dipole moments, the two corresponding left and right eigenvalue problems have to be solved separately.

The typical error for vertical excitation energies at LR-CC2 level is of the order of 0.2-0.3 eV. For LR-CC2 analytic gradients<sup>[161]</sup> are available as well, hence, geometry optimizations of excited states are possible. Just as in ground state calculations, commonly, the RI approximation is employed in LR-CC2 calculations. A major drawback of LR-CC2 is the restriction to rather small molecules (< 40 atoms), particularly for geometry optimizations. Moreover, like all other single reference methods, LR-CC2 breaks down in regions close to conical intersections.

### 3.6.3 Algebraic Diagrammatic Construction Scheme

Besides LR-CC2 another very powerful and robust approach to compute excited state energies and properties is provided by the algebraic diagrammatic construction (ADC) scheme for the polarization propagator<sup>[162–166]</sup>. Using Møller-Plesset perturbation theory, different ADC schemes of different order  $n$  can be derived namely, ADC(1), ADC(2) and ADC(3). ADC(2), the second-order scheme, for instance, is based on the MP2 ground state. ADC(2) is available in two different variants: the strict ADC(2)-s and the extended ADC(2)-x variants. The latter one is not used in this work and will thus not be discussed here. Among the three available models, ADC(2)-s is the most commonly used one, which is most likely because it presents a good compromise between computational effort and accuracy. Typically, the ending “-s” is omitted and I will follow this convention in this work. While ADC(2) scales as  $O(N^5)$ , ADC(3) scales as  $O(N^6)$  and additionally requires huge amounts of memory and disk space. Moreover, it provides a balanced description of the different excited states e.g.  $\pi\pi^*$ , Rydberg, charge transfer and doubly excited states.

Originally, the ADC scheme for the polarization propagator was derived from a diagrammatic Green’s function (propagator) formalism.<sup>[162,163]</sup> However, a more convenient way to derive the ADC equations, especially from a computational perspective, is via the so-called *intermediate state representation* (ISR).

#### Intermediate State Representation

In the (algebraic) ISR reformulation the basic ADC secular matrix (see Fig. 3.5) is written as a representation of the shifted Hamiltonian  $\mathcal{H} - E_0$  (where  $E_0$  is the exact ground state energy) in terms of explicitly constructible states namely the intermediate states  $|\tilde{\Psi}_J\rangle$ .

Firstly, based on the exact ground state  $|\Psi_0\rangle$ , a set of correlated, precursor, excited states

$$|\Psi_J^0\rangle = \hat{C}_J |\Psi_0\rangle \quad (3.51)$$

is constructed, with  $\hat{C}_J$  being excitation operators used to create different classes of excitations in a way so that  $|\Psi_J^0\rangle$  can be grouped into single, double, . . . excitations. The first class is named particle-hole (p-h), the second two-particle-two-hole (2p-2h), etc..<sup>[167]</sup> However, the  $|\Psi_J^0\rangle$  states

are not yet orthogonal to each other. Thus, at next, the precursor states  $|\Psi_J^0\rangle$  are successively orthogonalized with respect to the ground state  $\Psi_0$  (as the 0th-order class) and additionally with respect to one another and each other excitation class, starting with the p-h class and continuing with higher excitation classes. Eventually, the orthonormal basis of intermediate states  $|\tilde{\Psi}_J\rangle$  is obtained. Those states are employed to construct the aforementioned matrix representation of the shifted Hamiltonian

$$M_{IJ} = \langle \tilde{\Psi}_I | \mathcal{H} - E_0 | \tilde{\Psi}_J \rangle. \quad (3.52)$$

The excitation energies  $\omega_n = E_n - E_0$  are eigenvalues of the Hermitian eigenvalue problem:

$$\mathbf{M}\mathbf{X} = \mathbf{X}\omega, \quad \text{with } \mathbf{X}^\dagger\mathbf{X} = \mathbf{1} \quad (3.53)$$

for the ISR secular matrix  $\mathbf{M}$ . Here,  $\omega$  is the diagonal matrix of the eigenvalues and  $\mathbf{X}$  is the matrix of eigenvectors (corresponding to the transition vectors). Up to this point the formalism is exact. However, since neither the exact ground state nor the exact ground state energy are known, approximations have to be made.

By systematically truncating the configuration space and using a perturbation expansion for the ISR matrix elements,

$$\mathbf{M} = \mathbf{M}^{(0)} + \mathbf{M}^{(1)} + \mathbf{M}^{(2)} + \dots \quad (3.54)$$

assuming the Møller-Plesset partitioning  $\mathcal{H} = H^0 + V$  the aforementioned hierarchy of approximation schemes ADC(1), ADC(2) and ADC(3) (see Fig. 3.5) is obtained. Using the  $n$ th order MP theory results in the same  $n$ th order ADC equations. In practice, ADC excitation energies are obtained by diagonalization of the corresponding ADC matrix  $\mathbf{M}$  (see Fig. 3.5), like in CIS. Transition moments (and thus oscillator strengths) can be computed from the eigenvectors. Since building up the complete ADC matrix is quite cumbersome, usually only a few (of the lowest) eigenvalues ( $\omega$ ) are computed using diagonalization procedures like the Davidson algorithm.

ADC methods are both size consistent and Hermitian. The beneficial unification of important properties like size consistency, Hermiticity, fairly high accuracy and comparably low computational cost makes particularly ADC(2) the method of choice for photochemical studies of medium and large molecules (with up to 80 atoms,  $\approx 500$  basis functions). Like for MP2 and CC2 calculations, the RI approximation can also be employed for ADC(2) calculations. All ADC(2) results shown in this work have been obtained by using RI-ADC(2)-s.

In a benchmark study including 28 small to medium-sized organic molecules it was found that

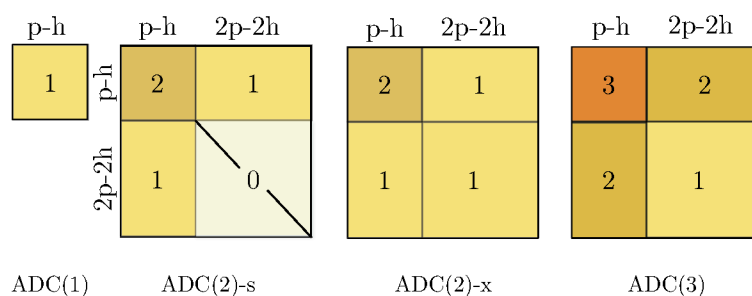


FIGURE 3.5: Graphical representation of the structures of the ADC matrix in the first order ADC(1), strict and extended second-order ADC(2)-s and ADC(2)-x, as well as the third-order scheme ADC(3). The level of perturbation theory is given as follows: white: zeroth-order; light yellow: first-order; dark yellow: second-order; orange: third-order). The figure is adapted from ref.<sup>[165]</sup>

ADC(2) calculations of vertical excitation energies have typical mean errors of  $0.22 \pm 0.38$  eV<sup>[166,168]</sup> ( $\pm$  standard deviation) for singlet and  $0.12 \pm 0.16$  for triplet states. Hence, ADC(2) yields a similar accuracy as LR-CC2. However, its Hermitian structure offers a clear advantage in the computation of excited-state properties. This is because left and right eigenvectors are the same and the eigenvalue equations have not be solved separately, like in LR-CC2.

The restricted ADC scheme of third order ADC(3) was found to exhibit a low mean error of  $0.08 \pm 0.27$  eV for singlet states and  $-0.10 \pm 0.13$  eV for triplet states.<sup>[166]</sup> Thus, it can be considered as a highly accurate method with a computational effort of  $\mathcal{O}(N^6)$ . In comparison, alternative methods of similar accuracy such as the excited state extensions (LR or equation of motion (EOM)) of CC3, CCSD(T) or CCSDT scale as  $\mathcal{O}(N^7)$ ,  $\mathcal{O}(N^7)$  and  $\mathcal{O}(N^8)$ <sup>[138,148]</sup>, hence, in general less favorably. A further great advantage of ADC over CC and CI is its compactness. In short, the compactness property means that the explicit configuration spaces of the secular problem are smaller than those of comparable CI or CC expansions. This property is also responsible for the higher computational efficiency of ADC(2) and ADC(3) as compared to the excited state extensions of CC2 and CC3 for instance.

Like CIS, CIS(D) and LR-CC2, also ADC(2) and ADC(3) are only suitable for systems with single reference (non-degenerate) ground states.

### 3.6.4 Linear Response Time-Dependent Density Functional Theory

Linear response time-dependent density functional theory (LR-TDDFT) is a very popular and widely used method to study excited states and still an active area of research.<sup>[169]</sup> The basic

idea of TDDFT is to extend DFT to the treatment of time-dependent phenomena. Instead of propagating the time-dependent Kohn-Sham wave function in time, like in real-time TDDFT<sup>[170]</sup>, in LR-TDDFT<sup>[170]</sup> excitation energies and oscillator strength are obtained from the linear time-dependent response of the time-independent ground state density  $\rho_0(\mathbf{r})$  to a time-dependent external electric field.

The foundation of modern TDDFT lies in two theorems by E. Runge and E. K. U. Gross<sup>[171,172]</sup> which provide the time-dependent generalization of the Hohenberg-Kohn theorems.

In short, the first RG theorem states that there is a one-to-one correspondence between the time-dependent electron density  $\rho(\mathbf{r}, t)$  evolving from a fixed initial state  $\Psi_0$  and the time-dependent external potential  $V_{ext}(\mathbf{r}, t)$ . Or in other words, it proves that  $\rho(\mathbf{r}, t)$  is a unique functional of  $V_{ext}(\mathbf{r}, t)$ :  $V_{ext}[\rho; \Psi_0](\mathbf{r}, t)$ . This also means that the wave function  $\Psi(t)$  can be regarded as a function of the density and the initial state and thus, that the expectation value of any Hermitian operator  $\hat{O}(t)$  is a unique functional of the density and initial state, analogous to the time-independent case. This theorem also implies that if the density of a system is known, the external potential can be obtained and with the external potential in hand the time-dependent Schrödinger equation can be solved, yielding all properties of the system. It should be noted, that for the original proof of this theorem two conditions are assumed to be fulfilled, namely that  $V_{ext}(\mathbf{r}, t)$  can be represented as the electric potential due to a normalizable charge distribution and that it has a time dependence that can be expressed as a Taylor series expansion in  $t$  about  $t = 0$ . Thus, potentials that turn on adiabatically from  $t = -\infty$  are, strictly speaking, not covered by the RG theorem, since they do not satisfy the latter requirement. Moreover, it should also be noted, that even though the RG theorem proves the uniqueness of  $V_{ext}(\mathbf{r}, t)$  it does not prove its existence, especially its existence for a non-interaction KS systems.

The second RG theorem presents a stationary action principle (the Euler equation eq. 3.55) in analogy to the HK variational principle for the time-independent system by introducing the so-called *action integral* (or action functional)  $\mathcal{A}_{xc}[\rho(\mathbf{r}, t)]$ . Under appropriate boundary conditions the variation of the action integral with respect to the density yields the exact density  $\rho(\mathbf{r}, t)$ .

$$\frac{\delta \mathcal{A}_{xc}[\rho]}{\delta \rho(\mathbf{r}, t)} = 0 \quad (3.55)$$

However, it turned out to be inadequate and was replaced later with a more appropriate action formalism<sup>[173]</sup> by defining a new action functional. A detailed discussion including complete proof of the relevant theorems of TDDFT can be found in the review articles by A. Dreuw et

al.<sup>[154]</sup> and Casida et al.<sup>[174,175]</sup>.

The difficulty in the formulation of a correct and conveniently applicable TDDFT formalism is that in the time-dependent system, an initial-value problem, i.e., the time-dependent Schrödinger equation:

$$i\frac{\partial}{\partial t}\Psi(\mathbf{r}_1, \dots, \mathbf{r}_N, t) = \mathcal{H}(t)\Psi(\mathbf{r}_1, \dots, \mathbf{r}_N, t) \quad (3.56)$$

has to be solved. In contrast to the stationary system, in which the (specific) ground state density of a noninteracting system is used (this density  $\rho(\mathbf{r}, t)$  is called *noninteracting  $v$ -representable*), it is more difficult to find such a noninteracting  $v$ -representable density for a time-dependent system. Or to put it differently, it is more difficult to prove the existence of a noninteracting system that possesses the same ground state density  $\rho(\mathbf{r}, t)$  as the interacting system.

One important step towards a solution of the so-called noninteracting  $v$ -representability problem and towards the time-dependent extension of the ground state KS formalism was provided by R. van Leeuwen<sup>[176,177]</sup>. Based on the fact that the initial state of the noninteracting system need not be an eigenstate of the system, he showed that under certain mild restrictions on an initial state with a right specified density and initial time derivative of the density, in a noninteracting system with this initial state a unique time-dependent external potential  $V_{ext}(\mathbf{r}, t)$  exists that reproduces a properly behaved density  $\rho(\mathbf{r}, t)$  at all times. Additionally, assuming a linear response regime, van Leeuwen proved the existence of a time-dependent Kohn-Sham scheme by proving the invertibility of the density response function for perturbations from a non-degenerate ground state. The huge advantage of this proof is that it circumvents the constraint of time analytic external potentials.

In practical applications, most commonly instead of KS-TDDFT, the linear response approach is used. Here, it is assumed that the system is perturbed by an external oscillating electric field with the additional assumption that the amplitude of the electric field is small enough such that the effects may be treated as a weak perturbation. Furthermore it is assumed that the perturbation is turned on adiabatically (slowly).

In LR-TDDFT vertical excitation energies and oscillator strengths are obtained by solving the following non-Hermitian eigenvalue equation also known as Casida's equation:

$$\begin{pmatrix} \mathbf{A} & \mathbf{B} \\ \mathbf{B}^* & \mathbf{A}^* \end{pmatrix} \begin{pmatrix} \mathbf{X} \\ \mathbf{Y} \end{pmatrix} = \omega \begin{pmatrix} \mathbf{1} & \mathbf{0} \\ \mathbf{0} & -\mathbf{1} \end{pmatrix} \begin{pmatrix} \mathbf{X} \\ \mathbf{Y} \end{pmatrix} \quad (3.57)$$

With matrices  $\mathbf{X}$  and  $\mathbf{Y}$  corresponding to excitation and “de-excitation” amplitudes and matrix elements  $A_{ia,jb}$  and  $B_{ia,jb}$  are given by:

$$A_{ia,jb} = \delta_{ij}\delta_{ab}(\varepsilon_a - \varepsilon_i) + \langle ij|ab \rangle + \langle ij|f_{xc}|ab \rangle \quad (3.58a)$$

$$B_{ia,jb} = \langle ib|aj \rangle + \langle ib|f_{xc}|aj \rangle \quad (3.58b)$$

with  $f_{xc}$  being the so-called *xc kernel* eq. (3.60) which is the main ingredient of LR-TDDFT. Such as in DFT, in practice approximations are made for  $f_{xc}$  as well. The LR approach has the advantage over the “original” KS-TDDFT method that solution of the time-dependent KS equations can be avoided. A further approximation which is usually made in conventional TDDFT is the so-called adiabatic approximation<sup>[175,178]</sup> eq. (3.59) (a local approximation in time). It assumes that the xc-potential  $V_{xc}$  changes instantaneously when the electron density is changed. This, however, also means that retardation effects and also the dependence on the history of the density are neglected.

$$V_{xc} = \frac{\delta A_{xc}[\rho]}{\delta \rho(\mathbf{r}, t)} \xrightarrow{\text{adiabatic approximation}} V_{xc} = \left. \frac{\delta E_{xc}[\rho(\mathbf{r}, t)]}{\delta \rho(\mathbf{r}, t)} \right|_{\rho=\rho(\mathbf{r}, t)} \quad (3.59)$$

Although, at first sight, the adiabatic approximation appears to be a rather crude approximation, it also brings with it a huge advantage, namely that all ground state time-independent xc-functionals can also be used in TDDFT calculations.

Often, in LR-TDDFT calculations in addition to the adiabatic approximation the so-called *adiabatic local density approximation* (ALDA) to the xc-kernel  $f_{xc}$  is employed. This means that  $f_{xc}$  is assumed to be time-independent (and its Fourier transform to be frequency independent), meaning  $f_{xc}$  is local in space and time and takes the form:

$$f_{xc}[\rho](\mathbf{r}, t) = \frac{\delta E_{xc}[\rho]}{\delta \rho(\mathbf{r})\delta \rho(\mathbf{r}')} \quad (3.60)$$

When hybrid xc functionals are used the matrix elements  $A_{ia,jb}$  and  $B_{ia,jb}$  have to be slightly adjusted, whereas, the eigenvalue problem eq. (3.57) remains the same. In the canonical basis,  $A_{ia,jb}$  and  $B_{ia,jb}$  can be written as:

$$A_{ia,jb} = \delta_{ij}\delta_{ab}(\varepsilon_a - \varepsilon_i) + \langle ij|ab \rangle - c_{HF}\langle ia|jb \rangle + (1 - c_{HF})\langle ij|f_{xc}|ab \rangle \quad (3.61a)$$

$$B_{ia,jb} = \langle ib|aj \rangle - c_{HF}\langle ia|bj \rangle + (1 - c_{HF})\langle ib|f_{xc}|aj \rangle \quad (3.61b)$$

with the coefficient  $c_{HF}$  being a measure of the amount of exact HF exchange in the employed hybrid functional. Neglecting matrix  $\mathbf{B}$  leads to the so-called Tamm-Dancoff approximation (TDA)<sup>[154]</sup>.

Overall, TDDFT results for excitation energies tend to be fairly good but depend significantly on the system and character of the excitation. The error for excitation energies of low-lying valence excited states (e.g.,  $\pi\pi^*$  and  $n\pi^*$ ) is typically small ( $\approx 0.1-0.5$  eV)<sup>[154]</sup>, when reasonably large basis sets are employed e.g. triple- $\zeta$  sets), which is comparable with the error of high-level correlated approaches. Errors for charge-transfer (CT) and Rydberg excitations, however, are usually much larger.<sup>[154,169,179]</sup> Vertical excitation energies of CT states, for instance, are often strongly underestimated and the PESs of CT states do not have the correct attractive  $\frac{1}{R}$  (Coulomb potential) dependence along the charge-separation coordinate  $R$ ,<sup>[179]</sup> even when hybrid functionals like the popular B3LYP functional are employed.

### 3.6.4.1 Charge-Transfer Failure

The failures of TDDFT in the description of CT states<sup>[154,179,180]</sup> can be best understood by analyzing the matrix elements of  $\mathbf{A}$  eq. (3.61).

As mentioned above, in a typical CT state the involved occupied and unoccupied MOs do not overlap (or overlap only weakly). Consequently, all terms containing products of such non-overlapping orbitals i.e., the second and fourth term i.e.,  $\langle ij|ab\rangle$  and  $\langle ij|f_{xc}|ab\rangle$  corresponding to the response of the Coulomb potential (having the appearance of an exchange term) and the xc potential of the KS operator, respectively, vanish. The only terms of  $\mathbf{A}$  which survive are the first term containing the orbital energy difference and the third term  $c_{HF}\langle ia|jb\rangle$  originating from the non-local HF exchange part of the KS operator. This exchange term, however, can be much more considered as a Coulomb term since the created “holes” (the positive charge in the CT state) in the occupied orbitals and the electrons in the unoccupied orbitals attract one another. Thus, this term is crucial for the correct  $\frac{1}{R}$  dependence of the PES of a CT state. Consequently, in the case of pure (local) DFT functionals without the inclusion of non-local HF exchange, the xc potential exhibits the wrong asymptotic behavior.

Moreover, since the terms of matrix  $\mathbf{B}$  are all zero the excitation energy of a CT state in the case when a pure local DFT functional is used is mainly determined by the orbital energy difference

$(\varepsilon_a - \varepsilon_i)$ . Since the negative of the LUMO energy  $-\varepsilon_a$  in DFT is much larger than the true electron affinity (EA) (the KS orbital energies are evaluated by using the same KS potential for all orbitals),  $(\varepsilon_a - \varepsilon_i)$  is usually a strong underestimation of the correct excitation energy. It is assumed that this  $\frac{1}{R}$  failure for CT states can be viewed as a self-interaction error (SIE) similar to the one present in ground state DFT. This interpretation becomes more evident if one analyses the matrix elements eq. (3.61) for two cases namely once for TDHF for which the amount of non-local HF exchange is 100% and  $c_{HF} = 1$  and once for pure TDDFT i.e.,  $c_{HF} = 0$ .<sup>[154]</sup> As mentioned above, for CT states the vertical excitation energy is dominated by the orbital energy difference  $\varepsilon_a - \varepsilon_i$ .  $\varepsilon_a$  contains the Coulomb interaction of orbital  $a$  with all occupied orbitals of the ground states (including orbital  $i$ ). But, orbital  $i$  is no longer occupied in the case of a CT transition. Nevertheless, the Coulomb interaction  $\langle ai|ai \rangle$  is contained within the energy difference  $\varepsilon_a - \varepsilon_i$  which means that the electron in orbital  $a$  experience the Coulomb interaction with itself still occupying orbital  $i$ . In hybrid TDDFT, however, this effect commonly named *electron-transfer self-interaction error* is canceled by the Coulomb-like term  $c_{HF}\langle ia|jb \rangle$  arising from the "hole" electron attraction being  $\langle ia|ia \rangle$ . If, this term, however, is  $c_{HF}\langle ia|jb \rangle$  this effect is not exactly canceled.

These deficiencies can be significantly mitigated by either using hybrid functionals with large HF exchange or range-separated functionals.

### 3.7 SPIN-FLIP APPROACH

In certain situations, e.g. bond breaking or cis-trans isomerization about a double bond strong static correlation effects arise which result in a strong multireference character of the system. In such situations, usually the systems intermediately adopt diradical character. According to Salem<sup>[181]</sup> diradicals can be described as systems with two electrons occupying two (near)-degenerate bonding and anti-bonding MOs. Due to this near degeneracy a conventional single-reference approach based on a single Slater determinant as reference wave function is no longer adequate. Only a multireference (or multideterminantal) approach that treats the important determinants on an equal footing provides an appropriate 0th-order reference function for a diradical. The spin-flip approach<sup>[182,183]</sup> provides one solution for such a "special" electronic situation. Here, the 'high-spin' triplet configuration  $\tilde{\Psi}_{M_s=+1}^t (\uparrow\uparrow)$  (see Fig. 3.6) which is accurately described by a single-reference wave function is used as the reference. The "problematic" target

states, e.g. open shell singlet or triplet states are then obtained by so-called spin-flip excitations as:

$$\Psi_{M_s=0}^{s,t} = \hat{R}_{M_s=-1} \tilde{\Psi}_{M_s=+1}^t \quad (3.62)$$

The operator  $\hat{R}_{M_s=-1}$  is an excitation operator that upon excitation flips the spin of an electron. In the SF approach, all three singlet determinants ( $\Psi^s$ ) and the  $M_s = 0$  triplet determinant ( $\Psi^t$ ) are treated on an equal footing. A further great advantage of this method is that due to the recent implementation of analytic derivative couplings<sup>[184]</sup> it can also be used to optimize conical intersections involving the ground state and an excited state at comparably low computational costs which alternatively is only possible by employing cost-intensive and complicated multireference approaches. For this thesis the SF approach has been used in conjunction with CIS and TDDFT,

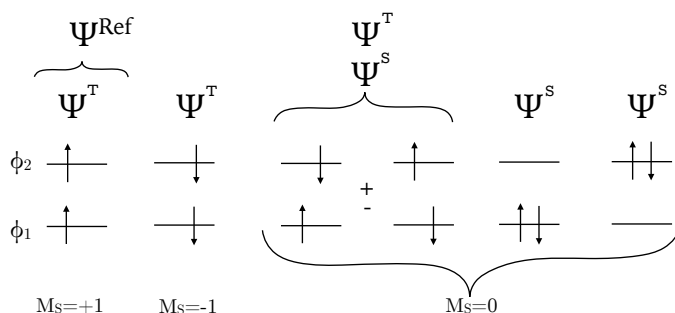


FIGURE 3.6: Schematic illustration of the electronic structure of a diradical. Six Slater determinants that can be generated by distributing two electrons in two molecular orbitals ( $\phi$ ) are shown. From these three singlet  $\Psi^s$  and three triplet states  $\Psi^t$  can be composed.

respectively.

### 3.8 SOLVATION EFFECTS

Commonly, theoretical photochemical studies are based on equilibrium geometries, energies and other properties computed in vacuum. Often, these are already sufficiently accurate to obtain a qualitatively correct picture of the studied reactions and processes. But why is it common to assume gas phase conditions, even though most chemical and biochemical reactions take place in solution?

The main reason for this is the unfavorable scaling of the computational effort for *ab initio* electronic structure methods with respect to system size. In most cases, it is simply not feasible to account for explicit solvation, i.e. to include a sufficient amount of explicit solvent molecules to

embed the solute and to correctly recover the bulk solvent effects and all possible intermolecular interactions.<sup>[185]</sup>

However, since, in fact, solvation changes the solute's electronic structure and thus also any property that depends on it (e.g., electric dipole moments) it can become very important, if not even necessary, to account for solvation effects. This is particularly relevant for the study of biochemical or catalytic reactions, solvatochromic effects and for a realistic comparison with experimental data which are often obtained in solution.

### 3.8.1 Continuum Solvation Models

One computationally very convenient and well-established approach for inclusion of approximate solvent effects are implicit continuum solvation models (CSMs). There are several different models which are closely related to another. Two very popular and widely used versions are the conductor-like screening model (COSMO)<sup>[186,187]</sup>, initially derived by Klamt and Schüürmann and the conductor-like polarizable continuum model (C-PCM)<sup>[186,188,189]</sup> by Cossi and Barone. I mention these two models here since they are the ones I use for the photochemical studies presented in **chapters 4-9** of this thesis. Their general ideas, basic concepts, advantages, and limitations are briefly presented in the subsequent paragraph. The focus of this work lies on the application of quantum chemical methods to study photochemical reactions of molecules and solvent effects on molecular properties and such reactions. Thus, I refrain here from a mathematical derivation and detailed discussion of the solvent models. Mathematical and technical details and a comprehensive discussion of continuum solvation models can be found in the review papers by Tomasi, Menucci and Cammi<sup>[190]</sup> and Cramer and Truhlar<sup>[191]</sup>.

In short, the basic idea of CSMs is to approximate the solute-solvent interactions as electrostatic interactions of a molecule with an isotropic environment. With this, the solvent itself is only described by macroscopic properties.

The great advantages of implicit CSMs are their comparably low computational costs, straightforward application and efficiency, which are most likely also responsible for their widespread use. By using CSMs one circumvents the partially very time-consuming computation of the large number of possible energetically close-lying local minima arising from small variations in the solvent structure, which often exhibits a poor convergence behavior. A significant limitation, however, is that they mainly account for electrostatic solute-solvent interactions. Thus, one can

expect them to be suitable for use only if other interactions like hydrogen-bonding and hydrophobic interactions and cavitation, dispersion and viscosity effects are negligibly small. Nevertheless, even though CSMs are based on many approximations, they usually provide a reasonable estimate of the influence of a solvent in a single calculation at comparably low computational costs.

CSMs compute the electrostatic component  $\mathcal{G}_{elec}$  eq. (3.63) of the free energy of solvation  $G$  which refers to the change in free energy for a molecule leaving the gas phase and entering a condensed phase.<sup>[99]</sup>

$$\mathcal{G}_{elec} = \langle \Psi | \hat{H}^0 | \Psi \rangle + \frac{1}{2} \langle \Psi | \hat{V} | \Psi \rangle \quad (3.63)$$

Where  $\hat{H}^0$  is the solute Hamiltonian in vacuum and the operator  $\hat{V}$  (sometimes also named  $\hat{R}$ ) accounts for the electrostatic solute-solvent interaction and depends on the solute electron density. The second term in the expression of  $\mathcal{G}_{elec}$  arises because one must account for the work associated with polarizing the solvent which amounts to half of the electrostatic interaction energy.  $\mathcal{G}_{elec}$  is obtained by solving an electrostatic problem, the Poisson equation, nested within a quantum chemical framework.

The main idea of CSMs is to mimic the solvent as a continuous, homogeneous, isotropic medium at thermal equilibrium characterized by a dielectric constant ( $\epsilon$ ) having properties consistent with those of the solvent itself. In the original mathematical formulation of the electrostatic problem within the *polarizable continuum model* (PCM)<sup>[192]</sup> by Miertuš and coworkers the medium is modeled as a *dielectric* characterized by  $\epsilon$  (a finite value  $> 1$ ). In this case, a set of dielectric boundary conditions have to be considered.

On the contrary, in the COSMO and C-PCM models, the medium is modeled as a *conductor* by defining  $\epsilon = \infty$ , rather than as a dielectric medium, circumventing the exact dielectric boundary conditions of the electrostatic problem. In this way, the mathematical formulation of the electrostatic problem is much simpler. Corrections for dielectric behavior are made *a posteriori* by introducing a scaling function ( $f_\epsilon$ ).<sup>[190,191]</sup>

An essential concept in all CSMs is the cavity that is embedded in the continuous medium. Its construction is non-trivial and often critical for the accuracy of the CSMs. Several different construction schemes exist for the cavity, resulting in different versions of CSMs. The cavity contains within its boundaries the largest possible part of the solute charge distribution ( $\rho(\mathbf{r})$ ) (with  $\mathbf{r} \in \mathbb{R}^3$ ). Commonly the exact electron density is used. In C-PCM and COSMO the molecular surface representing the solute-solvent boundary has molecular shape instead of simply spherical. It is constructed as an interlocked superposition of atomic spheres with radii close to the van der

Waals values centered on the atoms of the solute to reproduce its shape as best as possible. Those radii are then scaled by a factor of 1.1, 1.2 or 1.3, depending on the implementation of the model. Different values for both scaling factor and radii can be chosen. The choice can strongly affect the computational results. The most widely used set of radii is that defined by Bondi<sup>[193]</sup>.

### The electrostatic Problem

The physics of the electrostatic problem can be imagined as follows. First of all, it is assumed that the solute has an electric moment and that the equilibrium electrostatic interaction with the solvent is negative, meaning attractive. To keep it mathematically simple only dipole moments are considered. It is further assumed that when the solute is brought into the solvent, the solvent molecules reorient (are polarized) such that averaged over thermal fluctuations, their own dipole moments oppose that of the solute. The net orientation (polarization) induced by introducing the solute in the solvent results in an electric field, the *reaction field* ( $\phi(\mathbf{r})$ ).

Since, in conductor-like continuum models the medium is assumed to be conducting ( $\epsilon = \infty$ ) the solvent reaction field is represented by a surface charge density or *apparent surface charges* (ASC) ( $\sigma(\mathbf{s})$ ) (with  $\mathbf{s}_i$  being points on the cavity surface  $\Gamma$ ) which develops on the conductor surface in contact with the solute i.e., on the boundary. Calculation of the surface charge density is approached through discretization of the surface into small elements of known area ( $a_i \subset \Gamma$ ) and calculation of Gaussian-blurred point charges ( $q_i$ ) located at the center of each surface element.<sup>[194]</sup> In practice, a term that is central to all CSMs namely the reaction field or response operator ( $\hat{V}$  or  $\hat{R}$ ), accounting for the electrostatic interaction of the solute electron density with the ASC, is added to the solute Hamiltonian (see eq. (3.63)). This is realized in a way such that the solutes polarity increases proportional to its polarizability and the strength of the external field, hence, that its dipole moment increases. In response, the solvent itself polarizes and increases its own orientation to oppose the dipole moment of the solute and so on. Since it is assumed that the response of the medium to the introduction of the solute charge density is linear, it can be expressed in terms of the Poisson equation:

$$\nabla^2 \phi(\mathbf{r}) = -\frac{4\pi\rho(\mathbf{r})}{\epsilon} \quad (3.64)$$

The solute charge density  $\rho(\mathbf{r})$  is inside the cavity, the induced reaction field  $\phi(\mathbf{r})$ , however, is on the cavity surface. Consequently two regions, one inside and one outside the cavity have to be

considered. Thus, the Poisson equation takes the form:

$$\nabla\epsilon\nabla\phi(\mathbf{r}) = -4\pi\rho(\mathbf{r}) \quad (3.65)$$

To solve eq (3.65) within a quantum chemical framework, usually the potential  $\phi(\mathbf{r})$  is rewritten as a sum of two terms: the potential produced by the solute charge density in vacuum and the potential induced by the ASC, which is only due to the presence of the conducting continuum. The Poisson equation (3.65) is reformulated to yield a set of linear equations of the form:

$$\mathbf{K}\mathbf{q} = \mathbf{R}\mathbf{v} \quad (3.66)$$

The ASC  $q_i$  are computed from the values  $v_i$  of the solute's electrostatic potential containing both electronic and the nuclear part. The matrix  $\mathbf{K}$  contains the Coulomb interaction between the ASC and  $\mathbf{R}$  consists of the product  $-f_\epsilon\mathbf{1}$ <sup>[194]</sup>. In conductor like models  $\mathbf{K}$  consists only of the matrix  $\mathbf{S}$  with matrix elements  $S_{ij} = \frac{1}{|s_i-s_j|}$ , for  $i \neq j$ , since then the product  $S_{ij}q_j$  is the electrostatic potential due to  $q_j$  and the diagonal elements  $S_{ii} = 1.06\left(\frac{4\pi}{a_i}\right)^{\frac{1}{2}}$ .

COSMO and C-PCM implementations differ in the scaling function  $f_\epsilon$ . This is the main difference between the two models.  $f_\epsilon$  has the form  $\left(\frac{\epsilon-1}{\epsilon}\right)$  in C-PCM in compliance with Gauss's law<sup>[195]</sup> while in COSMO it has the dipole-form  $\left(\frac{\epsilon-1}{\epsilon+0.5}\right)$  based on the Kirkwood-Onsager model<sup>[196,197]</sup> for the solvation energy.

There are different approaches to consider solvent effects within a CSM framework depending on the process investigated. The ones I will discuss in the following subsections are the nonequilibrium and equilibrium approach which can be combined with the so-called linear response (LR) and state specific (SS) approaches. If the solute is in its electronic ground state the interaction of the ground state electron density with the ASC has to be described. This can either be achieved by means of a simple single point SCF calculation or by performing a geometry optimization. In the latter case the interaction between the ground state electron density of the solute with the reaction field of the solvent is computed for every new geometry in a separate SCF calculation. If, however, the aim is to compute solvatochromic shifts or to investigate solvent effects on excited state properties further effects have to be taken into account. Upon photoexcitation the electron density of the solute undergoes an instantaneous change. This change in the electronic charge distribution induces a polarization of the solvent molecules, which in turn instantaneously adjust to the new electron distribution in the solute resulting in a mutual interaction. This so-called

electronic polarization of the solvent is very fast, on the fs time scale.

On a slower time scale, both the solute molecule and the solvent molecules relax geometrically. This geometric relaxation induced by interactions between permanent dipoles of solute and solvent molecules results in a so-called orientational polarization of the solvent. Since these two components of solute-solvent interactions occur on very different time scales, they can be considered separately. Thus, in a CSM calculation, solvent effects can be considered by either taking account only the electronic polarization component or both components.

### 3.8.2 Ground State Equilibrium Solvation

In the most simplest case, the free energy of solvation  $\mathcal{G}_{elec}$  for the ground state is obtained in a single-point calculation by solving non-linear HF or the equivalent KS equations (3.67) in a procedure named *self-consistent reaction field* (SCRF).

$$\mathbf{F}'\mathbf{C}' = E'\mathbf{S}\mathbf{C}' \quad (3.67)$$

This procedure is formally equal to the usual HF and KS SCF for isolated molecules with the difference that the equation contains the modified Fock matrix  $\mathbf{F}'$  which includes different solvent related terms. Explicit expressions of these terms can be found in ref.<sup>[198]</sup> During a SCRF calculation the solute's wave function and its reaction field are iterated to self-consistency. This approach ensures a variational optimization of both the MOs (either HF or KS orbitals) and the ASC. Hence, the polarized MOs contain the interaction with the ASC in the form of orbital energies and thus, every post-HF method necessarily include the interaction with the equilibrated ground-state solvent field. The ground state SCRF procedure is very important since every calculation of vertical excitation energies in solution needs a converged HF or KS SCRF calculation.

For the ground state gradients for geometry optimizations are available for COSMO and C-PCM implementations when HF, DFT or MP2 methods are used. Depending on the implementation empirical corrections for non-electrostatic effects like dispersion, cavitation and exchange repulsion can be included optionally.

Concerning the accuracy of ground state equilibrium CSMs it has been found that when non-electrostatic contributions are included, CSMs are capable of providing free energies of solvation with a reasonable accuracy of a few  $\frac{kcal}{mol}$  for small- to medium-sized (< 50 atoms) molecules.<sup>[199–202]</sup>

### 3.8.3 Considerations for Excited States

As mentioned above, investigation of solvatochromism or solvent effects on excited state properties requires consideration of two limit time regimes of solvation: nonequilibrium and equilibrium. The former one being suited to describe “fast” solvation effects and the latter one being suited to describe “slow” solvation effects. For studying solvatochromic effects on absorption and emission, a nonequilibrium treatment is necessary. This is because these processes are ultrafast (vertical) processes (occurring on a sub-fs time scale) and much faster than the solvent relaxation time, typically being in the order of sub-ps to ps. Hence, the solvent molecules can be regarded as frozen in place during absorption and emission.

Two well-established formalisms for the description of solvent effects in the excited state are available: State specific (SS) and linear response (LR). It should be noted, that both can be used for ground state calculations as well. In the LR approach<sup>[203–205]</sup>, solvation effects are considered as a coupling between a pair of transitions mediated by the solvent molecules. Excitation energies for a whole set of excited states are computed in a single step calculation by diagonalization of the response matrix. This makes the LR approach very fast, efficient and computationally inexpensive, especially when used in combination with TDDFT which is often the case. For the LR approach within the TDDFT framework gradients are available such that excited state geometry optimizations in solution can be performed<sup>[189,206]</sup>. A severe drawback of the LR approach is that the mutual relaxation between the solute’s electronic density and the reaction field is completely neglected. Concerning the accuracy, it was found that it provides reasonably accurate results for solvatochromic effects on absorption spectra, especially for excitations involving bright states characterized by a large transition dipole moment but is rather unsuitable for studying solvatochromic effects on emission spectra.<sup>[174,207–212]</sup> Particularly in the case of CT excitations, which involve large changes in the solute’s charge distribution, the LR approach was found to be unsuitable especially when combined with TDDFT<sup>[212–214]</sup>. To ameliorate these shortcomings corrected versions like the cLR method<sup>[215]</sup> or the ptSS formalism<sup>[216,217]</sup> have

been developed.

The state specific (SS) formalism<sup>[215,218–224]</sup> has a long history starting from the pioneering paper by Yomosa in 1974<sup>[218]</sup>. It computes solvation effects individually for a specific state of interest. In contrast to the LR approach which uses the transition density of the solute to describe the solute-solvent interactions, the SS approach uses the difference density to compute the solvent response. Since the SS formalism employs the excited states density, it correctly takes into account the variation of the solute-solvent interaction accompanying the change in the electronic density due to the excitation. Its big advantage over the LR approach is that it accounts for equilibrium effects since the electronic part of the solvent response is equilibrated with the electron density of the solute excited state of interest. Hence, in the case of an excited state calculation, not only the equilibrium free energy of solvation is obtained for the excited state of interest, but also its wave function, self-consistently equilibrated with the ASC. Since each excited state is treated separately, the SS approach is well-suited to study solvatochromic effects on emission energies and solvent effects on CT state energies and properties.

One of the most popular and widely used approaches for studying solvatochromic effects on absorption spectra is nonequilibrium LR-PCM/LR-TDDFT. An alternative is provided by the recent perturbation-theoretical state specific (ptSS)-PCM approach which is implemented within the ADC formalism<sup>[217]</sup>. Two very powerful methods to study solvatochromic effects on emission spectra are given by the recent ADC(2)/SS-PCM<sup>[217]</sup> and ADC(2)/SS-COSMO<sup>[224]</sup> approaches which only differ slightly in their implementations.

A general ansatz to describe nonequilibrium solvation is to explicitly separate response properties of the solvent, i.e., the bulk dielectric response, into slow and fast components.<sup>[225–228]</sup> For the fast 'optical' component it is assumed that it relaxes at the same speed as electronic motions, hence, is always equilibrated with the solute. The slow 'orientational' or 'nuclear' component is assumed to remain fixed during vertical excitation since it relaxes on the time scale of nuclear and molecular motions. For the two different regimes of the response two different dielectric constants are defined. If the frequency of the external field is very small (static regime) it is assumed that the apparent surface charges are always completely equilibrated to the field such that the response is well described by the static dielectric constant  $\epsilon$ . However, if the external field oscillates at high frequencies, i.e., optical frequencies, it is assumed that only the electronic polarization is fast enough to remain in equilibrium with the external field (electronic regime) and the response is determined by a so-called optical dielectric constant which is defined as

$$\epsilon_{\text{optical}} = n^2.$$

In general, as already described above, the solvent response is described by means of ASC. Once the ASC are computed they are used to correct the solute's Hamiltonian. There exists various partition schemes the most commonly used ones being the Pekar<sup>[227,229]</sup> and the Marcus<sup>[225,230]</sup> partition which do in practice yield identical result. The more recent scheme by Cossi and Barone<sup>[228]</sup> valid for all CSM versions, yields:

$$\mathbf{q}_f = \left( \frac{n^2 - 1}{\epsilon - 1} \right) \mathbf{q} \quad (3.68)$$

$$\mathbf{q}_s = \left( \frac{\epsilon - n^2}{\epsilon - 1} \right) \mathbf{q} = \mathbf{q} - \mathbf{q}_f \quad (3.69)$$

This scheme is employed in the nonequilibrium LR approaches which are briefly discussed in the following subsections.

### The LR-C-PCM/TDDFT approach

The following short description of the general LR approach within the CSM formalism largely follows the one given by Cammi and Mennucci<sup>[204]</sup> and Cossi and Barone<sup>[203]</sup>. In short, within the LR-C-PCM/LR-TDDFT approach excitation energies and transition strengths are obtained as poles and residues of a response function of the form:

$$\langle\langle B; A \rangle\rangle_{\omega} = \begin{pmatrix} \nabla B \\ B \nabla \end{pmatrix} [\Omega - \omega \Delta]^{-1} \begin{pmatrix} \nabla A \\ A \nabla \end{pmatrix} \quad (3.70)$$

Equation eq. (3.70) expresses the time-dependent change in the expectation value of an arbitrary quantity  $B$  (e.g., the free energy) as the result of a time-dependent perturbation containing the arbitrary operator  $A$  in terms of the linear response matrix  $[\Omega - \omega \Delta]^{-1}$ .

As a starting point for the derivation of the final LR equation eq. (3.70) within the CSM framework

serves the time-dependent Schrödinger equation containing an effective Hamiltonian:

$$H^{eff}\Psi = i\hbar \frac{\partial \Psi}{\partial t} \quad (3.71a)$$

with

$$H^{eff} = H^0 + H'(t) \quad (3.71b)$$

with

$$H'(t) = c(t)A \quad (3.71c)$$

Here,  $H'(t)$  is the perturbation in which  $c(t)$  can be considered as the (real) “strength” and  $A = \sum_i a'(i)$  is a “fixed” one-electron operator determining the shape of the perturbation; for an external electric field, for instance it would take the form  $H'(t) = \mu E_0(e^{-i\omega+\epsilon t} + e^{i\omega+\epsilon t})$  with  $\mu$  representing the electric dipole operator and  $e^{\epsilon t}$  being a convergence factor. The Schrödinger equation eq. (3.71a) can be solved variationally by exploiting Frenkel’s variational principle<sup>[231]</sup>. The time-dependent changes of the variational parameter are obtained by using the Frenkel theorem<sup>[231]</sup> thereby using the gradient and Hessian components,  $(\nabla \mathcal{G})_0$ ,  $(\nabla \mathcal{G} \nabla)_0$ ,  $(\nabla \nabla \mathcal{G})_0$  of the nonequilibrium free energy functional  $\mathcal{G}(\mathbf{p})$  and solution of

$$(\nabla \mathcal{G})_0 + (\nabla \nabla \mathcal{G})_0 \mathbf{d}^* + (\nabla \mathcal{G} \nabla)_0 \mathbf{d} = i\hbar (\nabla \mathcal{Q} \nabla)_0 \dot{\mathbf{d}} \quad (3.72)$$

evaluated around the stationary point  $\mathbf{p}_0$ . Thereby, the linear response of  $\mathbf{d}$  is obtained by considering in eq. (3.72) only first order terms in the time-dependent perturbation. Assuming that  $H'(t)$  is introduced at  $t = -\infty$  and the initial conditions are  $\mathbf{p} = \mathbf{p}_0$ ,  $(\nabla \mathcal{G}) = 0$ , the linear term  $\mathbf{d}'$  (dropping the subscript 0) can be expressed as:

$$\mathbf{d}' = \frac{1}{2}(\mathbf{X}' e^{-i\omega t} + \mathbf{Y}' e^{i\omega t}) \quad (3.73)$$

$\mathbf{X}'$  and  $\mathbf{Y}'$  represent perturbation densities and are obtained as solutions from a set of linear equations:

$$\begin{pmatrix} \nabla A \\ A \nabla \end{pmatrix} + [\Omega - \omega \Delta] \begin{pmatrix} \mathbf{X}' \\ \mathbf{Y}' \end{pmatrix} = 0 \quad (3.74a)$$

with

$$\Omega - \omega \Delta = \begin{pmatrix} \nabla \mathcal{G} \nabla & \nabla \nabla \mathcal{G} \\ \mathcal{G} \nabla \nabla & \nabla \mathcal{G} \nabla^* \end{pmatrix} - \omega \begin{pmatrix} \mathbf{V} & 0 \\ 0 & -\mathbf{V} \end{pmatrix},$$

and

$$\mathbf{V} = \nabla Q \nabla$$

$$(A \nabla)_j = \frac{\langle \Psi | A | \frac{\partial \Psi}{\partial p_j} \rangle}{\langle \Psi | \Psi \rangle}, \quad (\nabla A)_j = \frac{\langle \frac{\partial \Psi}{\partial p_j} | A | \Psi \rangle}{\langle \Psi | \Psi \rangle}$$

Finally, the general form of the above mentioned linear response function eq. (3.70) can be deduced by solving the generalized eigenvalue problem:

$$\begin{pmatrix} \nabla \mathcal{G} \nabla & \nabla \nabla \mathcal{G} \\ \mathcal{G} \nabla \nabla & \nabla \mathcal{G} \nabla^* \end{pmatrix} \begin{pmatrix} \mathbf{X} \\ \mathbf{Y} \end{pmatrix} = \omega \begin{pmatrix} \mathbf{V} & 0 \\ 0 & -\mathbf{V} \end{pmatrix} \begin{pmatrix} \mathbf{X} \\ \mathbf{Y} \end{pmatrix} \quad (3.75)$$

where the vectors  $[\mathbf{X}, \mathbf{Y}]$  represent the frequency dependent linear response of the electron density in the basis of the unperturbed molecular orbitals, which allows to convert the linear response matrix  $[\Omega - \omega \Delta]^{-1}$  into a spectral form:

$$[\Omega - \omega \Delta]^{-1} = \sum_{\omega_p} \left[ \frac{1}{\omega - \omega_p} \begin{pmatrix} \mathbf{X}_p \\ \mathbf{Y}_p \end{pmatrix} (\mathbf{X}_p^\dagger \mathbf{Y}_p^\dagger) - \frac{1}{\omega + \omega_p} \begin{pmatrix} \mathbf{X}_p^* \\ \mathbf{Y}_p^* \end{pmatrix} (\mathbf{X}_p^{*\dagger} \mathbf{Y}_p^{*\dagger}) \right] \quad (3.76)$$

from which the general expression of the linear response function eq. (3.70) just follows.

This formalism can easily be adapted to the LR-TDDFT method. In this case the starting point

for the derivation of the final response equation eq. (3.80a) is the time-dependent KS equation:

$$\left[ h(\mathbf{r}) + v^{ext}(\mathbf{r}, t) + \int \frac{\rho(\mathbf{r}', t)}{|\mathbf{r} - \mathbf{r}'|} d\mathbf{r}' + v_{xc}[\rho](\mathbf{r}, t) + v^{PCM}(\mathbf{r}, t) \right] \psi_i(\mathbf{r}, t) = i\hbar \frac{\partial \psi_i(\mathbf{r}, t)}{\partial t} \quad (3.77a)$$

with

$$v^{PCM}[\delta\rho](\mathbf{r}) = \int_{\Gamma} \int_{\Gamma} \delta\phi(\mathbf{s}', \omega) \mathcal{Q}(\epsilon_{optical}; \mathbf{s}', \mathbf{s}) \frac{1}{|\mathbf{s}' - \mathbf{r}|} ds ds' \quad (3.77b)$$

$$\delta\phi(\mathbf{s}', \omega) = \int_{\mathbf{R}^3} \frac{\delta\rho(\mathbf{r}', \omega)}{|\mathbf{s}' - \mathbf{r}'|} d\mathbf{r}' \quad (3.77c)$$

where  $\mathcal{Q}$  is the response operator or response matrix (in terms of finite charges) which acts on the solute's electrostatic potential at the point  $s'$  to generate a point charge at point  $s$ :  $q_I = \sum_J^{surf\ elem} \tilde{\mathcal{Q}}_{IJ} \phi_J$  (with  $\mathcal{Q}_{IJ} = \frac{1}{2}(\tilde{\mathcal{Q}}_{IJ} + \tilde{\mathcal{Q}}_{JI})$ ), since  $\tilde{\mathcal{Q}}$  can be symmetrized with respect to the exchange of the surface elements). Here, the solute-solvent interaction is introduced by using an effective KS operator  $\hat{\mathcal{F}}_{KS}(\mathbf{r}) = \hat{\mathcal{F}}_{KS}^0(\mathbf{r}) + v^{PCM}(\mathbf{r})$  which contains the solvent related PCM operator  $v^{PCM}[\delta\rho](\mathbf{r})$ . The variation of the density matrix  $\delta P(\omega)$  (in the frequency domain) eq. (3.78a, 3.78b)<sup>[203]</sup> is obtained by expanding the time-dependent KS equations to first order in the perturbation  $v^{ext}$ , thereby exploiting the diagonal nature of the unperturbed KS operator and dividing it into its particle-hole and hole-particle parts (which yields to a reduction by a factor of 2 in the dimension of the matrix equations which have to be solved).  $\delta P(\omega)$  contains the variation of the PCM operator  $v^{PCM}[\delta\rho](\mathbf{r})$  due to the sudden change in the electron density due to the external perturbation, thereby taking into account that, due to the idempotency condition for the density matrix  $P$ , the only nonzero elements in the expression for the time-dependent change of the density  $\delta\rho(\mathbf{r}, \omega) = \sum_{st} \delta P_{st}(\omega) \psi_s(\mathbf{r}) \psi_t(\mathbf{r})$  (in terms of time-independent KS orbitals) are those relating occupied and virtual 0th order orbitals (particle-hole and hole-particle blocks) which allows for its division as:<sup>[203,232]</sup>

$$(\epsilon_a - \epsilon_i + \omega) \delta P_{ia} + \sum_{jb} K_{ia,jb} \delta P_{jb} + \sum_{jb} K_{ia,bj} \delta P_{bj} = -\delta v_{ia}^{ext}(\omega) \quad (3.78a)$$

$$(\epsilon_a - \epsilon_i + \omega) \delta P_{ai} - \sum_{jb} K_{ai,bj} \delta P_{bj} + \sum_{jb} K_{ai,jb} \delta P_{jb} = -\delta v_{ai}^{ext}(\omega) \quad (3.78b)$$

When the solvent response is expressed in terms of finite point charges the coupling matrix element (on a molecular orbital basis) has the form

$$K_{st,uv} = K_{st,uv}^0 + \sum_{IJ}^{surf\ elem} \phi_{st}(\mathbf{s}_I) \mathcal{Q}_{IJ}(\epsilon_{optical}) \phi_{uv}(\mathbf{s}_J) \quad (3.79)$$

Where  $K_{st,uv}^0$  is the coupling matrix element for the isolated solute. With all the relevant terms defined, equations eq. (3.78a and 3.78b) can be rewritten to yield a more compact form:

$$\left[ \begin{pmatrix} \mathbf{A} & \mathbf{B} \\ \mathbf{B}^* & \mathbf{A}^* \end{pmatrix} - \omega \begin{pmatrix} 1 & 0 \\ 0 & -1 \end{pmatrix} \right] \begin{pmatrix} \delta \mathbf{P} \\ \delta \mathbf{P}^* \end{pmatrix} = - \begin{pmatrix} \delta \mathbf{v} \\ \delta \mathbf{v}^* \end{pmatrix}, \quad (3.80a)$$

where

$$A_{ai,bj} = \delta_{ab} \delta_{ij} (\epsilon_a - \epsilon_i) + K_{ai,bj} \quad (3.80b)$$

and

$$B_{ai,bj} = K_{ai,jb} \quad (3.80c)$$

Looking at the contributions of matrices  $\mathbf{A}$  and  $\mathbf{B}$  it can be seen that the only difference between the gas phase LR-TDDFT method and the one within the CSM framework is that to both expressions (3.80b and 3.80c), simply CSM-type potentials are added namely  $\sum_{IJ}^{surf\ elem} \phi_{st}(\mathbf{s}_I) \mathcal{Q}_{IJ}(\epsilon_{optical}) \phi_{uv}(\mathbf{s}_J)$ . This also reveals the difference to the SS approach. The LR ansatz follows because the reaction field, determined by solution of the SCF equations for the ground state interacts with the excited state density but is not changed by it.

Eventually, equation 3.80a is transformed into a non-Hermitian eigenvalue problem which is solved to obtain excitation energies.

### SS-PCM and ptSS-PCM Approaches

In the following, I will give a brief description of the SS-PCM/ADC(2) method with a focus on the basic working principle of this method. For the sake of compactness, only the most important equations are given. Readers interested in the mathematical derivation and implementation are referred to papers by Mewes et al. [216,217,233] and Lunkenheimer et al. [224]. The SS-PCM/ADC(2) method by Mewes et al. [217] involves either two or three separate calculations. In the first one the "initial" electrostatic potential  $V(r, s)$  and electron density of the excited state of interest (the one which is equilibrated) are computed in a nonequilibrium ptSS calculation using the ground state density as reference. The subsequent macro iteration, after convergence, yields the free (eq. 3.81), total and emission energy of the excited state  $|i\rangle$  in the frozen reaction field of the equilibrated reference state  $|k\rangle$ . In case of an excited state calculation, which is addressed here,

the excited state  $|i\rangle$  equals the solvent-equilibrated (reference) state  $|k\rangle$ .

$$\mathcal{G}_k^{(eq)} = \langle k | \hat{H}^{vac} + \frac{1}{2} \hat{R}_k | k \rangle \quad (3.81a)$$

with

$$\hat{R}_i = \int_{\Gamma} \hat{V}(r, s) \sigma_i(s) ds \quad (3.81b)$$

During the macro iteration ASC (represented by  $\hat{R}$ ) and energies are converged to self-consistency. In the first step, the electrostatic potential of the reference excited state from the initial SCF calculation is used to compute ASC which are separated into slow and fast components, the operator  $\hat{R}$  is split into slow and fast components  $\hat{R}^f$  and  $\hat{R}^s$  and used in the SCF calculation to obtain a new set of polarized MOs for the subsequent ADC(2) calculation which provides an updated excited state density. In the second step, the actual first iteration of the macro iteration, the electrostatic potential from the previous calculation is used to compute new ASC which are again separated and employed in the SCF performed in the frozen updated ASC. After this SCF calculation again the polarized MOs are subjected to an ADC(2) calculation in which a new excited state density is computed. This procedure usually takes about 4-8 iterations until convergence is achieved.

Besides the total and emission energy of the solvent-equilibrated excited state, also energies and wave functions of the other out-of-equilibrium states (e.g., ground state and other excited states) are obtained in each iteration, however, treated in the nonequilibrium limit eq. (3.82).

$$E_i^{Noneq(k)} = \langle i | \hat{H}^{vac} + \hat{R}_k^{f+s} + \lambda(\hat{R}_i^f - \hat{R}_k^f) | i \rangle \quad (3.82)$$

This is realized by employing the ptSS formalism which based on the perturbation-theoretical, state-specific Hamiltonian (in the case of absorption  $k = 0$  refers to the ground state) yields the 1st order correction to the energy:

$$E_i^{(1)} = \langle i^{(0)} | \hat{R}_i^f - \hat{R}_k^f | i^{(0)} \rangle \quad (3.83)$$

and the respective 1st order correction to the  $|0\rangle \rightarrow |i\rangle$  excitation energy:

$$G_i^{ptSS} = \langle i^{(0)} | \hat{R}_i^f | i^{(0)} \rangle - \langle i^{(0)} | \hat{R}_0^f | i^{(0)} \rangle - \frac{1}{2} \left( \langle i^{(0)} | \hat{R}_i^f | i^{(0)} \rangle - \langle 0 | \hat{R}_0^f | 0 \rangle \right) + \frac{1}{2} \int_{\Gamma} (\sigma_i^f(s) - \sigma_0^f(s)) V_{\sigma_0^s}(s) ds \quad (3.84)$$

where  $\langle i^{(0)} |$  refers to the 0th order wave function of state  $|i\rangle$  in the nonequilibrium limit and is computed *a posteriori* using polarized ground state MOs. In the third calculation, a ptSS (nonequilibrium) calculation which is commonly performed, but not necessary, the emission energy of the equilibrated excited state (and excited state properties) and if requested transition moments for excited-state absorption are computed. The emission energy is obtained as the vertical excitation energy from the reference state which is the equilibrated excited state plus the ptSS energy correction for the ground state obtained in the reaction field of the reference state. In contrast to the SS-PCM/ADC(2) method described above, the SS-COSMO/ADC(2) method by Lunkenheimer et al.<sup>[224]</sup> self-consistently include LR contributions into the ADC(2) equations and uses relaxed densities instead of ISR derived ones. However, despite some differences in these methods, it was found that they agree to within 0.1 eV.<sup>[217]</sup>

As already mentioned above, the ptSS scheme which was originally derived to compute solvent corrected vertical excitation energies (corrected to 1st order in perturbation theory eq. (3.83), compared to the ptSS scheme used in the SS approach contains a small modification. This modification is introduced to correct for the following "deficiency". The ASC used in the ADC(2) calculations are obtained for the HF ground state density and can be assumed to provide a poorer description of the electrostatic potential of the solute than ASC obtained for the correlated MP density and may lead to systematic errors in the excitation energies. This is the case, for instance, if the total MP2 dipole moment is significantly smaller than the HF dipole moment, which was observed for nitroaromatics<sup>[216]</sup>. Hence, additive corrections to both 0th order and 1st order excitation energy based on the MP2 ground state density are introduced which can, advantageously, be computed *a posteriori*. In short, for the computation of all terms which depend on the ASC of the ground state the MP densities are used. The respective approach is therefore named ptSS(PTD). A detailed derivation and implementation of this approach are given in the original paper by Mewes et al.<sup>[216]</sup> All vertical excitation energies presented in this work which have been obtained at the ptSS-PCM/ADC(2) level of theory refer to ptSS(PTD) corrected energies.

### 3.9 CHARACTERIZATION OF ELECTRONIC STATES

For the investigation of photochemical reactions and processes, molecular properties and structure-reaction relationships a basic understanding of the electronic structure of the studied molecular

systems is an essential prerequisite. In this context, it is very useful to characterize the involved electronic states not only with respect to the energetics but also with regard to certain key properties e.g. static dipole moments and especially their nature. A simple and “universal” characterization and nomenclature has the additional advantage of facilitating collaborative studies among experimentalists and theoreticians.

One very convenient and common way to achieve such a description is by analyzing molecular orbitals (MOs). This makes sense since in particular the low-lying excited states which are of major relevance for the photochemistry are usually well-described by a single or a few one-electron transition(s) from an occupied to an unoccupied orbital e.g. HOMO  $\rightarrow$  LUMO or HOMO-1  $\rightarrow$  LUMO.

For this purpose, the MOs are typically characterized with respect to their character (bonding, nonbonding or anti-bonding (the latter character is indicated by a “\*")), shape and properties as  $\sigma$ ,  $\pi$ ,  $n$  or Rydberg orbitals. The  $\sigma$  notation indicates orbitals that are symmetric to rotation about the line connecting the nuclei. The  $\pi$  notation indicates a change in sign of the wave function with a 180° rotation about the bond axis. The notation ‘ $n$ ’ for orbitals typically stands for lone pair orbitals on either nitrogen, sulfur or oxygen atoms. Rydberg orbitals are by nature very diffuse compared to valence orbitals and display little, if any, bonding or antibonding character. Accordingly, excited states can be described as S( $\pi\pi^*$ ), S( $\sigma\pi^*$ ), S(CT), T( $n\pi^*$ ) etc. transitions. Such a description has the great advantage that certain properties of the excited states which depend on the character of the involved orbitals are implicitly contained like for instance that  $\pi\pi^*$  states are usually optically allowed ‘bright’ states and  $n\pi^*$  or CT are forbidden, ‘dark’ states. Additionally, electronic states can also be described by analyzing so-called *natural transition orbitals* (NTOs) which are constructed through a singular value decomposition of the transition density matrix (TDM)<sup>[234]</sup>

$$T_{ia} = \langle \psi_i | \hat{T}(\mathbf{r}) | \psi_a \rangle \quad (3.85)$$

This matrix, however, cannot be directly diagonalized, since it is non-symmetric. For this reason, a singular value decomposition is performed yielding the NTOs as eigenfunctions of the TDM.

$$\mathbf{D}_{|MO|}^{0I} = \mathbf{U} \text{diag}(\sqrt{\lambda_1}, \sqrt{\lambda_2}, \dots) \mathbf{V}^T \quad (3.86)$$

where  $\mathbf{U}$  and  $\mathbf{V}$  are unitary matrices.  $\mathbf{U}$  is used to generate the hole NTOs and  $\mathbf{V}$  to generate the particle NTOs.<sup>[234]</sup>

The TDM couples the electronic ground state with a given excited state. NTOs are specific for one-electron transitions and always come in pairs (a “particle” “hole” pair) sharing the same eigenvalue which measures the fraction of electrons transferred.

Alternatively, so-called *attachment* and *detachment* densities can be analyzed which are obtained by diagonalization of the difference density matrix  $\Delta$

$$\Delta = \mathbf{P}_{ES} - \mathbf{P}_{GS} \quad (3.87)$$

where  $\mathbf{P}_{ES}$  is the single electron density matrix of the excited states and  $\mathbf{P}_{GS}$  the corresponding density matrix of the ground state. The detachment density can be seen as the part of the one-electron ground state density that is removed upon excitation and the attachment density is the rearrangement of this density.

---

## STUDY OF THE UNUSUAL FLUORESCENCE BEHAVIOR OF THE DONOR-ACCEPTOR MOLECULE N-PYRROLOBENZONITRILE (PBN)

---

In this chapter<sup>†</sup> the photochemistry of the title compound N-pyrrolobenzonitrile (PBN) is investigated by using different high-level *ab initio* methods including CC2, ADC(2) and the highly accurate ADC(3) method (compare sections 3.5.2 and 3.6.3). Solvation effects are considered by using different continuum solvation models like C-PCM and COSMO (see section 3.8).

This study conclusively explains all available experimental findings like the effects of excitation wavelength, temperature and solvent polarity on the emission spectra of PBN. According to the computational results, the following photochemical mechanism is proposed: After photoexci-

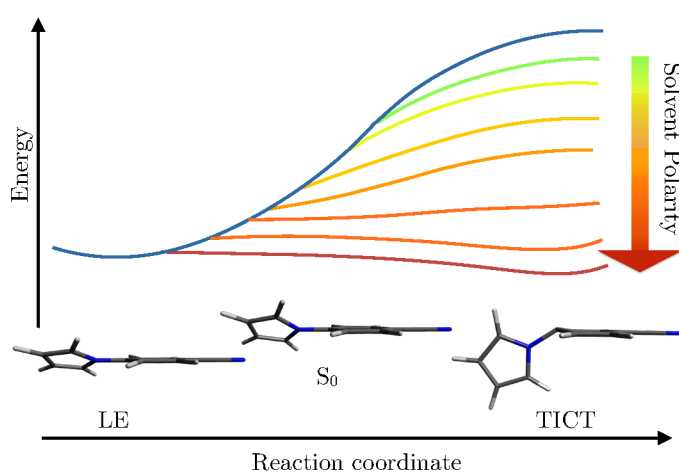


FIGURE 4.1: Schematic illustration showing the effect of solvent polarity on the potential energy curve of  $S_1$  state and the energy of the TICT state.

---

<sup>†</sup>Parts of this chapter are adapted from Bohnwagner, MV. Burghardt I. Dreuw, A. *J Phys Chem A*, **2016**, *120(1)*, pp 14-27<sup>[235]</sup>, Copyright 2015 with permission from the American Chemical Society and the corresponding editor

tation in the gas phase to the bright  $S_2$  ( $\pi\pi^*$ ) state, PBN relaxes on the  $S_2$  ( $\pi\pi^*$ ) state surface until a conical intersection with the energetically close-lying forbidden (dark)  $S_1$  (LE) state is reached. After passing this conical intersection, PBN further relaxes on the LE state surface towards a minimum from which emission may occur. In polar solvents, in contrast, the polar  $S_3$  (CT) state is strongly stabilized and an energy barrier along the twisting coordinate vanishes. Consequently, population of the twisted intramolecular CT (TICT) state minimum becomes the dominating decay process and red-shifted fluorescence occurs. Furthermore, this study shows that TICT formation in PBN not only involves twisting about the central C-N single bond but also a pyramidalization of the central carbon atom (the one connected to the nitrogen atom) of the benzene ring.

#### 4.1 MOTIVATION AND BACKGROUND

PBN (see Fig. 4.2) is a typical donor-acceptor (D/A) molecule for which dual fluorescence has been observed.<sup>[82,236–238]</sup> As already mentioned in section **Introduction**, today there is a consensus in the scientific community that dual fluorescence results from emission from a locally excited (LE) state as well as from a polar intramolecular charge-transfer (ICT) state. Energy and intensity of the anomalous fluorescence band thereby strongly depend on the solvents polarity and viscosity.<sup>[239]</sup> Just like in DMABN, the prototype dual fluorescent molecule and PBN (see Fig. 4.2),

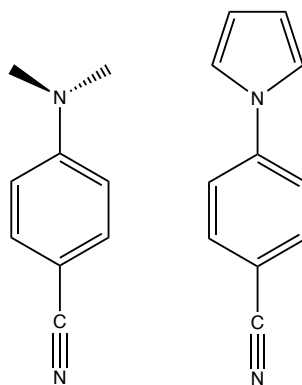


FIGURE 4.2: Structures of 4-(Dimethylamino)benzonitrile (DMABN) (left), 4-(1H-pyrrol-1-yl)benzonitrile (PBN) (right)

dual fluorescence was also found in many other small D/A systems e.g. phenyl pyrroles<sup>[240–242]</sup>, arylsilanes<sup>[242,243]</sup> 4-(dimethylamino)benzoic acid methyl ester (DMABME)<sup>[244]</sup>, stilbenes<sup>[84]</sup> and certain hemithioindigo photoswitches<sup>[245]</sup>.

In PBN, pyrrol serves as the donor (D) and benzonitrile as the acceptor (A) group. PBN in contrast to DMABN exhibits a higher electron density at the donor group due to the pyrrol ring possessing six  $\pi$ -electrons. Thus, an even more efficient ICT can be expected.

If slightly twisted (idealized) PBN has  $C_2$  point group symmetry<sup>[246]</sup>. This group contains only two symmetry operations: E the identity operation without any effect and a twofold symmetry axis  $C_2$  (see Fig. 4.3). Both in the planar conformation and when D and A groups are twisted by  $90^\circ$  (and not tilted), PBN has  $C_{2v}$  symmetry<sup>[246]</sup>.

Even though numerous experimental studies of PBN in the gas phase, the liquid phase at different temperatures and in solid phase and also a few theoretical studies have been carried out<sup>[68,83,236–238,241,247–254]</sup>, there remain open questions concerning the involved photochemical processes and the nature of the CT.

#### 4.1.1 Previous experimental studies

Cornelissen-Gude *et al.*<sup>[248]</sup> were the first to investigate the photochemistry of PBN spectroscopically in liquid and solid phase using solvents of different polarity. At room temperature, one broad absorption band has been observed at about 4.33 eV (286 nm), which was found to be rather insensitive to solvent polarity. Cornelissen-Gude *et al.* suggest that this band arises from an allowed  $L_a$ -type (in Platt's nomenclature<sup>[255]</sup>) state as well as an  $L_b$ -type state, which is hidden underneath the much stronger  $L_a$ -type band.

Platt's nomenclature is a widely used nomenclature for spectra of aromatic molecules and originally developed to facilitate the comparison of the spectra of benzene, naphthalene etc., and their derivatives. The lowest lying excited states of benzene are named:  $L_b$ ,  $L_a$ ,  $B_b$  and  $B_a$ . It has the advantage that it is independent of the molecular symmetry.

In emission spectra recorded at room temperature in polar solvents one broad emission band at about 2.58 eV (480 nm) has been found. This emission band has been assigned to a polar CT state. Dual fluorescence has been observed only in apolar *n*-hexane solution and frozen ethanol. In frozen ethanol, besides the broad red-shifted emission band at about 2.88 eV (430 nm), a second weaker emission band was found at about 3.87 eV (320 nm). Cornelissen-Gude *et al.* further report that the relative intensities of both emission bands and the solvatochromic shift of the red-shifted band strongly depend on temperature and excitation wavelength.

Murali *et al.*<sup>[68]</sup> report about dual fluorescence in an apolar solvent mixture which, however, is

only observed at room temperature. From the results of their fluorescence experiments Murali *et al.*<sup>[68]</sup> infer that the broad band occurring at longer wavelengths results from emission from a stable CT state while the vanishing vibrational feature observed for cooling of the sample results from emission from a less stable LE state which is thermodynamically populated only at higher temperatures.

Yoshihara *et al.*<sup>[241]</sup> report similar findings. It has been found that in *n*-hexane LE and CT emission bands have similar intensities. In more polar solvents, only red-shifted fluorescence has been observed.

In gas phase experiments under jet-cooled conditions<sup>[249]</sup> only single emission at about 4.0 eV (310 nm) has been observed. The fluorescence with a lifetime of  $17 \pm 2$  ns has been assigned to the forbidden L<sub>b</sub>-type S<sub>1</sub> state. In the gas phase absorption spectrum one broad band has been found which has been assigned to the allowed L<sub>a</sub>-type S<sub>2</sub> state. From their results Belau *et al.*<sup>[249]</sup> infer only a small energy gap of about 0.05 - 0.06 eV between S<sub>2</sub> and S<sub>1</sub> states and suggest that efficient coupling between them leads to the population of and emission from the S<sub>1</sub> state.

Fuß *et al.*<sup>[251]</sup> report on results obtained from gas phase pump-probe experiments. They suggest that after excitation to the allowed L<sub>a</sub>-type state S<sub>2</sub> state two possible relaxation pathways open up: 1) an ultrafast relaxation to the L<sub>b</sub>-type S<sub>1</sub> state minimum through a conical intersection as already proposed by Belau *et al.*<sup>[249]</sup> 2) relaxation from the L<sub>a</sub>-type S<sub>2</sub> state to a CT minimum without changing the potential energy surface. They further suggest that an equilibration between the two minima (L<sub>b</sub> and CT) occurs and that twisting around the central bond and elongation of the bonds in the benzonitrile ring are two components of the CT reaction coordinate.

In a more recent publication Roznowska *et al.*<sup>[238]</sup> report on the observation of dual fluorescence of PBN in different polyvinyl alcohol solvents and ethylene glycol and polymer matrices of polyvinyl alcohol. In acetonitrile solution at room temperature, the normal emission band has been found at about 3.44 eV (360 nm) and the anomalous band at about 2.61 eV (475 nm). In the highly polar ethylene glycol solvent, the corresponding bands have been observed at 3.54 eV (350 nm) and 2.45 eV (500 nm).

#### 4.1.2 Previous theoretical studies

Besides experimental studies several theoretical investigations<sup>[83,250,252,254,256,257]</sup> have been conducted as well. In those, however, mainly semi-empirical and DFT approaches have been

used which have some severe limitations. Semi-empirical methods have the major deficiency that they are parameterized. This means that their results are fitted by a set of parameters usually so as to produce results that best agree with experimental data. Consequently, they may work sufficiently well for the systems for which the parameters have been defined but are likely to fail when the target system strongly differs from those. Generally, it is very difficult to assess the reliability of their results and careful calibration is required. Moreover, they are typically less accurate than *ab initio* methods.<sup>[258]</sup> As already mentioned in chapter 3 one of the biggest deficiencies of DFT is that standard functionals often severely fail for charge-transfer states. Additionally, in most of these theoretical studies solvent effects on absorption and emission spectra are completely neglected or considered by using rather crude models<sup>[83]</sup> as the Kirkwood-Onsager model<sup>[196,197,259,260]</sup>.

Early semi-empirical CNDO/s-CI calculations performed by Rettig *et al.*<sup>[256]</sup> in which two different solvation models have been used predict four energetically low lying TICT states for the 90° twisted geometry of PBN and also a low lying PICT state for the planar conformation. From their results Rettig *et al.*<sup>[256]</sup> conclude that the observed red-shifted fluorescence is more likely emitted from the energetically lowest TICT state rather than from the energetically lowest PICT state. However, it is emphasized that emission from a PICT state should not be generally ruled out.

DFT/MRCI<sup>[83]</sup> excited state calculations for which point group symmetry<sup>[246]</sup> has been used (PBN has been assumed to be C<sub>2</sub> symmetric), provide two CT states 2B and 3A and two bright  $\pi\pi^*$  states 1B and 2A as the photochemically relevant excited states. At the ground state equilibrium (or FC geometry) 2B is the S<sub>1</sub> state and 2A is the S<sub>3</sub> state. A ground state potential energy surface scan along the twisting coordinate performed in the gas phase reveals a stabilization of the 1B state (S<sub>2</sub> at the FC geometry) which has a static dipole moment of  $\mu_{FC} = 6.20$  D at the FC geometry and the 3A state (S<sub>4</sub> at the FC geometry) which has a static dipole moment of  $\mu_{FC} = 18.48$  D at the FC geometry and an increase of the corresponding static dipole moments. At 90° the 1B state ( $\mu = 20.1$  D) which upon twisting evolves into a CT state has been found to be the lowest lying excited singlet state. Based on the computational results Parusel<sup>[83]</sup> suggest that the red-shifted fluorescence<sup>[248]</sup> is due to emission from the 1B TICT state. In this study, however, excited state geometry relaxation is completely neglected. But this structural relaxation is important to obtain emission energies which are comparable to experimental data. Furthermore, it should be considered that when molecular symmetry is used, principally, idealized conditions

are assumed. Under "realistic" conditions e.g., in solution a molecule vibrates and rotates and thus the symmetry is likely to be broken.

CASSCF/cc-pVDZ and CASPT2/cc-pVDZ calculations in which PBN has been assumed to be  $C_{2v}$  symmetric provide two CT minima located on the  $2^1A$   $S_2$  state potential energy surface.<sup>[250]</sup> Zilberg *et al.* suggest that the  $1B_2$   $S_1$  state corresponds to the LE state. One of the two  $2^1A$  state minima is found to have a  $90^\circ$  twisted conformation and is assigned as TICT minimum and the other one is found to be planar and is assigned as PICT minimum. Zilberg *et al.* report that the TICT minimum has an anti-quinoid (AQ) geometry i.e. lengthened central benzene bonds and a lengthened central C-N<sub>pyrrol</sub> bond and possesses a large static dipole moment of about 16 D. The PICT state minimum is reported to have a quinoid (Q) geometry i.e. shortened central bonds of the benzene ring and a short C-N<sub>pyrrol</sub> bond and to have a smaller static dipole moment in the range of 6-13 D. In the gas phase, the AQ structure has been found to be about 0.63 eV more stable than the Q structure. Zilberg *et al.* propose that the normal emission band corresponds to the  $1B_2$  LE state and the anomalous emission results from either the Q or the AQ CT state. However, Zilberg *et al.* note that the results refer to gas phase calculations only and in the gas phase the computed energies of the two CT states is too high for efficient crossing with the LE state.

A recent publication by Minezawa<sup>[254]</sup> focus on the effects of solvation on the CT states of PBN. The strong dependence of the computed potential energy curves of ICT states of PBN on the chosen solvation model is emphasized. Absorption and emission spectra of PBN have been calculated at TDDFT/LC-BLYP/DH+(d) level of theory using the LRFE model for acetonitrile solution, which predicts a bright  $S_1$  state of A symmetry which is assigned to the LE state and two dark states  $S_2$  and  $S_3$  of B symmetry. Minezawa suggests that in gas phase the TICT ( $1B$ ) state minimum is spontaneously reached by twisting only. In contrast, the LR-RISM-TDDFT level provided a completely different free energy profile for TICT formation being endergonic. However, the LRFE-TDDFT method predicts an exergonic reaction which is in agreement with experimental findings.

Conclusively, in view of the above-described studies, it is clear that still no common agreement on the molecular coordinates involved in the ICT and the character of the involved excited states has been reached.

The motivation of this study is to achieve this understanding of the reaction mechanism of dual fluorescence of PBN. For this purpose high-level *ab initio* calculations and the inclusion of

solvent effects using sophisticated solvent models are inevitable.

## 4.2 COMPUTATIONAL METHODS

Firstly the ground state ( $S_0$ ) geometry of PBN has been optimized using CC2 and DFT in combination with the range-separated hybrid CAM-B3LYP functional. CAM-B3LYP has 19% nonlocal exchange in the short range limit and 65% in the long range limit. In both calculations the correlation-consistent, polarized valence triple- $\zeta$  basis set cc-pVTZ<sup>[261–263]</sup> has been used. Additionally, molecular symmetry was exploited, i.e. PBN was constrained to have  $C_2$  symmetry (see Fig. 4.3). For CC2 calculations the resolution-of-the-identity (RI) approximation with the corresponding auxiliary basis set aux-cc-pVTZ<sup>[264]</sup> has been applied. Vibrational frequency analyses have been performed at the corresponding level of theory to verify the stationary points as local minima on the potential energy surfaces. For the investigation of TICT formation, the dihedral angle  $\beta(C1'-N-C1-C2)$  (numbering scheme in Fig. 4.3) between D and A moieties was chosen as the reaction coordinate  $\beta$ . A relaxed scan of the  $S_0$  PES along the twisting coordinate  $\beta$  has been carried out in the gas phase at CC2/cc-pVTZ level of theory. Starting from the equilibrium geometry,  $\beta$  was varied in increments of  $10^\circ$  and the geometry was determined by relaxing the remaining degrees of freedom.

Vertical excitation energies of the six lowest excited singlet states have been calculated at the  $S_0$  (1A in  $C_2$ ) state equilibrium geometry obtained at CC2/cc-pVTZ level of theory. Different excited state methods have been applied: ADC(3) and ADC(2), LR-CC2, CIS(D) and TDDFT (compare sections 3.6.3, 3.6.2, 3.6.1 and 3.7) using two types of xc functionals: hybrid BHLYP<sup>[265,266]</sup> and long-range corrected CAM-B3LYP. For ADC(2) and LR-CC2 calculations the RI approximation has been employed. All excited state calculations have been performed using the cc-pVTZ and corresponding aux-cc-pVTZ basis set.

To investigate solvent effects on absorption spectra I have employed state-specific (SS) equilibrium and nonequilibrium solvation approaches. Solvent effects on vertical excitation energies at the Franck-Condon (FC) geometry have been estimated by using the C-PCM model employing perturbative state-specific (ptSS) and linear-response-type (ptLR)<sup>[216]</sup> schemes as implemented in a development version of Q-Chem 4.3<sup>[267,268]</sup> and additionally the SS-COSMO model as implemented in TURBOMOLE V6.6<sup>[269]</sup>. The parameters of acetonitrile (ACN) ( $\epsilon = 36.6$ ,  $n = 1.344$ ) have been used for the solvent models for comparison with experimental data.

Excited state geometries have been optimized at CC2/cc-pVTZ and TD-CAM-B3LYP/cc-pVTZ levels of theory. All stationary points were confirmed as local minima or transition states by vibrational frequency analysis at TD-CAM-B3LYP/cc-pVTZ level of theory. Solvent effects on vertical excitation energies at the corresponding excited state equilibrium geometries have been estimated at ADC(2), TDA/CAM-B3LYP and TD-CAM-B3LYP levels of theory in conjunction with the cc-pVTZ basis set using COSMO as implemented in TURBOMOLE V6.6 and Orca 3.0.1<sup>[270]</sup> as well as ptSS-PCM.

In order to investigate the TICT mechanism, a relaxed scan of the bright 2A ( $S_2$  at the FC geometry) state potential energy surface (PES) along  $\beta$  has been performed first in the gas phase at CC2/cc-pVTZ level of theory. Starting from the equilibrium dihedral angle  $\beta_{2A} = 13^\circ$ ,  $\beta$  was varied in increments of  $10^\circ$ . Hereby, the geometries were constrained to have  $C_2$  symmetry. Along this scan TDDFT/CAM-B3LYP/cc-pVTZ and ADC(2)/cc-pVTZ single point calculations were carried out to obtain vertical excitation energies for the photochemically relevant excited states. The influence of polar solvents on the energy profile of the relevant CT state has been studied by employing SS equilibrium solvation at TDDFT/CAM-B3LYP/cc-pVTZ/C-PCM and ADC(2)/cc-pVTZ/COSMO and C-PCM level of theory, respectively, using the parameters of ACN.

All vacuum CC2 and CIS(D) calculations have been performed using TURBOMOLE V6.3.1<sup>[271]</sup>. Vertical excitation energies at ADC(2), ADC(3) and ADC(2)/C-PCM level of theory have been computed using the Q-Chem<sup>[267,268,272]</sup> package versions 4.2.0 and 4.3.0. For the computation of vertical excitation energies at TDDFT/CAM-B3LYP, TDDFT/CAM-B3LYP/C-PCM and TDDFT/BHLYP level of theory Gaussian 09 Rev D01.<sup>[273]</sup> has been used.

## 4.3 RESULTS

### 4.3.1 Ground state properties of PBN

Full ground state geometry optimizations using CC2 and CAM-B3LYP levels of theory yield a  $C_2$  symmetric equilibrium geometry of PBN (see Figures 4.5 and 4.3). At the theoretical level of CC2/cc-pVTZ the rings are planar but twisted against each other by an equilibrium dihedral angle of  $\beta_{S_0} = 33^\circ$ . With bond lengths of  $C2'-C1' = 1.379 \text{ \AA}$ ,  $C1'-N = 1.383 \text{ \AA}$ ,  $N-C_1 = 1.404 \text{ \AA}$ ,  $C1-C_2 = 1.400 \text{ \AA}$ ,  $C2-C_3 = 1.389 \text{ \AA}$  and  $C3-C_4 = 1.402 \text{ \AA}$  (numbering scheme in Fig. 4.3) the rings

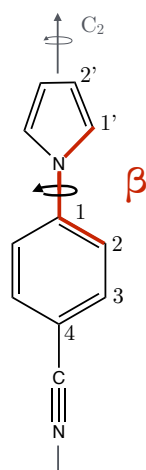


FIGURE 4.3: Structure of PBN and numbering of the relevant atoms. Additionally the twisting coordinate  $\beta$  (in red) and the twofold symmetry axis  $C_2$  are shown.

show the typical alternating bond length pattern of aromatic compounds.<sup>[274]</sup> At DFT/CAM-B3LYP/cc-pVTZ level of theory an equilibrium dihedral angle of  $\beta_{S_0} = 31^\circ$  is obtained. The bond lengths C2'-C1', C1'-N, C1-C2, C2-C3, C3-C4 are shortened by only 0.006, 0.007, 0.009 and 0.011 Å, respectively, compared to the CC2 optimized structure indicating that the geometries are very similar for both methods. The twist of the ground state geometry results in a less effective  $\pi$ -conjugation between the rings as compared to a planar structure, yielding a central N-C<sub>1</sub> bond length of 1.404 Å, an intermediate length between a single and a double bond.<sup>[275]</sup> In the ground state, PBN has a static dipole moment  $\mu_0$  of 3.4 D and 3.8 D along the z-axis at CC2/cc-pVTZ and DFT/CAM-B3LYP level of theory, respectively. At CC2/cc-pVTZ level of theory twisting is characterized by a flat potential which is symmetric around the planar ( $\beta = 0^\circ$ ) conformation. The potential has two barriers: a small barrier of 0.05 eV (1.15 kcal/mol  $\approx 2k_B T$ ) for the planar transition state, and a higher barrier of 0.13 eV (2.99 kcal/mol) for the perpendicular transition state ( $\beta = 90^\circ$ ) and two local minima corresponding to two "static" enantiomers with  $\beta = 32.5^\circ$  and  $\beta = -32.5^\circ$ , respectively. The interconversion between the two enantiomeric conformers at room temperature (298 K) is extremely fast, with a rate constant  $k$  of  $k = 8.12 \cdot 10^{11} \frac{1}{s}$  (corresponding to a half life of 80 ps) using the simple Arrhenius equation for an estimate. Thus, the enantiomers can not be isolated under experimental conditions at room temperature. Twisting up to  $90^\circ$ , however, is slightly hindered with  $k = 4.67 \cdot 10^{10} \frac{1}{s}$  (corresponding to a half life of 0.46 ns). Our ground state calculations confirm the DFT/MRCI results by Parusel *et al.*<sup>[83]</sup> described above.

### 4.3.2 Vertical excited states of PBN

Vertical excitation energies and properties of the lowest lying excited singlet states of PBN have been calculated at the equilibrium ground state geometry obtained at CC2/cc-pVTZ level of theory. Results for the first four excited singlet states obtained at ADC(3), LR-CC2, ADC(2), CIS(D), TDDFT/BHLYP and TDDFT/CAM-B3LYP levels of theory are summarized in Table 4.1, because only these four states are relevant for the investigated TICT mechanism. For the nomenclature of the excited states irreducible representations will be used independently of the energetic order of the states.

According to ADC(3), ADC(2), LR-CC2 and CIS(D) calculations, the  $S_1$  state is a forbidden  $\pi\pi^*$  state. It has B symmetry and thus will be named 1B in the following. The 1B state has a negligible oscillator strength and a static dipole moment of about 6 D at LR-CC2 and ADC(2) levels, respectively i.e.  $\mu$  is only slightly larger than the one of the ground state.

The largest component of the excitation vector of this state is an excitation from the HOMO-1 to the LUMO+1 (47% at ADC(3) level of theory) (Figure 4.4). While the HOMO-1 is delocalized over the whole molecule, the LUMO+1 is localized only on the benzene ring. A smaller

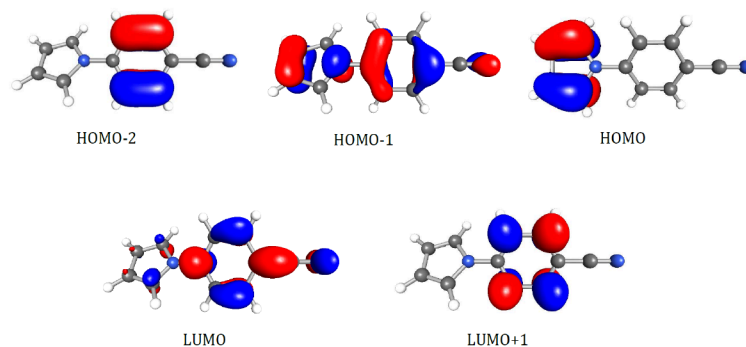


FIGURE 4.4: HF molecular orbitals obtained at LR-CC2/cc-pVTZ level of theory at the  $S_0$  equilibrium geometry (isovalue of 0.05). DFT/BHLYP and DFT/CAM-B3LYP orbitals are practically identical.

contribution of 1B corresponds to the HOMO-2  $\rightarrow$  LUMO (local  $\pi\pi^*$ ) excitation (30% at ADC(3) level of theory) on the benzonitrile moiety (see Fig. 4.4). This 1B state can be assigned to the experimentally observed forbidden  $L_b$ -type (LE) transition.<sup>[68,249,251]</sup> For the 1B (LE) state ADC(3), ADC(2), LR-CC2 and CIS(D) levels predict excitation energies of 4.58, 4.74, 4.76 and 4.82 eV, respectively. TDDFT with respect to the wave function based methods slightly overestimates the excitation energies of 1B. TD-CAM-B3LYP and TD-BHLYP calculations yield excitation energies of 4.95 and 5.09 eV, respectively.

TABLE 4.1: Comparison of excited state properties of the first four lowest singlet excited states obtained at different levels of theory at the  $S_0$  state equilibrium geometry (obtained at CC2/cc-pVTZ level of theory). Highest molecular orbital contributions and character of the states (in parenthesis), vertical excitation energies  $\omega$  (in eV), oscillator strengths (in parenthesis) and static dipole moments  $\mu$  (in Debye) are given.

State	MOs	ADC(3)		LR-CC2		ADC(2)		TD-CAM-B3LYP		TD-BHLYP	
		$\omega$	$\mu$	$\omega$	$\mu$	$\omega$	$\mu$	$\omega$	$\mu$	$\omega$	$\mu$
1B	H-1>L+1 ( $\pi\pi^*$ ) H-2>L (local $\pi\pi^*$ )	4.58(0.00)	4.4	4.76(0.00)	5.7	4.74(0.00)	6.2	4.95(0.00)	5.8	5.09(0.00)	6.0
2A	H-1>L ( $\pi\pi^*$ )	4.81(0.64)	8.3	4.82(0.64)	11.0	4.76(0.65)	11.3	4.82(0.61)	8.4	4.88(0.61)	8.1
2B	H>L (CT)	5.06(0.01)	14.1	4.93(0.01)	17.1	4.93(0.01)	18.1	4.78(0.01)	15.7	4.81(0.01)	16.0
3A	H>L+1 (CT)	5.83(0.03)	15.8	5.52(0.02)	17.8	5.55(0.02)	19.6	5.54(0.02)	16.3	5.58(0.02)	16.4

All applied levels of theory predict the  $S_2$  state to be a bright  $\pi\pi^*$  state exhibiting a large oscillator strength of about 0.6. The  $S_2$  has A symmetry (in  $C_2$ ) and will thus be referred to as 2A state hereafter. The 2A state is mainly characterized by the HOMO-1  $\rightarrow$  LUMO transition (77% at ADC(3) level of theory) (see Fig. 4.4), in which an electron is transferred from a delocalized MO to a MO localized on the benzonitrile moiety. Thus, this  $\pi\pi^*$  state acquires certain CT character explaining its relatively large static dipole moment of about 11 D (see Table 4.1). Concerning the prediction of vertical excitation energies and properties of the 2A state, wave function and density based methods agree very well. LR-CC2 and TD-CAM-B3LYP even predict the same excitation energy. Excitation energies of 4.81, 4.82, 4.76, 5.31, 4.82 and 4.88 eV are obtained at ADC(3), LR-CC2, ADC(2), CIS(D), TD-CAM-B3LYP and TD-BHLYP levels of theory, respectively. This state can be assigned to the optically allowed  $L_a$ -type transition that results in the broad absorption band observed at about 4.40 eV ( $\approx$  280 nm).<sup>[238,248,249]</sup>

All employed wave function based methods yield a dark  $S_3$  state of B symmetry exhibiting very small oscillator strength which will be named 2B in the following. The 2B state is characterized exclusively by the HOMO  $\rightarrow$  LUMO excitation (see Fig. 4.4). The localized nature of HOMO and LUMO results in a large static dipole moment of about 18 D (see Table 4.1). For the 2B state ADC(3), LR-CC2, ADC(2), CIS(D), TD-CAM-B3LYP and TD-BHLYP levels of theory predict excitation energies of 5.06, 4.93, 4.93, 5.46, 4.78 and 4.81 eV, respectively. As compared to wave function based methods TDDFT slightly underestimates the excitation energy of the 2B state.

The  $S_4$  state is predicted to be a dark state having a small oscillator strength ( $\approx$  0.02) and exhibiting A symmetry. It is mainly a HOMO  $\rightarrow$  LUMO+1 transition (75% at ADC(3) level of theory) (see Fig. 4.4). Again, the localized character of the involved MOs results in a substantial CT character and a large static dipole moment of about 18 D. This state will be referred to as 3A state. For the 3A state excitation energies of 5.52, 5.67, 5.54 and 5.58 eV are obtained at LR-CC2, ADC(2), TD-CAM-B3LYP and TD-BHLYP levels of theory, respectively.

In general, the results obtained via LR-TDDFT are in good agreement with those obtained at LR-CC2 and ADC levels of theory. One striking difference, however, is that at the FC geometry, the energetic order of the two states 1B (LE) and 2B (CT) is interchanged at TDDFT level as compared to LR-CC2 and ADC levels. To examine if the underestimation of the 2B (CT) state is due to the well-known charge-transfer failure of TDDFT which is related to the electron-transfer SIE (see subsection 3.7.1), the amount of HF exchange in CAM-B3LYP was varied. In CAM-B3LYP the contribution of non-local HF exchange is incorporated by two parameters  $\alpha$

and  $\beta$ , i.e. 19% HF exchange at short-range ( $\alpha = 0.19$ ) and 65% HF exchange at long-range ( $\alpha + \beta = 0.65$ )<sup>[276]</sup>. This study reveals that vertical excitation energies of the two CT states 2B and 3A strongly depend on the amount of HF exchange. When going from  $\alpha = 0.00$  to  $\alpha = 0.65$  they are increased by 0.65 eV and 0.90 eV, respectively. In contrast, those of the 2A ( $\pi\pi^*$ ) and 1B (LE) states are less affected. They are increased only by 0.33 eV and 0.47 eV, respectively. For 30% HF exchange at short-range ( $\alpha = 0.30$ ) and more, the energetic order of 2B (CT) and bright 2A ( $\pi\pi^*$ ) is interchanged. With full (100%) HF exchange at long-range ( $\alpha + \beta = 1.00$ ) and no short-range contribution ( $\alpha = 0.00$ ) the energetic order of the first three lowest excited states changes again: 2A ( $S_1$ ) and 1B ( $S_2$ ) states become energetically almost degenerate. Vertical excitation energies are 4.95 eV and 4.99 eV, respectively. And the 2B (CT) state becomes the  $S_3$  state, i.e. the energetic order predicted by ADC and LR-CC2 methods is obtained. This behavior of the excitation energies demonstrates that the underestimation of the excitation energies of the 2B (CT) state observed for TD-BHLYP and even for the range-separated TD-CAM-B3LYP functional is indeed related to the electron-transfer SIE and hence artificial.

The results for the two states with A symmetry  $S_2$  and  $S_4$  agree among all methods but CIS(D). The  $S_4$  state at CIS(D) level has B symmetry and no CT character.

All applied methods, except for CIS(D), provide nearly degenerate vertical excitation energies of  $S_1, S_2$  and  $S_3$  (1B, 2A and 2B) states and a very small energy gap ( $\Delta E(1B, 2A)$ ) between 1B ( $\pi\pi^*$ ) and 2A ( $\pi\pi^*$ ).  $\Delta E(1B, 2A)$  is 0.08 eV at LR-CC2/cc-pVTZ, 0.02 eV at ADC(2)/cc-pVTZ and 0.23 eV at ADC(3)/cc-pVTZ level of theory, respectively, indicating a strong mixing of these states. The vertical excitation energies of the 1B and 2A states obtained at the ADC and LR-CC2 levels of theory in gas phase are in very good agreement with gas phase experiments of PBN. These measurements taken at 80 C° show a strong broad absorption band centered at 4.59 eV<sup>[251]</sup> which is assigned to the  $L_a$  state and a weaker precursor band which is assigned to the  $L_b$  state<sup>[251]</sup>. Supersonic-jet spectra show the 0-0 band of this state at 4.27 eV.<sup>[249]</sup>

### Solvent effects on absorption energies

To get a first estimate of the extent to which solvent effects are involved in the stabilization of the photochemically relevant excited states, i.e. 1B (LE), bright 2A ( $\pi\pi^*$ ) and 2B (CT) vertical excitation energies have been computed using ADC(2)/cc-pVTZ employing the equilibrium state-specific (SS) COSMO and the nonequilibrium ptSS-PCM approaches. The parameters of

ACN have been used for the solvation model. To obtain state-specific solvent-corrected vertical excitation energies for each of the relevant states the apparent surface charges (ASC) of the COSMO model are equilibrated with respect to the corresponding states. The vertical energies of the other excited states are obtained as nonequilibrium corrections. For comparison, first the ground state has been used to equilibrate the solvent model yielding corrected excitation energies. In a second step the ASC are equilibrated with respect to the excited states and vertical excitation energies are recalculated. The difference in excitation energies then reveals the pure contribution of the fast solvent response to the solvatochromic shift at fixed geometry. The solvent-corrected vertical excitation energy of the bright 2A ( $\pi\pi^*$ ) state of 4.65 eV is in good agreement with the experimentally observed absorption maximum at about 4.36 eV<sup>[238,253]</sup> obtained in ACN solution at room temperature. Independent on the excited state to which the ASC are equilibrated, a strong red-shift of the vertical excitation energy of the 2B (CT) state is obtained in comparison to its vertical energy obtained when the ASC are equilibrated with respect to the  $S_0$  density. When the ASC are equilibrated with respect to the bright 2A ( $\pi\pi^*$ ) state, the red-shift of vertical excitation energy of the CT state is already so pronounced that the energetic order of bright 2A and 2B (CT) state changes: the 2B (CT) state becomes the energetically lowest excited state. In contrast, vertical excitation energies of 1B (LE) and bright 2A ( $\pi\pi^*$ ) states are shifted very little. With respect to the gas phase results, the dipole moments are generally enhanced. From these results it can be inferred that already the fast electronic solvent response has a strong influence on the stabilization of the 2B (CT) state and thus on the energetic order of the photochemically relevant excited states at the FC geometry. The calculations suggest, that in the gas phase, the energy of the 2B state is too high for efficient crossing with the bright 2A ( $\pi\pi^*$ ) state, while in polar solvents the polar CT state is stabilized so that crossing becomes feasible.

### 4.3.3 Structural relaxation in the excited states

In order to obtain emission energies which can be compared to experimental data, geometries of 1B, 2A and 2B states have been optimized in the gas phase at LR-CC2/cc-pVTZ (see Fig. 4.5) and TD-CAM-B3LYP/cc-pVTZ levels of theory enforcing  $C_2$  symmetry. For each stationary point a vibrational frequency analysis has been carried out at TD-CAM-B3LYP/cc-pVTZ level of theory in order to verify its identity as local minimum or transition state (TS).

TABLE 4.2: Comparison of vertical excitation energies  $\omega$  (in eV) of 1B (LE), bright 2A ( $\pi\pi^*$ ) and 2B (CT) states obtained at ADC(2)/cc-pVTZ, ADC(2)/cc-pVTZ/SS-COSMO and ADC(2)/cc-pVTZ/ptSS-PCM levels of theory. Vertical excitation energies in gas phase and solvent-corrected vertical excitation energies, static dipole moments  $\mu$  (relaxed) (in Debye) and solvent shifts  $\Delta\Delta\omega_{\text{sol}}^a$  and  $\Delta\Delta\omega^b$  (in eV) are given.)

State	ADC(2) <sub>gas</sub>		ADC(2) <sub>COSMO</sub>		ADC(2) <sub>COSMO</sub> wrt 1B			ADC(2) <sub>COSMO</sub> wrt 2A			ADC(2) <sub>COSMO</sub> wrt 2B			ADC(2) <sub>ptSS-PCM</sub>	
	$\omega$	$\mu$	$\omega$	$\mu$	$\omega$	$\mu$	$\Delta\Delta\omega_{\text{sol}}$	$\omega$	$\mu$	$\Delta\Delta\omega_{\text{sol}}$	$\omega$	$\mu$	$\Delta\Delta\omega_{\text{sol}}$	$\omega$	$\Delta\Delta\omega$
1B	4.74	5.5	4.80	5.7	4.76	7.8	-0.04	4.60	13.2	-0.20	4.40	17.2	-0.40	4.79	+0.05
2A	4.76	10.4	4.65	11.2	4.50	13.2	-0.15	4.12	17.7	-0.53	3.82	20.0	-0.83	4.66	-0.20
2B	4.93	16.0	4.77	16.8	4.50	18.1	-0.26	3.90	21.8	-0.86	3.41	23.5	-1.35	4.60	-0.24

<sup>a</sup>  $\Delta\Delta\omega_{\text{sol}}$  is the difference between the vertical excitation energies in solution within COSMO solvation when the reaction field is equilibrated with respect to the  $S_0$  density and with respect to the respective excited state density

<sup>b</sup>  $\Delta\Delta\omega$  is the difference between the vertical excitation energies computed in gas phase and with the C-PCM solvent model.

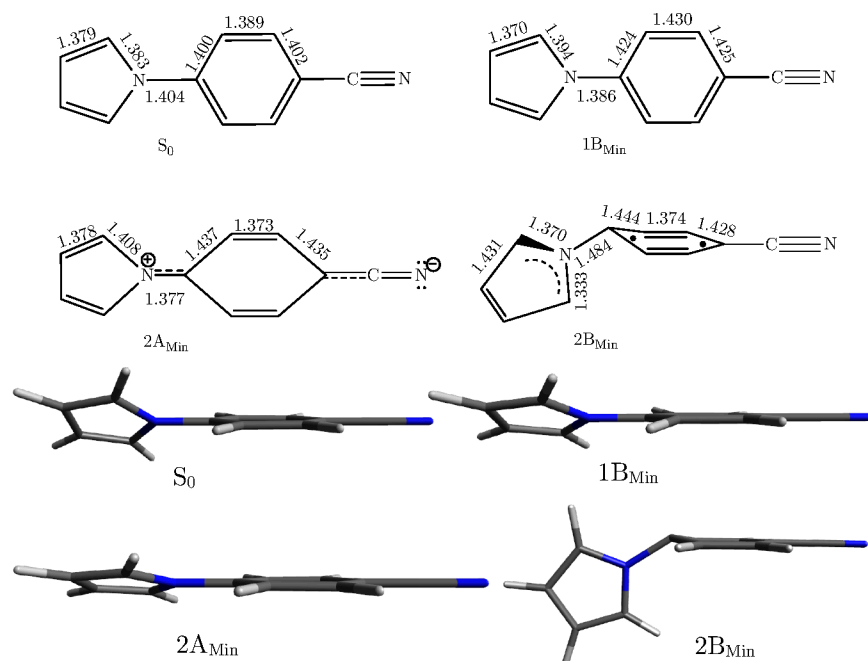


FIGURE 4.5: Schematic representation of the bond length pattern in the equilibrium geometries of ground ( $S_0$ ), 1B (LE), bright 2A ( $\pi\pi^*$ ) and 2B (CT) states obtained at LR-CC2/cc-pVTZ level of theory and corresponding geometries.

#### 4.3.3.1 The dark 1B (LE) state:

Symmetry-constrained geometry optimizations of the dark 1B (LE) state performed at LR-CC2/cc-pVTZ and TD-CAM-B3LYP/cc-pVTZ levels of theory converge to a local minimum ( $1B_{\text{Min}}$ ) (see Fig. 4.5) which is more planar than the  $S_0$  equilibrium structure (see Fig. 4.6). The  $1B_{\text{Min}}$  minimum has been confirmed by vibrational frequency analysis to have no imaginary frequencies. In its equilibrium geometry the 1B state is approximately 0.20 eV lower in energy than at the ground state equilibrium geometry at LR-CC2/cc-pVTZ level of theory. LR-CC2 and TD-CAM-B3LYP levels predict nearly identical equilibrium geometries of the 1B state. The TD-CAM-B3LYP optimized structure is slightly more planar than the LR-CC2 optimized one. The corresponding twisting angles  $\beta$  are  $18.9^\circ$  and  $20.8^\circ$ , respectively. This, however, is not surprising since generally DFT methods tend to favor delocalized solutions, thus geometry optimizations prefer more planar geometries.<sup>[277–279]</sup> Compared to the ground state equilibrium geometry, the bond C2'-C1' and its symmetry equivalent, as well as the central N-C<sub>1</sub> bond (numbering scheme in Fig. 4.3) are shortened in the  $1B_{\text{Min}}$  geometry, while symmetry equivalent bonds C1'-N and the C-C bonds of the benzene ring are elongated (see Fig. 4.5).

Total excited state energies, excitation energies and excited state properties for the first four

excited singlet states calculated at LR-CC2/cc-pVTZ level of theory at the  $1B_{\text{Min}}$  geometry are summarized in Table 4.3. The TD-CAM-B3LYP level provides the same state order with vertical excitation energies of the 1B, 2A and 2B states of 4.57, 4.59 and 4.85 eV, respectively. Emission

TABLE 4.3: Dominant MO contributions<sup>a</sup>, character, vertical excitation energies  $\omega$  (in eV), oscillator strengths (in parenthesis), total excited state energies<sup>b</sup> (in eV) and static dipole moments  $\mu$  (in Debye) of the four lowest excited states at the  $1B_{\text{Min}}$  geometry obtained at LR-CC2/cc-pVTZ level of theory are given.

State	MOs	Character	$\omega$	$E_{\text{total}}$	$\mu$
1B	H-1>L+1 (73) H-2>L (22)	$(\pi\pi^*)$ (local $\pi\pi^*$ )	4.35(0.01)	4.56	6.1
2A	H-1>L (88)	$(\pi\pi^*)$	4.59(0.66)	4.80	9.7
2B	H>L (96)	(CT)	4.99(0.01)	5.20	16.3
3A	H>L+1 (97)	(CT)	5.39(0.14)	5.60	17.8

<sup>a</sup> the squared value of the wave function expansion coefficient in percent is given in parenthesis.

<sup>b</sup> relative to the  $S_0$  state equilibrium geometry obtained at CC2/cc-pVTZ level of theory.

energies from  $1B_{\text{Min}}$  in the gas phase obtained at LR-CC2, ADC(2) and TD-CAM-B3LYP levels of theory are 4.35, 4.33 and 4.57 eV, respectively. These results agree well with gas phase fluorescence measurements<sup>[236,249]</sup> of isolated PBN which show only a single emission band at about 4.07 eV (305 nm) with an emission decay time of 17 ns<sup>[249]</sup>, which is assigned to the  $L_b$ -type state.

#### 4.3.3.2 The bright 2A ( $\pi\pi^*$ ) state:

Symmetry-constrained geometry optimizations of the bright 2A ( $\pi\pi^*$ ) state performed at LR-CC2/cc-pVTZ and TD-CAM-B3LYP/cc-pVTZ levels of theory converge to a nearly planar minimum geometry ( $2A_{\text{Min}}$ ) (see Fig. 4.5). This structure has been confirmed as a local minimum on the PES by vibrational analysis. No imaginary frequencies were found. The twisting angle  $\beta$  has values of  $12.9^\circ$  and  $8.6^\circ$  at the LR-CC2 and TD-CAM-B3LYP levels of theory, respectively. Energies and excited state properties of the first four excited singlet states calculated at LR-CC2/cc-pVTZ level of theory at the  $2A_{\text{Min}}$  geometry are summarized in Table 4.5.

The total energy of  $2A_{\text{Min}}$  obtained at LR-CC2/cc-pVTZ level of theory is 4.60 eV (relative to the ground state equilibrium geometry). Hence, the 2A state minimum ( $2A_{\text{Min}}$ ) lies energetically

approximately 0.04 eV above  $1B_{\text{Min}}$  ( $E_{1B_{\text{Min}}} = 4.56$  eV). The emission energy from the  $2A$  state in the gas phase is 4.40 eV at LR-CC2/cc-pVTZ level (Table 4.5). In the course of the constrained geometry optimization, symmetry equivalent bonds  $C1'-N, C1C2$  as well as  $C3-C4$  (numbering scheme in Fig. 4.3) are elongated (see Fig. 4.5). On the contrary, symmetry equivalent bonds  $C2'-C1'$  and  $C2'-C3$  and the central  $N-C_1$  bond are shortened. Hence,  $2A_{\text{Min}}$  can be described as the quinoid (Q) structure, which was previously suggested<sup>[237,250]</sup>.

Since in solution it is highly likely that the molecular symmetry is reduced or broken the geometry optimization of the bright  $2A S_2 (\pi\pi^*)$  state has been repeated without any constraints. This geometry optimization performed at LR-CC2/cc-pVTZ level does not usually converge to a stationary point. In the course of the optimization the symmetry equivalent  $C2-N$  bonds are elongated by about 0.02 Å, the central  $N-C_1$  bond is shortened by about 0.02 Å (numbering scheme in Figure 4.3). Additionally the  $C1$  atom is pyramidalized due to an out-of-plane motion of the  $C1$  atom of the benzene ring which in turn results in a tilting of the pyrrol ring driving PBN towards a surface crossing between the  $S_2 (2A)$  and  $S_1 (1B)$  states. Such an out-of-plane motion of one of the  $C$  atoms of the benzene ring (named prefulvene motion) is also involved in the ultrafast nonradiative decay of benzene via a low-lying CI between the  $S_1 (\pi\pi^*)$  and the ground state.<sup>[280]</sup> However, since LR-CC2 is a single-reference method a close lying  $S_2-S_1 (2A-1B)$  conical intersection (CI) can only be inferred and its energetic location can only be estimated from this result. In the following, the geometry in which the two states are energetically almost degenerate ( $\Delta E = 0.004$  eV) will be named approximate CI geometry (see Fig.4.6). The angle

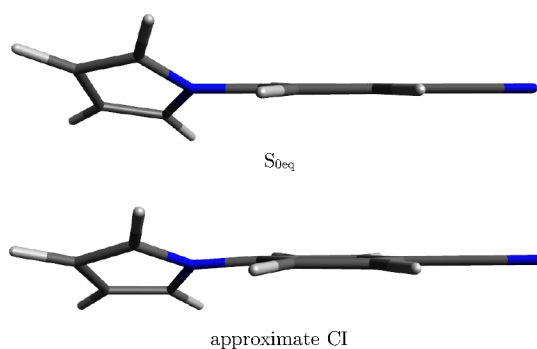


FIGURE 4.6: Top: Equilibrium geometry of the ground ( $S_0$ ) state, Bottom: approximate  $S_2-S_1$  intersection geometry obtained at LR-CC2/cc-pVTZ level of theory. One of the main coordinates leading to the  $S_2-S_1 (2A-1B)$  CI is the pyramidalization of the  $C1$  atom.

$\theta(N-C1-C4)$  (numbering scheme in Fig. 4.3) which describes the bending of the pyrrol ring out of the benzene plane changes from  $180^\circ$  at the FC geometry to  $175^\circ$  in the approximate intersection geometry. The total energy of the approximate CI geometry (relative to the  $S_0$  equilibrium

geometry) is 4.66 eV. Thus, this geometry lies only about 0.06 eV above the total energy of  $2A_{\text{Min}}$ . This result agrees well with gas phase fluorescence measurements<sup>[249]</sup>, which suggest an ultrafast internal conversion between the bright  $L_a$ -type ( $S_2$ ) and the forbidden  $L_b$ -type ( $S_1$ ) state.

Vertical excitation energies of the four lowest excited singlet states have been computed at the

TABLE 4.5: Dominant MO contributions<sup>a</sup>, character, vertical excitation energies  $\omega$  (in eV), oscillator strengths (in parenthesis), total excited state energies<sup>b</sup> (in eV) and static dipole moments  $\mu$  (in Debye) of the four lowest excited states at the  $2A_{\text{Min}}$  geometry obtained at LR-CC2/cc-pVTZ level of theory are given.

State	MOs	Character	$\omega$	$E_{\text{total}}$	$\mu$
2A	H>L (89)	( $\pi\pi^*$ )	4.40(0.77)	4.60	8.6
1B	H>L+1 (68) H-2>L (25)	( $\pi\pi^*$ ) (local $\pi\pi^*$ )	4.55(0.01)	4.75	5.7
2B	H>L (94)	(CT)	4.92(0.01)	5.12	16.1
3A	H-1 > L+1 (90)	(CT)	5.82(0.14)	6.02	16.5

<sup>a</sup> the squared value of the wave function expansion coefficient in percent is given in parenthesis.

<sup>b</sup> relative to the  $S_0$  state equilibrium geometry obtained at CC2/cc-pVTZ level of theory.

$2A_{\text{Min}}$  geometry additionally at ADC(2), TD-CAM-B3LYP and TDA/CAM-B3LYP levels of theory in conjunction with the cc-pVTZ basis set. The ADC(2) results agree very well with the LR-CC2 results (see Table 4.5). The respective ADC(2) excitation energies for states 2A, 1B, 2B and 3A are: 4.31, 4.52, 4.92 and 5.86 eV. At TD-CAM-B3LYP and TDA/CAM-B3LYP levels of theory excitation energies of 4.37, 4.78, 4.72, 5.89 eV and 4.57, 4.80, 4.89 and 5.93 eV are obtained, respectively. Comparing these energies with those obtained at LR-CC2 and ADC(2) levels reveals that i) the agreement of TD-CAM-B3LYP with LR-CC2 is very good for states 2A and 3A ii) TDA/CAM-B3LYP overestimates the excitation energies of states 2A, 1B and 3A. iii) At TD-CAM-B3LYP level states 1B and 2B strongly mix. Both wave functions have the same (most important) configurations, two of them having almost equal expansion coefficients. The energetically lower lying B state with an oscillator strength of 0.01 is composed mainly of the H-1  $\rightarrow$  L configuration (with an expansion coefficient of 0.56) and the H  $\rightarrow$  L+1 configuration (with an expansion coefficient of 0.34) for the energetically higher lying B state which has an oscillator strength of 0.00 the H-1  $\rightarrow$  L configuration has a coefficient of 0.41 and the H  $\rightarrow$  L+1 configuration has a coefficient of 0.49. According to the oscillator strengths it is reasonable to assume that the energetically lower lying B state is the 1B (LE) state and the higher lying B state

is the 2B (CT) state. This order corresponds to the one also predicted by the wave function based methods. When the TDA approximation is invoked the two B states do not mix.

To estimate solvation effects on the emission energy of the 2A state, the vertical excitation energy of the 2A state at the  $2A_{\text{Min}}$  geometry has been recomputed at TD-CAM-B3LYP/cc-pVTZ/SS-C-PCM and ADC(2)/cc-pVTZ/SS-COSMO levels of theory. For the TD-CAM-B3LYP/SS-C-PCM calculation Gaussian 09 Rev D has been used and for the ADC(2)/SS-COSMO calculation TURBOMOLE V6.6. In those calculations the ASC have been equilibrated with respect to the charge density of the 2A state. Again the parameters of ACN have been used for the solvent models. The corresponding solvent-corrected excitation energies of the 2A state and oscillator strengths ( $f$ ) obtained at TD-CAM-B3LYP/cc-pVTZ/SS-C-PCM and ADC(2)/cc-pVTZ/SS-COSMO are: 4.30 eV (288 nm) ( $f = 0.70$ ) and 3.96 eV (313 nm) ( $f = 0.89$ ).

However, the unconstrained geometry optimizations of the bright  $S_2$  (2A) state reveal a  $S_2$ - $S_1$  (2A-1B) CI. Hence, it can be assumed likely that this 2A minimum is not (sufficiently) populated. Thus, these results suggest that fluorescence emission from the 2A minimum is unlikely to occur.

#### 4.3.3.3 The 2B (CT) state:

Symmetry-constrained geometry optimizations of the 2B (CT) state at LR-CC2/cc-pVTZ and TD-CAM-B3LYP/cc-pVTZ levels of theory converge to a transition state ( $2B_{\text{TS}}$ ) (see Fig. 4.7). Vibrational analysis performed at TD-CAM-B3LYP/cc-pVTZ level of theory provides one

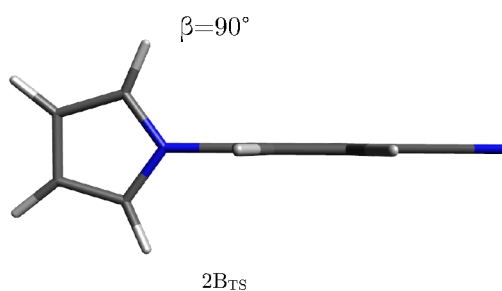


FIGURE 4.7: 2B transitions state (TS) structure of PBN obtained at LR-CC2/cc-pVTZ level of theory.

imaginary frequency of  $-69.9 \text{ cm}^{-1}$ . The corresponding eigenvector corresponds to an out-of-plane motion of the C1 atom and activates a bending of the pyrrol ring. In the  $2B_{\text{TS}}$  geometry the dihedral angle  $\beta$  is  $90^\circ$  at LR-CC2/cc-pVTZ and TD-CAM-B3LYP/cc-pVTZ levels of theory, respectively.

Unconstrained geometry optimizations of the  $S_1$  state starting at the  $2B_{TS}$  geometry performed at LR-CC2/cc-pVTZ and TD-CAM-B3LYP/cc-pVTZ levels of theory converge to a  $C_1$  symmetric equilibrium geometry ( $2B_{Min}$ ) with  $90.0^\circ$  twisted ring planes and a tilted pyrrol ring (see Fig. 4.5). Both levels predict the same tilt angle  $\theta(N-C1-C4)$  (numbering scheme in Figure 4.3) of  $158^\circ$ . Both geometries are almost identical. The  $2B_{Min}$  geometry was confirmed as a local minimum on the PES by vibrational analysis; only real frequencies were obtained. This minimum is assigned to the emissive CT state minimum observed in experiments<sup>[68,82,236,238]</sup>.

In the course of the geometry optimization i) a pyramidalization of the C1 atom inducing a bending of the pyrrol ring ii) quinoidization of the benzonitrile group i.e. a shortening of the two central C-C bonds in the benzene ring and elongation of the other four C-C bonds and iii) a bond length reversal in the pyrrol ring occur. Additionally, the central N-C<sub>1</sub> bond is significantly increased. Thus, facile rotation around the central bond is possible. The results concerning the structure of the emissive CT state contrasts earlier studies<sup>[68,250]</sup>, which report an antiquinoid (AQ) structure of the possible TICT state possessing A symmetry. Geometric relaxation from the FC geometry stabilizes the energy of the 2B (CT) state by about 0.61 eV (at LR-CC2/cc-pVTZ level of theory). LR-CC2 predicts the  $2B_{Min}$  minimum to be the lowest-lying local minimum ( $E_{tot,2B_{Min}} = 4.32$  eV) on the  $S_1$  state PES compared to the other two minima ( $E_{tot,2A_{Min}} = 4.60$  eV and  $E_{tot,1B_{Min}} = 4.56$  eV).

Gas phase vertical excitation energies at the  $2B_{Min}$  minimum obtained at LR-CC2/cc-pVTZ, ADC(2)/cc-pVTZ and TD-CAM-B3LYP/cc-pVTZ levels of theory are 3.07, 3.04 and 2.94 eV, respectively. Compared to the employed wave function based methods, TDDFT slightly underestimates the excitation energy of this CT state. The results show, that twisting is not the only important coordinate alone involved in formation of a stable TICT state. Instead, stretching modes e.g. quinoidization of the benzonitrile group and pyramidalization of the central C1 atom are also involved. This result agrees well with results reported by Fuß et al.<sup>[251]</sup> obtained from gas phase measurements. Vertical excitation energies and excited state properties of the first three lowest excited singlet states at the  $2B_{Min}$  geometry obtained at LR-CC2/cc-pVTZ level of theory in the gas phase are summarized in Table 4.7. Beside the lowest lying CT (HOMO  $\rightarrow$  LUMO)  $S_1$  (2B) state, there is a second low lying CT (HOMO-1  $\rightarrow$  LUMO)  $S_2$  (2A) state present at the  $2B_{Min}$  geometry. This CT state evolves out of the bright 2A (HOMO-1  $\rightarrow$  LUMO) state along the twisting coordinate because HOMO-1 in the  $C_2$  symmetric FC geometry is a linear combination of HOMO-1 and HOMO-2 in the  $C_1$  symmetric equilibrium geometry of the 2B state. HOMO,

TABLE 4.7: Dominant MO contributions<sup>a</sup>, character, corresponding irreducible representation (in  $C_2$  symmetry) vertical excitation energies  $\omega$  (in eV), oscillator strengths (in parenthesis), total excited state energies<sup>b</sup> (in eV) and static dipole moments  $\mu$  (in Debye) of the three lowest excited states at the  $2B_{\text{Min}}$  geometry obtained at LR-CC2/cc-pVTZ level of theory are given.

State	MOs	Character	Irrep	$\omega$	$E_{\text{total}}$	$\mu$
S <sub>1</sub>	H>L (95)	(CT)	2B	3.07(0.00)	4.32	16.1
S <sub>2</sub>	H-1 > L (82)	(CT)	2A	4.19(0.01)	5.44	11.8
S <sub>3</sub>	H-3 > L (65) H-2 > L+1 (21)	(local $\pi\pi^*$ ) (local $\pi\pi^*$ )	1B	4.65(0.01)	5.90	6.3

<sup>a</sup> the squared value of the wave function expansion coefficient in percent is given in parenthesis.

<sup>b</sup> relative to the  $S_0$  state equilibrium geometry obtained at CC2/cc-pVTZ level of theory.

LUMO and LUMO+1 remain the same as in the FC geometry. The  $S_3$  state corresponds to the dark 1B (LE) state.

In order to obtain emission energies which can be compared to experimental emission energies of which most of them were obtained in solution, the vertical excitation energy of the 2B state at the  $2B_{\text{Min}}$  minimum has been recomputed employing solvent models. Again, SS-C-PCM and SS-COSMO approaches and the parameters of ACN have been used for this purpose. In the calculations the ASC were equilibrated with respect to the density of the  $S_1$  (2B) state. The respective solvent-corrected emission energies obtained at TD-CAM-B3LYP/cc-pVTZ/SS-C-PCM and ADC(2)/cc-pVTZ/SS-COSMO levels of theory are 1.57 and 1.72 eV. The solvent corrected emission energy of 1.72 eV is in fair agreement with experimental emission energies of the CT state which are about 2.69 eV (460 nm)<sup>[68]</sup> and 2.58 eV(480 nm)<sup>[238]</sup>. The computed red-shift is 2.94 eV at ADC(2)/cc-pVTZ/SS-COSMO level of theory. For comparison with the experimentally observed Stokes' shift, it is computed with respect to the solvent-corrected vertical excitation energy of the 2A state at the FC geometry obtained by employing SS equilibrium solvation equilibrating the ASC with respect to the ground state density. The computed red-shift is larger as the experimental Stokes' shift of 1.6 eV (13104  $\text{cm}^{-1}$ <sup>[68]</sup>). Both, solvent-corrected emission energy and solvatochromic shift are overestimated at ADC(2)/SS-COSMO level of theory. Nevertheless, the expected and experimentally observed trend is well reproduced.

#### 4.3.4 TICT formation mechanism

To relate the identified equilibrium structures of 1B (LE), bright 2A ( $\pi\pi^*$ ) and 2B (CT) states to the experimentally observed occurrence of either single or dual fluorescence emission under different conditions, the reaction paths connecting these structures are investigated. The focus hereby lies on the formation of the TICT ( $2B_{\text{Min}}$ ) minimum on the  $S_1$  state PES. At first, a relaxed gas phase scan along the twisting coordinate  $\beta$  of the 2A state PES has been performed at LR-CC2/cc-pVTZ level of theory (see Fig. 4.8). This scan yields a direct pathway from the

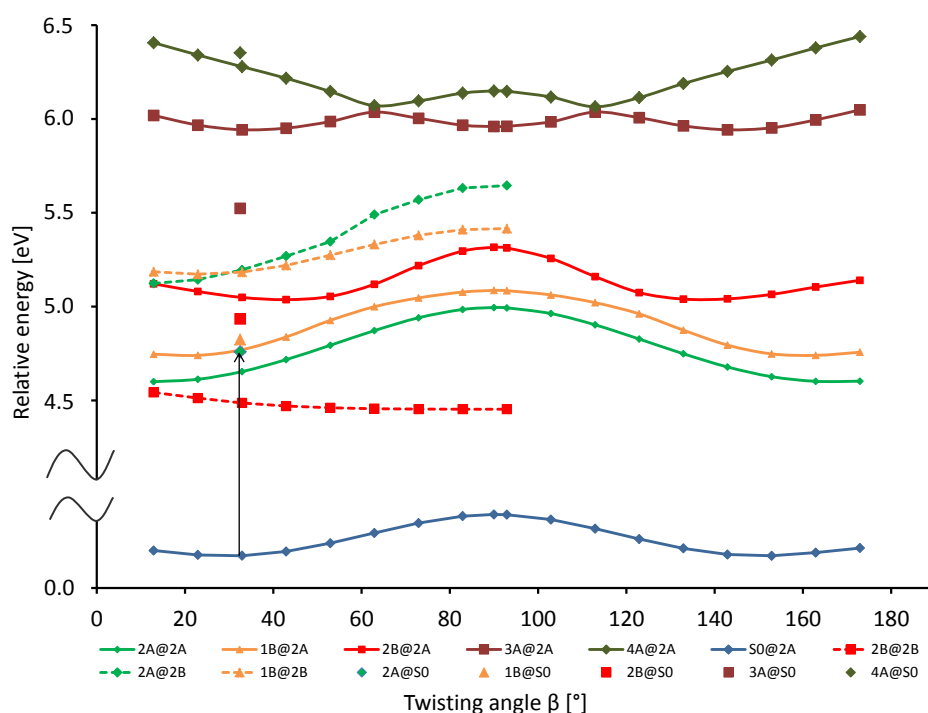


FIGURE 4.8: Relaxed scan of the PESs of the 2A state (green solid line) and 2B state (red dashed line) along the twisting coordinate  $\beta$  at LR-CC2/cc-pVTZ level of theory. Energies are relative to the FC geometry. The black arrow displays vertical excitation at the FC geometry.

FC geometry to the flat 2A state (light green solid line) minimum  $2A_{\text{Min}}$  at  $13^\circ$ . The 2A state potential energy curve has a maximum at  $90.0^\circ$  corresponding to an energy barrier of 0.39 eV along the twisting coordinate. This increased rotational barrier can be explained by the partial double bond character of the central N-C1 bond of PBN in the 2A state (see Fig. 4.5). The potential energy curve of the 2B state (red solid line) has a flat local minimum at  $43^\circ$  and a maximum at  $13^\circ$ . Along the twisting coordinate, an avoided crossing between the two states of B symmetry 1B and 2B is found around  $60^\circ$ . At this geometry, these two states strongly mix. The main contributions to both excited state wave functions arise from the HOMO  $\rightarrow$

LUMO configuration (1B: 47%, 2B: 48%), HOMO-1  $\rightarrow$  LUMO configuration (1B: 27%, 2B: 25%) and the HOMO-3  $\rightarrow$  LUMO configuration (1B: 20%, 2B: 21%) (see Fig. 4.9). Such an avoided crossing occurs since two potential energy curves corresponding to electronic states of the same symmetry cannot cross due to the non-crossing rule<sup>[281,282]</sup>. Also, both states exhibit

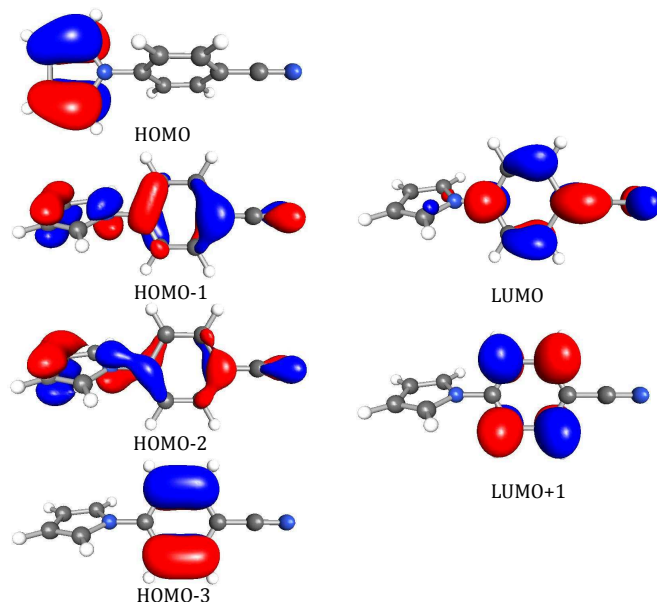


FIGURE 4.9: HF molecular orbitals obtained at LR-CC2/cc-pVTZ level of theory: HOMO, HOMO-1, HOMO-2, HOMO-3, LUMO and LUMO+1 at  $\beta = 63^\circ$  (isovalue = 0.05).

similar static dipole moments (1B:  $\mu = 10.6$  D, 2B:  $\mu = 12.2$  D). An analysis of the natural transition orbitals (NTOs) (see Figures 4.10 and 4.11) computed at ADC(2)/cc-pVTZ level of theory for states 1B and 2B at twisting angles of  $50^\circ$  and  $70^\circ$  reveals that the states 1B and 2B are interchanged.

In the gas phase neither a TICT state minimum has been found on the 2A state PES along the twisting coordinate nor a surface crossing between 2A and 2B states. This result is in agreement with gas phase experiments of PBN in which only a single emission band at about 4.00 eV corresponding to the forbidden  $L_b$  transition is observed.<sup>[249]</sup>

Since the equilibrium structure  $2B_{\text{Min}}$  has been identified as the lowest one in energy of all photochemically relevant excited states, a relaxed gas phase PES scan of the 2B state (red dashed line) along the twisting coordinate  $\beta$  has also been performed at LR-CC2/cc-pVTZ level of theory (see Fig. 4.8, dashed lines). Already at  $\beta = 13^\circ$ , i.e. the  $\beta$  value at which the 2A state has its minimum, the 2B state becomes the energetically lowest state when its geometry is relaxed. It is also readily apparent that the 2B state potential energy curve exhibits a minimum at the  $90^\circ$

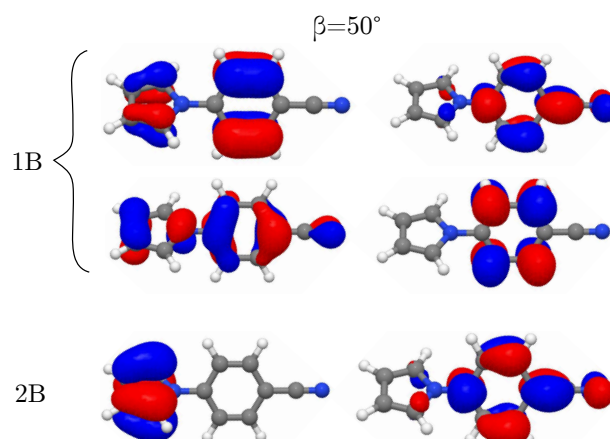


FIGURE 4.10: Particle and hole NTO pairs of the 1B and 2B states of PBN at the geometry with  $\beta = 50^\circ$  obtained at ADC(2)/cc-pVTZ level of theory (isovalue = 0.05).

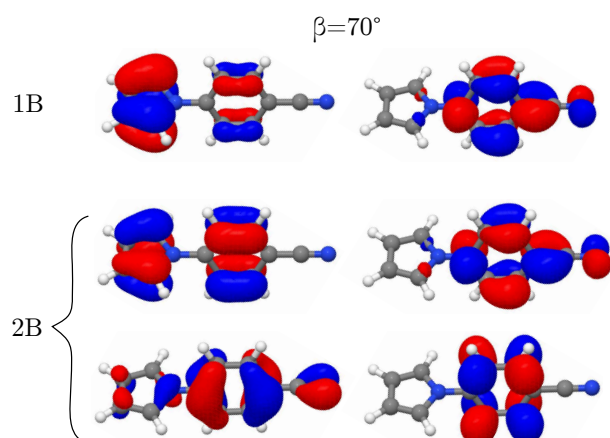


FIGURE 4.11: Particle and hole NTO pairs of the 1B and 2B states of PBN at the geometry with  $\beta = 70^\circ$  obtained at ADC(2)/cc-pVTZ level of theory (isovalue = 0.05).

twisted geometry, which corresponds to the previously identified 2B state TS. From this TS, however, when the symmetry constraint is lifted PBN may relax barrierless to the  $2B_{\text{Min}}$  (TICT) minimum.

From these results, it can be inferred that twisted ICT may only be possible in the gas phase if it is possible for the excited molecules to reach from the initially excited 2A state to the 2B state prior to twisting. The barrier height connected with this process can be estimated to be 0.2 eV. The total energy of the 2A state at  $13^\circ$  is 4.60 eV, hence the energy of the approximate intersection of states 2A and 2B of about 4.80 eV is as high as the initial vertical excitation energy of 4.82 eV. Hence, population of the  $2B_{\text{Min}}$  (TICT) minimum after vertical excitation to the bright 2A

state cannot be ruled out, but it appears very unlikely. Also, this result is in agreement with the experimental finding of Belau *et al.*<sup>[249]</sup> that in gas phase no red-shifted emission occurs.

Furthermore, vertical excitation energies have been recalculated along the relaxed scan of the PES of the 2A state using TD-CAM-B3LYP/cc-pVTZ (see supporting info) at the LR-CC2 optimized geometries. The TD-CAM-B3LYP curves agree with LR-CC2 in terms of the overall PES topologies. Only 2B and 1B are interchanged in energetic order, because the energy of the 2B (CT) state is underestimated, and hence the avoided crossing disappears. For the same reason TD-CAM-B3LYP, in contrast to LR-CC2, provides a crossing between the 2A and 2B state at 63° such that the 2B state becomes the S<sub>1</sub> state at 90°. However, to reach the 2B state minimum at 53°, a barrier of about 0.36 eV (8.3 kcal/mol) has to be overcome on the 2A state PES even for a too low 2B state. Like for the S<sub>0</sub> equilibrium geometry, the effect of the electron-transfer SIE

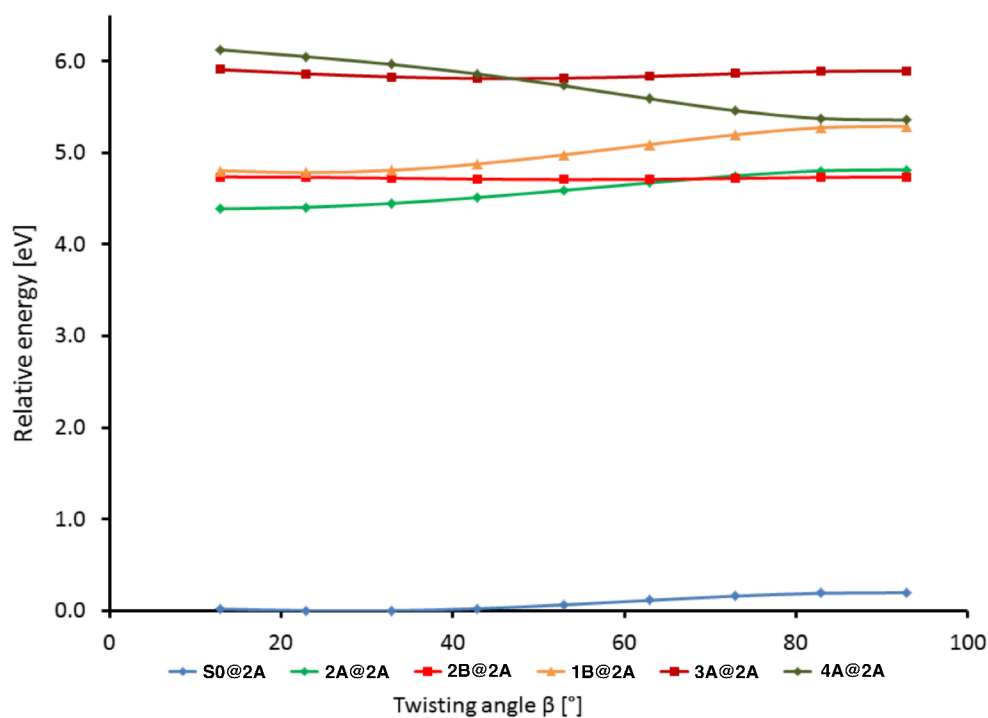


FIGURE 4.12: Relaxed scan of the 2A PES (light green) along the twisting coordinate  $\beta$  at TD-CAM-B3LYP/cc-pVTZ level of theory. As input geometries, LR-CC2/cc-pVTZ optimized 2A state geometries have been used. Energies are relative to the FC geometry.

of TD-CAM-B3LYP on the 2B (CT) state has also been investigated by increasing the amount of HF exchange gradually. Indeed, the 2B state was shifted upwards in energy corroborating the effect of the electron-transfer SIE: At 13° 2A ( $\pi\pi^*$ ), 2B (CT) and 3A (CT) states are shifted upwards by 0.24, 0.58 and 0.95 eV, respectively. The energy difference between the shifts of 2A

and 2B states is 0.34 eV. The energy shift of the CT states is equally large as observed at the FC geometry. At 73°, 83° and 93° the 2A state is shifted upwards by 0.55, 0.70 and 0.77 eV, respectively, while the 2B state is shifted by 0.80, 0.81 and 0.82 eV, respectively. The reason why the energy shift of the 2A (HOMO-1 → LUMO) state becomes more pronounced in twisted conformations is that HOMO-1 and LUMO decouple during rotation i.e. the contribution on the benzonitrile (of HOMO-1) and the pyrrol moiety (of LUMO), respectively, vanishes such that the 2A state evolves into a pure CT state. This decoupling leads to a more pronounced CT character of the 2B (HOMO → LUMO) state. Hence also the effect of the electron-transfer SIE becomes more pronounced. This result is highly significant for the investigation of energy profiles of CT states along twisting coordinates when using TDDFT and should be kept in mind when undertaking such computations.<sup>[283]</sup> However, even though the 2B (CT) excitation in PBN seems to suffer from the electron-transfer SIE and its vertical excitation energy is underestimated by TD-CAM-B3LYP, also at this level of theory there is no pronounced stabilization of its energy along the twisting coordinate and no TICT minimum is found in the gas phase.

To investigate solvent effects on the PESs of the 2A and 2B states, single point calculations employing a solvation model have been carried out along the previously calculated relaxed PES scan of  $\beta$ , respectively (see Fig. 4.13). Vertical excitation energies of the four lowest excited singlet states have been recalculated at ADC(2)/cc-pVTZ/SS-COSMO level of theory. Hereby, the solvent charges are equilibrated either for the 2A state or 2B state density, respectively. For the solvent model, again the parameters of ACN have been used. Along the potential energy curve of the 2A state, the 2A state is the lowest excited state at small twist angles  $\beta$ . However, the potential energy barrier for twisting present in the gas phase disappears when state-specific equilibrium CSOMO for ACN solution is used, and PBN can twist barrierless and reach a crossing between the 2A and 2B states at 43°. Once the 2B state is reached, the optimized geometry of this state ( $2B_{\text{Min}}$ ) is adopted (see Fig. 4.5) corresponding to the TICT state. Since the energy released is as large as 1.5 eV, the fluorescence wavelength is strongly red-shifted as shown above (section ??). For the occurrence of red-shifted fluorescence in ACN compared to the gas phase, the disappearance of the energy barrier along the twisting coordinate in the 2A state is decisive. Obviously, the barrier disappears because the 2A state is energetically stronger stabilized in polar solvents at twisted geometries than at planar geometries. The underlying reason is the increasing static dipole moment of the 2A state along the twisting motion from 9 to 12 D at LR-CC2/cc-pVTZ level, already in the gas phase, leading naturally to a stronger solute solvent

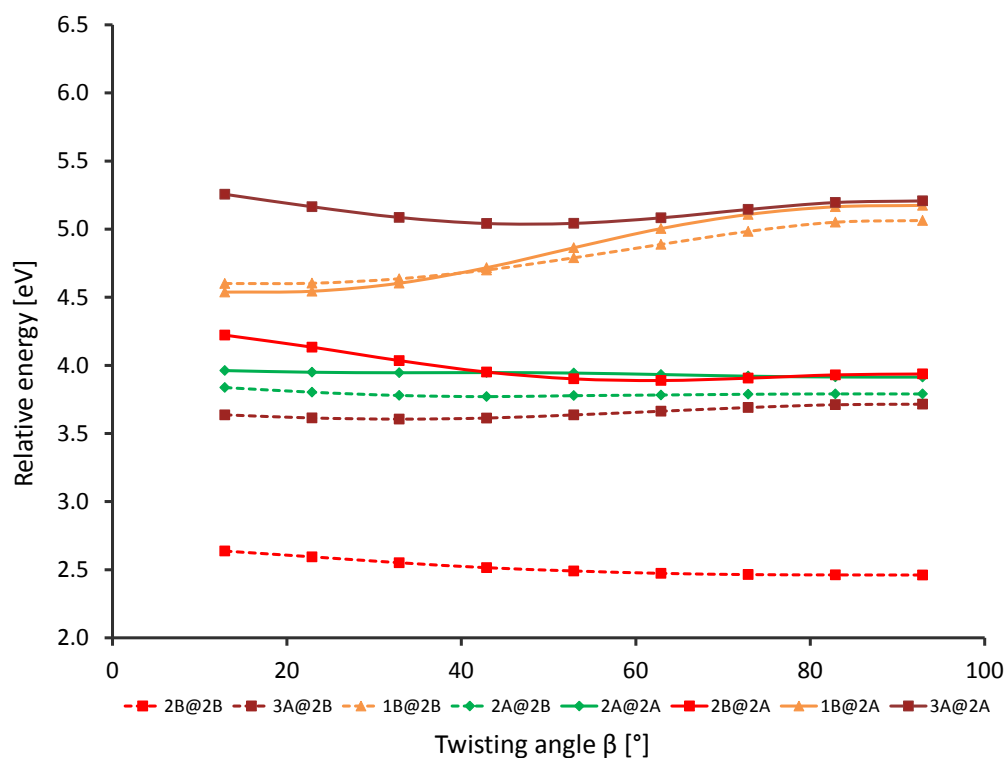


FIGURE 4.13: Relaxed PES scan of the 2A state (solid lines) and 2B state (dashed lines) along the twisting coordinate  $\beta$  at the ADC(2)/cc-pVTZ level of theory using SS-COSMO.

interaction.

At TD-CAM-B3LYP level this effect is strongly overemphasized since the static dipole moment of 2A along the twisting coordinate is much too large leading to even stronger solvent stabilization, as already emphasized above. Using TD-CAM-B3LYP the 2A state itself exhibits an artificial minimum at a twisted geometry (not shown here), however, this artefact of TDDFT has been observed before.<sup>[283]</sup>

#### 4.4 SUMMARY AND CONCLUSION

In analogy to DMABN, the prototype D/A molecule exhibiting dual fluorescence in polar solvents, it has been found experimentally that PBN also shows dual emission under certain experimental conditions. In frozen ethanol, apolar and medium polar solvents dual fluorescence has been observed, while in strongly polar solvents at room temperature both dual fluorescence and only red-shifted fluorescence have been observed.<sup>[68,236,238,248]</sup> In addition, the relative intensities of the dual fluorescence bands depend on the temperature and excitation wavelength suggesting

the existence of an energy barrier for red-shifted fluorescence to occur.<sup>[248,251]</sup> The red-shifted anomalous emission band has been assumed to arise from the emission from a polar CT state while for the normal band it is assumed that it arises due to emission from a locally excited (LE) state.

In this study, the photochemical mechanism underlying the experimentally observed unusual fluorescence behavior of PBN has been investigated theoretically with a focus on the intramolecular CT states. For these investigations, different levels of theory have been employed including high-level *ab initio* methods such as LR-CC2, ADC(2) and ADC(3). Solvent effects on transition energies of the relevant excited states of PBN have been described within the conductor-like polarizable continuum model (C-PCM) and the conductor-like screening model (COSMO) using the parameters of medium polar acetonitrile (ACN) to enable a better comparison with experiment.

CC2 and DFT/CAM-B3LYP methods predict PBN to have a linear ground state equilibrium geometry with  $C_2$  symmetry in which the rings are slightly twisted towards one another. In the gas phase to reach an orthogonal conformation a torsional barrier of only about 0.13 eV (3 kcal/mol) has to be overcome. Hence, rotation around the central C1-N bond, though not free, is quite facile. All applied levels of theory predict the  $S_1$  state of PBN to be a local dark  $\pi\pi^*$  state exhibiting B symmetry, here named 1B. This state can be assigned to the forbidden  $L_b$ -type (LE) state observed in fluorescence experiments. The  $S_2$  state is predicted to be the spectroscopically accessible bright  $\pi\pi^*$  state possessing A symmetry, here named 2A. This state can be assigned to the optically allowed  $L_a$ -type state observed in absorption experiments. The lowest lying CT state of PBN is the  $S_3$  state at LR-CC2, ADC(2) and ADC(3) levels of theory and the  $S_1$  state at TD-BHLYP and TD-CAM-B3LYP levels of theory. All levels predict this CT state to exhibit B symmetry, hence, here named 2B. In PBN these three relevant excited states: dark 1B (LE), bright 2A ( $\pi\pi^*$ ) and 2B (CT) lie energetically very close together in accord with experiment.

To find a possible pathway leading from the initially excited bright 2A ( $\pi\pi^*$ ) state to a 2B (TICT) state minimum, a relaxed scan of the PES of the 2A state along the twisting coordinate  $\beta$  has been performed in the gas phase and treating solvation with the above-mentioned solvent models. Based on my computations the following mechanistic picture of the photochemistry of PBN in the gas phase, as depicted in Figure 4.14, can be drawn. If excited to the bright 2A ( $\pi\pi^*$ ) state PBN only twists a few degrees until an intersection with the energetically very close lying 1B (LE) state is reached. After passing the 2A-1B state intersection, PBN relaxes to the 1B (LE) state minimum

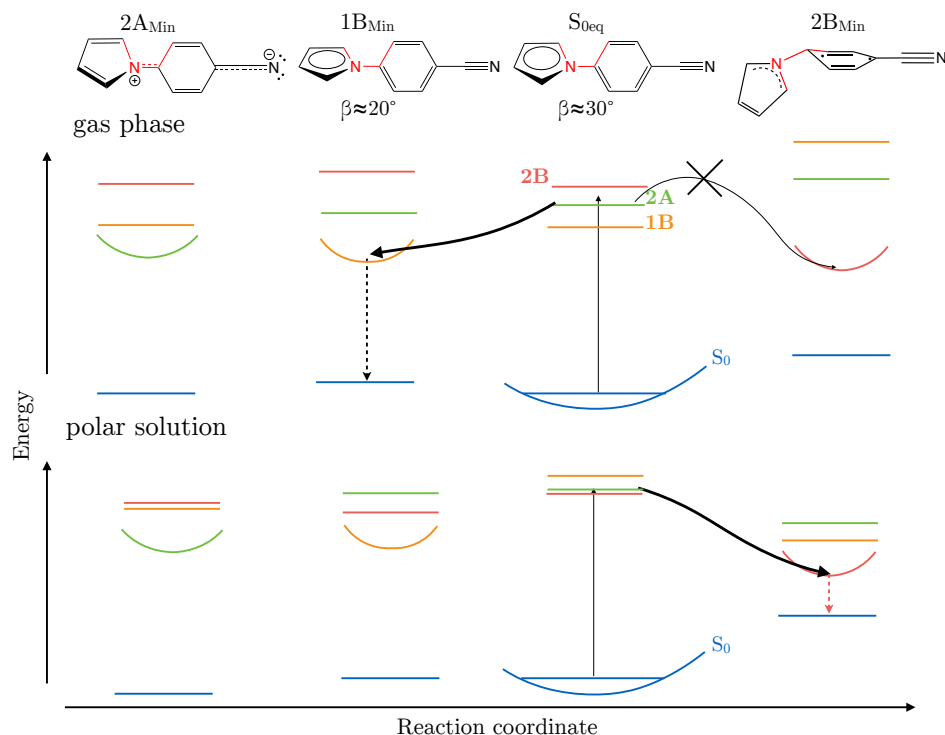


FIGURE 4.14: Schemes of the photochemical reaction of PBN in the gas phase and polar solution. In weakly polar solvents both pathways are possible and likely to occur.

from which emission can occur. This agrees with jet cooled fluorescence measurements<sup>[236,249]</sup> in which only single fluorescence emission at about 4.00 eV with a relatively long fluorescence lifetime of about 17 ns is observed.

The continuum solvent model calculations at the FC geometry reveal that already the electronic polarization part of the solvation alone suffices to stabilize the 2B (CT) state strongly. The 2B state even becomes the lowest lying excited state at ADC(2)/SS-COSMO level of theory. Furthermore, the relaxed potential energy surface scan of the 2A state along the twisting coordinate employing equilibrium state-specific solvation shows that solvation with a polar solvent not only stabilizes the polar 2B state but also the 2A state. As a result, the energy barrier along the twisting coordinate  $\beta$  vanishes and twisting is facilitated. Hence, the barrier height for twisting is tuned by the solvent polarity. At about  $60^\circ$  the 2B state becomes the lowest in energy and the twisted CT equilibrium structure of the 2B state is adopted. The occurrence of red-shifted fluorescence is directly connected with the ability to reach the 2B<sub>Min</sub> (TICT) minimum.

Summarizing, in the gas phase and non-polar solvents, 2A and 2B states are not sufficiently stabilized and an energy barrier for twisting exists such that only single emission from the 1B (LE) state occurs. With increasing polarity of the solvent, both the 1B (LE) and 2A states, the latter

exhibiting a larger static dipole moment, are stabilized and the energy barrier shrinks. Hence, already in *n*-hexane dual fluorescence may occur, but, the red-shift of the CT state emission band is not pronounced in this case. In solvents of medium polarity, the stabilization of both 2A state and 2B states becomes more distinct such that the emission bands are more separated and the red-shift is more pronounced. In polar solvents, the stabilization of the polar 2B (CT) state is so pronounced that the energy barrier disappears and only red-shifted fluorescence occurs.



---

REGULAR AND RED-SHIFTED FLUORESCENCE OF  
5-(1H-PYRROLE-1-YL)THIOPHENECARBONITRILE (TCN) IS EFFICIENTLY  
QUENCHED BY INTERNAL MODES OF THIOPHENE

---

In this chapter<sup>†</sup> the photochemical properties of thiophene analogs of PBN, namely the two isomers 5-(1H-pyrrole-1-yl)thiophene-2-carbonitrile (2-TCN) and 5-(1H-pyrrole-1-yl)thiophene-3-carbonitrile (3-TCN) are investigated. The aim of this study is to answer the question whether the thiophene based donor-acceptor molecule TCN shows a fluorescence behavior similar to its benzonitrile analogues PBN and DMABN. For this purpose high-level *ab initio* methods i.a. CC2, ADC(2) and the highly accurate ADC(3) model (compare sections 3.5.2 and 3.6.3). Solvent effects have been included using the COSMO and C-PCM solvation models (see section 3.8). In the gas phase, TCN is excited to the bright  $S_1$  ( $\pi\pi^*$ ) state. Subsequently, it most likely deactivates nonradiatively to the ground state via a low lying  $S_1$ - $S_0$  conical intersection. In polar solvents, the dark  $S_2$  (CT) state is stabilized below the  $S_1$  state already at the FC geometry, however, despite this stabilization, radiationless decay to the ground state remains the most likely deactivation pathway. Nevertheless, population of a twisted minimum of the CT state becomes energetically feasible. This study strongly suggests that TCN does not show any fluorescence in the gas phase, and if at all only weak red-shifted emission from a twisted intramolecular charge transfer (TICT) minimum may be observable in polar solvents.

---

<sup>†</sup>Parts of this chapter are reproduced from Bohnwagner, MV. Burghardt I. Dreuw, A. *Phys Chem Chem Phys*, **2017**, *19(21)*, pp 13951-13959 with permission from the PCCP Owner Societies

## 5.1 MOTIVATION AND BACKGROUND

In organic optoelectronics, the underlying materials are often based on organic polymers with donor-acceptor architectures possessing bipolar charge-transporting properties.<sup>[284–286]</sup> polymeric materials usually enable efficient and tunable photoinduced charge transfer and transport with high charge carrier mobilities, both of which are found to be crucial for efficient organic optoelectronic devices.<sup>[287–290]</sup> Of particular interest for application as ambipolar materials in optoelectronic components are thiophene-based donor-acceptor systems.<sup>[291–295]</sup> Reasons for this are that these materials are easily processable, feature high versatility in structural modification<sup>[296]</sup>, exhibit high charge carrier mobilities<sup>[294,297,298]</sup> and are stable against oxidative doping.

This study aims to examine the photochemical properties of TCN (Figure 5.1) as a small thiophene based donor-acceptor model compound with respect to its potential application as ambipolar charge transport material. In **Chapter 4** in which the photochemistry of PBN is discussed, I have shown that the employed quantum chemical methodology is suited to adequately describe the experimentally observed dual fluorescence in medium polar solution and single fluorescence emission in the gas phase and to gain new insights into the photochemical behavior of this small donor-acceptor molecule. In this study now the aim is to extend the previous study and to transfer the methodology to molecules containing thiophene. While no experimental data concerning the photochemistry of TCN is available yet, I hope to trigger experimental effort into this direction.

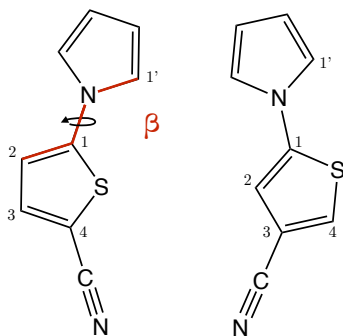


FIGURE 5.1: Structures of the two investigated isomers of TCN: 5-(1H-pyrrole-1-yl)thiophenecarbonitrile (2-TCN) (left) and 5-(1H-pyrrole-1-yl)thiophenecarbonitrile (3-TCN) (right) and numbering of the relevant atoms. The twisting coordinate  $\beta$  is indicated in red.

## 5.2 COMPUTATIONAL METHODS

Ground state ( $S_0$ ) PESs of both TCN isomers have been explored using the CC2 and MP2 methods (see section 3.5) in conjunction with the cc-pVTZ/aux-cc-pVTZ basis sets employing the RI approximation. Vibrational frequencies have been computed at the respective optimized geometries at the MP2/cc-pVTZ level of theory to verify them as local minima on the PES. Ground state relaxed PES scans along the twisting coordinate  $\beta$  defined by the dihedral angle  $\beta(\text{C1}'\text{-N-C1-C2})$  (numbering see Fig. 5.1) have been performed at MP2/cc-pVTZ level of theory simulating gas phase. The dihedral angle  $\beta$  was varied in steps of  $10^\circ$ . For a fixed value of  $\beta$ , all other geometric parameters were freely optimized.

Since it is known that photochemical reactions of thiophene containing donor-acceptor systems often involve triplet excited states and intersystem crossing (ISC)<sup>[299–302]</sup>, besides singlet excited states the two lowest excited triplet states have been investigated as well. Vertical excitation energies and excited state properties i.e oscillator strengths ( $f$ ) and static dipole moments ( $\mu$ ) of the four lowest excited states have been computed at the ground state equilibrium geometries employing various levels of theory. Like for the study of PBN (see **chapter 4**) in this study again the ADC(2), ADC(3), LR-CC2, CIS(D) and TDDFT methods have been used. In addition to the two different xc functionals BHLYP and CAM-B3LYP, for this study the range-separated hybrid PBE (LRC- $\omega$ PBEhPBE<sup>[303]</sup>) functional has been employed as well. In general, the cc-pVTZ/aux-cc-pVTZ basis sets have been employed, only for the ADC(3) computations, the smaller cc-pVDZ basis set has been used. The reason for this is mainly that TCN has no molecular symmetry which can be exploited in the calculation and thus the computational effort of a ADC(3)/cc-pVTZ is extremely high. For the cc-pVTZ basis set there are 448 basis functions .

Due to the well-known charge-transfer failure of TDDFT (see section 3.7.1) the employed xc functionals have been benchmarked against the most accurate wave function based method, ADC(3). The solvent's influence on vertical excitation energies and energy gap ( $\Delta E(S_1, S_2)$ ) between  $S_1$  and  $S_2$  states at the FC geometry have been estimated using nonequilibrium ptSS-PCM solvation as implemented in Q-Chem 4.3<sup>[267,268]</sup>. To investigate how a solvent stabilizes the CT state ( $S_2$ ) shortly after vertical excitation, two different time-scale regimes were approximately considered: i) A short time-scale regime, to capture the effect of electronic solvent polarization assuming the time-scale of solvent reorganization is faster than the decay of the initially excited state. For this purpose, the nonequilibrium ptSS-PCM has been used. ii) A longer time-scale regime capturing

also the effect of solvent polarization due to fast electronic and slow nuclear reorganization of the solvent. Therefore, the SS-COSMO model as implemented in TURBOMOLE V6.6<sup>[269]</sup> has been used. For the solvent corrected vertical excitation energies obtained using SS-COSMO the following nomenclature is used. When the apparent surface charge (ASC) is equilibrated with respect to the ground state density the solvent corrected vertical excitation energies ( $\omega$ ) are named  $\omega_{\text{ex,sol}}@S_0$ . When the ASC is equilibrated with respect to the density of the bright  $S_1$  ( $\pi\pi^*$ ) state, solvent corrected  $\omega$ 's are named  $\omega_{\text{ex,sol}}@S(\pi\pi^*)$ . When the ASC are equilibrated with respect to the CT state  $S_2$  the solvent corrected  $\omega$ 's are named  $\omega_{\text{ex,sol}}@S(\text{CT})$ .

Geometries of the photochemically relevant excited states, i.e. bright  $S_1$  ( $\pi\pi^*$ ) and  $S_2$  (CT) states have been optimized in the gas phase using LR-CC2/cc-pVTZ, TD-CAM-B3LYP/cc-pVTZ and TD-BHLYP/cc-pVTZ levels of theory. LR-CC2 calculations have been performed using TURBOMOLE V6.3.1<sup>[271]</sup>. For SS-COSMO calculations the TURBOMOLE V6.6<sup>[269]</sup> has been used. ADC(2), ADC(3), CIS(D), TDDFT and C-PCM calculations have been performed using Q-Chem 4.3.

Spin-orbit coupling (SOC) constants have been computed with the atomic-mean-field integral (AMFI)<sup>[304–306]</sup> program which has been interfaced to a developer version of Q-Chem 4.2. MO, attachment/detachment and electron/hole density plots have been generated using TmoleX<sup>[307]</sup> (for LR-CC2 computations) and VMD<sup>[308]</sup>.

## 5.3 RESULTS

### 5.3.1 Ground state properties of TCN

At first, the  $S_0$  equilibrium geometries of the two isomers of TCN have been optimized simulating gas phase. The geometrical parameters of the  $S_0$  equilibrium geometries of both TCN isomers obtained at CC2/cc-pVTZ and MP2/cc-pVTZ levels are practically the same with respect to bond lengths (Å), bond angles (°) and dihedral angles (°). Bond length deviations ( $\Delta x$ ) between the methods are 0.001-0.002 Å for C-C bonds and the central C-N bond. For the C-N bonds of pyrrole and the C1-S bond  $\Delta x$  is 0.005-0.006 Å. The largest deviation is observed for the cyano triple and the C4-S single bond ( $\Delta x = 0.009$  Å) (The corresponding x,y,z coordinates are given in A.1, A.2, A.3, A.4). The  $S_0$  equilibrium geometries of 2- and 3-TCN have been verified as local minima on the PES by vibrational frequency analyses. Only the geometries obtained at

CC2/cc-pVTZ level of theory are discussed in the following in order to facilitate comparability since excited state geometries have been optimized at LR-CC2/cc-pVTZ level of theory. The thiophene and pyrrole rings are almost planar and show a very similar bond length pattern as in isolated pyrrole<sup>[309]</sup> and thiophene<sup>[309]</sup>, respectively (Table 5.1). In both isomers the rings

TABLE 5.1: Relevant bond lengths (Å) in the  $S_0$  equilibrium geometries of 2- and 3-TCN obtained at CC2/cc-pVTZ level of theory and the corresponding ones in pyrrole<sup>[309]</sup> and thiophene<sup>[309]</sup>. For numbering of atoms see Figure 5.1.

Bonds	2-TCN	3-TCN	Pyrrole	Thiophene
C3'-C2'	1.423	1.422	1.417	
C2'-C1'	1.378	1.379	1.382	
C1'-N	1.384	1.384	1.370	
N-C1	1.390	1.391		
C1-S	1.730	1.734		1.714
C1-C2	1.383	1.376		1.370
C2-C3	1.407	1.421		1.423

are slightly twisted against each other by  $\beta = 141^\circ$  (2-TCN) and  $145^\circ$  (3-TCN), possibly due to steric hindrance between the sulfur atom and the hydrogen atoms of the pyrrole ring. The twisted orientation results in a less effective  $\pi$ -conjugation between the rings as compared to a planar structure, yielding central N-C1 bond lengths of 1.390 Å and 1.391 Å for 2- and 3-TCN, respectively which is of intermediate length between a single and a double bond<sup>[275]</sup>.

The energy barrier for twisting about  $\beta$  is relatively low ( $0.05 \text{ eV} \approx 2k_B T$  at room temperature) i.e. the rotation is only slightly hindered. In the ground state, both TCN isomers have static dipole moments of about 4 D at CC2/cc-pVTZ level of theory.

### 5.3.2 The gas phase photochemistry of TCN

To identify the photochemically relevant excited states vertical excitation energies of the four lowest excited states including singlet and triplet states have been computed at the FC geometries of 2- and 3-TCN using ADC(3), ADC(2), LR-CC2, CIS(D), TD-CAM-B3LYP and TD-BHLYP methods (Table 5.2). Hereby, the highly accurate ADC(3) method is used as benchmark method for the TDDFT functionals. Not surprisingly, the electronic structure of the isomers is very similar. In both cases, all employed methods predict the lowest lying singlet excited state  $S_1$  to be a bright state having oscillator strengths of about 0.5 and 0.2 for 2- and 3-TCN, respectively. Vertical excitation energies of the  $S_1$  state of 2-TCN are 4.32, 4.53 and 4.46 eV, respectively at

TABLE 5.2: Comparison of gas-phase vertical excitation energies and static dipole moments of the first two lowest singlet and triplet excited states of 2- and 3-TCN calculated at the  $S_0$  equilibrium geometries obtained at CC2/cc-pVTZ level of theory. Molecular orbital contributions and character of the states (in parenthesis), vertical excitation energies  $\omega$  (in eV), oscillator strengths (in parenthesis) and orbital-relaxed static dipole moments  $\mu$  (in Debye) are given.

State	MOs	ADC(3)		LR-CC2		ADC(2)		CIS(D)		TD-CAM-B3LYP		TD-BHLYP		LRC-wPBEh <sup>a</sup>	
		$\omega$	$\mu$	$\omega$	$\mu$	$\omega$	$\mu$	$\omega$	$\mu$	$\omega$	$\mu$	$\omega$	$\mu$	$\omega$	
2-TCN															
T <sub>1</sub>	H>L ( $\pi\pi^*$ )	2.79	4.5	3.31	5.0	3.28	5.2	3.51	4.8	2.56	4.7	2.26	4.2	2.29	
T <sub>2</sub>	H-1>L (CT)	3.72	7.5	4.04	9.2	4.01	9.5	4.29	6.6	3.42	8.4	3.15	8.3	3.25	
	H-1 >L+1 ( $\pi\sigma^*$ )														
S <sub>1</sub>	H>L ( $\pi\pi^*$ )	4.32(0.46)	7.3	4.53(0.51)	9.2	4.46(0.52)	9.5	4.81(0.55)	6.2	4.38(0.46)	7.3	4.42(0.46)	7.2	4.59(0.47)	
S <sub>2</sub>	H-1 >L (CT)	4.90(0.01)	12.7	4.88(0.01)	16.5	4.88(0.01)	17.7	5.33(0.05)	12.5	4.67(0.01)	15.3	4.68(0.01)	15.5	5.31(0.02)	
3-TCN															
T <sub>1</sub>	H-1>L ( $\pi\pi^*$ )	3.12	3.7	3.54	4.4	3.51	4.7	3.75	3.5	2.81	3.8	2.49	3.3	2.56	
T <sub>2</sub>	H>L (CT)	3.82	5.80	4.14	7.2	4.13	7.3	4.36	5.2	3.51	6.5	3.23	6.5	3.31	
	H >L+1 ( $\pi\sigma^*$ )														
S <sub>1</sub>	H-1>L ( $\pi\pi^*$ )	4.80(0.21)	6.7	4.79(0.24)	9.2	4.75(0.24)	9.8	5.19(0.21)	5.0	4.70(0.19)	7.1	4.73(0.18)	7.0	4.95(0.20)	
S <sub>2</sub>	H>L (CT)	5.14(0.01)	11.4	5.11(0.01)	14.8	5.12(0.01)	15.9	5.33(0.07)	8.9	4.95(0.01)	13.3	4.97(0.01)	13.7	5.57(0.03)	

<sup>a</sup> the long-range corrected  $\omega$ PBEh functional third derivatives are not avail yet, hence relaxed dipole moments could not be computed.

ADC(3)/cc-pVTZ, LR-CC2/cc-pVTZ and ADC(2)/cc-pVTZ levels of theory and 4.80, 4.79 and 4.75 eV, respectively, for 3-TCN. Results of these three wave function based methods agree very well among each other. Comparison of TDDFT with ADC(3) results reveals that CAM-B3LYP and BHLYP xc functionals are in very good agreement with ADC(3) with excitation energies of the bright  $S_1$  state showing deviations of only about 0.1 eV. The  $S_1$  state is mainly characterized by an electronic configuration of a single electron excitation from HOMO to LUMO in the case of 2-TCN and HOMO-1 to LUMO in the case of 3-TCN. These two excitations are identical because HOMO and HOMO-1 are interchanged for 2- and 3-TCN (see Fig. 5.2). Compared to the ground state, the  $S_1$  states exhibit relatively large static dipole moments of 7-9 D (Table 5.2). HOMO of 2-TCN and HOMO-1 of 3-TCN are  $\pi$  orbitals having four nodal planes, one along the sulfur atom. They correspond to the HOMO ( $\pi_3(a_2$  in  $C_{2v}$  symmetry)) orbital of unsubstituted thiophene<sup>[310–312]</sup>. The LUMOs are  $\pi^*$  orbitals localized only on the cyanothiophene group with a significant contribution on the sulfur atom. They correspond to the LUMO ( $\pi_4^*(b_1$  in  $C_{2v}$  symmetry)) orbital of thiophene<sup>[310–312]</sup>. Analysis of the MOs reveals that the  $S_1$  state possesses partial CT character. This is supported by an analysis of the attachment and detachment densities<sup>[234,313]</sup> (see Figures 5.3 and 5.4). Since the involved orbitals are  $\pi$  orbitals this state will be referred to as bright  $S(\pi\pi^*)$  state in the following. It corresponds to the  $1^1B_2$  (in  $C_{2v}$  symmetry) state of thiophene, which is one of the four valence excited states involved in its ultrafast radiationless decay.<sup>[314–317]</sup>

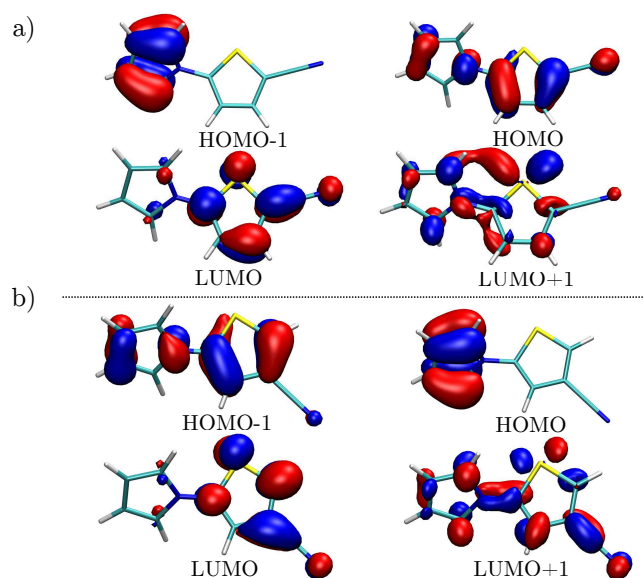


FIGURE 5.2: a) HOMO-1, HOMO, LUMO and LUMO+1 of 2-TCN b) HOMO-1, HOMO, LUMO and LUMO+1 of 3-TCN (bottom) computed at ADC(2)/cc-pVTZ level of theory at the FC geometry (isovalues = 0.05). Kohn-Sham MOs are practical identical

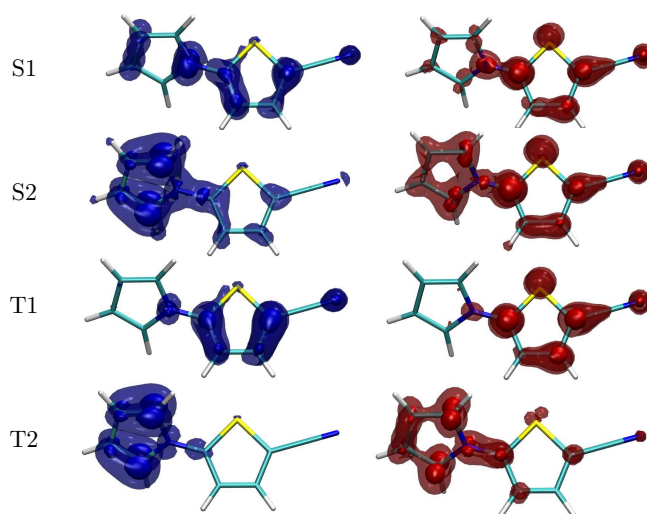


FIGURE 5.3: Electron detachment (blue) and attachment (red) density plots for the  $S_1$ ,  $S_2$ ,  $T_1$  and  $T_2$  states of 2-TCN obtained at the ADC(2)/cc-pVTZ level of theory at the CC2  $S_0$  equilibrium geometry. TD-BHLYP and TD-CAM-B3LYP electron detachment and attachment densities are practically identical. (Isovalues = 0.009 and 0.00225)

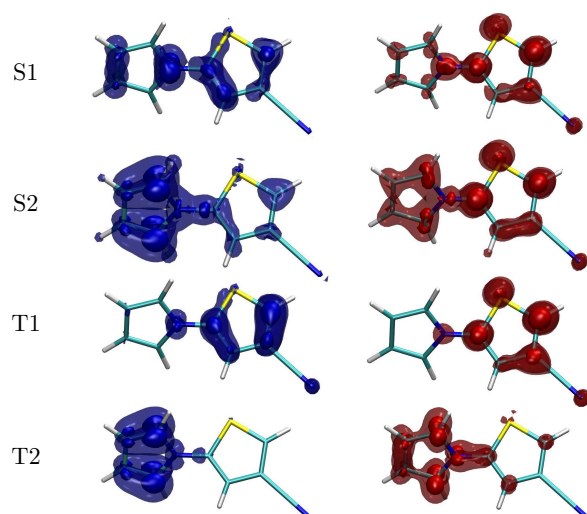


FIGURE 5.4: Electron detachment (blue) and attachment (red) density plots for the  $S_1$ ,  $S_2$ ,  $T_1$  and  $T_2$  states of 3-TCN obtained at the ADC(2)/cc-pVTZ level of theory at the CC2  $S_0$  equilibrium geometry. TD-BHLYP and TD-CAM-B3LYP electron detachment and attachment densities are practically identical. (Isovalues = 0.009 and 0.00225)

All applied methods predict the  $S_2$  state of both isomers to be a dark CT state with a small oscillator strength of only 0.01. Vertical excitation energies of 2-TCN are 4.90, 4.88 and 4.88 eV, respectively, at ADC(3)/cc-pVDZ, LR-CC2/cc-pVTZ and ADC(2)/cc-pVTZ levels of theory and 5.14, 5.11 and 5.12 eV, respectively, for 3-TCN (Table 5.2). The  $S_2$  state of 2-TCN is largely dominated by a single electron transition from HOMO-1 to LUMO while the one of 3-TCN is a transition between HOMO and LUMO (see Fig. 5.2). Both MO and attachment/detachment

density analyses (see Fig. 5.3) reveal this state to have CT character. Hence, it will be named S(CT) state in the following. Compared to  $S_0$  and the bright  $S(\pi\pi^*)$  state, S(CT) exhibits a large static dipole moment of 15-18 D (2-TCN) and 13-16 D (3-TCN), respectively.

CAM-B3LYP and BHLYP functionals provide very similar excitation energies and properties for the S(CT) state. Despite the CT character of this state the agreement of vertical excitation energies obtained using TD-CAM-B3LYP and TD-BHLYP with the ones obtained using ADC(3) is good, though not as good as in the case of the bright  $S(\pi\pi^*)$  state. Excitation energies of the singlet CT states of 2- and 3-TCN are underestimated by only at most 0.25 eV with respect to ADC(3). This deviation, however, is in the range of the error of TDDFT ( $\approx 0.3$  eV). Hence, both xc functionals CAM-B3LYP and BHLYP can be assumed to be suited to examine the ICT mechanism of TCN.

In both isomers the lowest lying triplet state  $T_1$  exhibits the same  $\pi\pi^*$  character as the  $S(\pi\pi^*)$  state and will thus be referred to as  $T(\pi\pi^*)$ . The wave function of the  $T_2$  state has two important electronic configurations: HOMO-1  $\rightarrow$  LUMO and HOMO-1  $\rightarrow$  LUMO+1 excitations (in 2-TCN) and HOMO  $\rightarrow$  LUMO and HOMO  $\rightarrow$  LUMO+1 excitations (in 3-TCN) (see Fig. 5.2). The LUMO+1 orbital is a mixture of a delocalized  $\pi^*$  orbital and a  $\sigma^*$  orbital localized on the thiophene ring. The attachment/detachment densities, however, show that the electronic structure of  $T_2$  is practically identical to the second excited singlet state  $S_2$ , which has charge-transfer character. Hence,  $T_2$ , will be named T(CT) in the following.

For the investigation of possible deactivation pathways *via* triplet states, following studies of thiophene<sup>[315,318]</sup>, the probability of ISC between the six lowest lying singlet and triplet excited states have been estimated. In good approximation, the probability of ISC depends mainly on two factors<sup>[319]</sup>: i) According to El Sayed's rule<sup>[320]</sup> ISC is particularly efficient if the electronic transition involves a change of orbital angular momentum leading to large spin-orbit coupling (SOC) elements. ii) The energy gap between initial and final state ( $\Delta E$ ) should be small ( $< 0.6$  eV) for efficient ISC.<sup>[321]</sup> Considering these factors, for 2-TCN,  $S_1 \rightarrow T_2$ ,  $S_1 \rightarrow T_3$  and  $S_3 \rightarrow T_4$  are the most likely transitions for ISC. The corresponding transitions found for 3-TCN are  $S_1 \rightarrow T_3$  and  $S_4 \rightarrow T_5$ . Energy gaps  $\Delta E$ 's and SOC constants have been computed at ADC(2)/cc-pVDZ level of theory at the ground state equilibrium geometries. For 2-TCN,  $\Delta E$  between  $S_1$  and  $T_2$  is relative large (0.51 eV) and the SOC is very small ( $1.92 \text{ cm}^{-1}$ ).  $\Delta E$ s between  $S_1$  and  $T_3$  and  $S_3$  and  $T_4$  are smaller 0.12 and 0.33 eV, respectively, but the respective SOC constants as well:  $14.17 \text{ cm}^{-1}$  and  $10.31 \text{ cm}^{-1}$ , respectively. For 3-TCN,  $\Delta E$ s between  $S_1$  and  $T_3$  and  $S_4$  and  $T_5$  are

again small 0.25 and 0.30 eV, respectively, but as for 2-TCN also for 3-TCN the SOC constants for the corresponding transitions are small 10.57 and 11.07  $\text{cm}^{-1}$ , respectively. These results suggest that ISC in TCN is unlikely and thus that triplet states are not relevant for the excited state deactivation of TCN. This result is in agreement with experimental and theoretical findings for thiophene.<sup>[315,318]</sup>

### 5.3.3 Nonradiative decay in the gas phase

To identify local minima of the bright  $S(\pi\pi^*)$  state of 2- and 3-TCN the respective states have been optimized simulating gas phase. Fully relaxed geometry optimizations at the LR-CC2/cc-pVTZ level of theory do not converge to local minima. For both isomers, geometry relaxation from the FC point proceeds *via* a barrierless pathway to an intersection with the ground state (see Fig. 5.5). One striking difference between the gas phase deactivation mechanisms of the two

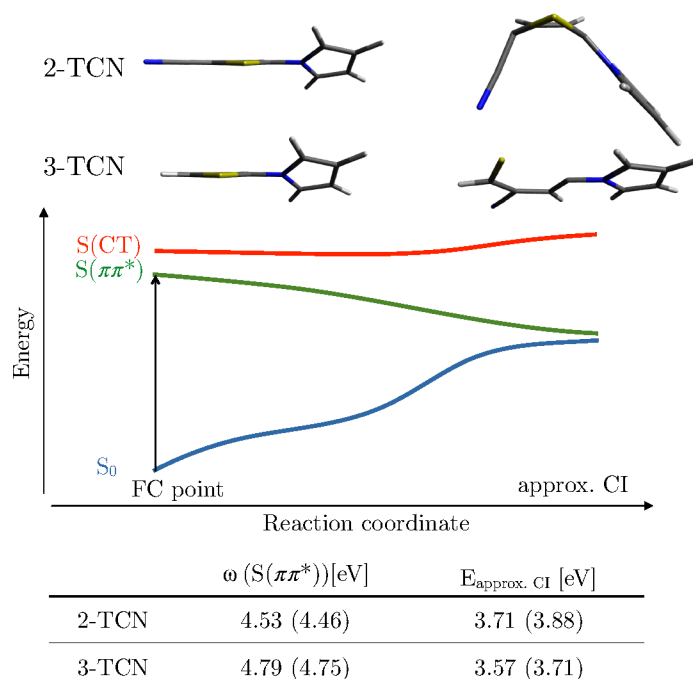


FIGURE 5.5: Schematic representation of the nonradiative decay of the bright  $S(\pi\pi^*)$  state of 2- and 3-TCN in the gas phase. Vertical excitation energies  $\omega$  of the bright  $S(\pi\pi^*)$  state and total energies  $E_{\text{approx. CI}}$  of the approximate conical intersection geometries (relative to the  $S_0$  equilibrium energy) are given in the table.

isomers, however, is that 2-TCN mainly undergoes a strong ring puckering during relaxation on the  $S(\pi\pi^*)$  state surface, while 3-TCN undergoes both a ring puckering and a ring opening leading to an open chain conformation with an almost planar thiophene ring and C1-C2 and S-C1

double bonds (numbering scheme see Fig. 5.1). Six vibrational modes have been found to be relevant for the relaxation path of the bright  $S(\pi\pi^*)$  state of 2-TCN to the  $S_1$ - $S_0$  CI seam along the reaction coordinate. These are symmetric stretching modes of the C1-C2, C3-C4 and C4-S bonds, a ring puckering mode of the thiophene ring, and two out-of-plane bending modes of the pyrrole ring and cyano group, respectively (see Fig. 5.5). For 3-TCN, mainly two modes have been identified to be relevant for the relaxation path of the bright  $S(\pi\pi^*)$  state to the  $S_1$ - $S_0$  CI seam i.e. a stretching mode of the C1-S bond and the ring puckering mode of the thiophene ring. In conclusion, this suggests an ultrafast radiationless decay of the bright  $S(\pi\pi^*)$  state through a ring-puckered (2-TCN) and an almost planar, ring-opened (3-TCN)  $S_1$ - $S_0$  CI, respectively. These results suggest that even though TCN in contrast to thiophene exhibits a low lying CT state which can be assumed to substantially change the photochemical behavior, its deactivation mechanism is governed by the same vibrational relaxation dynamics occurring in thiophene<sup>[322,323]</sup>. For thiophene it is found that the  $S_1$  state PES has multiple local minima, with the lowest energy minimum corresponding to a ring-opened conformation. It can be populated either via multiple CIs or via ISCs. The other two minima correspond to geometries, in which the sulfur atom is distorted out of the ring plane. They are connected by a path along C-H out-of-plane vibrational modes and the ring deformation mode that has only a very small energy barrier. Hence, these two minimum structures can easily be converted into one another.

Like already stated in the previous chapter, CC2 as a conventional single reference method is not suitable for describing CIs. Thus, geometries and energies of the intersection points found along the reaction coordinate on  $S(\pi\pi^*)$  can only be estimated at this level of theory. Here, geometries in which the energy gap between  $S(\pi\pi^*)$  and  $S_0$  along the reaction coordinate is minimal have been chosen as approximate CI geometries. For 2-TCN, the total energy of this geometry is 3.71 eV (relative to the  $S_0$  equilibrium energy), i.e. 0.82 eV below the FC  $S(\pi\pi^*)$  state. The total energy of the approximate CI in 3-TCN is 3.57 eV (relative to the  $S_0$  equilibrium energy) and lies 1.20 eV below the FC  $S(\pi\pi^*)$  state. The accessibility of the respective  $S_1$ - $S_0$  CIs of 2- and 3-TCN has been estimated by comparing the vertical excitation energy of  $S_1$  obtained at the FC geometry and the total energy of  $S_1$  at the approximate CI geometry. Indeed, their geometries of 2- and 3-TCN lie energetically about 1.8 eV and 1.7 eV below the  $S_1$  states at the FC geometries. Therefore, it can be inferred from the gas phase LR-CC2 results that after photoexcitation to the bright  $S(\pi\pi^*)$  state TCN undergoes radiationless deactivation to the ground state. In contrast, TD-BHLYP and TD-CAM-B3LYP erroneously predict a stationary point on

the  $S(\pi\pi^*)$  PES of 2-TCN (see Fig. 5.6). This local minimum has been verified by vibrational frequency analyses at the respective levels of theory. For 3-TCN this stationary point is only obtained when the BHLYP functional is used, in contrast TD-CAM-B3LYP, in agreement with LR-CC2, predicts an intersection with the  $S_0$  state. Yet, this failure of TDDFT is not entirely surprising because it is known that TDDFT tends to fail to describe conical intersections between excited states and the ground state<sup>[324,325]</sup>. However, it is well known that the influence of

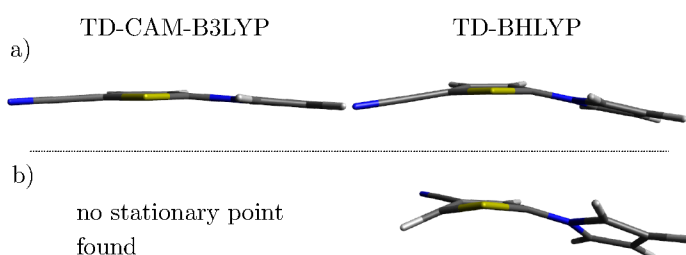


FIGURE 5.6:  $S_1$   $S(\pi\pi^*)$  state equilibrium geometries of 2-TCN a) and 3-TCN b) obtained at TD-CAM-B3LYP/cc-pVTZ and TD-BHLYP/cc-pVTZ levels of theory.

a solvent can significantly affect the photochemical behavior. Solvent calculations at the FC geometry employing nonequilibrium ptSS-PCM solvation (see Table ??), which will be discussed in more detail below, indicate a stabilization of the  $S(\text{CT})$  state due to solvation, and hence a surface crossing between the  $S(\pi\pi^*)$  and  $S(\text{CT})$  may be present in solution.

Fully relaxed geometry optimizations of the  $S(\text{CT})$  ( $S_2$ ) states of 2- and 3-TCN have been performed at the LR-CC2/cc-pVTZ level of theory. In both isomers, excited state relaxation from the FC geometry immediately leads to an intersection with the close lying  $S(\pi\pi^*)$  ( $S_1$ ) state (see Fig. 5.7) and only very small geometric changes are required. The reaction coordinate to the intersection involves mainly an out-of-plane tilting of the pyrrole ring, a planarization of the thiophene ring and an elongation of the central C1-N bond. As before, LR-CC2 has been used to approximately determine geometries and energies of the intersection points to obtain a qualitative correct picture of the deactivation pathway of  $S(\text{CT})$ . The total energy of the approximate  $S_2$ - $S_1$  CI geometry of 2-TCN is 4.54 eV. Hence, after photoexcitation to the  $S(\pi\pi^*)$  state ( $\omega = 4.53$  eV) a tiny energy barrier of only about 0.01 eV has to be overcome to reach the  $S_2$ - $S_1$  CI. After passing the CI, 2-TCN relaxes to a  $S(\text{CT})$  state minimum on the  $S_1$  state PES. In the case of 3-TCN the total energy of the approximate CI geometry is 4.76 eV. Hence, after photoexcitation to the  $S(\pi\pi^*)$  state ( $\omega = 4.79$  eV) relaxation to the  $S(\text{CT})$  minimum via the  $S_2$ - $S_1$  CI is barrierless. In both isomers relaxation of the  $S(\text{CT})$  state towards the local minimum is dominated by a strong out-of-plane tilting motion of the pyrrole ring. In the  $S(\text{CT})$

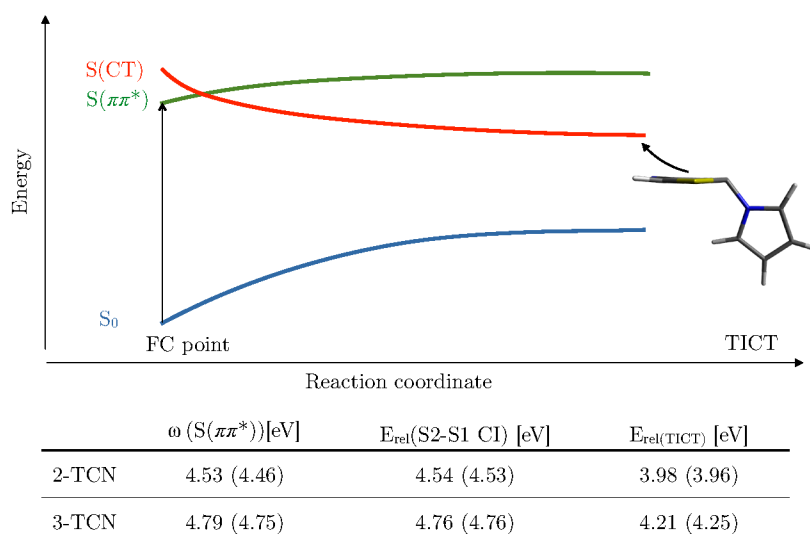


FIGURE 5.7: Schematic representation of the deactivation pathway of the S(CT) ( $S_2$ ) state of 2-TCN and 3-TCN obtained at LR-CC2/cc-pVTZ level of theory in the gas phase. Vertical excitation energies  $\omega$  of the  $S(\pi\pi^*)$  state and total energies of the approximate conical intersection (relative to the  $S_0$  equilibrium energy) and the S(CT) (TICT) minimum geometries of both isomers are given in the table. In parenthesis values obtained at ADC(2)/cc-pVTZ level of theory are given.

state minimum, the thiophene ring is almost planar, the pyrrole ring is strongly tilted and the two ring planes are almost orthogonal with respect to each other (see Fig. 5.7). Hence, these S(CT) minima can be characterized as TICT minima. The total energies of the TICT minima of 2- and 3-TCN obtained at LR-CC2/cc-pVTZ and ADC(2)/cc-pVTZ levels of theory in the gas phase are 3.98, 4.21 eV and 3.96 and 4.25 eV, respectively (relative to the  $S_0$  equilibrium energy). They lie energetically above the approximate  $S_1$ - $S_0$  CI and thus further decay to the ground state is in principle possible also from the TICT minimum. Even though an accessible TICT minimum exists, in gas phase fluorescence experiments of TCN, red-shifted fluorescence out of the TICT minima will probably not be observable due to missing energy dissipation<sup>[326]</sup>. In summary, the in vacuo calculations strongly suggest that after vertical excitation TCN deactivates radiationless to the ground state and thus should not show any fluorescence in the gas phase.

### 5.3.4 The photochemistry of TCN in solution

To investigate the influence of a solvent on absorption and emission spectra as well as on the excited state deactivation pathways, state specific COSMO and nonequilibrium ptSS-PCM solvation models have been employed. To consider the influence of solvent polarity, the parameters of

*n*-hexane ( $\epsilon = 2.0$ ,  $n = 1.37$ ), acetonitrile (ACN) ( $\epsilon = 37.5$ ,  $n = 1.34$ ) and water (H<sub>2</sub>O) ( $\epsilon = 78.0$ ,  $n = 1.33$ ) have been used. First, vertical excitation energies of the two lowest singlet and triplet states have been computed at the gas phase S<sub>0</sub> equilibrium geometries of 2- and 3-TCN using ADC(2)/cc-pVTZ/ptSS-PCM (Table 5.3).

TABLE 5.3: Comparison of vertical excitation energies of the first four lowest excited states of 2- and 3-TCN obtained at ADC(2)/cc-pVTZ and ADC(2)/cc-pVTZ/ptSS-PCM levels of theory<sup>a</sup>. Vertical excitation energies in the gas phase  $\omega$  (in eV), solvent-corrected vertical excitation energies  $\omega_{\text{sol}}$  (in eV), solvent shifts  $\Delta\omega^b$  (in eV) and the energy gap between S( $\pi\pi^*$ ) and S(CT) ( $\Delta E$  (in eV)) are given.

State	Gas				ACN			H <sub>2</sub> O		
	$\omega$	$\omega_{\text{sol}}$	$\Delta\omega$	$\Delta E$	$\omega_{\text{sol}}$	$\Delta\omega$	$\Delta E$	$\omega_{\text{sol}}$	$\Delta\omega$	$\Delta E$
2-TCN										
T( $\pi\pi^*$ )	3.28	3.27	-0.01		3.28	0.00		3.28	0.00	
T(CT)	4.01	3.94	-0.07		3.94	-0.07		3.94	-0.07	
S( $\pi\pi^*$ )	4.46	4.39	-0.07	+0.10	4.36	-0.10	+0.12	4.36	-0.10	+0.12
S(CT)	4.88	4.49	-0.39		4.48	-0.40		4.48	-0.40	
3-TCN										
T( $\pi\pi^*$ )	3.51	3.51	0.00		3.52	0.01		3.52	+0.01	
T(CT)	4.13	4.11	-0.02		4.15	+0.02		4.16	+0.03	
S( $\pi\pi^*$ )	4.75	4.65	-0.10	+0.13	4.64	-0.11	+0.23	4.64	-0.11	+0.24
S(CT)	5.12	4.78	-0.34		4.87	-0.25		4.88	-0.24	

<sup>a</sup> computed at the gas phase S<sub>0</sub> equilibrium geometry obtained at CC2/cc-pVTZ level of theory.

<sup>b</sup>  $\Delta\omega$  is the energy difference between the vertical excitation energies computed in the gas phase and with the ptSS-PCM solvent model.

Secondly, vertical excitation energies have been recomputed using ADC(2)/cc-pVTZ/SS-COSMO (Table A.5). Hereby, the solvent image charges are equilibrated with respect to the S<sub>0</sub>, the S( $\pi\pi^*$ ) and S(CT) state charge densities, respectively.

In the case of nonequilibrium ptSS-PCM solvation, the largest solvent effect is found for the S(CT) state. For all three solvents the excitation energy of S(CT) of 2-TCN is lowered by about 0.40 eV. Interestingly, for 3-TCN the lowering is most pronounced for apolar *n*-hexane i.e. by 0.34 eV. In ACN and H<sub>2</sub>O solution the excitation energy is lowered by only about 0.25 eV. Vertical excitation energies of the bright S( $\pi\pi^*$ ) state decrease only slightly by about 0.10 eV for all three solvent parameters. This observation can be explained as follows. The total energy correction due to fast relaxation (fast electronic polarization) is a function of the square of the refractive index ( $n^2$ ), which is almost identical for these solvents. The slow solvent term accounting for the nuclear motion of the solvent molecules and representing the interaction of the frozen ground state polarization with the electric field of the excited state is dependent on  $\epsilon - n^2$ . Since the ground state of TCN is relatively apolar ( $\mu \approx 4$  D) and the static dipole moments of ground and

excited states are not oriented parallel, the slow term is small and the fast term dominates the total energy correction. Hence, the ptSS-PCM correction is very similar for all solvents.

For 2-TCN the energy gap  $\Delta E$  is reduced from 0.42 eV in the gas phase to about 0.12 eV ( $\approx 1000 \text{ cm}^{-1}$ ) in solution. For 3-TCN,  $\Delta E$  is lowered from 0.37 eV in the gas phase to 0.13 eV in *n*-hexane and to about 0.23 eV in polar solution. Even though vertical excitation energies of the S(CT) states of 2- and 3-TCN are red-shifted and  $\Delta E$  is reduced, the energetic order of S( $\pi\pi^*$ ) and S(CT) states stays the same. In other words, when nonequilibrium pt-SS-PCM salvation is employed the vertical excitation energy of S(CT) is not lowered below the FC energy of S( $\pi\pi^*$ ). Nevertheless, these calculations suggest, that owing to the reduced  $\Delta E$ , the probability for population of the S(CT) state and further relaxation to the TICT minimum is higher in solution than in the gas phase. A more pronounced solvation effect is obtained using state specific COSMO solvation (see Table A.5). In this case, the stabilization of S(CT) depends more strongly on the polarity of the solvent. In apolar *n*-hexane, vertical excitation energies of the S(CT) state of both TCN isomers are shifted by only -0.05 - -0.07 eV when the solvent reaction field is equilibrated with respect to the bright S( $\pi\pi^*$ ) state. In contrast, vertical excitation energies of the S( $\pi\pi^*$ ) states, static dipole moments and  $\Delta E$  are almost unaffected.

In ACN, vertical excitation energies of both S( $\pi\pi^*$ ) and S(CT) states are strongly red-shifted when the solvent reaction field is equilibrated with respect to the bright S( $\pi\pi^*$ ) state. The shift amounts to 0.72 and 0.92 eV for the S(CT) state. This effect is so pronounced that the energetic order of S( $\pi\pi^*$ ) and S(CT) state changes and S( $\pi\pi^*$ ) and S(CT) become almost energetically degenerate at 3.9 and 4.1 eV. The static dipole moments of both states are enlarged. The effects of solvation with H<sub>2</sub>O are very similar to those observed for ACN. Vertical excitation energies of the S(CT) states of 2- and 3-TCN are decreased by 0.77 and 0.97 eV. From these results it can be inferred that in medium or polar solvents the S(CT) state of TCN is more easily accessible after photoexcitation than in gas phase or apolar solution.

To estimate the effect of polar solution on the deactivation pathways of bright S( $\pi\pi^*$ ) and S(CT) states, vertical excitation energies of both states have been recomputed at the ADC(2)/cc-pVTZ/SS-COSMO level of theory along the respective gas phase relaxed scans using the parameters of ACN (Figure 5.8 and 5.9). The PES scan of S( $\pi\pi^*$ ) in ACN solution reveals that even though S(CT) is stabilized below S( $\pi\pi^*$ ) at the FC geometry, the energy curve of S(CT) and also  $\Delta E$  increase along the S( $\pi\pi^*$ ) reaction coordinate which corresponds mainly to thiophene ring puckering. The total energies of the approximate CI geometries (relative to the solvent

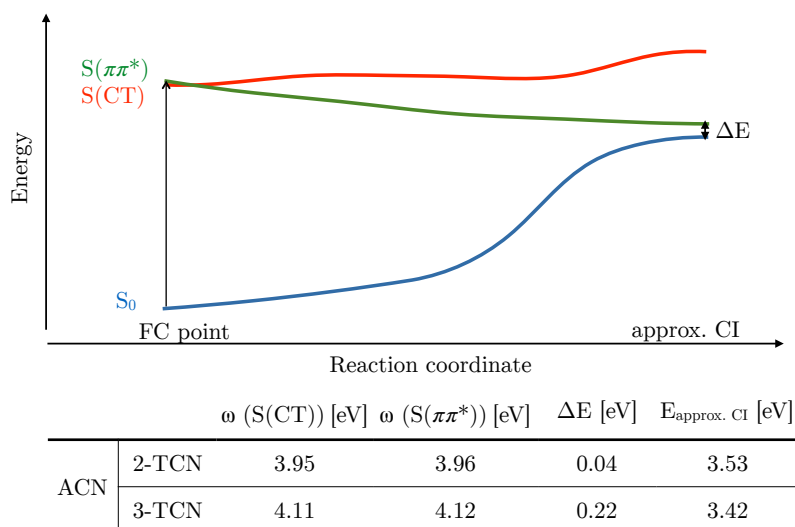


FIGURE 5.8: Schematic representation of the deactivation pathway of the  $S(\pi\pi^*)$  ( $S_1$ ) state of TCN simulating ACN solution. Vertical excitation energies  $\omega$  of  $S(\pi\pi^*)$  and  $S(\text{CT})$  states and total energies of the approximate conical intersection geometries (relative to the  $S_0$  equilibrium energy) obtained at ADC(2)/cc-pVTZ/SS-COSMO level of theory are given in the table.

corrected  $S_0$  energy) are 3.53 and 3.42 eV in ACN, hence lowered by about 0.3 eV compared to the gas phase (Figure 5.5). The PES scan of  $S(\text{CT})$  in ACN solution shows that in polar environments  $S(\text{CT})$  is stabilized significantly below  $S(\pi\pi^*)$  already at the FC geometry. Vertical excitation energies of  $S(\text{CT})$  and  $S(\pi\pi^*)$  states of 2- and 3-TCN are 3.32, 3.51 eV and 3.63, 3.77 eV, respectively. However, along the  $S(\text{CT})$  reaction coordinate which corresponds mainly to tilting and twisting of the pyrrole group, the energy curve of  $S(\text{CT})$  is only slightly lowered. The total energies of the  $S(\text{CT})$  state TICT minima of TCN in ACN are 2.73 and 3.06 eV. These results suggest that in contrast to the gas phase, in polar solution population of the TICT minimum of TCN becomes more likely due to the strong stabilization of the  $S(\text{CT})$  state at the ground state equilibrium geometry and along the  $S(\text{CT})$  reaction coordinate. These calculations reveal that in ACN, after vertical excitation to the bright  $S(\pi\pi^*)$  state, TCN can relax barrierless to the TICT minimum. Hence, in fluorescence experiments in polar solution red-shifted emission may be observable, however, most likely with very low quantum yield.

## 5.4 SUMMARY AND CONCLUSION

The photochemical behavior of the cyanothiophene isomers 2- and 3-TCN has been investigated in the gas phase using high-level quantum chemical methods. The influence of solvation on

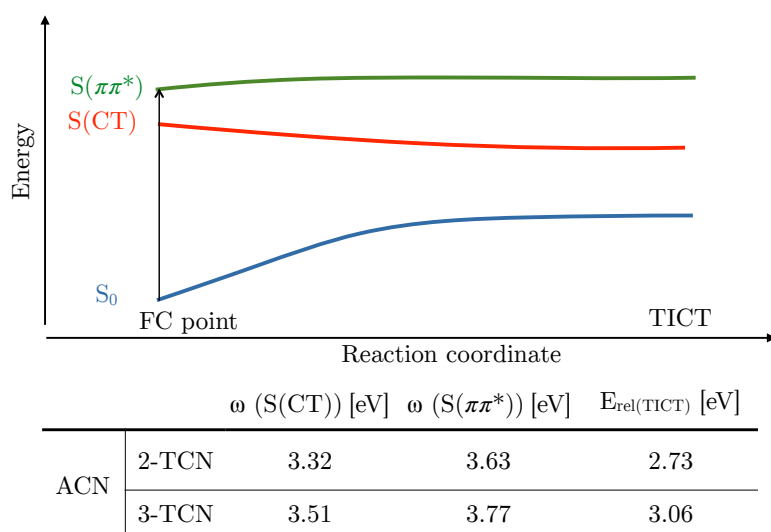


FIGURE 5.9: Schematic representation of the deactivation pathway of the  $S(\pi\pi^*)$  ( $S_1$ ) state of TCN simulating ACN solution. Vertical excitation energies  $\omega$  of  $S(\pi\pi^*)$  and  $S(\text{CT})$  states and total energies of the approximate conical intersection geometries (relative to the  $S_0$  equilibrium energy) obtained at ADC(2)/cc-pVTZ/SS-COSMO level of theory are given in the table.

absorption properties as well as the excited state deactivation pathways has been investigated using two different continuum solvation models i.e. nonequilibrium ptSS-PCM and equilibrium SS-COSMO.

The gas phase ground state equilibrium geometry of TCN is not planar. Like in the case of PBN and DMABN in both isomers, the rings are slightly twisted with respect to each other. Twisting to an orthogonal conformation of the rings is slightly hindered. Single reference methods predict the lowest singlet excited states  $S_1$  and  $S_2$  to be the photochemically relevant excited states. While the  $S_1$  state is an optically allowed bright  $\pi\pi^*$  state, the  $S_2$  state is a dark CT state. The possibility of intersystem crossing has been excluded, since the energy gaps of the ISC relevant transitions are relatively large ( $> 0.5$  eV) and the relevant SOCs are small (about  $1.8 \text{ cm}^{-1}$ ).

Two different deactivation mechanisms have been identified for the two TCN isomers. After photoexcitation to the bright  $S(\pi\pi^*)$  state, 2-TCN will most probably exhibit radiationless decay to the ground state via a low lying  $S_1$ - $S_0$  intersection along a ring puckering mode of thiophene. In contrast, for 3-TCN a cleavage of the C1-S bond occurs, leading to the formation of a C-C and S-C double bond and a subsequent radiationless deactivation to the ground state via a low lying  $S_1$ - $S_0$  intersection. Hence, even though an electron donor substituent is present in TCN yielding a low lying CT state, the results suggest that the deactivation pathway is dominated by vibrational modes of thiophene.

A TICT minimum has been found on the  $S_1$  state surface of both isomers. Gas phase LR-CC2

calculations of 2-TCN indicate that a tiny barrier of only about 0.01 eV has to be overcome to reach the TICT minimum. In 3-TCN there is no corresponding barrier. However, gas phase calculations suggest that population of the TICT minimum is rather unlikely due to the presence of a  $S_1$ - $S_0$  CI which can be reached barrierless after excitation to the bright  $S(\pi\pi^*)$  ( $S_1$ ) state. Solvation model calculations indicate that the  $S(CT)$  is stabilized in polar solvents and that population of the TICT minimum becomes more likely.

In conclusion, this study reveals that even though TCN is structurally very similar to dual fluorescent DMABN and PBN, it exhibits a different photochemistry. While PBN and DMABN show at least single emission from a locally excited (LE) state in the gas phase, the thiophene analogue TCN is predicted to deactivate radiationless to the ground state such as unsubstituted thiophene. While DMABN and PBN show dual fluorescence in medium polar and polar solvents or single red-shifted emission from a polar TICT state in strongly polar solvents, the solvation model results indicate that for TCN dual fluorescence will not occur and single red-shifted emission may only be observable in polar solvents. Thus, for the construction of thiophene containing donor-acceptor compounds, this study shows that the  $S(CT)$  state needs to be further stabilized for efficient charge separation via TICT formation to occur. One way to accomplish this is by increasing the donor strength, e.g. by lowering the local ionization potential of the donor group. Otherwise, thiophene's photochemistry will quench charge separation.

---

## REGULAR FLUORESCENCE OF 4-FLUORO-*N,N*-DIMETHYLANILINE (FDMA).

### AN AB-INITIO STUDY REVEALS: FDMA EXHIBITS NO TICT MECHANISM

---

This chapter<sup>†</sup> focus on the photochemistry of the small organic donor-acceptor compound 4-Fluoro-*N,N*-dimethylaniline (FDMA). This study is motivated by two recent contradicting experimental investigations by Zachariasse et al.<sup>[328]</sup> (from 2017) and Fujiwara et al.<sup>[329]</sup> (from 2013) on the fluorescence behavior of FDMA. Motivated by the discrepancies between these studies I have examined the deactivation pathways of photoexcited FDMA using TDDFT, LR-CC2, ADC(2) and ADC(3). Solvatochromic effects have been studied by employing COSMO and C-PCM solvation models. According to the computational results, the initial population of the bright  $S_2$  ( $\pi\pi^*$ ) state of FDMA relaxes to a linear, almost planar  $S_1$  state minimum from which emission occurs. This study further reveals TDDFT/B3LYP erroneously to predict a planar TICT  $S_1$  state minimum that vanishes when the amount of nonlocal HF exchange in the xc functional is increased.

## 6.1 MOTIVATION AND BACKGROUND

FDMA (see Fig. 6.2) is the fluorine analogue of the well-known and well investigated dual fluorescent DMABN molecule. It comprises an analogues electron donating dimethylamino (DMA) but a weaker electron accepting 4-Fluoroaniline group that are connected by a single bond.

---

<sup>†</sup>Parts of this chapter are adapted from Bohnwagner, MV. and Dreuw, A. *J. Phys. Chem. A.*, **2017**, *121* (31), pp 5834-5841<sup>[327]</sup>, Copyright 2017 with permission from the American Chemical Society and the corresponding editor

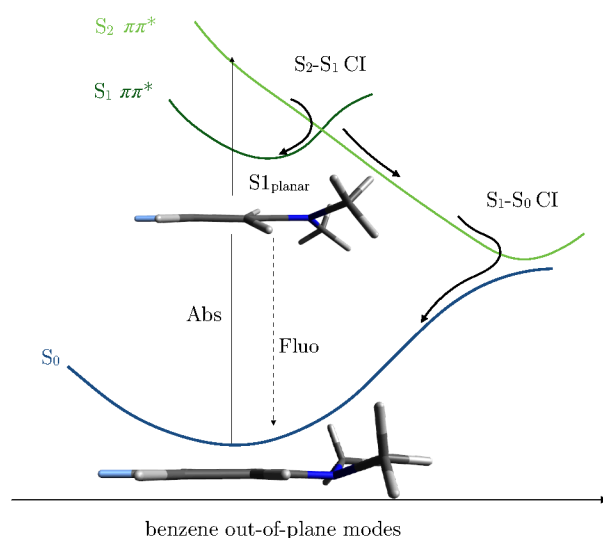


FIGURE 6.1: Schematic illustration of the deactivation mechanism of FDMA obtained at LR-CC2 level of theory.

It is still debated whether FDMA exhibits a similar fluorescence behavior as DMABN or not, i.e. whether it shows dual fluorescence in polar solvents or not. Two contradicting papers concerning the fluorescence properties of FDMA were recently published.<sup>[328,329]</sup> Zachariasse et al.<sup>[328]</sup> reported the observation of single fluorescence of FDMA in *n*-hexane as well as acetonitrile (ACN) solution. Their experimental findings agree with those of an earlier experimental study of FDMA<sup>[330]</sup>. In contrast, Fujiwara et al.<sup>[329]</sup> observed dual fluorescence of FDMA in *n*-hexane and ACN supported by data obtained from quantum chemical calculations using DFT and TDDFT employing the hybrid xc functionals B3LYP and PBE. Zachariasse et al. claim the previous observation of dual fluorescence of FDMA reported by Fujiwara et al. to be faulty.

A small energy gap  $\Delta E(S_2/S_1)$  ( $S_1$  denotes the LE and  $S_2$  the ICT state) depending on the solvent polarity and decreasing from *n*-hexane to ACN was pointed out to be needed for efficient ICT and the occurrence of dual fluorescence.<sup>[328]</sup> This condition was derived from comparison of numerous absorption and fluorescence experiments on related donor-acceptor systems, i.a. DMABN<sup>[77,331–333]</sup>, 1-tert-butyl-6-cyano-1,2,3,4-tetrahydroquinoline (NTC6)<sup>[334,335]</sup>, P-Pyrrolobenzonitrile (PBN)<sup>[66,336,337]</sup>, *N,N*-Dimethylaniline (DMA)<sup>[328]</sup> and *N*-Phenylpyrrole (PP)<sup>[337,338]</sup>. For FDMA Zachariasse et al. found a relatively large  $\Delta E(S_2/S_1)$  of about 1.0 eV ( $8300\text{ cm}^{-1}$ ) both in *n*-hexane and ACN excluding TICT formation. In general, also the quantum yield ratio  $\Phi(\text{ICT})/\Phi(\text{LE})$  should be solvent dependent, because ICT states are stabilized in polar solvents due to their typically large static dipole moments of about  $> 15\text{ D}$ <sup>[66,337,339]</sup>.

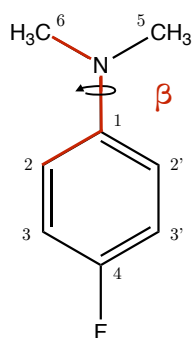


FIGURE 6.2: Structure of FDMA and numbering of the relevant atoms. The twisting coordinate  $\beta$  is shown in red.

### 6.1.1 Experimental and theoretical findings by Fujiwara et al.: the observation of dual fluorescence<sup>[329]</sup>

In steady state absorption experiments of FDMA in *n*-hexane and ACN at room temperature two absorption bands were observed for FDMA: an intense band with maxima at 4.96 and 4.86 eV (250 and 255 nm), respectively, and a weak red-shifted band at 3.94 and 3.87 eV (315 and 320 nm), respectively. Corresponding steady state fluorescence spectra were obtained by excitation at different wavelength. In *n*-hexane and ACN, two emission bands at 3.71 and 3.41 eV (334 and 364 nm) and at 3.56 and 3.12 eV (348 and 397 nm), respectively, are obtained. Furthermore, the observed dual fluorescence was reported to be wavelength dependent. Time-resolved fluorescence measurements revealed almost identical decay times of the two emission bands ( $\approx 1.4$  ns in *n*-hexane and  $\approx 3.7$  ns in ACN). Computations at DFT and TDDFT levels yielded vertical excitation energies of 4.35 eV (286 nm) and 5.39 eV (230 nm) for the  $S_1(A'')$  and  $S_2(A')$  states, respectively, using the B3LYP functional assuming  $C_s$  point group symmetry. The  $S_1$  and  $S_2$  states were assigned to the two observed absorption bands. Furthermore, three low-energy excited-state geometries of FDMA were found at TDDFT/B3LYP/cc-pVDZ level of theory. One almost planar  $\pi\pi^*$  minimum and two different TICT states, one with a planar and one with a pyramidalized amino nitrogen atom, with the former TICT state geometry being the most stable one. For the  $\pi\pi^*$  and the non-pyramidalized TICT state, emission wavelengths of 3.50 eV and 3.18 eV (354 nm and 390 nm) and dipole moments of 8 and 11 D were computed in the gas phase, respectively, and found to agree well with the two observed emission bands in ACN.

### 6.1.2 Experimental findings by Zachariasse et al.: the observation of single fluorescence<sup>[328]</sup>

In agreement with the findings by Fujiwara et al.<sup>[329]</sup> absorption spectra of FDMA measured in *n*-hexane and ACN at 25 °C show two bands, a weak one with maxima at 4.01 and 3.97 eV (309 and 312 nm) and a strong one at 5.04 and 4.98 eV (246 and 249 nm), respectively. The energy difference  $\Delta E(S_1, S_2)$  is 1.03 eV (8300 cm<sup>-1</sup>) in *n*-hexane and 1.00 eV (8130 cm<sup>-1</sup>) in ACN which is large compared to the ones for DMABN of 0.34 eV (2720 cm<sup>-1</sup>) and < 0.33 eV (< 2700 cm<sup>-1</sup>), respectively. This already makes the occurrence of dual fluorescence unlikely. In fluorescence measurements recorded in *n*-hexane and ACN, indeed, only single fluorescence emission was observed. The emission band was assigned to the LE state, which is in agreement with the large  $\Delta E(S_1, S_2)$ . The fluorescence quantum yield ( $\Phi$ ) has been found to be quite low in *n*-hexane ( $\Phi(\text{LE}) = 0.081$ ) and ACN ( $\Phi(\text{LE}) = 0.152$ ). In both fluorescence and excitation spectra of FDMA only one emission band and no excitation wavelength dependence has been observed. From these experimental results Zachariasse et al. concluded that, in contrast to the claims by Fujiwara et al., no LE  $\rightarrow$  ICT reaction occurs and that the TICT structure predicted by TD-B3LYP computations is not relevant for the experiments.

The aim of this theoretical study is twofold. Motivated by the discrepancies between the above presented studies, the assumption of Zachariasse et al. that the TD-B3LYP predicted, non-pyramidalized TICT  $S_1$  state minimum is a methodological artifact and the knowledge that TDDFT tends to over stabilize CT states<sup>[179,180]</sup>, the theoretical findings by Fujiwara et al.<sup>[329]</sup> are reexamined using various *ab-initio* methods such as CC2, ADC(2) and ADC(3). Furthermore, the effect of the amount of nonlocal HF exchange in TDDFT on both  $S_1$  state equilibrium geometries and the potential energy curves of the  $S_1$  state along the twisting coordinate  $\beta$  is investigated.

### 6.1.3 Computational details

The ground state ( $S_0$ ) geometry of FDMA has been fully optimized (within  $C_1$  symmetry) and for comparison with theoretical data by Fujiwara et al. in  $C_s$  symmetry using MP2 (again employing the RI approximation) in conjunction with the cc-pVTZ and corresponding auxiliary basis set RIMP2-cc-pVTZ. Also the range-separated CAM-B3LYP functional together with the cc-pVTZ

basis set and for comparison with computational results by Fujiwara et al. the B3LYP functional together with the cc-pVDZ basis set have been used. The optimized  $S_0$  geometries have been verified as minima on the PES by vibrational frequency analyses showing no imaginary frequencies. A relaxed PES scan of  $S_0$  along the twisting coordinate  $\beta C6-N-C1-C2$  (numbering see Fig. 6.2) has been performed at MP2/cc-pVDZ level of theory. Starting with  $0^\circ$ ,  $\beta$  has been increased to  $90^\circ$  in steps of  $10^\circ$ . While  $\beta$  was held fixed, all other coordinates were allowed to relax. The lowest two vertical singlet excitation energies have been computed at the  $S_0$  geometries along the PES scan using TD-B3LYP/cc-pVDZ and TD-CAM-B3LYP/cc-pVDZ methods. In the TD-CAM-B3LYP calculations triplet states have been included.

The lowest two vertical singlet and triplet excitation energies, oscillator strengths and static dipole moments ( $\mu$ ) have been computed at the  $C_s$  symmetric  $S_0$  equilibrium geometry obtained at MP2/cc-pVTZ level of theory using various methods: ADC(2), ADC(3), LR-CC2 and TDDFT using B3LYP and CAM-B3LYP functionals. For ADC(2) and LR-CC2 calculations, the cc-pVTZ/MP2-cc-pVTZ basis sets have been employed. Due to the resource requirements and computational costs of ADC(3)/cc-pVTZ computations only vertical excitation energies of the photochemically relevant excited singlet states observed in experiment ( $S_1$  and  $S_2$ ) have been computed. Spin-orbit coupling (SOC) constants between the six lowest lying singlet and triplet excited states have been computed at the  $S_0$  equilibrium geometry at ADC(2)/cc-pVDZ and ADC(2)/cc-TZVPP levels of theory using the atomic mean field integral (AMFI)<sup>[306,340]</sup> program interfaced with a developer's version of Q-Chem<sup>[341]</sup> 4.2 assuming  $C_s$  symmetry.

Solvent effects on vertical excitation energies at the  $S_0$  equilibrium geometry have been estimated at ADC(2)/cc-pVTZ level employing the nonequilibrium ptSS-PCM correction scheme. For comparison with experiments the parameters of *n*-hexane ( $\epsilon = 2.0$ ,  $n = 1.374$ ) and acetonitrile (ACN) ( $\epsilon = 37.5$ ,  $n = 1.344$ ) have been chosen for the solvent models. Even though both solvents are not typical hydrogen bond donors, the effects of hydrogen bonding interactions on vertical excitation energies have been investigated. For this purpose two solvent molecules have been added to the  $S_0$  equilibrium geometry, respectively, (see Fig. B.1 and B.2) and vertical excitation energies have been recomputed at TD-CAM-B3LYP/cc-pVDZ level of theory.

The geometries of the photochemically relevant excited states  $S_1$  and  $S_2$  ( $1A''$  and  $1A'$ , respectively, in  $C_s$  symmetry) have been fully optimized at LR-CC2, TD-CAM-B3LYP and TD-B3LYP levels of theory, respectively, using the cc-pVDZ basis set and auxiliary cc-pVDZ basis set (for LR-CC2) and additionally under  $C_s$  symmetry constraint for comparison with computational

data of Fujiwara et al.. The lowest lying triplet state  $T_1$  has been fully optimized at TD-CAM-B3LYP/cc-pVDZ level of theory. Stationary points obtained at TD-CAM-B3LYP and TD-B3LYP levels of theory have been verified as local minima or transition states on the PES by vibrationally frequency analysis.

Rigid PES scans of the  $S_1$  state along  $\beta$  have been performed at TD-B3LYP, TD-CAM-B3LYP and ADC(2) levels of theory, respectively. For this purpose, the  $1A''_{\text{planar}}$  geometry ( $\beta = 0^\circ$ ) has been taken as starting geometry and  $\beta$  was increased to  $90^\circ$  in steps of  $10^\circ$ . For rigid PES scans performed at TD-B3LYP/cc-pVDZ and TD-CAM-B3LYP/cc-pVDZ levels of theory the Gaussian 09 Rev D01 suit of program has been used and for the one performed at ADC(2)/cc-pVDZ level of theory Q-Chem 4.3 has been employed. For corresponding relaxed PES scans at TD-B3LYP/cc-pVDZ and TD-CAM-B3LYP/cc-pVDZ levels of theory Q-Chem 4.3 has been used. Emission energies have been computed at the most stable local minimum geometry ( $S_{1\text{planar}}$ ), employing ADC(2)/cc-pVTZ in conjunction with equilibrium SS-C-PCM accounting for solvation effects using again the parameters of *n*-hexane and ACN for the solvent model. SOC constants between the lowest four excited singlet and triplet states have been computed at the  $S_{1\text{planar}}$  geometry and the approximately determined  $S_1$ - $S_0$  conical intersection (CI) geometry, respectively, at the ADC(2)/cc-pVDZ and ADC(2)/def2-TZVPP levels of theory. CC2 calculations have been performed using TURBOMOLE V6.3.1<sup>[271]</sup>. For all ADC calculations Q-Chem versions 4.3 and 4.4 have been used. For TDDFT calculations both Q-Chem 4.4 and Gaussian 09 RevD01 have been used. Visualization and plotting of molecular orbitals (MOs) were done with the Avogadro program<sup>[342]</sup> version 1.0.3. Attachment and detachment densities have been displayed by VMD<sup>[308]</sup>. For PCM computations a developer's version of the Q-Chem<sup>[341]</sup> program version 5.0 has been used.

## 6.2 RESULTS

It has been observed in previous theoretical studies that TD-B3LYP, and also other standard xc functionals with low amounts of nonlocal HF exchange, severely over stabilizes higher symmetry geometries<sup>[343]</sup> and also mistakenly predict energetically very low lying TICT state minima<sup>[283,344,345]</sup>. To examine, if the same methodological error is responsible for the prediction of the non-pyramidalized TICT  $S_1$  state minimum reported by Fujiwara et al.,  $S_0$  and  $S_1$  state PESs have been investigated by using TD-B3LYP, TD-CAM-B3LYP, LR-CC2 and ADC(2)

methods. In line with the above mentioned findings<sup>[283,343–345]</sup> relaxed  $S_0$  PES scans along  $\beta$  at MP2//TD-CAM-B3LYP/cc-pVDZ and MP2//TD-B3LYP/cc-pVDZ levels of theory (see Fig. 6.3 and B.3) and rigid PES scans of  $S_1$  along  $\beta$  at TD-B3LYP/cc-pVDZ (see Fig. 6.4), TD-CAM-B3LYP/cc-pVDZ and ADC(2)/cc-pVDZ levels (see Fig. B.4 and Fig. 6.5), respectively, reveal that the non-pyramidalized  $S_1$  minimum at  $90^\circ$  predicted by TD-B3LYP/cc-pVDZ level of theory is artificial, since it vanishes when TD-CAM-B3LYP or ADC(2) methods are employed.

The TD-B3LYP/cc-pVDZ level of theory predicts a twisted ( $\beta \approx 90^\circ$ )  $S_1$  state minimum ( $S_{1\text{twisted}}$ ) with planar fluoroaniline and dimethylamino group with a total energy of 3.97 eV (relative to  $S_0(\text{eq})$ ) and a linear planar stationary structure ( $1A''_{\text{planar}}$ ) (see Fig. 6.6) with a total energy of 4.13 eV, that is 0.16 eV less stable than  $S_{1\text{twisted}}$ . This study, however, reveals that these equilibrium structures are again artifacts of the B3LYP functional since they also disappear when TD-CAM-B3LYP or LR-CC2 is employed. From these results it can be inferred that TD-B3LYP is not suitable to study the photochemistry of FDMA and the study by Fujiwara et al.<sup>[329]</sup> have to be considered as flawed.

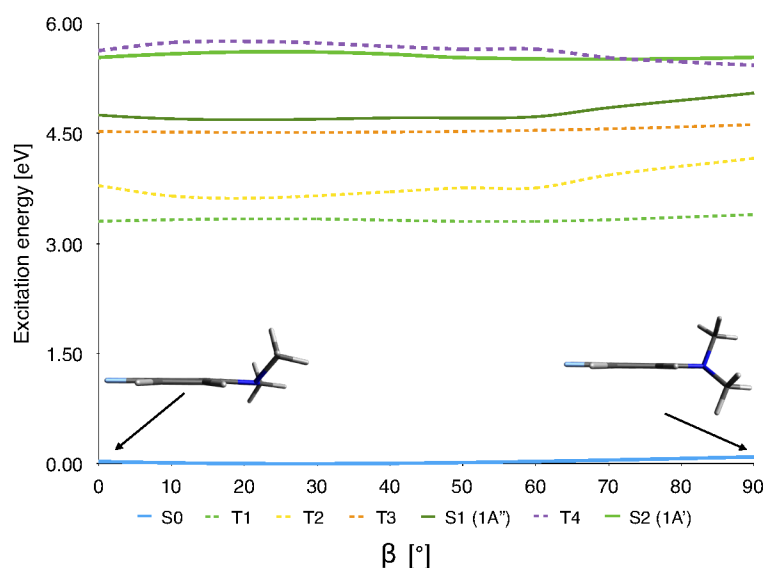


FIGURE 6.3: Relaxed PES scan of the ground state along the twisting coordinate  $\beta$  obtained at MP2//TD-CAM-B3LYP/cc-pVDZ level of theory. Vertical excitation energies of the first six lowest excited states considering singlet and triplets states have been computed at each ground state geometry along the PES scan.

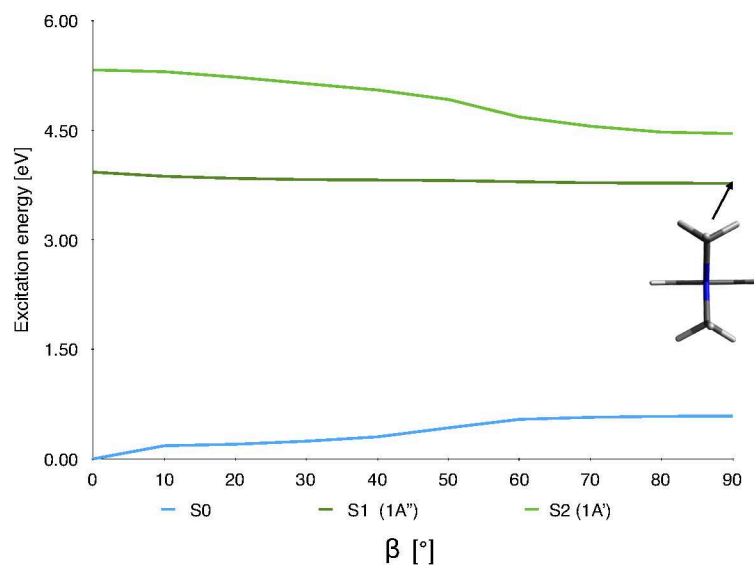


FIGURE 6.4: Rigid PES scan of the S<sub>1</sub> state along the twisting coordinate  $\beta$  obtained TD-B3LYP/cc-pVDZ level of theory. As starting geometry, the 1A''planar ( $\beta = 0^\circ$ ) equilibrium geometry has been used.

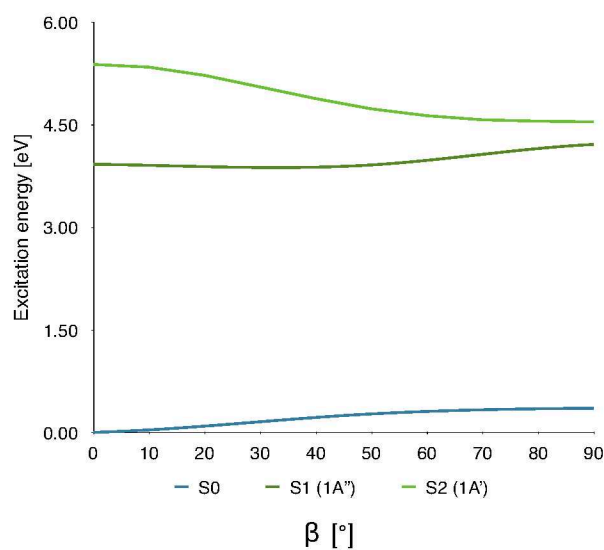


FIGURE 6.5: Rigid PES scan of the S<sub>1</sub> state along the twisting coordinate  $\beta$  obtained ADC(2)/cc-pVDZ level of theory. As starting geometry, the 1A''planar ( $\beta = 0^\circ$ ) equilibrium geometry computed at the TD-B3LYP/cc-pVDZ level of theory has been used.

### 6.2.1 Simulated absorption spectra of FDMA

For the validation of the chosen methodology, vertical excitation energies  $\omega$  of the four lowest lying excited states of FDMA have been computed at the gas phase MP2 optimized S<sub>0</sub>(eq) (see Fig. B.5) geometry using different wave function based methods and two TDDFT methods. (Table

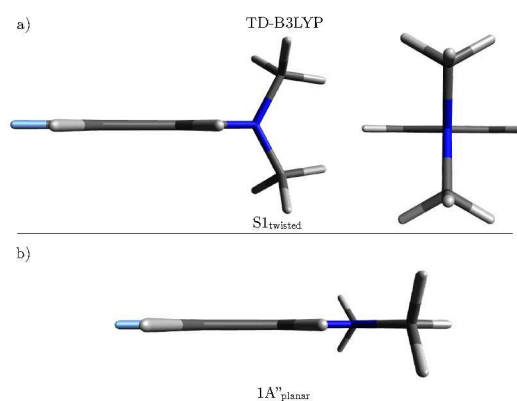


FIGURE 6.6:  $S_1$  state equilibrium geometries of FDMA a)  $S_{1\text{twisted}}$  and b)  $1A''_{\text{planar}}$  obtained at TD-B3LYP/cc-pVDZ level of theory.  $1A''_{\text{planar}}$  is predicted to be a transition state ( $\nu = 100.4$   $\text{cm}^{-1}$ ) at TD-CAM-B3LYP/cc-pVDZ level of theory. The  $S_{1\text{twisted}}$  geometry is not found at CAM-B3LYP and LR-CC2 levels of theory.

6.1). For comparison with the experimental data reported by Fujiwara et al. and Zachariasse et al. a solvation model has been included as well. The MP2 optimized  $S_0$  equilibrium geometry

TABLE 6.1: Comparison of gas-phase vertical excitation energies and static dipole moments of the first two lowest singlet and triplet excited states of FDMA calculated at the  $S_0(\text{eq})$  geometry obtained at MP2/cc-pVTZ level of theory using different wave function based and TDDFT methods. Irreducible representation (in parenthesis) and character of the excited states, vertical excitation energies  $\omega$  (in eV), oscillator strengths (in parenthesis) and relaxed static dipole moments  $\mu$  (in Debye) are given.

State	ADC(3)		ADC(2)		LR-CC2		CAM-B3LYP		B3LYP	
	$\omega$	$\omega$	$\mu$	$\omega$	$\mu$	$\omega$	$\mu$	$\omega$	$\mu$	
$S_1$ ( $1A''$ ) ( $\pi\pi^*$ )	4.44 (0.05)	4.35 (0.05)	6.7	4.38 (0.05)	5.8	4.63 (0.05)	5.6	4.36 (0.04)	6.4	
$S_2$ ( $1A'$ ) ( $\pi\pi^*$ )	5.68 (0.22)	5.44 (0.33)	6.5	5.52 (0.32)	4.9	5.56 (0.21)	4.2	5.28 (0.17)	1.2	
$T_1$ ( $1A''$ ) ( $\pi\pi^*$ )		3.90	6.5	3.93	5.9	3.43	3.5	3.48	5.7	
$T_2$ ( $1A'$ ) ( $\pi\pi^*$ )		4.10	4.2	4.13	3.9	3.61	5.4	3.61	3.8	

( $S_0(\text{eq})$ ) is almost planar ( $\beta = 20^\circ$ ) with a pyramidalized amino nitrogen atom ( $\delta = 23^\circ$ , with  $\delta(\text{C6-C5-C1-N})$ , numbering see Fig. 6.2). The central C1-N bond length is  $1.394 \text{ \AA}$ , hence almost the same as in anilin ( $1.407 \text{ \AA}$  in the gas phase)<sup>[346]</sup>. The  $S_0(\text{eq})$  geometries obtained at DFT levels of theory are more planar ( $\beta = 13^\circ$  at CAM-B3LYP/cc-pVTZ and B3LYP/cc-pVTZ levels, respectively) and the nitrogen atom is less pyramidalized,  $\delta = 15^\circ$  at both levels. The energy barrier for rotation about  $\beta$  ( $0.04 \text{ eV} \approx 0.9 \text{ kcal/mol}$ ) obtained at MP2/cc-pVDZ level of theory indicates an essentially free rotation in the gas phase.

With respect to vertical excitation energies and properties of the  $S_1$  ( $1A''$ ) and  $S_2$  ( $1A'$ ) states, wave function and TD-CAM-B3LYP show an overall good agreement. However,  $\omega$  of  $S_1$  obtained at

TD-CAM-B3LYP level of theory is slightly overestimated with respect to ADC methods.

The  $S_1$  state of FDMA has only little oscillator strength of about 0.05 and a static dipole moment of about 6 D, twice as large as the one of  $S_0(\text{eq})$  which is about 3 D. Gas phase vertical excitation energies are 4.44 and 4.35 eV at ADC(3)/cc-pVTZ and ADC(2)/cc-pVTZ levels of theory, respectively. The  $S_1$  state can mainly be characterized as a single electron excitation out of the HOMO into LUMO. Analyses of the MOS (see Fig B.6 and Fig. B.7) and attachment and detachment densities (see Fig. 6.7) reveal this state to be a typical  $\pi\pi^*$  state. This  $S_1$  ( $\pi\pi^*$ ) state can be assigned to the experimentally observed weak absorption band at about 4.00 eV (in *n*-hexane and ACN solution)<sup>[328,329]</sup>.

The  $S_2$  state is a bright state with a static dipole moment of about 4 - 6 D, i.e. of about the

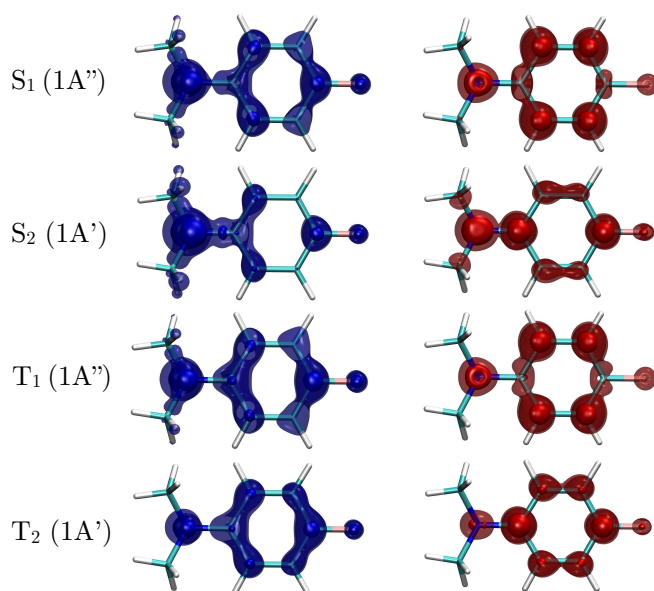


FIGURE 6.7: ADC(2)/cc-pVTZ electron detachment (blue) and attachment (red) density plots for the  $S_1$  ( $1A''$ ) and  $S_2$  ( $1A'$ ) states of FDMA calculated at the MP2  $S_0$  equilibrium geometry.

same size as the one of  $S_1$ . Gas phase vertical excitation energies are 5.68 and 5.44 eV at ADC(3)/cc-pVTZ and ADC(2)/cc-pVTZ levels of theory, respectively. This transition is largely dominated by a single electron transition from HOMO to LUMO+2 and can be characterized as  $\pi\pi^*$  state (see Fig. 6.7 and Fig. B.6).

The lowest lying triplet state  $T_1$  ( $1A''$ ) obtained at ADC(2)/cc-pVTZ level of theory exhibits the same  $\pi\pi^*$  character as  $S_1$  and the  $T_2$  ( $1A'$ ) state has the same  $\pi\pi^*$  character as  $S_2$ . Since Zachariasse et al. report high ISC quantum yields for FDMA of 0.90 and 0.80 in *n*-hexane and ACN, respectively, the probability of ISC between the energetically lowest four singlet and triplet states of FDMA has been estimated at ADC(2)/cc-pVDZ (and ADC(2)/def2-TZVPP) levels of

theory considering the size of SOC as well as the energy gap between initial and final state ( $\Delta E$ ).  $\Delta E$  should be small ( $< 0.5$  eV) for efficient ISC<sup>[321]</sup>. Considering these two factors the most likely transitions for ISC at the FC geometry are  $S_1-T_1$ ,  $S_1-T_2$ ,  $S_2-T_1$ ,  $S_3-T_4$  and  $S_3-T_5$ . For those transition the  $\Delta E$ 's are smaller than 0.5 eV. However, the corresponding SOC constants are also very small 0.10, 0.30, 0.03, 0.02 and 0.20  $\text{cm}^{-1}$ , respectively, at ADC(2)/cc-pVDZ level of theory. Even with the larger def2-TZVPP basis set SOC for these transitions remain negligible ( $< 1$   $\text{cm}^{-1}$ ). These results suggest that at the FC geometry ISC in FDMA is unlikely. However, in earlier experimental and theoretical studies of bare benzene<sup>[347–350]</sup>, strong evidence was found for ultrafast ISC as competing nonradiative deactivation processes in the excited state dynamics, even though SOC between  $S_1$  and  $T_1$  at the FC geometry is tiny. Furthermore, it was found that computed SOC constants are strongly dependent on the geometry and increase noticeably along the prefulvene reaction coordinate towards the  $S_1-S_0$  CI, even though they still remain small ( $< 10$   $\text{cm}^{-1}$ )<sup>[350,351]</sup>. Hence, ISC in FDMA cannot be generally excluded.

### Solvent effects on absorption spectra

For comparison with experimental absorption data obtained in solution, vertical singlet excitation energies of FDMA have been computed at the MP2 optimized  $S_0(\text{eq})$  geometry employing ADC(2)/cc-pVTZ in combination with nonequilibrium ptSS-PCM (Table 6.2). Additionally,

TABLE 6.2: Comparison of vertical excitation energies of the first two lowest excited singlet states of FDMA obtained at ADC(2)/cc-pVTZ and ADC(2)/cc-pVTZ/ptSS-PCM levels of theory at the gas phase  $S_0(\text{eq})$  geometry. Solvent-corrected vertical excitation energies  $\omega_{\text{sol}}$  (in eV) and dipole moments, wavelengths  $\lambda$  of the absorption band maxima obtained by Zachariasse et al.<sup>[328]</sup> ( $\lambda_{(\text{Zach})}$  (in eV)) and Fujiwara et al.<sup>[329]</sup> ( $\lambda_{(\text{Fuj})}$  (in eV) and deviation of computed energies from experimental ones  $\Delta\omega_{\text{exp}}$  (in eV) are given.

State	<i>n</i> -hexane		<i>n</i> -hexane solution				ACN		ACN solution			
	$\omega_{\text{sol}}$	$\mu$	$\lambda_{(\text{Zach})}$	$\Delta\omega_{\text{exp}}$	$\lambda_{(\text{Fuj})}$	$\Delta\omega_{\text{exp}}$	$\omega_{\text{sol}}$	$\mu$	$\lambda_{(\text{Zach})}$	$\Delta\omega_{\text{exp}}$	$\lambda_{(\text{Fuj})}$	$\Delta\omega_{\text{exp}}$
$S_1$	4.27	7.3	4.01	0.26	3.94	0.33	4.24	8.1	3.97	0.27	3.87	0.37
$S_2$	5.35	7.5	5.04	0.31	4.96	0.39	5.30	8.5	4.98	0.32	4.86	0.44

vertical excitation energies of the four lowest excited singlet states have been computed at the gas phase  $S_0(\text{eq})$  geometry incorporating two *n*-hexane and two ACN molecules (see Fig. B.1 and Fig. B.2), respectively, employing the TD-CAM-B3LYP/cc-pVDZ level of theory. Vertical excitation energies of the bright  $S_1$  ( $H > L$ ) and  $S_2$  ( $H > L+1$ ) states (the MOs are shown in Fig. B.8)

are 4.23 and 4.95 eV, respectively, for the *n*-hexane cluster. Corresponding vertical excitation energies of  $S_1$  ( $H > L$ ) and  $S_3$  ( $H > L+1$ ) states (see Fig. B.9) of the ACN cluster are 4.23 and 5.08 eV, respectively. As expected, the results indicate no evidence for hydrogen bond interactions and reveal that inclusion of two explicit *n*-hexane and ACN solvent molecules has no significant influence on the absorption energies of the two experimentally observable transitions. Hence, it can be assumed that to investigate solvatochromic effects in absorption and emission spectra, accounting for electrostatic interactions using continuum solvation models is sufficient. The agreement between computed vertical excitation energies employing the nonequilibrium ptSS-PCM correction scheme and the experimentally observed absorption maxima in solution<sup>[328,329]</sup> is reasonably good with deviations of  $< 0.3$  eV for the  $S_1$  state and of about 0.31 eV for the  $S_2$  state with respect to the data by Zachariasse et al.<sup>[328]</sup>. ]Deactivation mechanism of FDMA To identify local minima on both  $S_1$  and  $S_2$  state PESs geometry optimizations have been performed in the gas phase first without applying symmetry constraints. Two equilibrium geometries are obtained, respectively at TD-CAM-B3LYP/cc-pVDZ level of theory namely  $S1_{\text{planar}}$  and  $S1_{\text{pyr}}$  (see Fig. 6.8). Both have been verified as minima on the PES by vibrational frequency analysis. The  $S1_{\text{planar}}$  geometry has a total energy of 4.41 eV (relative to  $S_0(\text{eq})$ ) at TD-CAM-B3LYP/cc-

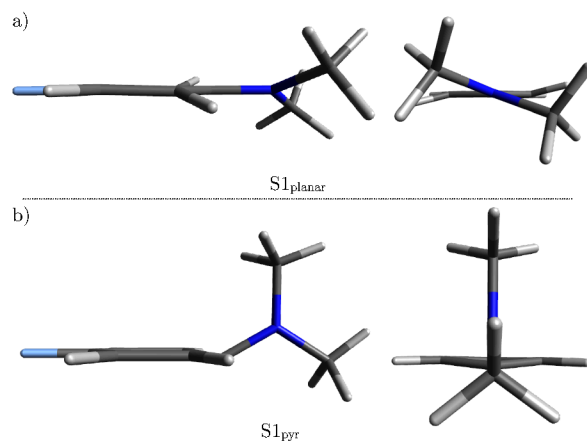


FIGURE 6.8: a) planar ( $S1_{\text{planar}}$ ) and b) twisted (and pyramidalized) ( $S1_{\text{pyr}}$ )  $S_1$  state minima of FDMA obtained at the TD-CAM-B3LYP/cc-pVDZ level of theory.

pVDZ level of theory, and is 0.25 eV more stable than the twisted  $S1_{\text{pyr}}$  geometry which has a total energy of 4.66 eV. Static dipole moments of FDMA in  $S1_{\text{planar}}$  and  $S1_{\text{pyr}}$  are 6.0 and 8.2 D, respectively at TD-CAM-B3LYP/cc-pVDZ level of theory. Even though the  $S1_{\text{pyr}}$  minimum has a twisted conformation and structurally resembles the TICT state geometry of PBN (compare to **chapter 4**) the relative small static dipole moment does not indicate a TICT character. At

LR-CC2 level the same two equilibrium geometries are obtained with only slightly different bond length and bond angles. At ADC(2)/cc-pVTZ level, total energies of 4.00 and 4.56 eV have been obtained, respectively and the energy difference is even more pronounced.

Full geometry optimizations in the  $S_2$  state performed at TD-CAM-B3LYP/cc-pVDZ and LR-CC2/cc-pVDZ levels of theory yield an intersection with the  $S_1$  state. To obtain a qualitative picture of the deactivation pathway of the  $S_2$  state, geometry and energy of the  $S_2$ - $S_1$  intersection point have been estimated at the TD-CAM-B3LYP/cc-pVDZ level of theory. The total energy of the approximate  $S_2$ - $S_1$  CI geometry (see Fig. 6.9) is 5.34 eV (relative to  $S_0$ (eq)). This geometry lies 0.2 eV below the  $S_2$  state at the FC geometry and 0.93 eV above the  $S_{1\text{planar}}$  minimum. At

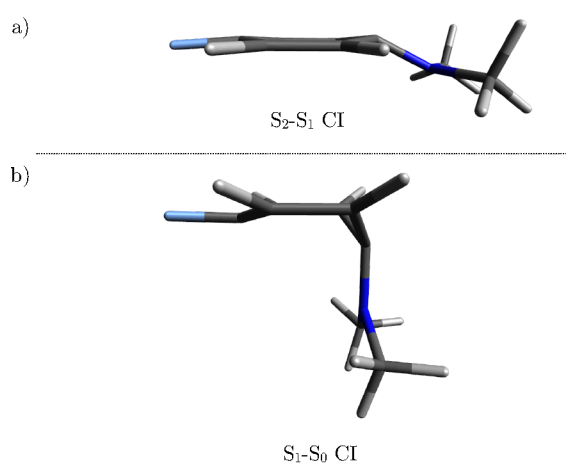


FIGURE 6.9: a) Approximate  $S_2$ - $S_1$  conical intersection geometry obtained with and without applying  $C_s$  symmetry constraints and b) approximate  $S_1$ - $S_0$  conical intersection geometry both obtained at the TD-CAM-B3LYP/cc-pVDZ level of theory.

TD-CAM-B3LYP and LR-CC2 levels of theory relaxation from the FC point on the  $S_2$  PES to the approximate  $S_2$ - $S_1$  CI is barrierless and proceeds along a prefulvene-like motion consisting of a symmetric out-of-plane motion of C1 and C4 out of the benzene ring plane accompanied by a bending of the dimethylamino group and a symmetric out-of-plane motion of the four benzene H-atoms out of the plane spanned by atoms C2, C2', C3 and C3' (numbering see Fig. 6.2). After passing the  $S_2$ - $S_1$  CI, FDMA continues to relax on the  $S_1$  PES to the  $S_{1\text{planar}}$  minimum.

$C_s$  symmetry constrained geometry optimizations of the  $1A'$  ( $S_2$ ) state performed at TD-CAM-B3LYP/cc-pVDZ and LR-CC2/cc-pVDZ levels of theory yield two intersections: the above mentioned  $S_2$ - $S_1$  CI (see Fig. 6.9) and a further one with the ground state ( $S_1$ - $S_0$ ) CI (see Fig. 6.9 and Fig. B.11). Geometry and energy of the  $S_1$ - $S_0$  intersection found along the reaction

coordinate on the 1A' ( $S_2$ ) PES have been estimated at TD-CAM-B3LYP/cc-pVTZ and LR-LR-CC2/cc-pVDZ levels of theory. The approximate  $S_1$ - $S_0$  CI has a total energy of 4.49 eV (relative to  $S_0(\text{eq})$ ) and lies 0.08 eV above the  $S_{1\text{planar}}$  geometry. However, the energy difference between the  $S_1$  and the  $S_0$  state at this geometry is still relatively large (0.6 eV). Thus, it may be assumed that the total energy of the exact  $S_1$ - $S_0$  CI will be lower. The total energy of the approximate  $S_1$ - $S_0$  CI (relative to  $S_0(\text{eq})$ ) obtained at LR-CC2/cc-pVDZ level is 3.99 eV and lies 0.61 eV below the  $S_{1\text{planar}}$  minimum geometry obtained at LR-CC2/cc-pVDZ level of theory. The energy difference between  $S_1$  and  $S_0$  at the approximate CI geometry is 0.07 eV for LR-CC2. Unconstrained reoptimizations of the  $S_1$  state performed at TD-CAM-B3LYP and LR-CC2 levels, starting at the respective approximate  $S_2$ - $S_1$  CI geometries give different results, either the  $S_{1\text{planar}}$  geometry or the identified  $S_1$ - $S_0$  intersection geometry are obtained.

These results suggest that after passing the  $S_2$ - $S_1$  CI, FDMA may continue relaxation along a prefulvene-like and an out-of-plane bending mode of the dimethylamino group towards a  $S_1$ - $S_0$  CI and return to the ground state nonradiatively, or localize in the  $S_{1\text{planar}}$  minimum and fluoresce. They further suggest that radiationless deactivation via internal conversion may play a role in the excited state dynamics of FDMA and provide one possible explanation for the low fluorescence quantum yields ( $8.1 \times 10^{-2}$  and  $1.5 \times 10^{-1}$ )<sup>[328]</sup> observed in experiments<sup>[328,330]</sup>.

SOC constants between the lowest four excited singlet and triplet states have been computed at the  $S_{1\text{planar}}$  minimum,  $T_1$  equilibrium (see Fig. B.12) and  $S_1$ - $S_0$  CI geometries, respectively, at the ADC(2)/def2-TZVPP level of theory, to examine whether the estimated ISC probability, analogous to benzene<sup>[350,351]</sup>, increases at these geometries. Considering again the above mentioned factors ( $\Delta E$  and magnitude of SOC) the following transitions have been found to be most likely for ISC at the  $S_{1\text{planar}}$  geometry:  $S_1 \rightarrow T_1$ ,  $S_1 \rightarrow T_2$  and  $S_2 \rightarrow T_4$ . The corresponding  $\Delta E$ 's are: 0.43, 0.16 and 0.27 eV and SOC constants are: 0.16, 1.06 and 1.60  $\text{cm}^{-1}$ , hence SOC constants between  $S_1$  and  $T_1$  and  $S_1$  and  $T_2$  at the at the  $S_{1\text{planar}}$  geometry are indeed increased with respect to the FC geometry. Nevertheless, they still remain small. Also at the approximate  $S_1$ - $S_0$  CI and the  $T_1$  equilibrium geometries, SOC constants between the lowest lying four singlet and triplet states remain small ( $< 2 \text{ cm}^{-1}$ ) and the energy gaps for the lowest lying transitions relatively large ( $> 0.6 \text{ eV}$ ). These results, are in agreement with a recent theoretical study for benzene<sup>[351]</sup>, where a SOC constant of 1.8  $\text{cm}^{-1}$  between  $S_1$  and  $T_1$  at CASSCF(10/10)/6-31G\* level of theory at the optimized CI geometry was reported. These small SOC constants do not indicate efficient ISC of FDMA and benzene. However, in solid and liquid benzene ISC was

found to be induced by vibronic coupling rather than by SOC leading to efficient radiationless decay to the ground state<sup>[347,347–349,352–355]</sup> and the absence of phosphorescence in liquid benzene at room temperature<sup>[356]</sup>.

### Solvent effects on emission spectra

Solvent effects in emission spectra have been investigated by employing equilibrium SS-C-PCM. For comparison with the experimental data obtained by Fujiwara et al. and Zachariasse et al. again the parameters of *n*-hexane and ACN have been used for the solvent model. Vertical excitation energies of the S<sub>1</sub> state have been computed at the gas phase equilibrium geometry S1<sub>planar</sub> at the ADC(2)/cc-pVTZ/SS-C-PCM level of theory. The reaction field has been equilibrated with respect to the S<sub>1</sub> state. Solvent-corrected emission energies are 3.55 and 3.23 eV, respectively, for the parameters of *n*-hexane and ACN. The respective fluorescence band maxima measured by Zachariasse et al. are at 3.55 eV (28670 cm<sup>-1</sup>) and 3.36 eV (27070 cm<sup>-1</sup>), respectively.<sup>[328]</sup> The agreement with these experimental data is excellent. Deviations between computed and experimental values are only 0.00 eV and 0.13 eV. The deconvoluted fluorescence bands reported by Fujiwara et al.<sup>[329]</sup> are at 3.71 eV (334 nm) and 3.56 eV (348 nm) in *n*-hexane and ACN, respectively. The deviations of the computed energies from these ones are 0.16 and 0.33 eV, hence, slightly larger.

Additionally, triplet-triplet transition energies for the 7 lowest lying triplet states have been computed at the T<sub>1</sub> equilibrium geometry (see Fig. B.12) obtained at TD-CAM-B3LYP/cc-pVDZ level of theory using ADC(2)/cc-pVTZ/SS-C-PCM employing again the parameters of *n*-hexane and ACN for comparison with experimental triplet-triplet absorption spectra reported by Zachariasse et al.<sup>[328]</sup>. Absorption maxima were found at 2.81 eV (442 nm) and 2.63 eV (472 nm) in *n*-hexane and ACN solution, respectively. The computed transition with the largest oscillator strength of about 0.20 corresponds to the T<sub>1</sub>-T<sub>4</sub> transition. Transition energies of 2.93 and 2.92 eV have been obtained, for ACN and *n*-hexane, respectively in fairly good agreement with the experimental values.

### 6.3 SUMMARY AND CONCLUSION

The photochemical behavior of FDMA has been investigated in the gas phase and simulating solution using high-level quantum chemical methods. The influence of solvation on absorption as well as emission energies has been investigated using two different continuum solvation models, i.e., nonequilibrium ptSS-PCM and equilibrium SS-C-PCM. The overall agreement of computed solvent-corrected absorption and emission energies with experimental ones is excellent. Additionally, the role of hydrogen bonding interactions has been estimated by adding two acetonitrile molecules and two *n*-hexane molecules, respectively, to the gas phase optimized MP2 ground state equilibrium geometry and calculating vertical excitation energies at the corresponding cluster structures. Not surprisingly, the two explicit solvent molecules hardly affect the vertical excitation energies. No indications of relevant hydrogen bonding interactions have been found. In agreement with the experimental results by Fujiwara et al. and Zachariasse et al. all employed *ab initio* methods predict the  $S_1$  and  $S_2$  ( $1A''$  and  $1A'$  in idealized  $C_s$  symmetry) to be the photochemically relevant excited states. The  $S_2$  state is a bright  $\pi\pi^*$  state that can be assigned to the strong blue-shifted absorption band observed in experiments conducted in *n*-hexane and acetonitrile. The  $S_1$  state is also a  $\pi\pi^*$  state with only small oscillator strength that can be assigned to the experimentally observed weaker slightly red-shifted absorption band. Due to reported triplet yields of 0.90 and 0.80 in *n*-hexane and acetonitrile<sup>[328]</sup> the probability of intersystem crossing has been estimated by computing energy gaps and spin-orbit coupling constants between the lowest lying singlet and triplet states at four important geometries: the  $S_0$  equilibrium geometry, the most stable  $S_1$  state equilibrium geometry ( $S_{1\text{planar}}$ ), the approximately determined  $S_1$ - $S_0$  conical intersection geometry and the  $T_1$  equilibrium geometry. Irrespective of the geometry, the computed spin-orbit coupling constants are tiny ( $< 2 \text{ cm}^{-1}$ ). Additionally, triplet-triplet transition energies for the 7 lowest lying triplet states have been computed at the  $T_1$  equilibrium geometry obtained at TD-CAM-B3LYP/cc-pVDZ level of theory using ADC(2)/cc-pVTZ/SS-C-PCM. My results agree well with theoretical findings on benzene where also only very small spin-orbit coupling constants ( $< 2 \text{ cm}^{-1}$ ) were obtained. Computed solvent-corrected triplet-triplet transition energies also show a good agreement with the experimental triplet-triplet absorption data obtained by Zachariasse et al..

From these results, the following picture of the photochemical deactivation mechanism can be drawn (see Fig. 6.10). After photoexcitation to the bright  $S_2$  state, FDMA may either relax

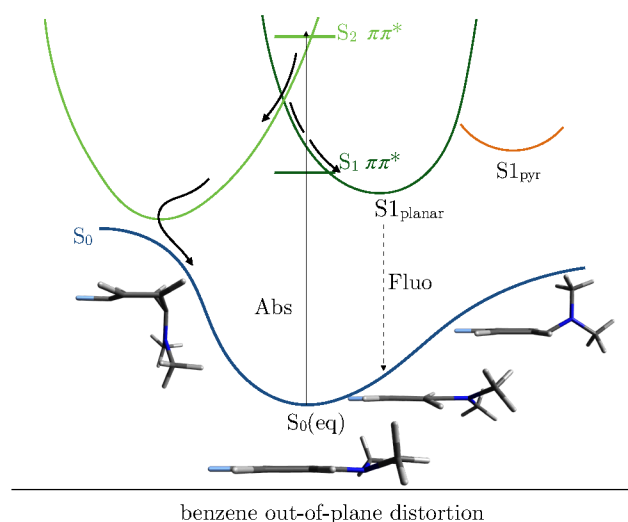


FIGURE 6.10: Schematic illustration of the suggested deactivation mechanism of FDMA: After photoexcitation to the bright  $S_2$  ( $\pi\pi^*$ ) state, FDMA may either relax to an almost planar  $S_1$  state minimum  $S_{1\text{planar}}$  and fluoresce or it may decay nonradiatively to the ground state via a  $S_1$ - $S_0$  conical intersection.

to a planar  $S_1$  state minimum through a well accessible  $S_2$ - $S_1$  conical intersection from which fluorescence emission can occur. Alternatively, it may decay radiationless to the ground state via a low lying  $S_1$ - $S_0$  conical intersection along a prefulvene-like vibrational mode of benzene. My computational results perfectly explain the experimental observations of Zachariasse et al.<sup>[328]</sup>. Of course, for the prediction of probabilities for the different nonradiative and radiative decay pathways, advanced quantum dynamical calculations would be required, which, however, are beyond the scope of this work. This study shows that even though FDMA is structurally related to dual fluorescent DMABN and PBN (see **chapter 4**), it exhibits a different photochemistry as also found in the case of the thiophene analogue of PBN namely, TCN (see **chapter 5**). While DMABN and PBN show dual fluorescence in medium polar and polar solvents due to TICT formation, the here presented computations support the experimental finding of single fluorescence emission in apolar and polar solution by Zachariasse et al.<sup>[328]</sup>. Similar to TCN, in which internal modes of thiophene quench the fluorescence and lead TCN to a  $S_1$ - $S_0$  conical intersection in the gas phase, the photochemistry of FDMA seems to be governed by the photochemistry of benzene and internal modes of benzene open up a competitive nonradiative deactivation pathway. The computations further reveal that the TICT minimum reported by Fujiwara et al.<sup>[329]</sup> used to explain the seemingly observation of dual fluorescence is a methodological artifact of the employed TD-B3LYP method.



---

CIS-TRANS ISOMERIZATION VERSUS TWISTED INTRAMOLECULAR  
CHARGE-TRANSFER: A PHOTOCHEMICAL STUDY OF FOUR  
HEMITHIOINDIGO-HEMISTILBENE DERIVATIVES

---

In recent experimental studies<sup>[245,357]</sup> an interesting photochemical behavior was found for several hemithioindigo-hemistilbene (HTI) (see Fig. 7.1) derivatives. It was reported that in apolar solution cis-trans (*Z/E*) photoisomerization with high efficiency was observed for all studied HTIs. In polar solvents, in contrast, it was found that the isomerization is quenched and for some of the HTI derivatives, dual fluorescence was observed. As an explanation for the occurrence of dual fluorescence twisted intramolecular charge-transfer (TICT) state formation has been suggested. In this chapter, the deactivation mechanisms of the four HTI derivatives are investigated theoretically using different *ab initio* methods. The focus hereby is on two alternative relaxation pathways namely single-bond and double-bond rotation in relation to experimental findings. Solvent effects are accounted for by employing both nonequilibrium and equilibrium state specific C-PCM solvation. The role of hydrogen bonding interactions is examined by including a small number of explicit solvent molecules in the calculations.

New insights into the ultrafast decay from the initially populated first excited singlet state  $S_1$  of HTIs Z1-Z4 are provided. *Ab initio* calculations reveal that *Z/E* photoisomerization involves the potential energy surfaces of the ground state  $S_0$ , the lowest lying singlet  $S_1$  and the lowest lying triplet  $T_1$  state. Along the *Z/E* photoisomerization coordinate conical intersections between  $T_1$  and  $S_0$  and  $S_1$  and  $S_0$  are found. Spin-orbit coupling calculations at the FC geometry reveal that the  $T_1$  state of all four *Z* isomers is easily accessible explaining the absence of phosphorescence. The current results suggest that the occurrence of dual fluorescence in polar solvents is due to formation of a polar TICT state which, however, is only stable in solvents which are able to form

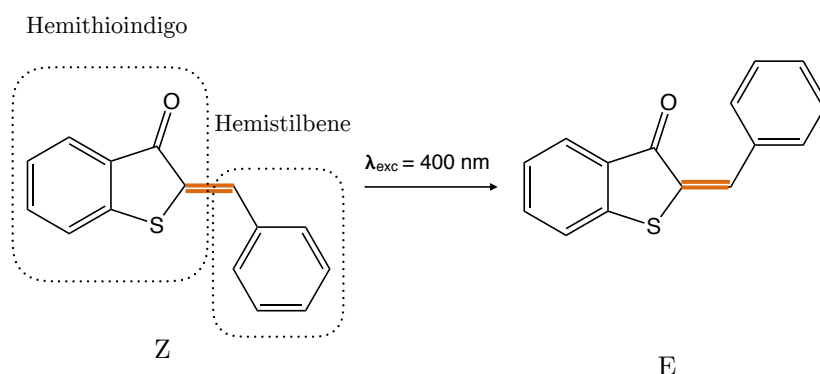


FIGURE 7.1: Structures of Z and E isomers of hemithioindigo (HTI) and the Z/E isomerization about the double bond (indicated in orange) induced by visible light.

hydrogen bonds with the HTI molecules.

Although the project is not yet complete, the results obtained so far are very promising and inspiring and already provide some interesting insights into the photochemistry of the four HTI derivatives. In the following, a summary of the current status of this study is given. A publication on the photochemistry of the four HTIs providing a more complete picture of the different deactivation mechanisms is in preparation.

Some of the results concerning HTI Z3 as presented in this chapter have been obtained in collaboration with A. Fink who wrote his bachelor thesis with the title "Quantum chemical case study of the isomerization, absorbance and fluorescence of a hemithioindigo derivate in vacuum and solution" under my supervision.

## 7.1 MOTIVATION AND BACKGROUND

Molecules that can reversibly be converted from one isomer, or state, into another by irradiation with light are named photoswitches. A well-known and well-investigated class of photoswitches are stilbenes<sup>[358–360]</sup>. The molecular systems under study, hemithioindigo-hemistilbenes, in short hemithioindigos (HTIs) belong to a fairly new class of photoswitches that recently have become subjects of significant interest.<sup>[361,362]</sup> HTIs consist of a stilbene component and a thioindigo fragment connected through a central photoisomerizable double bond (see Fig. 7.1). By irradiation with visible light, this system undergoes reversible isomerization between the Z and E isomer (see Fig. 7.1). HTI based photoswitches have some particularly advantageous properties. Z and E isomers exhibit well-separated absorption bands in the visible region which makes them

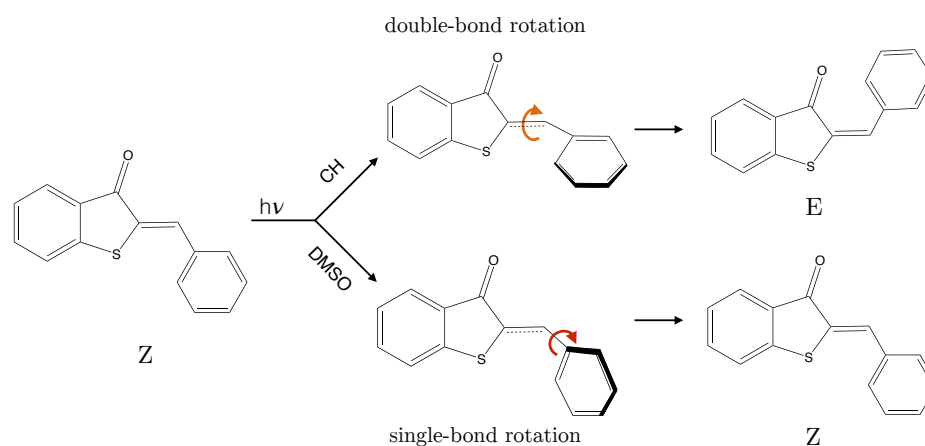


FIGURE 7.2: Schematic representation of two possible excited-state decay pathways of photoexcited HTIs Z1-Z3. In polar solvents mainly single-bond rotation occurs while in apolar solvents primarily Z/E photoisomerization of the double bond takes place.<sup>[245]</sup>

especially suitable for medical applications. Furthermore, the switching process is reversible and fatigue resistant, their photochemical behavior is synthetically tunable, and they can easily be implemented in other molecular systems or materials.<sup>[245,357,361,363–368]</sup> These properties make them suitable for various applications in different fields like material science, biochemistry and biology.<sup>[365,367,369–374]</sup>

In unsubstituted HTI the Z/E isomerization is induced with light of 400 nm wavelength and the reverse E/Z isomerization is induced by light of  $\approx 500$  nm wavelength.<sup>[375]</sup> The Z/E photoisomerization occurs on a sub-ps timescale.

Several experimental and theoretical studies<sup>[361,375–378]</sup> have been conducted already for unsubstituted HTI. Substitution of the stilbene segment of HTI with a donor like dimethylamine (DMA) renders HTI into a potential donor-acceptor push-pull system, like DMABN and PBN. For such HTI derivatives a few experimental studies<sup>[357,376,379]</sup> have been performed; however, there has been no theoretical studies up to now.

Recently Wiedbrauk et al. reported an interesting observation concerning the photochemical behavior of a number of donor substituted HTI photoswitches.<sup>[245,357]</sup> For some of the derivatives e.g. Z1-Z3 (see Fig. 7.3) it was found that depending on the choice of the solvent either double-bond or single-bond rotation is induced (see Fig. 7.2). It was stated that these two reaction coordinates are independent of one another and can be targeted separately using different solvents. It was reported that in apolar solvents like cyclohexane (CH) Z/E isomerization is the dominant excited state relaxation pathway.<sup>[245]</sup> Among HTIs Z1-Z4 the highest Z/E isomerization quantum yield ( $\phi_{Z/E}$ ) of  $56 \pm 12\%$  was observed for Z1 in CH solution. In DMSO a quantum yield of only

$1.8 \pm 0.4\%$  was obtained.<sup>[245]</sup> For HTIs Z2, Z3 and Z4 the corresponding values of  $\phi_{Z/E}$  were reported to be  $44 \pm 9\%$ ,  $30 \pm 7\%$  and  $32 \pm 7\%$ .

It was further reported that in medium polar solvents e.g. dichloromethane (DCM) and polar solvents, e.g., dimethyl sulfoxide (DMSO), the predominant relaxation mechanism is single-bond rotation leading to the formation of a polar long wavelength emitting state and the occurrence of dual fluorescence.<sup>[245]</sup> Time-resolved absorption spectra of HTIs Z1, Z2 and Z3 conducted in DCM show long-wavelength excited-state absorption (ESA) and red-shifted stimulated emission (SE) features (SE, was only observed for Z1 and Z2).<sup>[245]</sup> Wiedbrauk et al. suggest that those features result from the formation of a polar excited state with significant CT character. It was reported that the time constant of this new polar state first increases with increasing polarity up to values of 356 and 250 ps in THF for Z1 and Z2, respectively and then decreases again with increasing polarity to 13 and 7 ps, respectively in DMSO.<sup>[245]</sup> For Z3 a slightly different behavior was observed. In DMSO solution a time constant of 54 ps was obtained; and it was further stated that for THF solution an unambiguous assignment was not possible.<sup>[245]</sup> From these results Wiedbrauk et al. conclude that this state is a TICT state. In time-resolved fluorescence measurements of HTI Z1-Z3 conducted in DCM and DMSO two fluorescence components with two different decay constants were detected, the fluorescence of the long-lived one being strongly red-shifted.<sup>[245]</sup> Wiedbrauk et al. assigned the short-lived component to the decay of the minimum of the initially populated  $S_1$  state and the long-lived solvent polarity dependent component to the decay of the polar CT state. Motivated by the above described experimental findings of Wiedbrauk et al.<sup>[245]</sup> I have performed *ab initio* calculations on the four donor substituted HTI derivatives shown in Fig. 7.3. The main goal of this study is to gain more profound insights into the photochemistry and electronic structure of these HTI derivatives. The focus lies on the following questions: Which electronic states are involved in the Z/E photoisomerization? Is the experimentally observed dual fluorescence of HTI Z1 and Z2 in polar solvents related to the formation of a TICT state? What are the differences in the electronic structure of HTI Z1, Z2 and Z3? What are the prerequisites for TICT formation and the occurrence of dual fluorescence?

## 7.2 COMPUTATIONAL METHODS

To investigate the Z/E photoisomerization mechanism, first ground state ( $S_0$ ) geometries of HTIs Z1-Z4 and E1-E4 have been optimized at MP2/cc-pVDZ level of theory. Crystal structures



TABLE 7.1: Values for the dielectric constant  $\epsilon$  and the optical dielectric constant ( $n^2$ ) of the five different solvents used in the C-PCM calculations in the order of increasing polarity (top to down) are presented. All solvents are aprotic. The hydrogen bond acceptor (HBA) ability is given in the last column.

Solvent	$\epsilon$	$n^2$	H-bonding property
Cyclohexane (CH)	2.015	2.016	-
Tetrahydrofuran (THF)	7.58	1.980	HBA
Dichloromethane (DCM)	8.93	2.027	-
Acetonitrile (ACN)	37.5	1.806	HBA
Dimethyl Sulfoxide (DMSO)	46.7	2.184	strong HBA

along the Z/E isomerization pathway on the  $S_0$  and  $S_1$  state surfaces have been performed using the spin-flip (SF) approach in combination with TDDFT invoking the TDA together with the hybrid B5050LYP<sup>[381]</sup> xc-functional and the 6-31G\* basis set. For consistency, the ground state geometry has also been optimized at the SF-B5050LYP/6-31G\* level. The small 6-31G\* basis has been chosen as a reasonable compromise between accuracy and computational effort. The main reason is that the gradient calculations for such large systems at the SF-TDDFT/TDA level take a lot of computational time (since the TDDFT implementation is not yet fully parallelized in the Q-Chem program package). The B5050LYP functional has been chosen, since in a computational study<sup>[381]</sup> on different multireference systems, i.a. diradicals and ethylene, employing the SF-TDDFT/TDA approach, it demonstrated an overall good performance and good accuracy. The Z/E isomerization coordinate  $\theta$  is defined by two dihedral angles: To ensure a simultaneous torsion of the H atom attached to the central double bond and the hemistilbene fragment and to avoid a pyramidalization of the C2 atom the dihedral angles  $\theta_1$ (C1-C2-C5-C6) and  $\theta_2$ (S-C2-C5-H) have been chosen (for numbering see Fig. 7.4). For the PES scan  $\theta$  has been varied from  $180^\circ$  ( $\theta_1 = \theta_2 = 180^\circ$ ) (Z isomer) to  $0^\circ$  ( $\theta_1 = \theta_2 = 0^\circ$ ) (E isomer) in steps of  $10^\circ$ . For fixed values of  $\theta$ , all other geometric parameters were freely optimized. Conical intersections (CIs) found along the isomerization coordinate  $\theta$  have been optimized at SF-TDDFT/TDA/6-31G\* level of theory. Spin-orbit couplings (SOCs) between the six lowest lying singlet and triplet states and singlet-triplet energy gaps ( $\Delta E(T/S)$ ) have been computed at the FC geometries of HTIs Z1-Z4 employing the ADC(2)/cc-pVDZ level of theory. To find local  $S_1$  minima from which fluorescence emission can occur, the  $S_1$  state of HTIs Z1-Z4 has been fully optimized at LR-CC2/cc-pVDZ and TD-CAM-B3LYP/cc-pVDZ levels of theory simulating gas phase. The stationary points obtained at TD-CAM-B3LYP level of theory have been confirmed as local

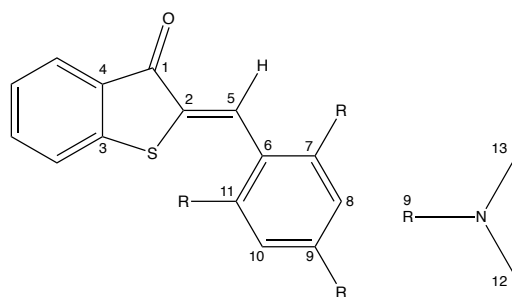


FIGURE 7.4: Skeleton structure of the HTI core and numbering of the atoms.

minima on the PES by frequency analysis performed at the same level of theory showing no imaginary frequencies.

To verify the existence of TICT minima, first constrained geometry optimizations of the  $S_1$  state of HTIs Z1-Z3 have been performed at TD-CAM-B3LYP/cc-pVDZ level of theory simulating gas phase. For this purpose,  $\beta(C2-C5-C6-C7)$  (see Fig. 7.5, 7.4) of HTIs Z1 and Z2 has been set to  $90^\circ$  and  $\beta(C2-C5-C6-C11)$  of HTI Z3 to  $-90^\circ$  and kept fixed during the geometry optimization. Subsequently, firstly the obtained  $90^\circ$  twisted  $S_1$  (TICT) stationary structures have been fully reoptimized at TD-CAM-B3LYP/cc-pVDZ level of theory, simulating gas phase. Secondly, full  $S_1$  geometry optimizations of those stationary structures have been performed at TD-CAM-B3LYP/LR-C-PCM/cc-pVDZ level of theory using the parameters of DMSO for the solvent model.

Furthermore, first test calculations with explicit solvent molecules have been carried out to examine the relevance of hydrogen bond interactions for TICT state formation. For this purpose solvents being able to act as both hydrogen bond acceptor and donor have been chosen. For HTI Z1, on the one hand, the fully optimized  $S_1$  equilibrium geometry ( $S_{1\text{Min}}$ ) ( $\beta \approx 40^\circ$ ) has been used incorporating two DMSO molecules. The DMSO molecules have been placed close to the carbonyl oxygen atom and the central double bond. On the other hand,  $\beta$  of  $S_{1\text{Min}}$  has been set to  $80^\circ$  and two DMSO molecules have been incorporated analogously. These two HTI Z1 DMSO cluster structures have been fully optimized in the  $S_1$  state at the TD-CAM-B3LYP/6-31G\* level of theory. For HTI Z3, firstly, the  $S_1$  state has been fully optimized starting from the gas phase MP2  $S_0$  equilibrium geometry incorporating six  $H_2O$  molecules which are positioned close to the oxygen, sulfur and dimethylamino (DMA) group using the TD-CAM-B3LYP/6-31G\* level of theory. Secondly, the thus obtained  $S_1$  state geometry has been taken and a constrained geometry optimization with  $\beta = -90^\circ$  has been performed at the same level of theory. Thirdly, a full geometry optimization has been carried out at the previously obtained twisted geometry of

the HTI Z3 H<sub>2</sub>O cluster.

Additionally, a relaxed S<sub>1</sub> PES scan along  $\beta$  has been performed at TD-CAM-B3LYP/6-31G\* level of theory. For this purpose  $\beta$  of HTI Z1 and Z2 has been varied from 0° to 90° in steps of 10°. For HTI Z3,  $\beta$  has been varied from 0° to -90°. While at each scan point  $\beta$  was kept fixed all other coordinates were relaxed. Vertical excitation energies of the few energetically lowest singlet (and triplet) excited states have been recomputed at the constrained-optimized geometries along the scan using the TD-CAM-B3LYP/cc-pVDZ level. Furthermore, vertical excitation energies of the S<sub>1</sub> state have been computed at the geometry with  $\beta=90^\circ$  employing the SOS-ADC(2)/SS-C-PCM/VDZ level of theory. Depending on the HTI derivative and respective experimental findings concerning dual fluorescence emission, different solvent parameters have been used, varying from DCM to DMSO.

The T<sub>1</sub> state of HTIs Z1-Z4 has been optimized at LR-CC2/cc-pVDZ level of theory. All ADC(2) and SF calculations have been performed with the Q-Chem program versions 4.4 and 5.0. For LR-CC2 calculations TURBOMOLE V 6.3 has been used and for MP2 and TD-CAM-B3LYP calculations the programs Q-Chem 4.4 and 5.0 and Gaussian 09 Rev. D01. Molecular orbitals and attachment and detachment densities have been visualized using Avogadro and VMD.

## 7.3 RESULTS

### 7.3.1 Ground state properties and static absorption spectra

In general the computed gas phase S<sub>0</sub> equilibrium geometries of HTIs Z1-Z4 (see Fig. 7.5 and Fig. C.1, C.2, C.3, C.4) show a good agreement with the crystal structures reported by Wiedbrauk et al.<sup>[245]</sup>, especially concerning the photochemically relevant coordinates like  $\theta$  and  $\beta$ . The computed S<sub>0</sub> equilibrium geometries of HTIs E1-E4 are shown in Figures C.5 and C.6, no experimental data are available for comparison.

Reference HTI derivative Z4 having no bulky substituents in *ortho* positions is almost planar in the ground state. Values for  $\theta_1$  and  $\theta_2$  are -177°(-180°) and 179°(-180°). All values given in parenthesis correspond to crystal structure data. The out-of-plane dihedral angle  $\alpha$ (C2-C1-C3-C5) (numbering see Fig. 7.4) is 1°(-1°) and  $\beta$  is 15° (7°). The DMA group is slightly pyramidalized. In the ground state the Z isomer of HTI 4 is 0.20 eV (4.6  $\frac{\text{kcal}}{\text{mol}}$ ) more stable than the E isomer. HTI Z1 having methyl group substituents in *ortho* positions is more twisted ( $\beta=59^\circ$  (73°)) than

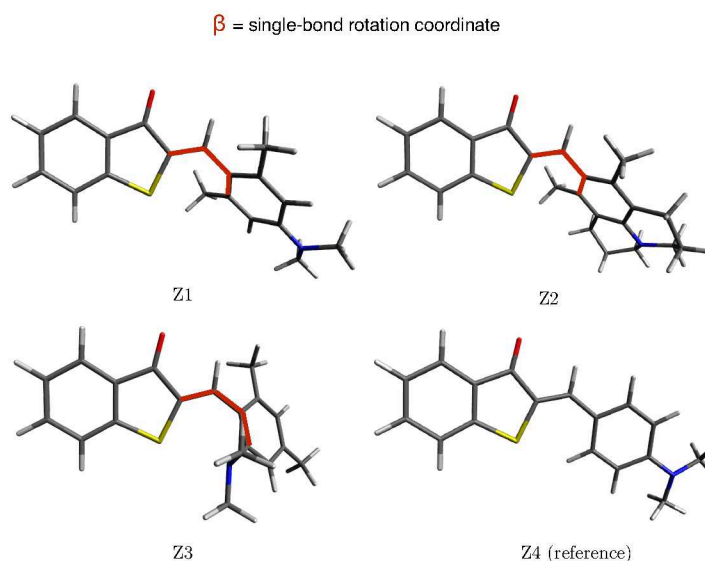


FIGURE 7.5: Local ground state minima nearest to the initial structures of HTIs Z1-Z4 obtained at MP2/cc-pVDZ level of theory. The twisting coordinate  $\beta$  is indicated in red. For Z4 it is assumed that no single-bond rotation resulting in TICT formation occurs, hence, this coordinate is not considered.

HTI Z4 and the central double bond is slightly bent out of the thioindigo plane ( $\alpha = 2^\circ (2^\circ)$ ). In HTI Z, like in HTI Z4, the DMA group is pyramidalized. The MP2 optimized geometry is by  $14^\circ$  less twisted than the crystal structure. The values for  $\theta_1$  and  $\theta_2$  are  $-173^\circ (-175^\circ)$  and  $178^\circ (-177^\circ)$ , respectively. In the ground state HIT Z1 is by  $0.15 \text{ eV}$  ( $3.5 \frac{\text{kcal}}{\text{mol}}$ ) more stable than HTI E1.

HTI Z2 the largest derivative, having no freely rotatable DMA group, has a twist angle of  $62^\circ (60^\circ)$  similar to HTI Z1. The crystal structures of HTIs Z1 and Z2 show a more pronounced difference in  $\beta$ . Like HTI Z1, the double bond is slightly bent out of the thioindigo plane ( $\alpha = 1^\circ (3^\circ)$ ). Dihedral angles  $\theta_1$  and  $\theta_2$  are  $-176^\circ (-173^\circ)$  and  $179^\circ (179^\circ)$ , respectively. HTI Z2 is  $0.16 \text{ eV}$  ( $3.7 \frac{\text{kcal}}{\text{mol}}$ ) more stable than HTI E2.

The  $S_0$  equilibrium geometry of HTI Z3, the derivative having the DMA group substituent in *ortho* position, exhibits the most pronounced out of plane bending of the central double bond with  $\alpha = -4^\circ (-4^\circ)$ . Compared to HTIs Z1 and Z2, HTI Z3 is less twisted in the ground state ( $\beta = -34^\circ (-32^\circ)$ ). The values for  $\theta_1$  and  $\theta_2$  are  $176^\circ (179^\circ)$  and  $-172^\circ (-173^\circ)$ , respectively. The Z isomer of HTI derivative 3 is  $0.01 \text{ eV}$  ( $0.23 \frac{\text{kcal}}{\text{mol}}$ ) more stable than the E isomer. The static dipole moments of HTI Z1-Z4 are moderate with values of 3-4 D. The static dipole moments of HTIs E1-E4 are even smaller ( $< 2 \text{ D}$ ).

Turning to the calculation of the vertical excited states of HTIs Z1-Z4, computed vertical excitation energies, their oscillator strengths ( $f$ ), static dipole moments ( $\mu$ ) and character obtained at ADC(2)/cc-pVDZ, LR-CC2/cc-pVDZ and TD-CAM-B3LYP levels of theory are compiled in Table 7.2. Excitation energies, oscillator strengths and static dipole moments of the respective E isomers computed at the ADC(2)/cc-pVDZ level of theory are summarized in Table C.1.

Vertical excitation energies of the lowest four excited singlet and triplet states obtained at ADC(2)

TABLE 7.2: Comparison of the gas-phase vertical excitation energies and static dipole moments of the few lowest singlet and triplet states of HTIs Z1-Z4 calculated at the FC geometry. Orbital transitions ( $> 20\%$ )<sup>a</sup>, character of the transition, vertical excitation energies  $\omega$  (in eV), oscillator strengths (in parenthesis) and relaxed static dipole moments  $\mu$  (in Debye) are given.

State	MOs	Character	ADC(2)		LR-CC2		TD-CAM-B3LYP	
			$\omega$	$\mu$	$\omega$	$\mu$	$\omega$	$\mu$
Z1								
T <sub>1</sub>	H > L	$\pi\pi^*$ (CT)	2.56	6.6	2.60	6.4	2.10	4.90
	H-1 > L	$\pi\pi^*$ (Thioindigo)						
T <sub>2</sub>	H-6 > L	$n\pi^*$	3.00	1.3	3.18	3.2	2.97	4.37
S <sub>1</sub>	H > L	$\pi\pi^*$ (CT)	3.14(0.19)	8.2	3.23(0.34)	11.2	3.38(0.31)	8.3
	H-6 > L	$n\pi^*$						
S <sub>2</sub>	H-6 > L	$n\pi^*$	3.33(0.14)	4.1	3.49(0.03)	2.8	3.60(0.04)	2.6
	H > L	$\pi\pi^*$ (CT)						
Z2								
T <sub>1</sub>	H > L	$\pi\pi^*$ (CT)	2.57	7.2	2.60	6.9	2.11	4.8
	H-1 > L	$\pi\pi^*$ (Thioindigo)						
T <sub>2</sub>	H-6 > L	$n\pi^*$	2.98	2.0	3.14	5.4	2.93	4.9
S <sub>1</sub>	H > L	$\pi\pi^*$ (CT)	3.09(0.19)	12.9	3.15(0.29)	15.0	3.36(0.26)	9.8
S <sub>2</sub>	H-6 > L	$n\pi^*$	3.33(0.10)	3.9	3.49(0.04)	3.3	3.59(0.05)	2.9
	H-1 > L	$\pi\pi^*$ (Thioindigo)						
Z3								
T <sub>1</sub>	H > L	$\pi\pi^*$ (CT)	2.40	4.5	2.44	4.3	1.88	3.9
T <sub>2</sub>	H-1 > L		3.01	0.8	3.20	5.6	2.91	3.6
	H-6 > L	$n\pi^*$						
S <sub>1</sub>	H > L	$\pi\pi^*$ (CT)	3.12(0.15)	3.1	3.23(0.25)	4.6	3.33(0.29)	4.7
	H-6 > L	$n\pi^*$						
S <sub>2</sub>	H-1 > L	$\pi\pi^*$ (CT')	3.26(0.10)	10.8	3.29(0.06)	10.1	3.58(0.07)	6.2
	H > L	$\pi\pi^*$ (CT)						
Z4								
T <sub>1</sub>	H > L	$\pi\pi^*$	2.32	7.2	2.35	<sup>-b</sup>	1.80	5.6
T <sub>2</sub>	H-5 > L	$n\pi^*$	3.03	1.3	3.24	<sup>-b</sup>	2.98	4.4
T <sub>3</sub>	H-1 > L	$\pi\pi^*$	3.44	7.9	3.45	<sup>-b</sup>	3.14	2.1
S <sub>1</sub>	H > L	$\pi\pi^*$	3.10(0.64)	11.2	3.17(0.73)	10.9	3.31(0.66)	7.9
S <sub>2</sub>	H-5 > L	$n\pi^*$	3.26(0.01)	1.2	3.49(0.00)	2.7	3.60(0.00)	2.4

<sup>a</sup> For the sake of compactness only the two leading configurations are given.

<sup>b</sup> At the time of writing calculations of relaxed properties were not yet finished.

and LR-CC2 levels of theory agree well among one another (see Table 7.2). Vertical excitation

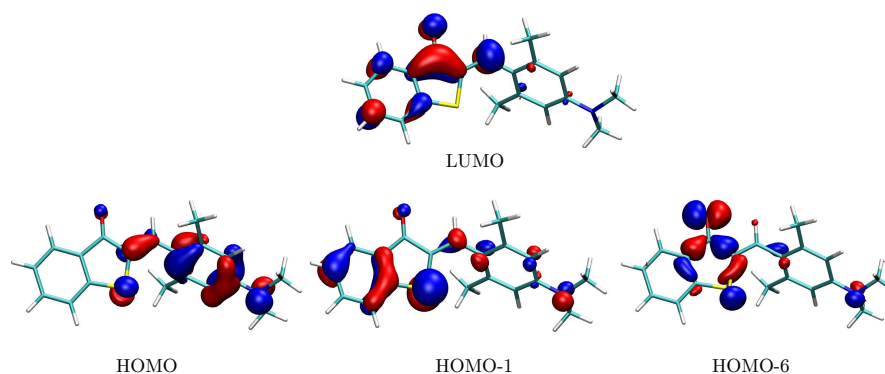


FIGURE 7.6: Valence molecular orbitals of HTI Z1 computed at ADC(2)/cc-pVDZ level of theory (Isovalue = 0.05).

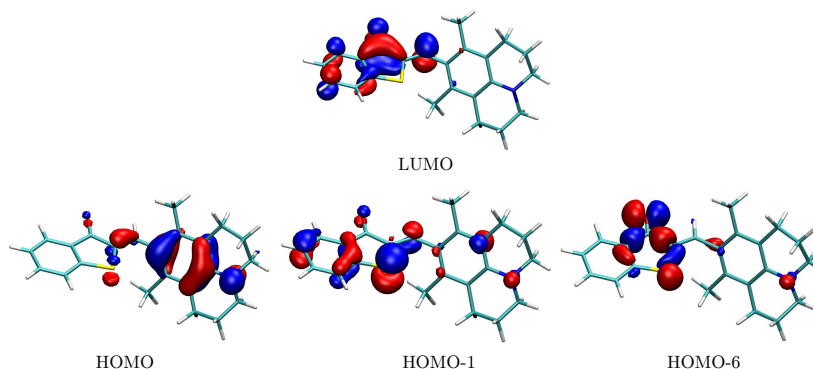


FIGURE 7.7: Valence molecular orbitals of HTI Z2 computed at ADC(2)/cc-pVDZ level of theory (Isovalue = 0.05).

energies of  $S_1$  and  $S_2$  obtained at the TD-CAM-B3LYP/cc-pVDZ level of theory are slightly overestimated with respect to the ADC(2)/cc-pVDZ level. For the  $S_1$  state the maximum deviation is 0.27 eV. The corresponding deviation in the excitation energies of the  $S_2$  state amounts to 0.34 eV. The  $T_1$  states computed using TD-CAM-B3LYP level of theory are strongly underestimated with respect to ADC(2). For the  $T_2$  state the agreement between TDDFT and ADC(2) is very good.

For all four HTI derivatives of both Z and E isomers, the lowest excited singlet state  $S_1$  is an optically allowed  $\pi\pi^*$  state with a slight CT character exhibiting an oscillator strength of  $> 0.15$ . The  $S_1$  state is represented by a transition from the HOMO to the LUMO (see Fig. 7.6, 7.7, 7.8, 7.9). While the HOMO has bonding character along the central C2-C5 double bond, the LUMO has a node along this bond. Hence, excitation to the  $S_1$  state weakens this double bond. Static dipole moments of the  $S_1$  state of both isomers of HTIs 1, 2 and 4 are significantly larger than in the  $S_0$  state, having values of  $\approx 8$ -13 D at ADC(2)/cc-pVDZ level of theory. In the case of HTI 3, the Z isomer has a comparably small static dipole moment of about 3 D, while the E isomer

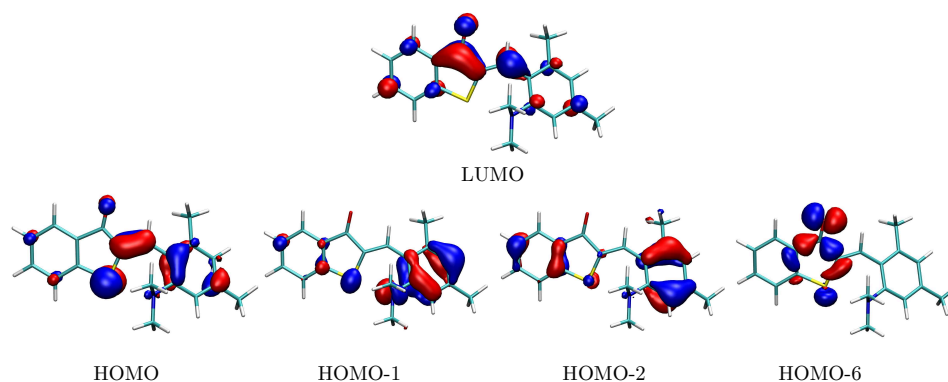


FIGURE 7.8: Valence molecular orbitals of HTI Z3 computed at ADC(2)/cc-pVDZ level of theory (Isovalue = 0.05).

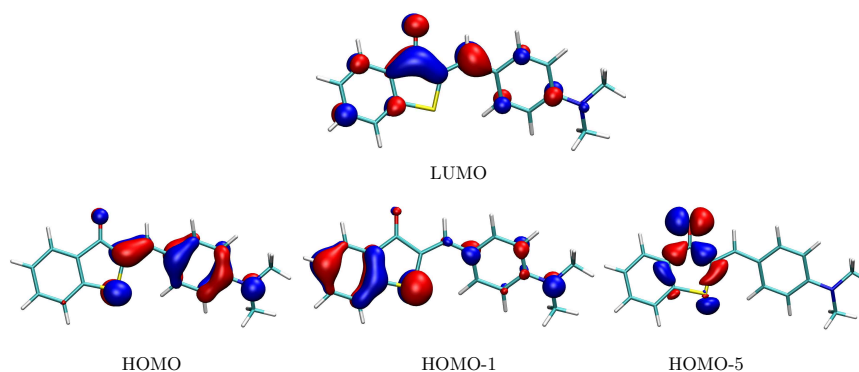


FIGURE 7.9: Valence molecular orbitals of HTI Z4 computed at ADC(2)/cc-pVDZ level of theory (Isovalue = 0.05).

exhibits a relative large one of about 8 D, like the other E isomers. This state can be assigned to the intense absorption bands observed at about 2.82 eV (440 nm) in CH solutions<sup>[245]</sup>. The absorption spectra of the E isomers of HTI 1-4 are similar to the ones of the Z isomers, however, are slightly red-shifted by about 30-80 nm with respect to the absorption spectra of the Z isomers. The  $S_2$  state of HTIs Z1-Z4 (and E1-E3) is a  $n\pi^*$  state with little oscillator strength ranging from 0.01 up to 0.14, where the  $n$ -orbital is a lone pair of the carbonyl oxygen. This state is described primarily by a HOMO-6 to LUMO excitation. Except for Z3, corresponding static dipole moments are small (1-4 D). This state can be assigned to the shoulder observed at shorter wavelengths.<sup>[245]</sup> The lowest lying triplet states,  $T_1$  (HOMO  $\rightarrow$  LUMO) and  $T_1$  (HOMO-6  $\rightarrow$  LUMO) can be considered as the twin state of  $S_1$  and  $S_2$ .

Energy gaps ( $\Delta E(S,T)$ ) between  $S_1$  and  $T_2$  states of HTIs Z1-Z4 at the FC geometry are strikingly small having values of 0.14, 0.11, 0.12 and 0.07 eV, respectively, at the ADC(2)/cc-pVDZ level of theory. SOC constants for the  $S_1$ - $T_2$  transitions of HTIs Z1-Z4 are 18.57  $\text{cm}^{-1}$ , 16.71  $\text{cm}^{-1}$ , 20.88  $\text{cm}^{-1}$ , 23.65  $\text{cm}^{-1}$ , respectively, suggesting a moderate SOC coupling at the FC geometry.

TABLE 7.3: Comparison of computed absorption energies of the lowest excited singlet states of HTIs Z1-Z4 obtained ADC(2)/cc-pVDZ/ptSS-PCM levels of theory with experimental stationary absorption spectra<sup>[245]</sup> recorded in different solvents. Solvent-corrected vertical excitation energies  $\omega_{\text{sol}}$  (in eV) and wavelengths of the absorption bands  $\lambda$  (in nm) reported by Wiedbrauk et al.<sup>[245]</sup> and deviation of computed energies from experimental ones  $\Delta\omega$  (in eV) are given.

State	CH			THF			DCM			ACN			DMSO		
	$\omega_{\text{sol}}$	$\lambda$	$\Delta\omega$												
Z1															
S <sub>1</sub>	3.04	2.91	0.13	2.97	2.72	0.25	2.76	2.72	0.04	2.95	2.72	0.23	2.93	2.64	0.29
Z2															
S <sub>1</sub>	2.87	2.72	0.15	2.76	2.63	0.13	2.75	2.58	0.22	2.75	2.58	0.22	2.69	2.53	0.16
Z3															
S <sub>1</sub>	3.09	2.92	0.17	3.08 <sup>a</sup>	2.88	0.20	3.08 <sup>a</sup>	2.88	0.20	3.08 <sup>a</sup>	2.88	0.20	3.07 <sup>a</sup>	2.82	0.25
S <sub>4</sub>	4.21	3.87	0.34	4.17	3.76	0.41	4.16	3.81	0.35	4.15	3.76	0.39	4.14	3.76	0.38
Z4															
S <sub>1</sub>	2.97	2.70	0.27	2.88	2.64	0.24	2.87	2.58	0.27	2.85	2.58	0.27	2.83	2.53	0.30
S <sub>4</sub>	3.71	3.35	0.36	3.64	3.26	0.38	3.64	3.26	0.38	3.62	3.26	0.36	3.61	3.18	0.43

<sup>a</sup>  $\omega$  corresponds to the S<sub>2</sub> state. In THF, DCM, ACN and DMSO the bright states S<sub>1</sub> and S<sub>2</sub> are interchanged.

The energy gaps between S<sub>1</sub> and T<sub>1</sub> states are distinctly larger being 0.58 eV, 0.51 eV and 0.72 eV for HTIs Z1-Z3. The one for Z4 is larger than 0.80 eV and will thus not be considered here. Respective SOC constants for the corresponding S<sub>1</sub>-T<sub>1</sub> transitions are 17.13 cm<sup>-1</sup>, 13.67 cm<sup>-1</sup> and 14.54 cm<sup>-1</sup>. These results suggest that ISC from S<sub>1</sub> into the triplet manifold may occur. Stationary absorption spectra of reference HTI Z4 in different solvents show two absorption bands, a very intense one at longer wavelength and a low-intensity one at shorter wavelengths. The long-wavelength band is located at about 2.70 eV (460 nm), 2.64 eV (470 nm), 2.58 eV (480 nm), 2.58 eV (480 nm) and 2.53 eV (490 nm) in CH, THF, DCM, ACN and DMSO, respectively.<sup>[245]</sup> The blue-shifted band was found at about 3.35 eV (370 nm), 3.26 eV (380 nm), 3.26 eV (380 nm), 3.26 eV (380 nm) and 3.18 eV (390 nm) in CH, THF, DCM, ACN and DMSO, respectively. There is a trend between solvent polarity and solvatochromic shift of the absorption maxima. The smallest bathochromic shift is observed for apolar CH and the strongest one for very polar DMSO. This shift, however, is small ( $\approx$  10 nm). The agreement between computed excitation energies and the experimental values for the intense longer wavelength band are fairly good showing a maximal deviation of 0.30 eV (see Table 7.3). The agreement between computed energies and experimental values for the low-intensity band is only fairly good. The strongest deviation of 0.43 eV has been found for the parameters of DMSO. Still, the solvatochromic shift is well reproduced. This is in line with what one would expect from continuum solvation model calculations, since those mainly describe electrostatic interactions while hydrogen bonding

interactions are neglected.

Stationary absorption spectra of HTI Z1 in different solvents exhibit one broad intensive absorption peak. The bands are located at about 2.91 eV (425 nm), 2.81 eV (440 nm), 2.72 eV (455 nm), 2.72 eV (455 nm) and 2.64 eV (470 nm) in CH, DCM, THF, ACN and DMSO, respectively.<sup>[245]</sup>

There is, at least to some extent, a trend between solvent polarity and solvatochromic shift of absorption maxima. Like for HTI Z4, the smallest bathochromic shift is observed for apolar CH and the strongest one for very polar DMSO. However, even though the polarity of THF and ACN differs significantly, they show the same shift. In contrast to DCM, they are both hydrogen bond acceptors, which might be a possible explanation for this observation. If one would consider solvent polarity alone to explain the bathochromic shift of the absorption spectrum (meaning mainly the dielectric constant) one would expect the band in DCM to be stronger red-shifted than in THF, which is not the case. Thus, besides solvents polarity, also other properties seem to be responsible for the solvatochromic shift. Computed energies are in fairly good agreement with the experimental ones showing a maximal deviation of 0.29 eV (see Table 7.3). The smallest errors are found for apolar CH and medium polar DCM both having no hydrogen bonding abilities.

Like for HTI Z1, stationary absorption spectra of HTI Z2 in CH, THF, DCM, ACN and DMSO solution show one broad absorption. The corresponding bands were observed at about 2.72 eV (455 nm), 2.63 eV (470 nm), 2.58 eV (480 nm), 2.58 eV (480 nm) and 2.53 eV (490 nm), respectively.<sup>[245]</sup> The agreement between computed and experimental energies of HTI Z2 is good. The maximal deviation from the experimental values is 0.22 eV (see Table 7.3).

Stationary absorption spectra of HTI Z3 present two absorption bands having almost equal intensity. The long wavelength bands have been found at about 2.92 eV (425 nm), 2.88 eV (430 nm), 2.88 eV (430 nm), 2.88 eV (430 nm) and 2.82 eV (440 nm), in CH, THF, DCM, ACN and DMSO, respectively.<sup>[245]</sup> The short wavelength band were found at about 3.87 eV (320 nm), 3.76 eV (330 nm), 3.81 eV (325 nm), 3.76 eV (330 nm), 3.65 eV (340 nm) in CH, THF, DCM, ACN and DMSO, respectively. Computed vertical excitation energies of the  $S_1$  state are in good agreement with the experimental absorption energies of the longer wavelength band showing a maximal deviation of 0.25 eV (see Table 7.3). In contrast, the deviation between computed vertical excitation energies of the  $S_4$  state and the experimental absorption energies of the short wavelength band are comparably large. The largest deviation of 0.41 eV has been found for the parameters of THF (see Table 7.3).

### 7.3.2 Excited state properties and fluorescence spectra of HTIs Z1-Z4

Stationary and transient fluorescence experiments<sup>[245]</sup> of HTIs Z1-Z4 suggest the existence of two different  $S_1$  state minima in medium polar and polar solvents; one of which being more polar than the other one and structurally distinctly different. To gain a better understanding of the different fluorescence behavior of HTIs Z1-Z4 the bright  $S_1$  ( $\pi\pi^*$  (CT)) states have been optimized starting from two different geometries. Full geometry optimizations of the  $S_1$  states of HTIs Z1-Z4 performed at the LR-CC2/cc-pVDZ and TD-CAM-B3LYP/cc-pVDZ levels of theory, respectively, yield four local  $S_1$  minima ( $S_{1\text{Min}}$ ) (see Figures 7.10, 7.11, 7.12, 7.13). In general, the equilibrium geometries obtained at both levels of theory are very similar concerning bond lengths and the relevant coordinates like  $\beta$ ,  $\alpha$  and  $\theta$ . From these minima, fluorescence emission may occur. The  $S_{1\text{Min}}$  geometries are very similar to the respective FC geometries (see Fig. C.1, C.2, C.3, C.4). In HTIs Z2 and Z4  $\beta$  is decreased by about  $4^\circ$  in the  $S_{1\text{Min}}$  structure compared to the FC geometry. The deviation of  $\beta$  in the TD-CAM-B3LYP optimized  $S_{1\text{Min}}$  geometry of HTI Z2 is distinctly more pronounced. Here,  $\beta$  is  $80^\circ$ , meaning increased by almost  $20^\circ$  with respect to the FC geometry ( $\beta=62^\circ$ ). In HTIs Z1 and Z3  $\beta$  is decreased by about  $11^\circ$ . Furthermore, the central double bond is elongated by 0.04 - 0.05 Å in the excited state geometries with respect to the ground state structures. This can be explained by the additional node of the LUMO at that double bond (see Fig. 7.6, 7.7, 7.8, 7.9), since an electron is excited to  $S_1$  from the HOMO to the LUMO, resulting in a weakening of the bond. This facilitates isomerization from Z to E on the  $S_1$  state PES. To obtain emission energies which can be compared to experimental fluorescence wavelengths, vertical excitation energies of the  $S_1$  state of HTIs Z1, Z2, Z3 and Z4 have been computed at the respective  $S_{1\text{Min}}$  geometries using the SOS-ADC(2)/VDZ/SS-C-PCM level of theory together with the parameters of CH, THF, DCM, ACN and DMSO, respectively. Due to the experimental observed strong solvatochromism and dual emission, vertical excitation energies of the  $S_1$  state of HTIs Z1-Z3 have also been computed at TICT geometries ( $\beta=90^\circ$ ). In stationary fluorescence experiments of reference derivative Z4 solutions narrow emission bands were observed at about 2.58 eV (480 nm), 2.32 eV (535 nm), 2.25 eV (550 nm), 2.18 eV (570 nm) and 2.14 eV (580 nm), respectively, in CH, THF, DCM, ACN and DMSO solution.<sup>[245]</sup> Computed emission energies are 2.75 eV, 2.38 eV, 2.25 eV, 2.23 eV and 2.24 eV for the parameters of CH, THF, DCM, ACN and DMSO, respectively. With increasing solvent polarity the vertical excitation energy is slightly down shifted. The bathochromic shift can be explained by the relative

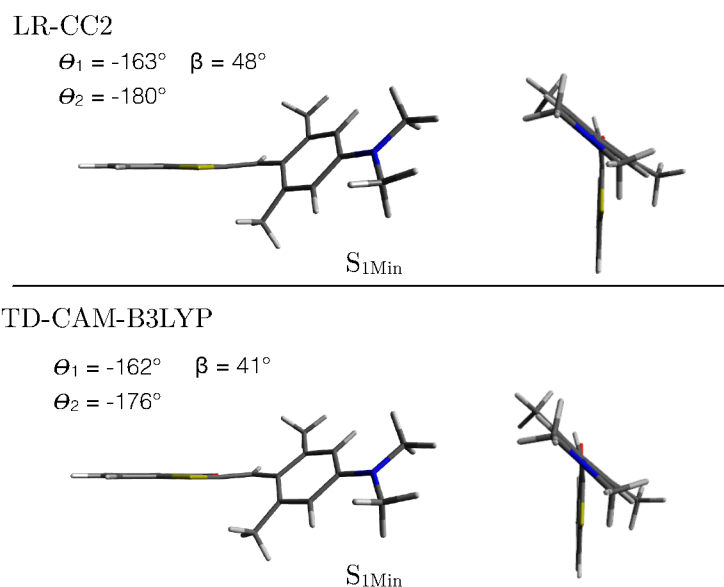


FIGURE 7.10: Local  $S_1$  state minimum geometries of HTI Z1 obtained at LR-CC2/cc-pVDZ and TD-CAM-B3LYP/cc-pVDZ levels of theory, respectively (shown from two different views).

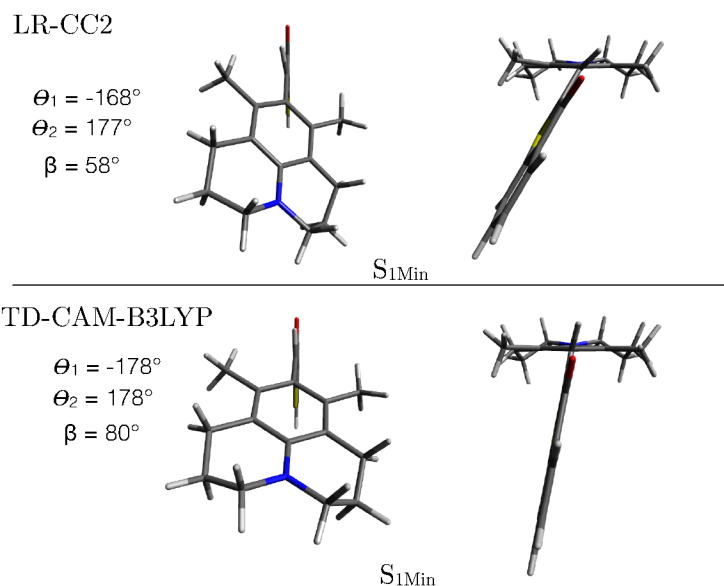


FIGURE 7.11: Local  $S_1$  state minimum geometries of HTI Z1 obtained at LR-CC2/cc-pVDZ and TD-CAM-B3LYP/cc-pVDZ levels of theory, respectively (shown from two different views). The TD-CAM-B3LYP structure, in contrast to the LR-CC2 one, has a planar benzene ring and the out-of-plane bending of the central double bond out of the thioindigo plane is  $8^\circ$  smaller.

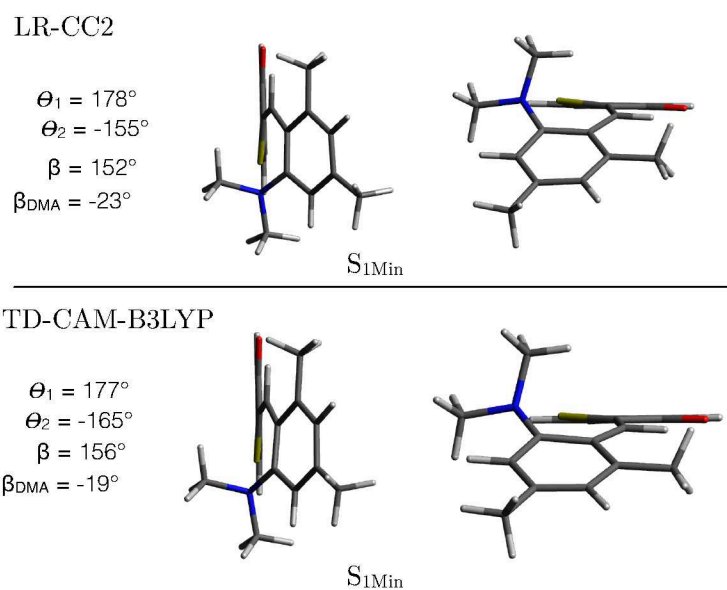


FIGURE 7.12: Local  $S_1$  state minimum geometries of HTI Z3 obtained at LR-CC2/cc-pVDZ and TD-CAM-B3LYP/cc-pVDZ levels of theory, respectively (shown from two different views).

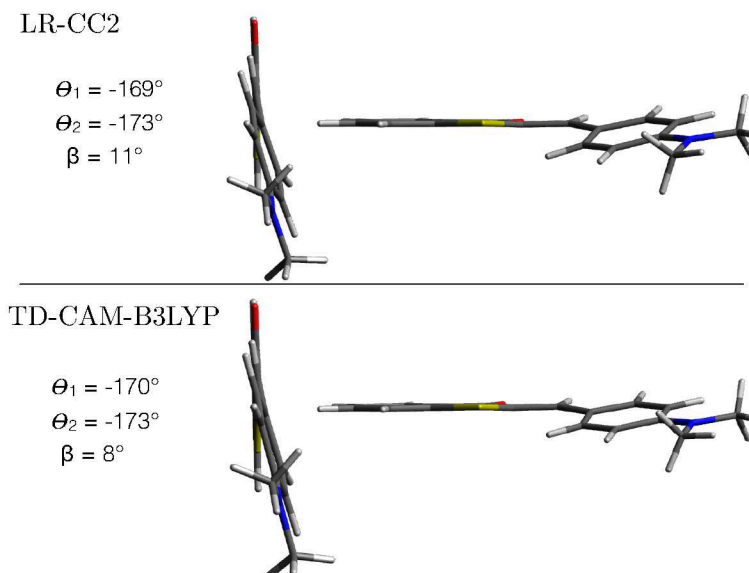


FIGURE 7.13: Local  $S_1$  state minimum geometries of HTI Z4 obtained at LR-CC2/cc-pVDZ and TD-CAM-B3LYP/cc-pVDZ levels of theory, respectively (shown from two different views).

large static dipole of the  $S_1$  state being  $> 18$  D, for all employed solvent parameters. Computed and experimental emission energies are in very good agreement with a maximal deviation of only 0.17 eV. The computed emission energies are slightly overestimated with respect to the experimental ones.

Emission spectra of HTI Z1 in THF and DCM solutions show one broad red-shifted emission band with maxima at about 2.02 eV (615 nm) and 1.84 eV (670), respectively.<sup>[245]</sup> The emission spectra in ACN and DMSO solution show two emission bands, a short wavelength and a strongly red-shifted one, having similar intensities. The short wavelength bands are located at about 2.25 eV (550 nm) and 2.10 eV (590 nm), respectively and the red-shifted ones at about 1.61 eV (770 nm) and 1.68 eV (740 nm), respectively.<sup>[245]</sup> The emission band in CH solution is observed at about 2.48 eV (500 nm). Computed emission energies of the  $S_1$  state of HTI Z1 obtained at the  $S_{1\text{Min}}$  geometry are 2.72 eV, 2.01 eV and 2.04 eV, respectively, for the parameters of CH, ACN and DMSO. They show a fairly good agreement with the energies of the short wavelength bands. For CH the computed emission energy is overestimated by 0.24 eV with respect to the experiment. For ACN and DMSO the computed emission energies are underestimated by 0.24 and 0.06 eV with respect to the energies of the short wavelength band. Computed emission energy computed at the constrained-optimized  $\beta=90^\circ$  geometry obtained along the  $S_1$  PES scan of  $\beta$  (see Fig. C.13) are 1.81 eV, 1.75 eV, 1.36 eV and 1.45 eV for the parameters of THF, DCM, ACN and DMSO which is in good agreement with the emission energies of the red-shifted bands. The largest error of 0.25 eV has been found for the parameters of ACN. These results indicate TICT state formation of HTI Z1 in medium polar and polar solvents, in line with the hypothesis of Wiedbrauk et al.<sup>[245]</sup>

For HTI Z2, emission spectra<sup>[245]</sup> recorded in DCM and DMSO show two emission bands. The short wavelength bands were found at about 2.13 eV (580 nm) and 2.00 eV (620 nm), respectively in DCM and DMSO. The corresponding red-shifted bands were found at about 1.60 eV (775 nm) and 1.65 eV (750 nm). Emission spectra in CH and THF solutions present only one emission band. In THF a strong bathochromic shift of the emission band was observed. This experimental finding suggests that this red-shifted band results from emission from a different  $S_1$  minimum. The band in CH solution has been found at about 2.43 eV (510 nm). In THF the emission band was observed at about 1.72 eV (720 nm). Computed emission energies obtained at the  $S_{1\text{Min}}$  geometry are 2.64 eV, 1.52 eV and 1.24 eV for the parameters of CH, DCM and DMSO, respectively. The emission energy obtained using the parameters of CH is in fairly good agreement with the

experimental value. However, emission energies obtained using the parameters of DCM and DMSO are severely underestimated by  $> 0.60$  eV with respect to experimental values. The emission energies obtained at the constrained-optimized  $\beta=90^\circ$  geometry are 1.57 eV, 1.51 eV and 1.23 eV, respectively, for the parameters of THF, DCM and DMSO. While the error in the computed emission energies for the parameters of THF and DCM are relatively small being 0.15 eV and 0.09 eV, respectively. The deviation between the computed emission energy using the parameters of DMSO and the energy of the red-shifted emission band found in DMSO is large. The computed energy is underestimated by 0.42 eV. These results suggest, that the local  $S_{1\text{Min}}$  minimum ( $\beta=80^\circ$ ) as predicted by TD-CAM-B3LYP/cc-pVDZ deviates structurally from the experimentally observed one. It seems like TD-CAM-B3LYP overestimates the twist angle of HTI Z2 in the excited state. The results further suggest TICT state formation of HTI Z2 in medium polar and polar solution resulting in either red-shifted emission or dual fluorescence, in line with experimental findings by Wiedbrauk et al.<sup>[245]</sup>.

Emission spectra of HTI Z3 in THF and ACN show broad red-shifted emission bands with maxima at about 1.91 eV (650 nm) and 1.73 eV (715 nm), respectively. The spectrum in DMSO presents two emission bands, similar to HTIs Z1 and Z2. The corresponding bands were found at about 2.48 eV (500 nm) and 1.72 eV (720 nm). The single emission bands observed in CH and DCM solutions were found at about 2.41 eV (515 nm) and 2.07 (600 nm), respectively. Computed emission energies of the  $S_1$  state of HTI Z3 obtained at the  $S_{1\text{Min}}$  geometry are 2.60 eV, 2.28 eV and 2.18 eV, respectively, for the parameters of CH, DCM and DMSO. While the computed emission energies are overestimated by 0.21 eV for CH and DCM it is underestimated by 0.30 eV for DMSO. SS-C-PCM calculations at the constrained-optimized  $\beta=90^\circ$  geometry were not yet converged at the time writing.

### 7.3.3 Mechanism of the Z/E photoisomerization of HTIs Z1-Z4

To study the Z/E isomerization of HTIs Z1-Z4 initiated upon photoexcitation into the  $S_1$  state, relaxed PES scans of the respective  $S_0$  and the  $S_1$  states along  $\theta$  have been performed at the SF-B5050LYP/6-31G\* level of theory simulating gas phase. In the case of HTI 4 only the range between  $180^\circ$  and  $80^\circ$  has been considered so far.

Besides the minimum at about  $180^\circ$  on the  $S_1$  surface of HTI Z4 (see Fig. 7.14) the presence of two conical intersections (CIs),  $S_1$ - $S_0$  and  $T_1$ - $S_0$  (indicated by the black circles in Fig. C.16)

could be identified both located about  $\theta=90^\circ$ . The  $T_1$ - $S_0$  CI having a total energy of 2.31 eV (relative to the  $S_0$  equilibrium geometry obtained at SF-B5050LYP/6-31G\*) is predicted to lie energetically 0.65 eV below the  $S_1$ - $S_0$  CI which has a total energy of 2.96 eV. To reach the

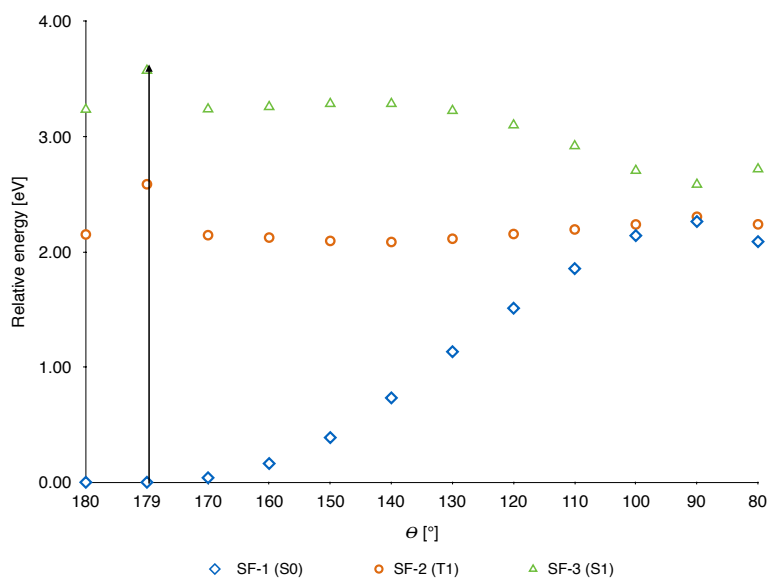


FIGURE 7.14: Relaxed scan of the  $S_1$  PES of HTI 4 for the Z/E isomerization obtained at SF-B5050LYP/6-31G\* level of theory. Energies are relative to the  $S_0$  equilibrium energy at  $\theta=180^\circ$ .

$S_1$ - $S_0$  CI excited HTI Z4 has to overcome a small barrier of only 0.05 eV. The  $S_1$  state at the FC geometry (indicated by the black arrow in Fig. C.16) lies energetically above the barrier and the initial energy is in principle sufficient to overcome it. From the relaxed PES scan it can be inferred that after photoexcitation to the  $S_1$  state HTI Z4 relaxes rapidly to the nearby local  $S_{1\text{Min}}$  minimum. This fast process can be assigned to the short decay component of 0.9 ps measured in CH solution.<sup>[245]</sup> From  $S_{1\text{Min}}$  either fluorescence emission or Z/E isomerization may occur. For these two competing processes time constants of 4.8 ps have been suggested.<sup>[245]</sup> This relatively short decay constant for Z/E isomerization can be explained with the small barrier of only 0.05 eV present along the isomerization coordinate  $\theta$ . The SF-B5050LYP results suggest that Z/E isomerization may either proceed through a  $S_1$ - $S_0$  CI or a  $T_1$ / $S_0$  CI. This result is in line with transient absorption measurements in CH which yield an additional decay time constant of 318 ps which can be assigned to relaxation in the  $T_1$  state. Both relaxation processes result in formation of ground state E and Z isomers. Experimentally determined quantum yields for Z/E photoisomerization  $\phi_{Z/E}$  and fluorescence emission ( $\phi_{flu}$ ) are 32% and 0.1% which suggest that deactivation through Z/E isomerization is more efficient than deactivation through fluorescence

emission. Like for HTI Z4, also for HTI Z1 two CIs have been found in the vicinity of  $\theta=90^\circ$  along the relaxed  $S_0$  state PES scan of  $\theta$  (see Fig. C.14). The total energies of  $S_1-S_0$  and  $T_1/S_0$  are 2.67 eV and 2.17 eV (relative to the  $S_0$  equilibrium geometry), respectively. Along the relaxed PES scan of the  $S_1$  state of HTI Z1 (see Fig. 7.15) besides the local minimum at about  $\theta=180^\circ$  two discontinuities have been found at  $\theta=150^\circ$  and  $\theta=140^\circ$ . Since the energy of the geometry

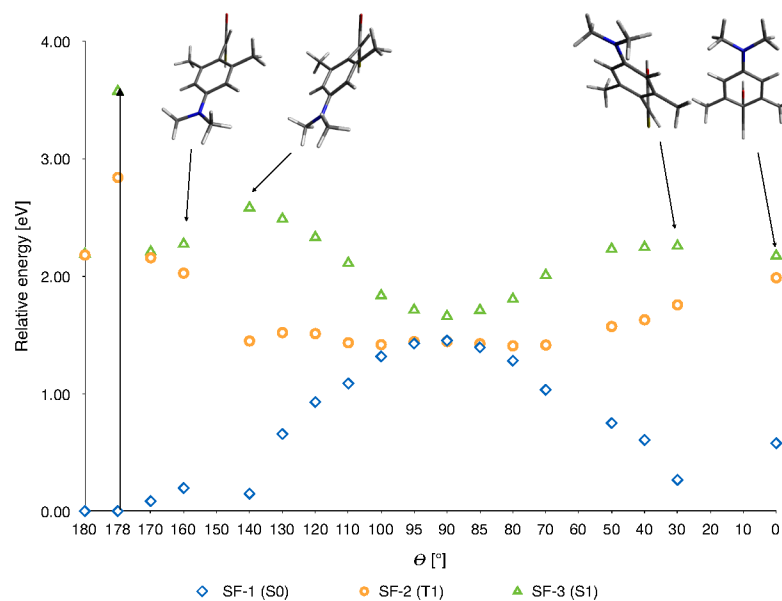


FIGURE 7.15: Relaxed scan of the  $S_1$  PES of HTI 1 for the Z/E isomerization obtained at SF-B5050LYP/6-31G\* level of theory. Energies are relative to the  $S_0$  equilibrium energy at  $\theta=180^\circ$ .

with  $\theta=150^\circ$  deviates significantly from the other ones this scan point has not been included in the graph. At  $\theta=140^\circ$  a pronounced out-of-plane motion of the stilbene benzene ring occurs which causes a strong change in the energy. With the present data it is not possible to compute the energy barrier height for Z/E isomerization in the  $S_1$  state along  $\theta$ . However, the corresponding barrier for rotation from  $\theta=0^\circ$  to  $\theta=30^\circ$  which has to be overcome to reach the CI at about  $\theta=90^\circ$  is 0.08 eV. From the current theoretical data and the experimental results it can be inferred that the barrier height for Z/E isomerization is even smaller. Since, in addition, the energy of  $S_1$  at the FC geometry is about 1 eV higher than the maximum at  $\theta=140^\circ$  and 1.32 eV higher than the maximum at  $\theta=30^\circ$ , it can be assumed that the access energy suffices to overcome the barrier. From these results it can be inferred that after photoexcitation to the  $S_1$  state HTI Z1 rapidly relaxes to the close lying local  $S_{1\text{Min}}$ . One part of the initial excited state population is likely to get trapped in the minimum and fluorescence emission occurs. This process can be assigned to the experimentally determined decay time constant of 16 ps in CH.<sup>[245]</sup> Due to the high initial energy,

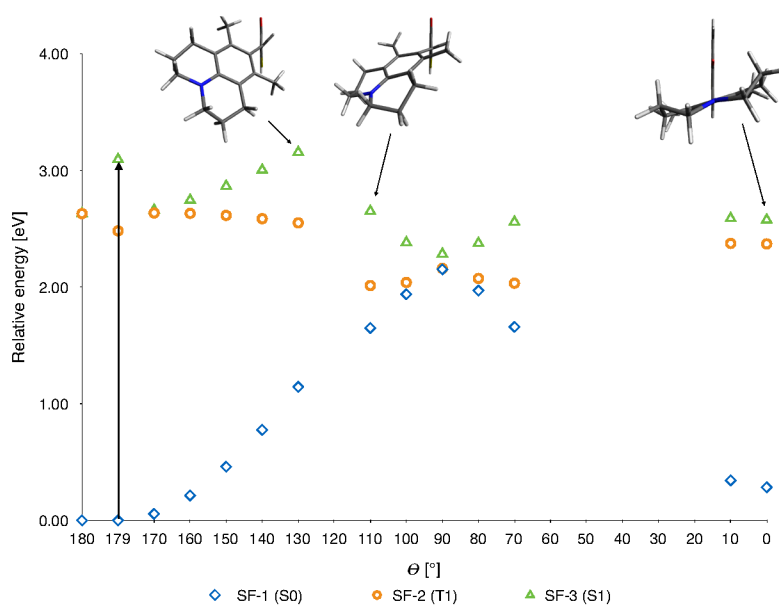


FIGURE 7.16: Relaxed scan of the  $S_1$  PES of HTI 2 for the Z/E isomerization obtained at SF-B5050LYP/6-31G\* level of theory. Energies are relative to the  $S_0$  equilibrium energy at  $\theta=180^\circ$ .

it can be assumed that a large part of the excited state population undergoes efficient and fast Z/E isomerization, which is in agreement with experimental findings<sup>[245]</sup>. These two processes can be assigned to the two decay time constants of 0.8 ps and 1.8 ps, respectively, obtained from time resolved absorption measurements in apolar CH solution.<sup>[245]</sup> SOC calculations predicting small energy gaps between the  $S_1$  and  $T_2$  and  $T_2$  states and moderate coupling constants of  $19\text{ cm}^{-1}$  and  $17\text{ cm}^{-1}$  for the  $S_1$ - $T_2$  and  $S_1$ - $T_1$  transitions, indicate that ISC may play a role as an alternative nonradiative deactivation process. The short decay time constant of only 1.8 ps, however, suggests, that the preferred relaxation pathway is the one via the singlet manifold. Still this result together with the identified  $T_1$ - $S_0$  CI explains the absence of phosphorescence. Quantum yields for Z/E isomerization and fluorescence  $\phi_{Z/E}$  and  $\phi_{fluo}$  for HTI Z1 are reported to be 56% and 0.02%, respectively.<sup>[245]</sup> One explanation for why the experimentally observed Z/E photoisomerization of HTI Z1 in CH solution is more efficient than the one of HTI Z4 could be that the excess energy is higher for HTI Z1 and thus more energy can be funnelled into the reaction coordinate upon photoexcitation.

The two CIs  $S_1$ - $S_0$  and  $T_1$ - $S_0$  identified on the  $S_0$  PES along  $\theta$  (see Fig. C.15) have total energies (relative to the  $S_0$  equilibrium geometry) of 2.73 eV and 2.31 eV, respectively. During the computations of the  $S_1$  PES scan along  $\theta$  (see Fig. 7.16) different convergence problems have been encountered. For this reason there are some scan points missing. Like for HTI Z1, also for

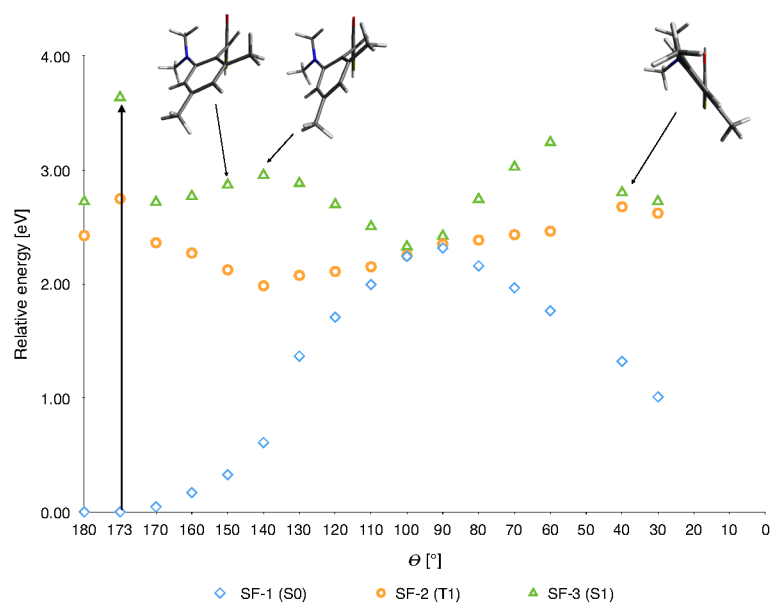


FIGURE 7.17: Relaxed scan of the  $S_1$  PES of HTI 3 for the Z/E isomerization obtained at SF-B5050LYP/6-31G\* level of theory. Energies are relative to the  $S_0$  equilibrium energy at  $\theta=180^\circ$ .

HTI Z2 a discontinuity has been found along the scan at  $\theta=130^\circ$ . In this geometry the julolidine group is planar. When  $\theta$  is  $110^\circ$  the benzene ring of the julolidine group undergoes strong out of plane motions during the geometry optimization which leads to a strong drop of the energy. Eventhough no barrier height can be computed with the current data, the results suggest that the initial energy is sufficient to overcome the barrier on the  $S_1$  state PES such that the  $S_1$ - $S_0$  CI can be reached. Transient absorption experiments of HTI Z2 in CH solution revealed three time constants of 1.2 ps, 17 ps and 381 ps.<sup>[245]</sup> Considering the current computational results, the 1.2 ps component most likely corresponds to relaxation from the FC point to the local  $S_{1Min}$  from which fluorescence emission with a decay constant of 17 ps may occur. The relative long living 381 ps component may be assigned to the decay of the  $T_1$  state which is populated via indirect  $S_1$ - $T_2$  ISC or direct  $S_1$ - $T_1$ . Similar as for HTIs Z1 and Z2, along the  $S_1$  PES scan of  $\theta$  for HTI Z3 (see Fig. 7.17) two discontinuities have been found at  $\theta=150^\circ$  and  $\theta=60^\circ$ . When  $\theta$  is varied from  $\theta=150^\circ$  to  $\theta=140^\circ$  an out of plane distortion of the stilbene benzene ring occurs upon optimization in the  $S_1$  state which leads to a different reaction pathway. Due to the discontinuities it is again not possible to compute a barrier height. At  $\theta=100^\circ$  the energies of  $S_1$ ,  $T_1$  and  $S_0$  are almost degenerate indicating the presence of different CIs. The optimizations of the corresponding  $S_1$ - $S_0$  and  $T_1$ / $S_0$  CIs have been not yet been converged at the time writing. Since, however, the FC  $S_1$  state lies energetically about 0.7 eV above the energy of the  $S_1$  state at  $\theta=140^\circ$  where the energy

of the  $S_1$  state is maximal, it can be assumed as highly likely that the initial energy is sufficient to overcome the barrier along the path from the  $S_1$  state minimum to the  $S_1$ - $S_0$  CI. Considering the current result the photoisomerization of HTI Z3 can be understood as follows. Like in HTIs Z4, Z1 and Z2, upon photoexcitation the excited state population rapidly relaxes to the close lying  $S_{1\text{Min}}$  of HTI Z3. From there a part of the population quickly relax to the  $S_1$ - $S_0$  CI and isomerize into the ground state E isomer. Another fraction populates the triplet manifold via ISC and isomerize via the  $T_1$  state. Some part of the initial excited state population may also get trapped in the  $S_{1\text{Min}}$  minimum and decays back to the ground state via fluorescence emission. These different relaxation processes agree well with experimental decay time constants of 1.5 ps, 6.1 ps, 15 ps, 75 ps and 783 ps in CH solution. Most likely the short components of 1.5 ps, 6.1 ps, 15 ps correspond to rapid relaxation to the  $S_{1\text{Min}}$  minimum, Z/E isomerization and fluorescence emission, respectively. The long 783 ps component can be attributed to the isomerization via the  $T_1$  state. The decay constant of 75 ps may be assigned to a further nonradiative relaxation process which will be discussed further below.

### 7.3.4 TICT formation in HTIs Z1-Z3

Full  $S_1$  state geometry optimization of HTI Z1 at the constrained-optimized geometry with  $\beta=90^\circ$  performed at TD-CAM-B3LYP/cc-pVDZ level in the gas phase yields a TICT stationary structure which will be named TICT geometry in the following. However, subsequent frequency analysis shows the presence of an imaginary frequency of  $-22\text{ cm}^{-1}$ , revealing this TICT stationary structure as a transition state. The corresponding normal mode corresponds to torsion about  $\beta$ . Full reoptimization of the TICT ( $\beta=90^\circ$ ) geometry performed at LR-CC2/cc-pVDZ level of theory yields a  $S_1$  (HOMO-5  $\rightarrow$  LUMO) state stationary structure ( $S_{1\text{Npyr}}$ ) with a slightly pyramidalized DMA nitrogen atom ( $\beta=46^\circ$ ) (see Fig. C.12). This result is in agreement with the relaxed scan of the PES of  $S_1$  along the twisting coordinate  $\beta$  (see Fig. C.13). The  $S_1$  state torsional potential (light green solid line) is very flat showing a minimum at  $\beta=40^\circ$ . However, for twisting to  $\beta=90^\circ$  a tiny barrier of only 0.05 eV has to be overcome. In the gas phase no TICT state minimum has been found neither at TD-CAM-B3LYP nor at LR-CC2 level of theory. Full reoptimization of the TICT geometry performed at TD-CAM-B3LYP/cc-pVDZ/LR-CPCM level of theory using the parameters of DMSO provides a different  $S_1$  stationary structure ( $\beta=30^\circ$ ), however, no TICT minimum. Full geometry optimizations of the  $S_1$  state of two different HTI Z1

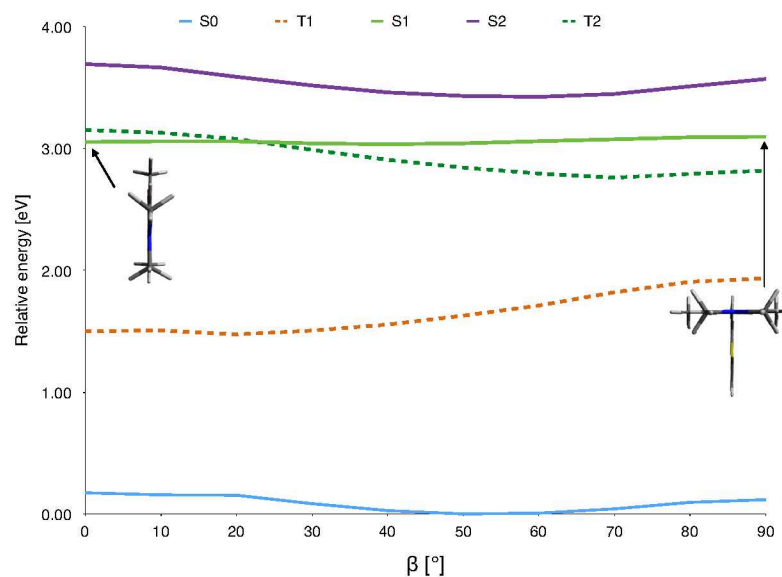


FIGURE 7.18: Relaxed  $S_1$  PES scan of HTI Z1 along  $\beta$  obtained at TD-CAM-B3LYP/6-31G<sup>\*</sup>//TD-CAM-B3LYP/cc-pVDZ level of theory. Energies are relative to the ground state minimum at  $\beta=50^\circ$ .

DMSO cluster geometries yield two slightly different strongly twisted stationary structures (see Fig. C.9) which can be considered as potential TICT minima. The frequency analyses have not yet been converged. Hence, it cannot be said for sure that those geometries are local minima on the  $S_1$  state PES. Both the orientation of the two DMSO molecules with respect to the thioindigo fragment and a mean distance between the four hydrogen atoms of the two DMSO molecules nearest to the oxygen atom and the oxygen atom of 2.3 Å indicate that hydrogen bonding interactions are operative.<sup>[382]</sup> These calculations strongly suggest that in a solvent which is able to form hydrogen bonds with HTI Z1 like DMSO (being both hydrogen bond acceptor and donor) formation of a TICT state may occur.

The gas phase relaxed  $S_1$  PES scan of HTI Z2 along  $\beta$  (see Fig. 7.19) reveals that twisting in the  $S_1$  state exhibits a very shallow potential energy curve. By plotting relative energies a continuous curve for the  $S_1$  state (light green line) is obtained having a minimum at  $\beta=40^\circ$ . For rotation to  $\beta=90^\circ$  a tiny barrier of only 0.005 eV has to be overcome. The total energy curve of the  $S_1$  state (see Fig. C.13) shows a discontinuity at  $\beta=40^\circ$ . A careful analysis of the geometries with  $\beta=40^\circ$  and  $\beta=50^\circ$  indicates that a simultaneous change along the out-of-plane bending mode  $\alpha$  and a change in  $\theta_1$  are responsible for the discontinuity. It seems like a change in these coordinates together with a change in  $\beta$  towards more strongly twisted geometries results in a strong decrease in the total energy of  $S_1$ . While single bond rotation about  $\beta$  alone seems

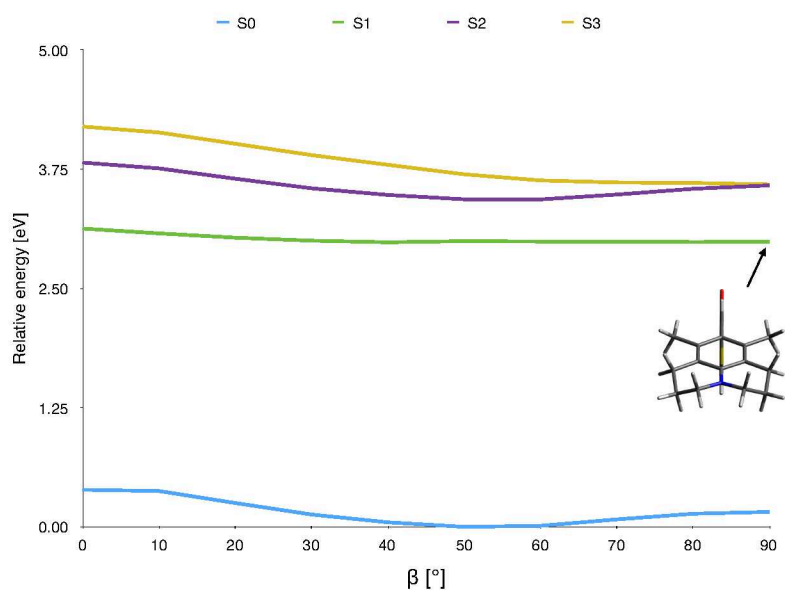


FIGURE 7.19: Relaxed  $S_1$  PES scan of HTI Z2 along  $\beta$  obtained at TD-CAM-B3LYP/6-31G\*//TD-CAM-B3LYP/cc-pVDZ level of theory. Energies are relative to the ground state minimum at  $\beta=50^\circ$ .

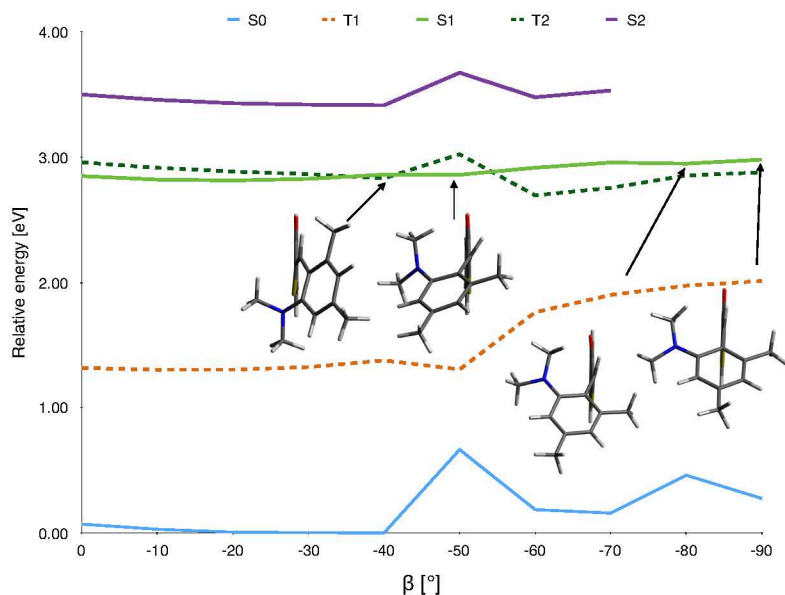


FIGURE 7.20: Relaxed  $S_1$  PES scan of HTI Z3 along  $\beta$  obtained at TD-CAM-B3LYP/6-31G\*//TD-CAM-B3LYP/cc-pVDZ level of theory. Energies are relative to the ground state minimum at  $\beta=-40^\circ$ .

to have a rather flat potential. Considering only values  $> \beta=40^\circ$  the total energy curve has a minimum at  $80^\circ$ . This is in agreement with a full geometry optimization of the  $S_1$  state performed at the constrained-optimized  $\beta=90^\circ$  twisted geometry at TD-CAM-B3LYP/cc-pVDZ level of theory simulating gas phase which provides a TICT stationary structure with  $\beta=88^\circ$ . However, this structure has not yet been confirmed as a local minimum on the PES. A full geometry optimization of the  $S_1$  state starting at the constrained-optimized  $\beta=90^\circ$  TICT structure using TD-CAM-B3LYP/cc-pVDZ/LR-CPCM together with the parameter of DMSO, however, does not yield a TICT structure, but a  $S_1$  stationary structure with  $\beta=145^\circ$  which can be considered as the rotational isomer of  $S_{1\text{Min}}$ .

Also for HIT Z3, no minimum has been found at  $90^\circ$  along the relaxed gas phase  $S_1$  PES scan of  $\beta$  (see Fig. 7.20). Again discontinuities in the potential energy curves have been found which seem to be induced by changes in the coordinates  $\theta_1$  and  $\alpha$ . This result is in line with geometry optimizations of the  $S_1$  state performed at start geometries in which  $\beta$  has been set to  $-90^\circ$  performed at TD-CAM-B3LYP/cc-pVDZ and LR-CC2/cc-pVDZ level of theory simulating gas phase. These optimizations do not converge to stationary structures but indicate a CI of  $S_1$  and  $S_0$ . They suggest that mainly twisting about  $\beta$  and an out of plane bending of the thiophenone ring drive HTI Z3 towards a  $S_1$ - $S_0$  CI. In the geometry (see Fig. C.11) in which  $S_1$  and  $S_0$  are almost degenerate, the thiophenone ring is slightly bent and the C2 atom (for numbering see Fig. 7.4) is pyramidalized resulting in a bending of the central double bond. This out of plane bending of the central double bond in turn causes a pronounced bending of the whole stilbene fragment out of the thioindigo plane. This geometry resembles the  $S_{1\text{Min}}$  geometry, with one difference, namely that the stilbene group is bent in the opposite direction out of the thioindigo plane. The values of  $\alpha$  are  $-6^\circ$  in the  $S_{1\text{Min}}$  geometry and  $+5^\circ$  in the geometry in which  $S_1$  and  $S_0$  are almost degenerate. This result suggests that after excitation of HTI Z3 at the FC point, besides rapid relaxation to the nearby  $S_{1\text{Min}}$ , a further nonradiative pathway may be taken leading to reformation of the ground state Z isomer via a  $S_1$ - $S_0$  CI different from the one found at  $\theta \approx 100^\circ$  in which the thiophenone ring is planar. Such a relaxation process would explain the aforementioned fifth decay time constant of 75 ps obtained from time resolved absorption measurements in CH.<sup>[245]</sup>

Full geometry optimization of the  $S_1$  state starting with the  $\beta=-90^\circ$  TICT geometry at TD-CAM-B3LYP/cc-pVDZ/LR-CPCM level of theory does not yield a TICT minimum but the local  $S_{1\text{Min}}$  minimum. This result is in line with the findings for HTI Z1 and Z2 discussed above.

Geometry optimization of the  $S_1$  state of a HTI Z3  $\text{H}_2\text{O}$  cluster including six water molecules

yields a TICT minimum (see Fig. C.10). The vertical emission energy of this TICT state obtained at TD-CAM-B3LYP/cc-pVDZ level of theory is 1.36 eV and the corresponding oscillator strength is negligible small ( $f=0.00$ ). This result agrees well with the experimental stationary emission spectrum of HTI Z3 in very polar DMSO in which the second red-shifted band is located at about 1.72 eV (720 nm). Even though DMSO is not such a strong hydrogen bond donor like H<sub>2</sub>O it still tends to built hydrogen bonds to amino groups and carbonyl groups<sup>[383,384]</sup>. From this result it can be inferred that also in DMSO and related solvents which are able to form hydrogen bonds with both the amino and the carbonyl group like H<sub>2</sub>O, TICT state formation is likely to occur. This result would also explain the comparably large decay time constant of 131 ps obtained in DMSO solution<sup>[245]</sup> which can be attributed to fluorescence emission from the TICT minimum.

#### 7.4 SUMMARY AND CONCLUSION

Recent experiments employing transient absorption and fluorescence spectroscopy have shown that four hemithioindigo-hemistilbene (HTI) derivatives HTIs 1-4 can be selectively isomerized from the stable Z isomer to the E isomer in apolar solution. They have further shown that when a polar solvent is used the photoisomerization is quenched to a large extent and either red-shifted emission or dual fluorescence emission becomes the dominant deactivation pathway of HTIs Z1-Z3. It has been stated that red-shifted and dual fluorescence emission is due to the formation of a polar twisted intramolecular charge-transfer (TICT) state.

I have employed high-level quantum chemical methods to thoroughly study the mechanism of the Z/E photoisomerization of HTIs Z1-Z4. The calculations demonstrate that both Z and E isomers correspond to stable isomers in the electronic ground state. While in the ground state the Z isomers of HTIs 1-4 are predicted to be more stable than the E isomers, the current calculations indicate that they are practically degenerate in the optically accessible S<sub>1</sub> ( $\pi\pi^*$ ) state with the E isomer being slightly more stable. Calculated absorption energies obtained using the ptSS-C-PCM solvation approach agree very favorably with experimental<sup>[245]</sup> ones. Local S<sub>1Min</sub> minima have been found close to the Franck-Condon region. Computed emission energies obtained at both, S<sub>1Min</sub> and TICT geometries, employing equilibrium SS-C-PCM solvation, show a reasonably good agreement with stationary fluorescence data<sup>[245]</sup>. In view of the current results and taking experimental findings into account, the mechanism of photoisomerization of HTIs Z1-Z4 and TICT formation of HTIs Z1-Z3 can be understood as follows. In apolar solvents like

cyclohexane upon photoexcitation to the bright  $S_1$  ( $\pi\pi^*$ ) state, having slight CT character, the excited state population rapidly relaxes from the FC point to the nearby local  $S_1$  minimum,  $S_{1\text{Min}}$ . This process proceeds within a few sub-picoseconds with decay time constants<sup>[245]</sup> ranging in between 0.8 to 1.5 ps for the four different derivatives. This relaxation is very fast because only tiny nuclear rearrangements are needed to bring the HTI molecules to the local  $S_{1\text{Min}}$  minimum. During relaxation, the major changes are a decrease in the dihedral angle  $\beta$  a slight elongation of the central C-C double bond and an out of plane bending of the hydrogen atom attached the C-C double bond out of the thioindigo plane. A few HTI molecules will remain trapped in  $S_{1\text{Min}}$  and decay back to the ground state via regular fluorescence obeying Kasha's rule. Decay time constants<sup>[245]</sup> for the fluorescence emission are about 15 - 17 ps. However, most of the excited state population has enough energy to quickly reach the  $S_1$ - $S_0$  CI located at about  $\theta=90^\circ$  and thus to isomerize into the ground state E isomer. The SF-B5050LYP/6-31G\* level of theory predicts that the excess energy provided by photoexcitation is the largest for HIT Z1. This result explains why the experimentally obtained isomerization quantum yield of HTI Z1 is the largest amongst the four HTI derivatives being 56%.

The calculations revealed that an alternative triplet isomerization pathway exists. SOC calculations indicate that  $S_1$ - $T_2$  and  $S_1$ - $T_1$  ISC at the FC point may occur enabling Z/E isomerization through a  $T_1$ - $S_0$  CI located at about  $\theta=90^\circ$ . This result explains the long decay component of 381 ps, 783 ps and 318 ps, respectively, reported for HTI Z2-Z4 cyclohexane solutions<sup>[245]</sup>.

Full  $S_1$  geometry optimizations of HTIs Z1 and Z3, including explicit solvent molecules, suggest that in solvents of high polarity which can form hydrogen bonds, TICT state formation occurs resulting in red-shifted or dual fluorescence emission. This result explains the experimental finding of dual fluorescence emission in medium polar and polar solvents like dichloromethane and dimethyl sulfoxide and supports the hypothesis of Wiedbrauk et al.<sup>[245]</sup> on TICT state formation in medium polar and polar solvents. Geometry optimizations of the  $S_1$  state employing LR-C-PCM solvation together with the parameters of dimethyl sulfoxide reveals that a continuum solvation model like C-PCM is not able to describe the solvent effects resulting in TICT state formation.

In order to provide a sound explanation for the different behavior of the four HTI derivatives and to enable a more solid comparison with experimental data like decay time constants, energy barrier heights are needed for which further calculations have to be performed to complete the

excited state potential energy surface scans. Concerning the TICT mechanism, further calculations such as  $S_1$  state geometry optimizations and single point calculations at TICT geometries including explicit solvent molecules, e.g., dimethyl sulfoxide and dichloromethane should be carried out for HTIs Z1-Z3 to confirm the current results and to obtain emission energies which can be compared to experimental data.

Summarizing, it can be stated that the current results support the experimental finding of two mutually independent relaxation pathways namely double-bond and single-bond rotation which can be separately targeted by choice of the solvent. Exhibiting these properties donor substituted HTI compounds can be used as both photoswitches and molecular rotors.

---

## THE ROLE OF DISPERSION AND STERIC INTERACTIONS IN THE CRYSTAL PACKING OF TRIS(QUINOXALINOPHENANTHROPHENAZINE)

---

In this chapter<sup>†</sup> the influence of some particular intermolecular interactions on the structure of and cohesion in four quinoxalinophenanthrophenazine (QPP) based (see Fig. 8.1) dimers is investigated using DFT and the XSAPT(KS) method including dispersion corrections.

This theoretical study was carried out within a collaborative project with the group of Prof. Mastalerz from the Institute of Organic Chemistry of Heidelberg University, in particular with B. Kohl who synthesized and crystallized the here investigated compounds. Full details about the synthesis, experimental details and crystallographic information can be found in Ref.<sup>[385]</sup> and the dissertation of B. Kohl<sup>[386]</sup>. This theoretical study shows that when the *tert*-butyl groups in the QPP dimer model systems have a staggered conformation, dispersion interactions of the triptycene end groups overrule dispersion interactions between the *tert*-butyl substituents. However, when the *tert*-butyl groups adopt an eclipsed arrangement, dispersion interactions resulting from both the triptycene groups and the *tert*-butyl groups balance one another out. The results suggest that the well-balanced dispersion interactions of *tert*-butyl groups and one triptycenylenylene group are responsible for the unique honeycomb like packing motif.

---

<sup>†</sup>Parts of this chapter are adapted from Kohl B, Bohnwagner, MV., Rominger F., Wadepohl H., Dreuw, A., and Mastalerz M. **Attractive Dispersion Interactions Versus Steric Repulsion of *tert*-Butyl groups in the Crystal Packing of a D<sub>3h</sub>-Symmetric Tris(quinoxalinophenanthrophenazine)***Chem. Eur. J.*, **2016**, *121*, pp 646-655, Copyright Wiley-VCH Verlag GmbH & Co. KGaA. Reproduced with permission.

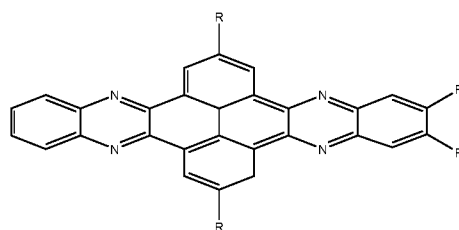


FIGURE 8.1: Structure of the Quinoxalinophenanthrophenazines (QPP) core. R stands for an organic substituent e.g. H, *tert*-butyl or triptycene.

## 8.1 MOTIVATION AND BACKGROUND

Pyraacene based tQPPs (see Fig. 8.2) have been found to have large internal molecular free volumes.<sup>[386,387]</sup> Due to this particular property, tQPPs possess intrinsic microporosity which in turn classifies them as organic porous materials. These materials have recently become subject of great interest due to their potential application in gas storage<sup>[388,389]</sup> and catalysis<sup>[389,390]</sup>. Additionally, due to their large stability, good solubility, the presence of extended  $\pi$  systems and the particular crystal structure QPP derivatives also represent potential candidates as organic semiconductors<sup>[391–393]</sup>

The motivation for this study was a unique packing motif in the crystal structure  $D_{3h}$  symmet-

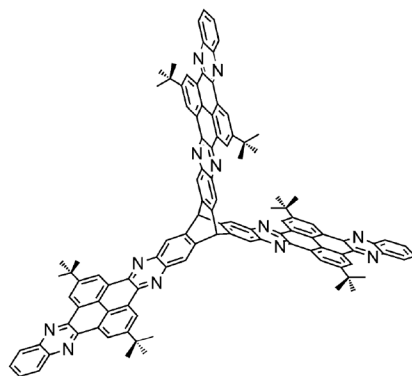


FIGURE 8.2: Structure of a  $D_{3h}$  symmetric tris(quinoxalinophenanthrophenazines) (tQPP) molecule.

ric tris(quinoxalinophenanthrophenazine) tQPP (see Fig.8.2) showing a striking resemblance with honeycomb cells (see Fig. 8.3), which was identified by B. Kohl and his colleagues.<sup>[385]</sup> However, the *tert*-butyl groups are typically oriented in a staggered manner in decorated  $\pi$  aromatic systems,<sup>[394–397]</sup> most probably to avoid or minimize steric repulsion. In order to get a better understanding of how the crystal packing is influenced by intermolecular interactions like dispersion and steric interactions, I have performed quantum chemical calculation on four model

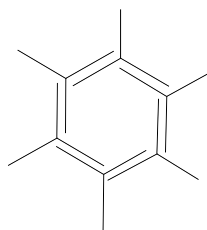


FIGURE 8.3: Schematic representation of the observed particular honeycomb crystal packing motif.

systems, specifically four differently substituted QPP dimers (D-QPP **2-5** see Fig. 8.4)) whose crystal structures (CSs) were provided by B. Kohl.

The dimers have been analyzed theoretically in terms of the influence of intermolecular interactions with a focus on 1) dispersion interactions between the triptycenylenyl unit (see Fig. 8.4, blue) of one monomer and the  $\pi$  electrons of the quinoxaline unit of the other, 2) dispersion interactions of the *tert*-butyl groups (see Fig. 8.4, red) and 3) steric interactions between the *tert*-butyl groups.

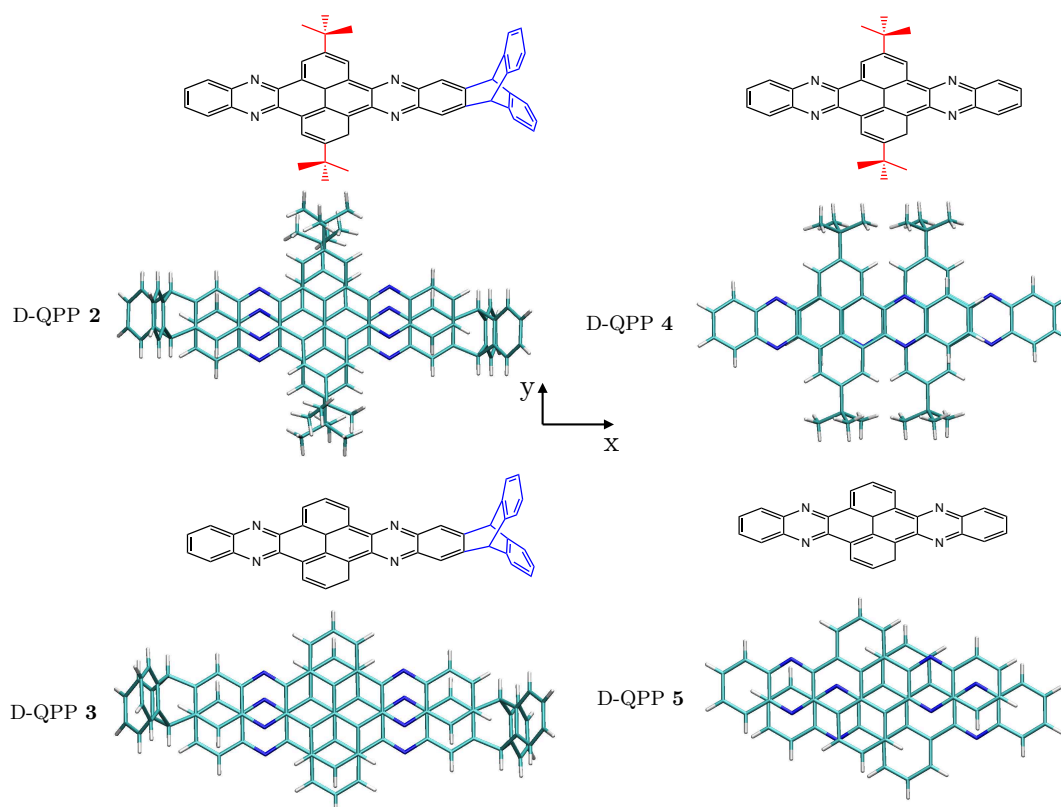


FIGURE 8.4: Skeletal formula of the monomers QPP **2-5** and wireframe model of the crystal structures of the investigated dimers D-QPP **2-5** (top view).

## 8.2 COMPUTATIONAL METHODS

Ground state equilibrium geometries and interaction energies of D-QPPs **2-5** have been calculated at DFT level of theory using the B98<sup>[398,399]</sup> functional and its dispersion-corrected variants: B97D<sup>[131]</sup> and B97D3<sup>[132]</sup> in conjunction with the cc-pVDZ basis set. DFT methods use a so called supramolecular approach to predict interaction energies. A severe drawback of this approach is that it suffers from the so-called basis set superposition error (BSSE)<sup>[400]</sup>. BSSE causes the intermolecular interactions to be artificially too attractive, hence binding tends to be overestimated.

An alternative method to compute interaction energies is symmetry-adapted perturbation theory (SAPT). In contrast to DFT this method is based on a perturbational approach. Main advantages of this method over the supramolecular approach are i) that it is free from BSSE and ii) that the interaction energy components, such as polarization and dispersion contributing to the total intermolecular interaction energy  $E_{int}^{SAPT(KS)}$  8.1 are computed separately.

$$E_{int}^{SAPT(KS)} = E_{elst}^{(1)} + E_{exch}^{(1)} + E_{ind}^{(2)} + E_{exch-ind}^{(2)} + E_{disp}^{(2)} + E_{exch-disp}^{(2)} \quad (8.1)$$

$E_{elst}$  is the electrostatic energy contribution originating from Coulomb-like interactions between the monomers.  $E_{ind}$  is the induction energy and accounts for mutual polarization of the monomers originating from induced dipole-dipole and higher multipole-induced multipole moment interactions.  $E_{disp}$  is the dispersion energy component originating from interactions of instantaneous fluctuations of dipoles on the monomers. The exchange energy  $E_{exch}$  accounts for the Pauli repulsion of electrons between the monomers. The terms  $E_{exch-ind}$  and  $E_{exch-disp}$  represent exchange corrections for the induction and dispersion interactions. For the aforementioned reasons, a dispersion corrected low-order-scaling version of the SAPT method, XSAPT(KS)-D3<sup>[96,401-403]</sup>, which is especially well-suited for large molecular systems, has been employed to calculate total interaction energies ( $E_{int}^{SAPT(KS)}$ ). Even though this version is less accurate than the regular SAPT method, it has been chosen since the studied molecular systems are too large (for D-QPP **4** with the small 6-31G basis the system size already comprises more than 800 basis functions) to be studied with the SAPT method, which scales as  $O(N^7)$  with the system size. XSAPT(KS)-D3 uses Kohn-Sham (KS)-DFT instead of MP2 to account for intramolecular electron correlation effects. Furthermore, the terms  $E_{disp}^{(2)}$  and  $E_{exch-disp}^{(2)}$  in eq. (8.1) are not computed explicitly, but

instead empirical atom-atom dispersion potentials (“+D3”) are computed to correct dispersion energies, which are only poorly described by the standard SAPT(KS) method<sup>[403,404]</sup>.

Interaction energies have been computed at CSs of D-QPP **2-5** and at modified versions of the CS of D-QPP **2** using XSAPT(KS)+D3 in conjunction with a long-ranged corrected version of the  $\omega$ PBE functional (LRC- $\omega$ PBE)<sup>[405]</sup> and a value of  $\omega = 0.4 \text{ bohr}^{-1}$  (the default value is 0.3) for the monomers (Table 8.1). Due to the high memory and disk space requirements of the XSAPT(KS)+D3 method, the small 6-31G<sup>[406–411]</sup> basis set has been used for all computations. This small basis, however, can be assumed to be sufficiently large for the purpose of this study, namely to get an idea to what extent the interactions of *tert*-butyl and triptycenylenyl groups, respectively, contribute to the total interaction energy. At first, the interaction energy  $E_{int}^{SAPT(KS)}$  has been computed at the CS of D-QPP **2**. Then, *tert*-butyl groups and triptycenylenyl groups have been substituted with protons one after another and interaction energies have been recomputed at the corresponding modified CSs (D-QPP **2(4)**, D-QPP **2(3)** and D-QPP **2(5)**), respectively. To obtain the separate dispersion contributions of the *tert*-butyl and triptycenylenyl groups to the total binding energy,  $E_{int}^{SAPT(KS)}$  has also been computed at the CS of D-QPP **4** and **3**. XSAPT(KS)+D3 calculations have been performed with Q-Chem 4.3. For DFT calculations Gaussian 09 Rev. D01 has been used.

## 8.3 RESULTS

D-QPPs **2-5** have first been analyzed with respect to structural differences between crystal and optimized structures using DFT and dispersion corrected DFT. Secondly, intermolecular interaction energies have been analyzed with respect to energy contributions originating from both dispersion interactions of the *tert*-butyl groups and between the triptycenylenyl group and the  $\pi$ -system (i.e. the quinoxaline unit) using the XSAPT(KS)+D3 method (Table 8.1).

### 8.3.1 Structural study

Already by comparing CSs of D-QPP **2-5** with the respective geometry-optimized structures obtained with and without employing dispersion corrections, important insights about the influence of dispersion interactions on the crystal packing can be obtained. Firstly, the structure

of the unsubstituted QPP dimer (D-QPP **5**) has been analyzed. The most concise structural characteristics of the CS of D-QPP **5** are a distinct displacement of the  $\pi$ -surfaces against each other along x-y-axis and y-axis (see Fig. 8.4) and a slight intramolecular twist ( $\beta_{\text{twist}}$ ) of those along the x-axis of about  $4^\circ$  (see Fig. 8.5). The shift along the y-axis and the intramolecular twist are also present in the CS of the QPP dimer of interest, D-QPP **2** (see Fig. 8.8 and 8.4). In

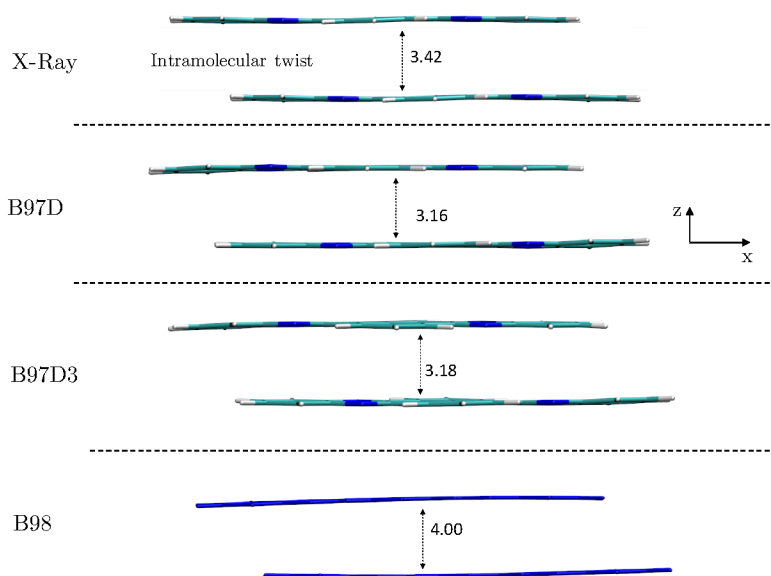


FIGURE 8.5: Wireframe models of the crystal structure (X-Ray) and the B97D, B97D3 and B98 optimized geometries of D-QPP **5**. Distances between the monomers are shown in dashed lines. The values are taken from Ref. <sup>[385]</sup>.

the CS of D-QPP **4** (see Fig. 8.6 and 8.4), the  $\pi$ -surfaces are displaced solely along the x-axis. However, the displacement is more pronounced than in D-QPP **5**. The  $\pi$  planes are separated by about  $3.5 \text{ \AA}$  similarly as in D-QPP **5**. From a purely sterical point of view, one would assume that the *tert*-butyl groups repel each other strongly so that the  $\pi$  systems are significantly displaced along the x-axis. Geometry optimizations of D-QPP **4**, with and without employing dispersion corrections (see Fig. 8.6), however, suggest that attractive interactions between the *tert*-butyl groups are also operative. Those seem to not only lead to the adoption of a more eclipsed arrangement as opposed to a fully staggered conformation in the CS but also to result in a slightly tighter binding (the distance between the  $\pi$  planes is reduced) and a less pronounced shift along the x-axis. In D-QPP **4**, however, it seems that the steric interactions of the bulky (staggered) *tert*-butyl groups overrule the attractive dispersion interaction between them.

In contrast with D-QPP **4**, the  $\pi$  planes are displaced solely along the y-axis in the CS of D-QPP **3** (see Fig. 8.7). Along the x-axis, they are aligned in parallel with each other (the nitrogens

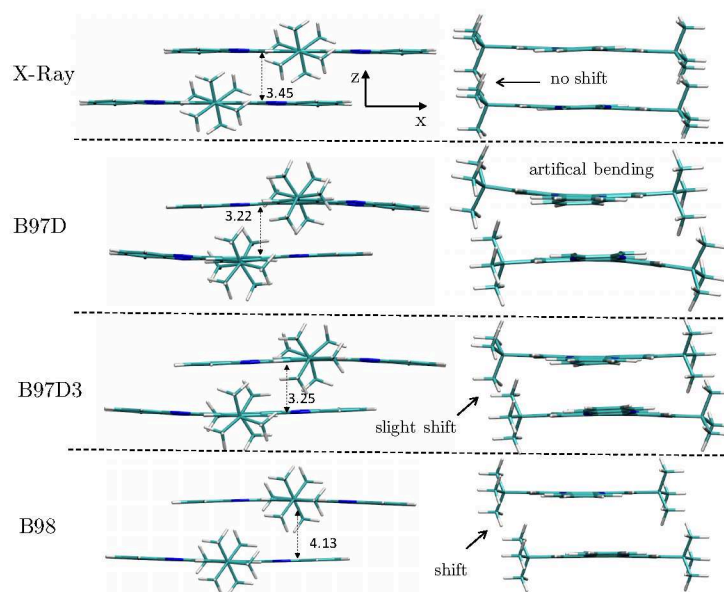


FIGURE 8.6: Wireframe models of the crystal structure (X-Ray) and the B97D, B97D3 and B98 optimized geometries of D-QPP **4**. Distances between the monomers are shown in dashed lines. The values are taken from Ref. [385].

of both monomers are on top of one another), which leads to an almost maximal overlap. The structural differences between the CSs of D-QPP **4** and D-QPP **3** already strongly suggest that attractive dispersion interactions between the triptycenylenes and the quinoxaline unit are responsible for the parallel arrangement of the  $\pi$  planes and also affect the intramolecular twist  $\beta_{\text{twist}}$ . A comparison of the four structures shown in Fig. 8.7 supports this hypothesis. It suggests that dispersion interactions not only affect the distance between the  $\pi$  planes and thus the tightness of packing but also the shift and to some extent  $\beta_{\text{twist}}$ . In the CS of D-QPP **3**,  $\beta_{\text{twist}}$  is about  $8^\circ$  which is more pronounced than in the CS of D-QPP **5** and D-QPP **2**, where it is about  $4^\circ$ , in both cases. In contrast in the B98 optimized geometry of D-QPP **3**  $\beta_{\text{twist}}$  is only  $2^\circ$ . It seems that the dispersion correction is needed to capture the twist at least to some extent. Compared to the CS, the distance between the  $\pi$  planes is with  $3.85 \text{ \AA}$  significantly larger in the B98 optimized geometry, while it is smaller in the B97D and B97D3 optimized geometries. Furthermore, it becomes apparent that in the B98 optimized structure, contrary to the CS, the  $\pi$  planes are slightly displaced along the x-axis. The nitrogen atoms are not aligned on top of one another as in the CS. In contrast, the displacement along the y-axis is not affected by the optimization. Concerning  $\beta_{\text{twist}}$  and the displacement along the x-axis the B97D optimized geometry shows the best agreement with the CS.

One striking characteristic of the CS of D-QPP **2** (see Fig. 8.8) is the eclipsed conformation of the

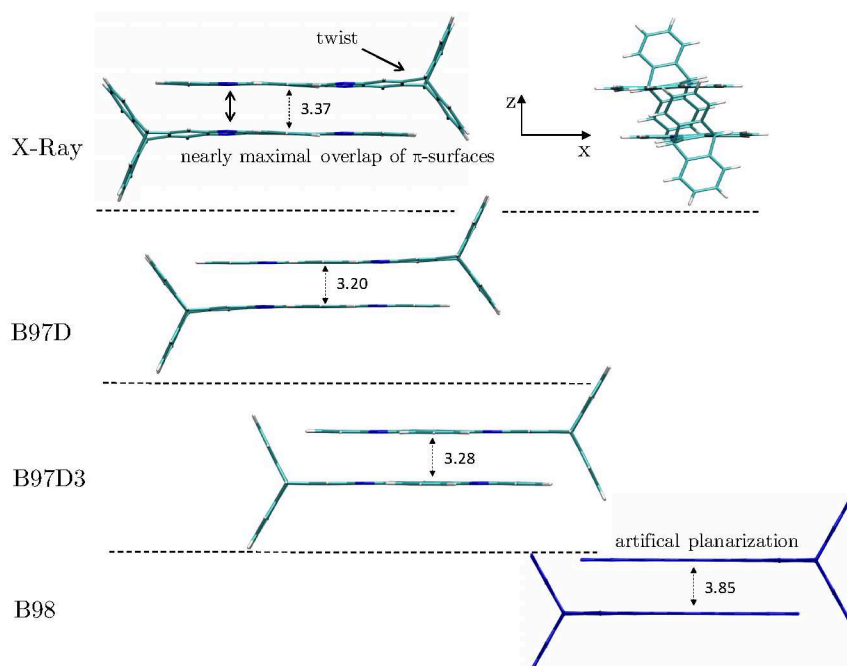


FIGURE 8.7: Wireframe models of the crystal structure (X-Ray) and the B97D, B97D3 and B98 optimized geometries of D-QPP **3**. Distances between the monomers are shown in dashed lines. The values are taken from Ref. [385].

*tert*-butyl groups. Both repulsive interactions of the *tert*-butyl groups and attractive interactions between triptycenylyne groups and the quinoxaline unit seem to balance each other. The most decisive geometric changes upon geometry optimization of the CS without using dispersion corrections are a complete bending of the  $\pi$  planes along the x-axis and a pronounced increase in the distance by about 0.3 Å. When dispersion interactions are included in the calculation the artificial bending is corrected and the  $\pi$  planes are packed tighter, as in the CS. This result is in agreement with the hypothesis obtained from analysis of D-QPP **4**, that the *tert*-butyl groups, when arranged in an eclipsed conformation as in D-QPP **2**, not only repel but also attract each other due to dispersion interactions.

### 8.3.2 Energetic study

Having studied the structures, intermolecular interaction energies were analyzed next. As already mentioned above, first, the interaction energy  $E_{int}^{SAPT(KS)}$  has been computed at the CS of D-QPP **2**. Then, *tert*-butyl groups and triptycenylyne groups have been substituted with protons one after another and interaction energies have been recomputed at the corresponding modified CSs

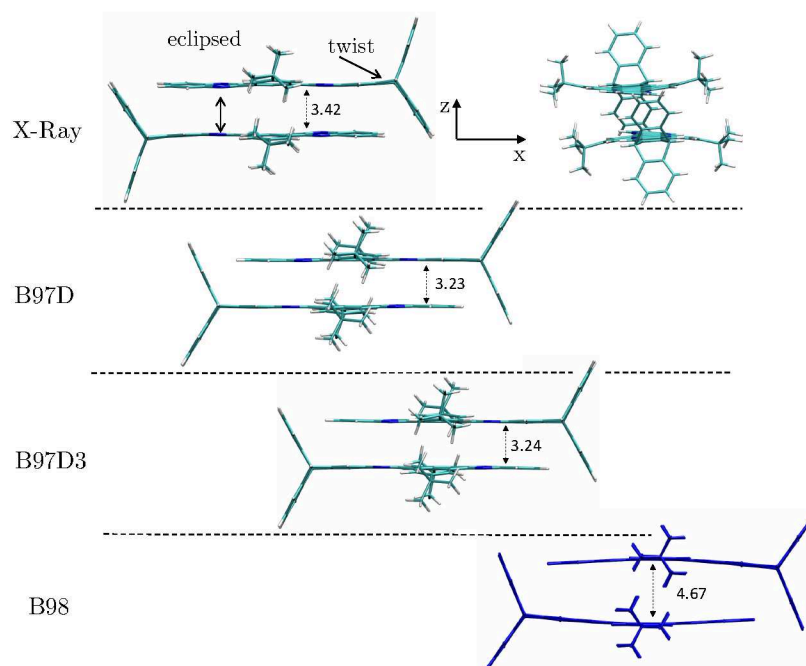


FIGURE 8.8: Wireframe models of the crystal structure (X-Ray) and the B97D, B97D3 and B98 optimized geometries of D-QPP 2. Distances between the monomers are shown in dashed lines. The values are taken from Ref. [385].

(D-QPP 2(4), D-QPP 2(3) and D-QPP 2(5)), respectively. To obtain the separate dispersion contributions of the *tert*-butyl and triptycenylenic groups to the total binding energy,  $E_{int}^{SAPT(KS)}$  has also been computed at the CSs of D-QPP 4 and 3. The results obtained at XSAPT(KS)-D3/wPBE/6-31G level of theory are summarized in Table 8.1

### 8.3.2.1 Total binding energies and dispersion energy contribution

The dispersion interaction contribution  $E_{disp}^{(2)}$  to the interaction energy obtained at the CS of D-QPP 4 (the one with staggered *tert*-butyl groups) is  $-49.68 \frac{kcal}{mol}$ . The dispersion contribution obtained at structure D-QPP 5 (the dimer without *tert*-butyl and triptycenylenic groups) is almost the same. Hence, it can be inferred that the dispersion interactions between the *tert*-butyl groups, when not aligned on top of each other as in D-QPP 2 (in which they are eclipsed) by adopting a staggered arrangement, will alone not significantly influence the packing in the direction of the observed honeycomb motif.  $E_{disp}^{(2)}$  for structure D-QPP 4 is  $8.05 \frac{kcal}{mol}$  smaller than the one obtained at D-QPP 2(4) of  $-57.73 \frac{kcal}{mol}$  in which the triptycenylenic groups are substituted by protons and the *tert*-butyl groups have an eclipsed conformation. From this result it can be concluded that

TABLE 8.1: Total interaction energy ( $E_{int}$ ) and relevant energy components of the total interaction energy calculated at the X-ray single crystal structures of D-QPPs **2-5** as provide by B. Kohl and modified versions of the crystal structure of D-QPP **2** obtained at the XSAPT(KS)-D3/wPBE/6-31G level of theory.

Structure	$E_{int}$ [ $\frac{kcal}{mol}$ ]	$E_{elst+exch}^{(1)}$ [ $\frac{kcal}{mol}$ ]	$E_{ind}^{(2)}$ [ $\frac{kcal}{mol}$ ]	$E_{disp}^{(2)}$ [ $\frac{kcal}{mol}$ ]
D-QPP <b>2</b>	-64.81	5.23	-0.92	-69.12
D-QPP <b>2</b> (3)	-54.29	3.38	-0.67	-57.00
D-QPP <b>2</b> (4)	-53.00	5.41	-0.67	-57.73
D-QPP <b>2</b> (5)	-42.51	3.60	-0.43	-45.68
D-QPP <b>3</b>	-61.89	5.68	-0.78	-66.79
D-QPP <b>4</b>	-45.30	4.90	-0.52	-49.68
D-QPP <b>5</b>	-46.57	3.68	-0.48	-49.77

the eclipsed arrangement and parallel alignment due to attractive dispersion interactions indeed affect the crystal packing, strengthening it.

The value of  $E_{disp}^{(2)}$  obtained at structure D-QPP **3** is  $-66.79 \frac{kcal}{mol}$  that is  $17.11 \frac{kcal}{mol}$  larger than the one of D-QPP **4** and  $9.79 \frac{kcal}{mol}$  larger than that of D-QPP **2**(3). Furthermore, it is almost as large as the dispersion contribution obtained for D-QPP **2** which is  $-69.12 \frac{kcal}{mol}$ . From this, it can be inferred that dispersion interactions between the triptycylene groups and the quinoxaline unit are stronger than dispersion interactions of the *tert*-butyl groups when those are displaced along the x-axis and have a staggered conformation. In the model system of interest D-QPP **2**,  $E_{disp}^{(2)}$  of the triptycylene groups is  $12.12 \frac{kcal}{mol}$  thus slightly larger than the one of the *tert*-butyl groups which is  $11.39 \frac{kcal}{mol}$ . In the CS of D-QPP **2** both dispersion contributions balance each other out. This becomes obvious if one compares the  $E_{disp}^{(2)}$  values of D-QPP **2**(4) and D-QPP **2**(3); they are equally large.

## 8.4 CONCLUSION

Conclusively, it can be stated that the dispersion interactions resulting from both the triptycylene groups and the *tert*-butyl groups are well-balanced in the crystal structure of D-QPP **2**, when the *tert*-butyl groups adopted an eclipsed arrangement and are aligned on top of each other along the x-axis which, in turn is guaranteed by dispersion interactions between triptycylene groups and the  $\pi$  system. Thus, this study reveals that the unique crystal packing motif observed in  $D_{3h}$  symmetric tQPP (see Fig. 8.2 is caused by cooperative dispersion interactions of different

molecular parts. In particular, the well-balanced dispersion contributions of *tert*-butyl groups of two monomers and one triptycene group of one monomer with the  $\pi$  system of another, both seem to be responsible for this unique honeycomb packing motif. The relative orientation of  $\pi$  planes of extended  $\pi$  systems to each other was found to be of great importance for the charge transport in molecular organic field effect transistors<sup>[412–415]</sup>, which are important optoelectronic devices. Theoretically brick-wall arrangements as found in QPPs **2** and **3** should enable more efficient charge transport than herringbone-type arrangements.<sup>[416,417]</sup>



---

## GLOBAL SUMMARY & OUTLOOK

---

### 9.1 GLOBAL SUMMARY

In this thesis, I have presented the research conducted during the time of my Ph.D. In the following, I will briefly summarize the most important results of these projects. All, but one, involve the study of photochemical reactions and are connected by being concerned with intramolecular charge-transfer states. The exception is the project on tris(quinoxalinophenanthrophenazine) (tQPP) which is a ground state study.

The first project, presented in **chapter 4**, is the theoretical investigation of the photochemistry of the well-known, and experimentally well-investigated, donor-acceptor molecule N-pyrrolobenzonitrile (PBN). PBN is the pyrrol analogue of 4-N,N-dimethylaminobenzonitrile (DMABN), the molecule for which the phenomenon of dual fluorescence has been observed first. It has been found experimentally that PBN shows an unusual photophysical behavior in medium polar and polar solvents, namely dual fluorescence emission. To study the photochemical behavior of PBN, ground and excited state potential energy surfaces (PES) have been explored, using different high-level *ab initio* methods, i.a., the second-order approximate coupled-cluster (CC2) method. Furthermore, relaxed PES scans of the photochemically relevant excited states have been performed along the twisting coordinate, namely the central C-N single bond. Solvent effects on transition energies of the relevant excited states have been described within the conductor-like polarizable continuum model (C-PCM) and the conductor-like screening model (COSMO). According to the computational results, the following deactivation mechanism of PBN has been suggested. Upon photoexcitation to the spectroscopically accessible 2A ( $\pi\pi^*$ )

(S<sub>2</sub>) state, PBN only twists a few degrees until an intersection with the energetically very close lying 1B (LE) (S<sub>1</sub>) state is reached. After passing the 2A-1B state intersection, PBN relaxes to an almost planar local 1B (LE) state minimum from which emission occurs. The relaxed PES scan of the 2A state along the twisting coordinate employing equilibrium state-specific solvation revealed that a polar solvent not only stabilizes the polar 2B (CT) (S<sub>3</sub>) state, but also the 2A state. As a result, the energy barrier along the twisting coordinate vanishes and twisting around the central single bond is facilitated. It was found that in the gas phase and apolar solvents, 2A and 2B states are not sufficiently stabilized and an energy barrier for twisting exists, such that only single emission from the 1B (LE) state occurs. With increasing polarity of the solvent, both the 1B (LE) and 2A states, the latter exhibiting a larger static dipole moment, are stabilized and the energy barrier shrinks such that relaxation to the twisted intramolecular charge-transfer (TICT) (2B) state minimum becomes feasible. This study conclusively explained all available experimental findings, like the occurrence of dual fluorescence in medium polar solvents and the effects of temperature and solvent polarity on the emission spectra of PBN.

The second project, discussed in **chapter 5**, focuses on the photochemistry of two thiophene analogues of PBN, namely the two isomers 5-(1H-pyrrole-1-yl)thiophene-2-carbonitrile (2-TCN) and 5-(1H-pyrrole-1-yl)thiophene-3-carbonitrile (3-TCN). The aim of this study was to examine, whether the thiophene based donor-acceptor molecule TCN shows a fluorescence behavior similar to its benzonitrile analogue PBN, and also exhibits dual fluorescence in medium polar solution. Since the chosen methodology has been demonstrated to be well-suited to describe the photochemical behavior of PBN, it has also been employed for the study of TCN. Again ground and excited state PESs have been optimized at different levels of theory and relaxed PES scans of the charge-transfer state along the twisting coordinate, the central C-N single bond, have been performed. A TICT minimum has been found on the S<sub>1</sub> state surface of both isomers. Gas phase calculations of 2-TCN revealed that a small barrier of only about 0.01 eV has to be overcome to reach the TICT minimum. In 3-TCN no corresponding barrier has been found. It has been further found that population of the TICT minimum of 2- and 3-TCN is rather unlikely due to the presence of a S<sub>1</sub>-S<sub>0</sub> state intersection, which can be reached barrierless after excitation to the bright S(ππ\*) (S<sub>1</sub>) state. Solvation model calculations have shown that the S(CT) is stabilized in polar solvents, and that population of the TICT minimum becomes more likely. In conclusion, this study revealed that even though TCN is structurally very similar to dual fluorescent PBN, TCN exhibits a different photochemistry. While PBN shows at least single emission from a locally

excited (LE) state in the gas phase, the thiophene analogue TCN has been found to deactivate radiationless to the ground state, such as unsubstituted thiophene. Furthermore, It has been found that, in contrast to PBN, dual fluorescence is unlikely to occur in TCN and single red-shifted emission may only be observable in polar solvents.

The next project, given in **chapter 6**, deals with another small donor-acceptor compound, namely 4-Fluoro-*N,N*-dimethylaniline (FDMA). FDMA, like PBN and TCN, is a derivative of the well-known TICT compound DMABN. In FDMA, the strong electron-withdrawing cyano-group is substituted with a fluorine atom that has a significantly smaller electron-withdrawing effect. This study was motivated by two contradicting experimental investigations on the fluorescence behavior of FDMA. In one of these investigations, dual fluorescence of FDMA was observed while in the other one only single fluorescence emission was found. Motivated by those discrepancies, I have computed absorption and emission energies and investigated the deactivation pathways of photoexcited FDMA. For this purpose different methods, i.a., time-dependent density functional theory (TDDFT), CC2 and the highly accurate third-order algebraic diagrammatic construction method (ADC(3)) for the polarization propagator have been used. Based on my results, the following deactivation mechanism of FDMA has been proposed: After photoexcitation to the bright  $S_2$  state, FDMA may either relax to a planar  $S_1$  state minimum through a well accessible  $S_2$ - $S_1$  conical intersection, from which fluorescence emission can occur. Alternatively, it may decay radiationless to the ground state via a low lying  $S_1$ - $S_0$  conical intersection along a prefulvene-like vibrational mode of benzene. My computational results perfectly explain the experimental observation of single fluorescence emission in both apolar and polar solution. Furthermore, this study has shown that, even though FDMA is structurally related to dual fluorescent DMABN and PBN, FDMA exhibits a different photochemistry, like also observed for TCN. Similar to TCN, for which it has been found that internal modes of thiophene lead TCN to a  $S_1$ - $S_0$  conical intersection in the gas phase, the photochemistry of FDMA has been found to be governed by the photochemistry of benzene. Internal modes of benzene seem to open up a competitive nonradiative deactivation pathway. This study has further revealed that the TICT minimum reported by Fujiwara et al.<sup>[329]</sup>, used to explain the asserted observation of dual fluorescence as a methodological artifact of the employed TD-B3LYP method.

In **Chapter 7** the focus lies on a more recent project. Here, current results of a photochemical study on four different donor-substituted hemithioindigo-hemistilbene (HTI) derivatives are presented. These HTI derivatives are so-called photoswitches. A photoswitch is a molecule that

can exist in two different configurations: the Z and the E isomer. Upon absorption of light energy, the structure of a photoswitch changes from one configuration to the other by rotation about a double bond. It was found experimentally that the four HTI derivatives, here named HTIs Z1-Z4, exhibit a very different photochemical behavior in apolar and polar solvents. For HTIs Z1-Z3, those derivatives having bulky substituents in *ortho* positions of the stilbene benzene ring, dual fluorescence emission has been observed experimentally in polar solvents. Consequently, the formation of a TICT state was suggested. In apolar solution, Z/E photoisomerization has been observed experimentally for all four HTIs. It has been stated that the two different deactivation pathways, found in apolar and polar solution, are mutually independent and can be targeted separately by choosing different solvents. I have investigated the deactivation mechanism of HTIs Z1-Z4 with a focus on two alternative relaxation pathways, namely single bond and double bond rotation, in relation to the experimental findings. Solvent effects on absorption and emission energies have been accounted for by employing both nonequilibrium and equilibrium state specific solvation models. The role of hydrogen bonding interactions on TICT state formation has been examined by including a small number of explicit solvent molecules in the calculations. Geometry optimizations of the ground states of the four HTIs performed at TD-DFT/CAM-B3LYP and LR-CC2 levels of theory predicted two stable local minima on the ground state PES corresponding to the Z and E isomers. The Z isomers have been predicted to be slightly more stable than the E isomers in the ground state. Geometry optimizations of the bright  $S_1$  ( $\pi\pi^*$ ) states of HTIs Z1-Z4 predicted local  $S_1$  ( $\pi\pi^*$ ) minima, located close to the Franck-Condon region. Based on the current results the following mechanism of photoisomerization of HTIs Z1-Z4 has been suggested. In apolar solvents, upon photoexcitation to the bright  $S_1$  state, the excited state population rapidly relaxes from the FC point to the nearby local  $S_1$  minimum. This relaxation is very fast because only small nuclear rearrangements are needed to bring the HTI molecules to the local  $S_1$  minimum. A few HTI molecules will remain trapped in  $S_1$  minimum and decay back to the ground state via regular fluorescence. Most of the excited state population has enough energy to overcome the barrier on the  $S_1$  PES, to quickly reach the  $S_1$ - $S_0$  conical intersection located at about  $\theta=90^\circ$  and thus to isomerize into the ground state E isomer. Furthermore, an alternative triplet isomerization pathway has been found. Spin-orbit calculations indicate that  $S_1$ - $T_2$  and  $S_1$ - $T_1$  ISC at the FC point may occur, enabling Z/E isomerization through a  $T_1$ - $S_0$  conical intersection located at about  $\theta=90^\circ$ . Concerning the TICT mechanism of HTIs Z1-Z3, the current results suggest that TICT state formation may occur in polar solvents that can form

hydrogen bonds, resulting in red-shifted or dual fluorescence emission. The computational results have been found to be in good agreement with experimental ones. Additionally, they support the experimental finding of two mutually independent relaxation pathways, double bond and single bond rotation.

In the last chapter, **chapter 8**, the final study of this dissertation is presented. This study was performed within the framework of a collaborative project with the group of Prof. Mastalerz from the Institute of Organic Chemistry of Heidelberg University. Here, the crystal structure packing of a  $D_{3h}$ -symmetric  $\pi$ -extended triptycene based pyrene fused pyrazaacene molecule, shortly named tQPP, has been investigated theoretically. This study was motivated by the observation made by B. Kohl and his coworkers of an extraordinary  $\pi$ -stacking motif in the crystal packing of tQPP, resembling a honeycomb. To obtain a better understanding of how the crystal packing is influenced by intermolecular interactions like dispersion and steric interactions, four dimer model systems, named D-QPP **2-5**, have been investigated quantum chemically. The dimers have been analyzed with a focus on 1) dispersion interactions between the triptycenylenic unit of one monomer and the  $\pi$  electrons of the quinoxaline unit of the other, 2) dispersion interactions of the *tert*-butyl groups and 3) steric interactions between the *tert*-butyl groups. For this purpose ground state equilibrium geometries of D-QPPs **2-5** have been calculated at DFT level of theory using the B98 functional and its dispersion-corrected variants: B97D and B97D3. Additionally, total interaction energies have been computed, using symmetry-adapted perturbation theory, in which interaction energy components like polarization and dispersion energies, are computed separately. This study revealed that when the *tert*-butyl groups in the QPP dimer model systems have a staggered conformation, dispersion interactions of the triptycene end groups overrule dispersion interactions between the *tert*-butyl substituents. Thus, this study showed that the unique honeycomb packing motif is caused by cooperative dispersion interactions of different molecular parts. In particular, the well-balanced dispersion contributions of *tert*-butyl groups of two monomers and one triptycenylenic group of one monomer with the  $\pi$  system of another seem to be responsible for this unique packing motif.

In summary, in this dissertation it is demonstrated for a number of small- and medium-sized organic compounds that by using modern quantum chemical methods, it is possible to well reproduce experimental results and also to gain a better understanding of those.

## 9.2 OUTLOOK

The photochemical study of TCN revealed an interesting behavior of the two isomers. It has been found that the gas phase photochemistry of both isomers is dominated by the photochemical behavior of thiophene. Furthermore, it has been found that both isomers rapidly deactivate back to the ground state via a well accessible  $S_1$ - $S_0$  conical intersection. For the 3-TCN isomer, this nonradiative decay is accompanied by a ring-opening of the thiophene ring. For 2-TCN, such a ring opening has not been observed. In the gas phase, TICT formation and thus red-shifted fluorescence has been found to be quenched. This result gave me the idea to test some further donor substituents and to further explore how different donor substituents i) influence the energy of CT state at the Franck-Condon geometry ii) prevent the decay via a  $S_1$ - $S_0$  conical intersection. It would be very interesting to see if TICT formation becomes more feasible if a donor with increased electron donating strength is used. For this purpose, I prepared some further calculations using dimethylamine, di-*tert*-butylamine and carbazole as donor substituents, instead of pyrrol. Those have to be analyzed in the future. Of course, depending on the results of the first test calculations, one could also extend the screening of donor groups. The results of concerning FDMA suggest to also test some further acceptor substituents. It would be very interesting to see if there exists a general rule for the properties of donor and acceptor moieties, which are related to the probability of TICT formation.

Clearly, in order to obtain a more complete and sound picture of the photochemistry of the four HTI photoswitches, some further calculations are needed. Firstly, some further constrained  $S_1$  state geometry optimizations of HTIs Z1-Z4 have to be performed to complete the relaxed potential energy surface scans of the  $S_1$  states along the Z/E photoisomerization coordinate. By doing so,  $S_1$  energy barriers along the isomerization path can be obtained. The current results indicate that the HTI derivative problem is a multidimensional problem. Thus, it could be very helpful to carry out some molecular mechanic based conformational sampling calculations to explore the ground and excited state potential energy surfaces of HTIs Z1-Z4. Concerning the TICT mechanism of HTIs Z1-Z3, single point solvent model calculations performed at constrained optimized TICT structures and geometry optimizations performed by including some explicit solvent molecules indicate that TICT formation may occur. To support these first results, further calculations should be carried out, both using a solvent model and also including a number

---

of explicit solvent molecules. Hereby, different solvent molecules which exhibit both hydrogen bond donor and acceptor properties should be used.



---

**APPENDIX FOR CHAPTER 5**

---

**A.1 THE PHOTOCHEMISTRY OF TCN**

TABLE A.1: Cartesian coordinates of the ground state equilibrium geometry of 2-TCN obtained at RI-MP2/cc-pVTZ level of theory

Atom	x	y	z
S	-0.918723	-0.902058	-0.267189
C	0.222914	0.338137	0.095324
C	-2.231057	0.184142	-0.005544
C	-0.389325	1.541928	0.379145
C	-1.791081	1.456572	0.316242
H	-2.471172	2.270191	0.516682
H	0.165955	2.428205	0.644886
C	-3.567251	-0.265322	-0.111020
N	-4.676457	-0.641546	-0.202430
N	1.588474	0.075342	0.037513
C	2.532495	0.927582	-0.494267
C	2.206955	-1.068715	0.494531
C	3.558782	-0.938444	0.253896
C	3.763667	0.318667	-0.368969
H	2.232438	1.858629	-0.941924
H	4.699716	0.733177	-0.700990
H	1.635497	-1.840150	0.980900
H	4.309420	-1.666258	0.508790

TABLE A.2: Cartesian coordinates of the ground state equilibrium geometry of 2-TCN obtained at RI-CC2/cc-pVTZ level of theory

Atom	x	y	z
S	-4.802297	4.980847	-0.881293
C	-4.799836	5.457621	-2.544259
C	-3.072820	4.867594	-0.879853
C	-3.520092	5.551001	-3.059247
C	-2.536843	5.219669	-2.10826
H	-1.473824	5.208739	-2.298515
H	-3.321588	5.818405	-4.086153
C	-2.382702	4.440427	0.276232
N	-1.807003	4.085299	1.247413
N	-5.996915	5.737746	-3.193626
C	-6.173489	6.739750	-4.132030
C	-7.194142	5.068845	-3.006710
C	-8.131428	5.648076	-3.834624
C	-7.488622	6.701667	-4.542388
H	-5.360432	7.400210	-4.378553
H	-7.936666	7.365382	-5.262148
H	-7.246702	4.225194	-2.339808
H	-9.159196	5.340323	-3.924911

TABLE A.3: Cartesian coordinates of the ground state equilibrium geometry of 3-TCN obtained at RI-MP2/cc-pVTZ level of theory

Atom	x	y	z
S	0.461614	-1.712654	0.169718
C	-0.123202	-0.100526	-0.030495
C	2.085422	-1.191492	0.108558
C	0.902805	0.812887	-0.114786
C	2.169193	0.182944	-0.028633
H	0.751119	1.871318	-0.257915
H	2.897779	-1.896681	0.161255
N	-1.489822	0.160747	-0.042089
C	-2.093326	1.228391	0.587688
C	-2.447493	-0.599238	-0.678876
C	-3.671468	-0.004523	-0.453817
C	-3.448256	1.146034	0.344024
H	-1.507543	1.914502	1.173696
H	-4.189599	1.834224	0.711391
H	-2.163302	-1.459221	-1.259959
H	-4.614843	-0.359046	-0.831243
C	3.407547	0.880378	-0.101696
N	4.427058	1.458880	-0.160598

TABLE A.4: Cartesian coordinates of the ground state equilibrium geometry of 3-TCN obtained at RI-CC2/cc-pVTZ level of theory

Atom	x	y	z
S	-4.797803	4.979371	-0.879879
C	-4.805928	5.470395	-2.542992
C	-3.087418	4.888440	-0.859762
C	-3.531978	5.584494	-3.051607
C	-2.548413	5.256062	-2.080153
H	-3.315381	5.861222	-4.072204
H	-2.561208	4.562892	0.022559
N	-6.007983	5.741971	-3.188973
C	-6.200531	6.749589	-4.117440
C	-7.194058	5.053232	-3.007402
C	-8.141802	5.626711	-3.827954
C	-7.515606	6.695425	-4.527196
H	-5.396853	7.422644	-4.360931
H	-7.973881	7.358439	-5.241128
H	-7.233757	4.204657	-2.345926
H	-9.165831	5.306530	-3.917581
C	-1.147324	5.276406	-2.332649
N	0.014939	5.298638	-2.544458

TABLE A.5: Comparison of vertical excitation energies and static dipole moments of the first four lowest excited states of 2- and 3-TCN obtained at ADC(2)/cc-pVTZ and ADC(2)/cc-pVTZ/SS-COSMO levels of theory at the gas phase ground state equilibrium geometry using the parameter of *n*-hexane, acetonitrile and water for the solvent model. Vertical excitation energies in gas phase  $\omega$  (in eV), solvent-corrected vertical excitation energies  $\omega_{\text{sol}}$  (in eV) and solvent shifts  $\Delta\omega_{\text{gas}}^a$  and  $\Delta\Delta\omega_{\text{sol}}$  (in eV) and relaxed static dipole moments (in Debye) are given.

SS-COSMO <i>n</i> -hexane										
State	$\omega$	$\omega(@S_0)$	$\Delta\omega_{\text{gas}}$	$\mu$	$\omega_{\text{sol}}(@S(\pi\pi^*))$	$\Delta\Delta\omega_{\text{sol}}$	$\mu$	$\omega_{\text{sol}}(@S(\text{CT}))$	$\Delta\Delta\omega_{\text{sol}}$	$\mu$
2-TCN										
T( $\pi\pi^*$ )	3.28	3.28	0.00	5.4	3.27	0.00	6.4	3.28	0.00	7.6
T(CT)	4.01	3.97	-0.04	9.2	3.95	-0.03	10.8	3.93	-0.04	12.8
S( $\pi\pi^*$ )	4.46	4.34	-0.12	9.3	4.32	-0.02	10.8	4.30	-0.04	13.8
S(CT)	4.88	4.64	-0.24	15.7	4.59	-0.05	16.9	4.55	-0.10	18.0
3-TCN										
T( $\pi\pi^*$ )	3.51	3.51	0.00	4.7	3.51	0.00	5.9	3.51	0.00	7.0
T(CT)	4.13	4.12	-0.01	7.1	4.10	-0.03	8.5	4.09	-0.03	10.0
S( $\pi\pi^*$ )	4.75	4.64	-0.11	8.9	4.60	-0.04	10.7	4.59	-0.05	12.1
S(CT)	5.12	4.92	-0.20	13.8	4.85	-0.07	15.6	4.81	-0.11	16.7
SS-COSMO acetonitrile										
State	$\omega$	$\omega(@S_0)$	$\Delta\omega_{\text{gas}}$	$\mu$	$\omega_{\text{sol}}(@S(\pi\pi^*))$	$\Delta\Delta\omega_{\text{sol}}$	$\mu$	$\omega_{\text{sol}}(@S(\text{CT}))$	$\Delta\Delta\omega_{\text{sol}}$	$\mu$
2-TCN										
T( $\pi\pi^*$ )	3.28	3.29	+0.01	6.1	3.18	-0.10	10.5	3.10	-0.19	14.6
T(CT)	4.01	3.99	-0.02	9.9	3.56	-0.44	16.3	3.10	-0.89	20.5
S( $\pi\pi^*$ )	4.46	4.34	-0.12	10.1	3.96	-0.38	15.3	3.62	-0.72	18.5
S(CT)	4.88	4.67	-0.21	16.4	3.95	-0.73	20.5	3.32	-1.35	22.6
3-TCN										
T( $\pi\pi^*$ )	3.51	3.53	+0.02	5.2	3.34	-0.19	10.6	3.20	-0.33	14.4
T(CT)	4.13	4.17	+0.04	7.3	3.78	-0.40	14.3	3.33	-0.84	19.1
S( $\pi\pi^*$ )	4.75	4.65	-0.10	9.4	4.12	-0.53	15.6	3.77	-0.88	18.5
S(CT)	5.12	5.03	-0.09	13.5	4.11	-0.92	19.2	3.51	-1.52	21.8
SS-COSMO water										
State	$\omega$	$\omega(@S_0)$	$\Delta\omega_{\text{gas}}$	$\mu$	$\omega_{\text{sol}}(@S(\pi\pi^*))^c$	$\Delta\Delta\omega_{\text{sol}}$	$\mu$	$\omega_{\text{sol}}(@S(\text{CT}))$	$\Delta\Delta\omega_{\text{sol}}$	$\mu$
2-TCN										
T( $\pi\pi^*$ )	3.28	3.29	+0.01	6.2	3.18	-0.11	10.6	3.04	-0.25	15.0
T(CT)	4.01	4.00	-0.02	10.0	3.53	-0.47	16.5	3.01	-0.99	20.8
S( $\pi\pi^*$ )	4.46	4.34	-0.12	10.1	3.94	-0.40	15.5	3.59	-0.75	18.7
S(CT)	4.88	4.68	-0.20	16.4	3.91	-0.77	20.6	3.26	-1.42	22.8
3-TCN										
T( $\pi\pi^*$ )	3.51	3.53	+0.02	5.2	3.32	-0.21	10.8	3.17	-0.36	15.2
T(CT)	4.13	4.18	+0.05	7.3	3.75	-0.43	14.6	3.27	-0.91	19.0
S( $\pi\pi^*$ )	4.75	4.65	-0.10	9.5	4.09	-0.56	15.8	3.72	-0.93	18.7
S(CT)	5.12	5.04	-0.08	13.4	4.07	-0.97	20.1	3.45	-1.59	22.0

<sup>a</sup>  $\Delta\omega_{\text{gas}}$  is the difference between vertical excitation energies in gas phase and computed using SS-COSMO equilibrating the ASC with respect to the ground state density.

<sup>b</sup>  $\Delta\Delta\omega_{\text{sol}}$  is the difference between vertical excitation energies in solution within COSMO solvation when the ASC is equilibrated with the ground state density and with the respective excited state density.

<sup>c</sup> relaxed convergence criteria have been used due to convergence problems.

---

APPENDIX FOR CHAPTER 6

---

**B.1 THE PHOTOCHEMISTRY OF FDMA**

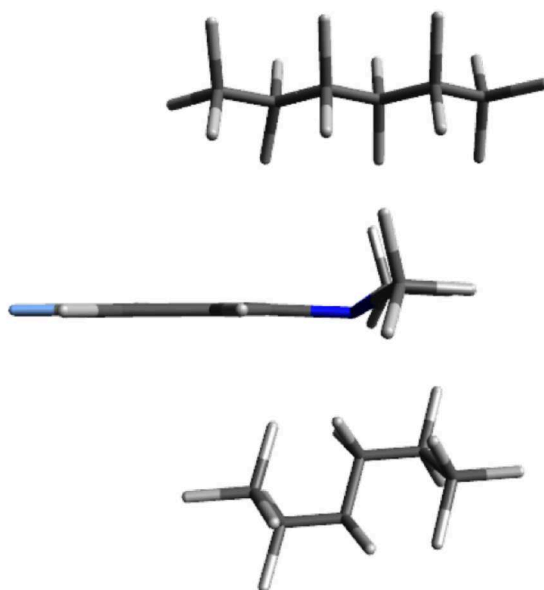


FIGURE B.1: Ground state equilibrium geometry obtained at MP2/cc-pVDZ level with two *n*-hexane molecules added. No reoptimization has been performed

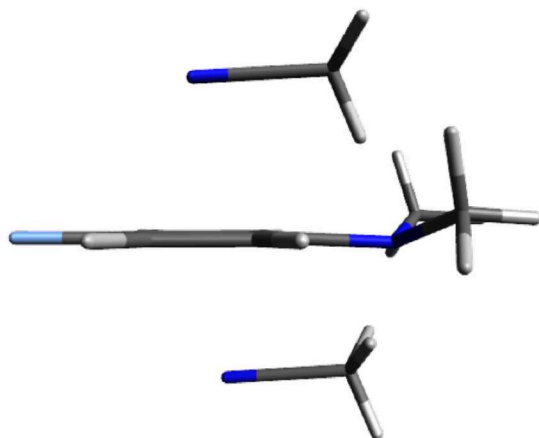


FIGURE B.2: Ground state equilibrium geometry obtained at MP2/cc-pVDZ level with two ACN molecules added. No reoptimization has been performed

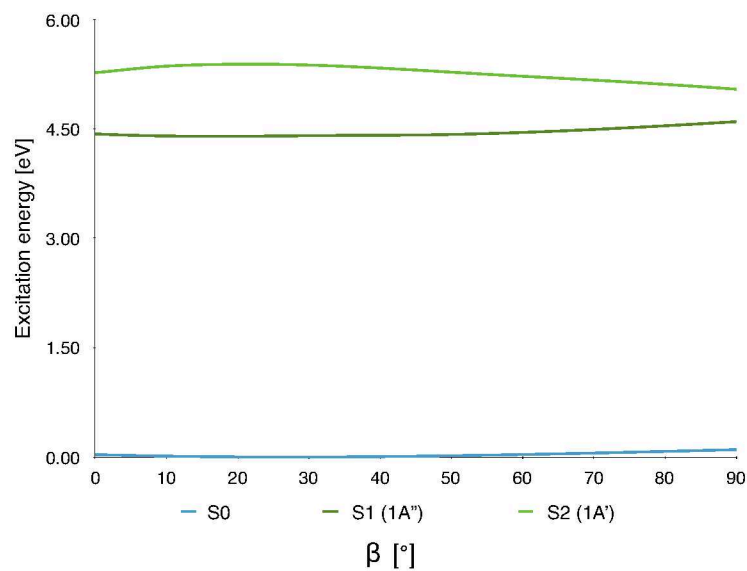


FIGURE B.3: Relaxed PES scan of the ground state along the twisting coordinate  $\beta$  obtained at MP2/TD-B3LYP/cc-pVDZ level of theory.

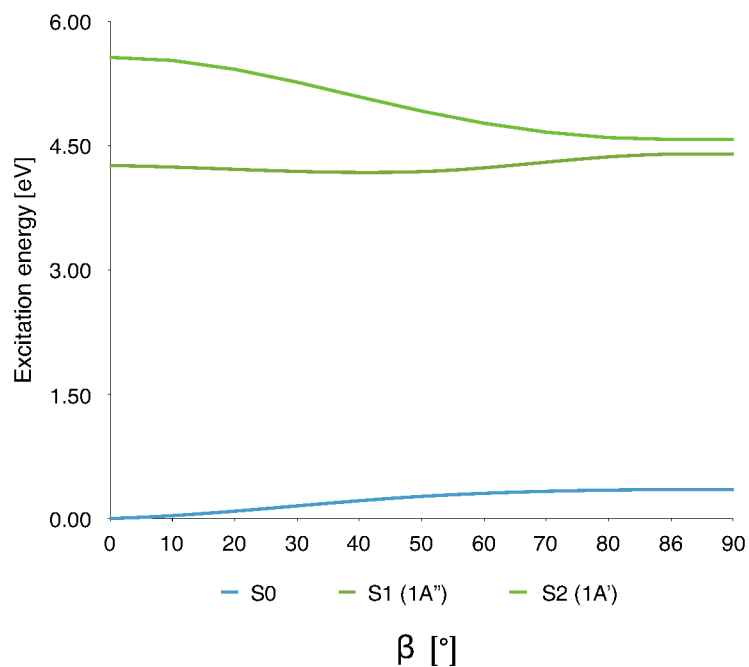


FIGURE B.4: Rigid PES scans of the  $S_1$  ( $1A''$ ) state along the twisting coordinate  $\beta$  obtained at TD-CAM-B3LYP/cc-pVDZ level of theory. As starting geometry, the  $1A''$  planar ( $\beta = 0^\circ$ ) equilibrium geometry computed at TD-B3LYP/cc-pVDZ level of theory has been used.

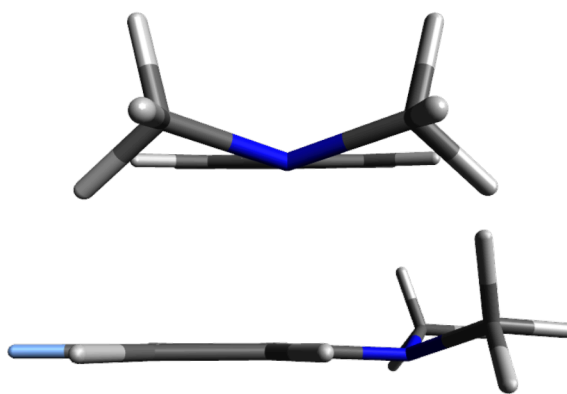


FIGURE B.5:  $C_s$  symmetric ground state equilibrium geometry obtained at MP2/cc-pVTZ level of theory.

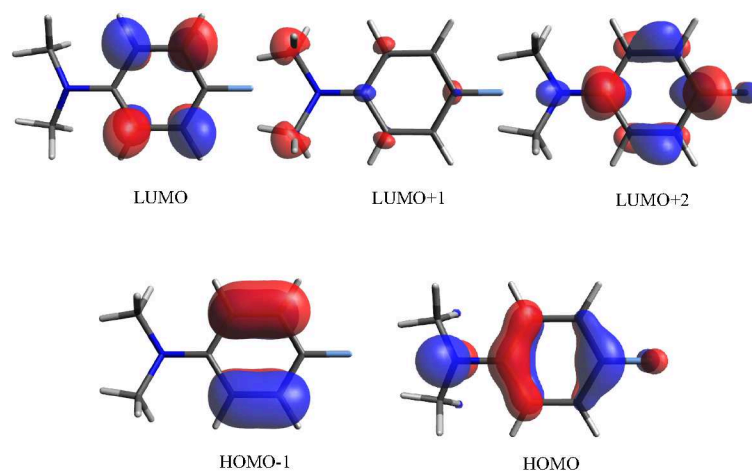


FIGURE B.6: HF valence MOs obtained at ADC(2)/cc-pVTZ level of theory at the MP2 ground state equilibrium geometry (Isovalue = 0.05).

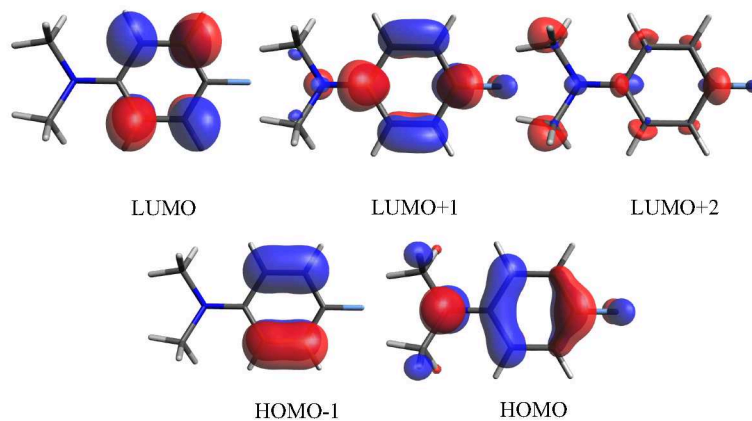


FIGURE B.7: KS valence MOs obtained at TD-CAM-B3LYP/cc-pVTZ level of theory at the MP2 ground state equilibrium geometry (Isovalue = 0.05).

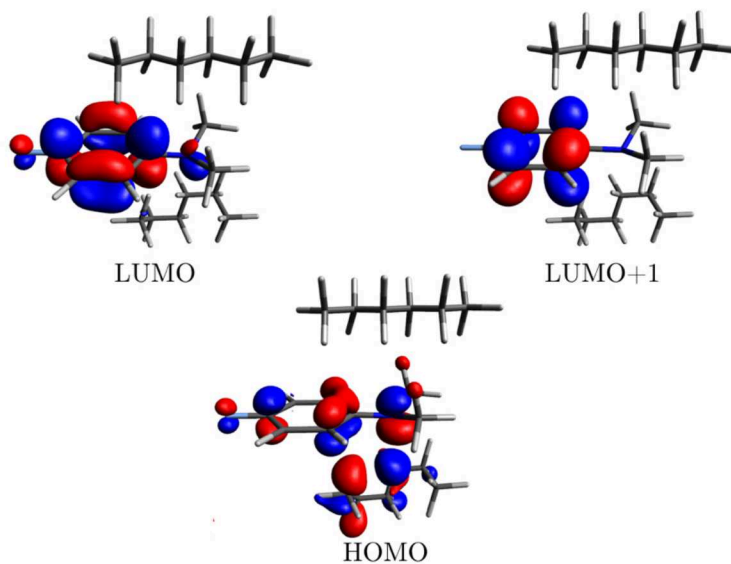


FIGURE B.8: KS MOs obtained at TD-CAM-B3LYP/cc-pVTZ level of theory at the MP2 ground state equilibrium geometry with two *n*-hexane molecules added (Isovalue = 0.05). Without reoptimization of the FDMA-*n*-hexane cluster.

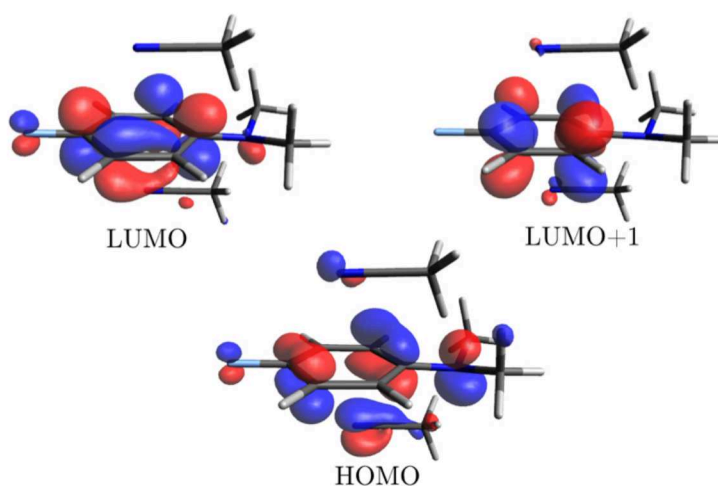


FIGURE B.9: KS MOs obtained at TD-CAM-B3LYP/cc-pVTZ level of theory at the MP2 ground state equilibrium geometry with two acetonitrile (ACN) molecules added (Isovalue = 0.05). Without reoptimization of the FDMA-ACN cluster.



FIGURE B.10: Approximate  $S_2$ - $S_1$  conical intersection geometry obtained at LR-CC2/cc-pVDZ level of theory without applying symmetry constraints during geometry optimization

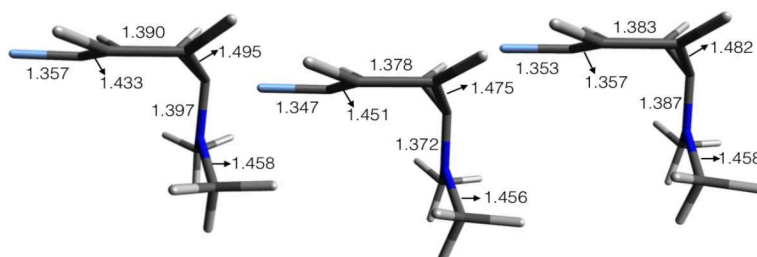


FIGURE B.11: Approximate  $S_1$ - $S_0$  conical intersection geometries obtained at LR-CC2/cc-pVDZ (left), TD-CAM-B3LYP (middle) and TD-B3LYP/cc-pVDZ (right) levels of theory without applying symmetry constraints during geometry optimization

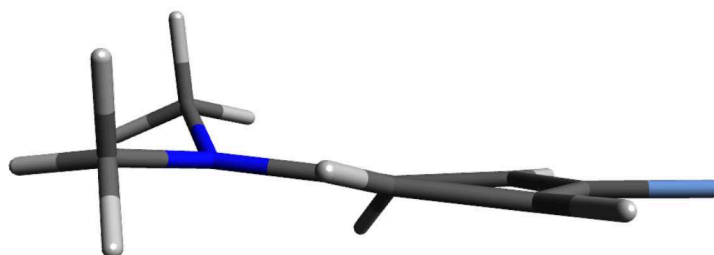


FIGURE B.12:  $T_1$  equilibrium geometry obtained at CAM-B3LYP/cc-pVDZ level of theory.

## APPENDIX FOR CHAPTER 7

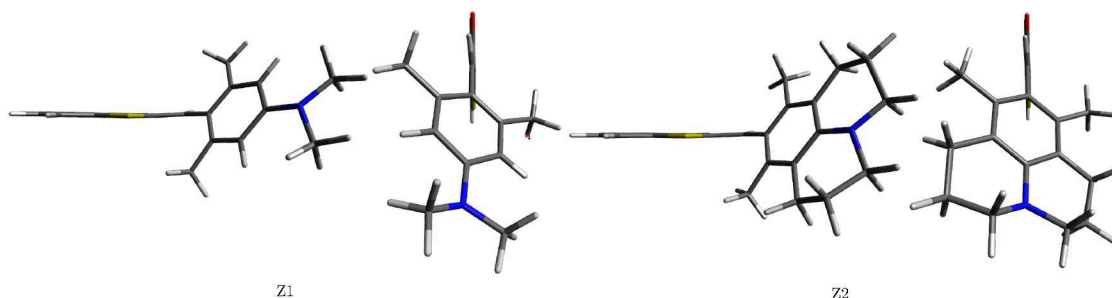
**C.1 Z/E PHOTOISOMERIZATION OF HEMITHIOINDIGO DERIVATIVES  
Z1-Z4**

FIGURE C.1:  $S_0$  equilibrium geometry of HTI Z1 obtained at MP2/cc-pVDZ level of theory.

FIGURE C.2:  $S_0$  equilibrium geometry of HTI Z2 obtained at MP2/cc-pVDZ level of theory.

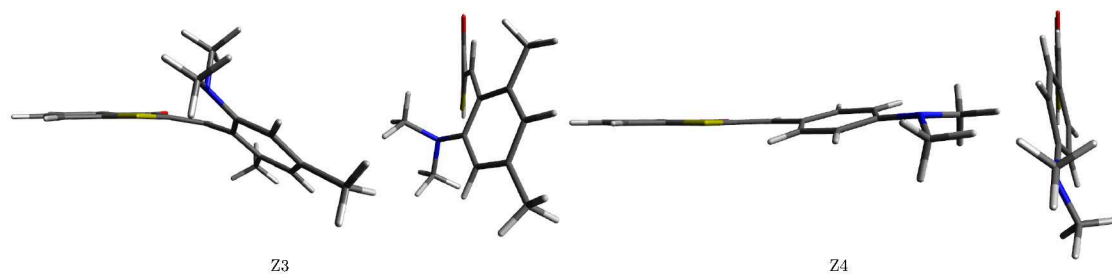


FIGURE C.3:  $S_0$  equilibrium geometry of HTI Z3 obtained at MP2/cc-pVDZ level of theory.

FIGURE C.4:  $S_0$  equilibrium geometry of HTI Z4 obtained at MP2/cc-pVDZ level of theory.

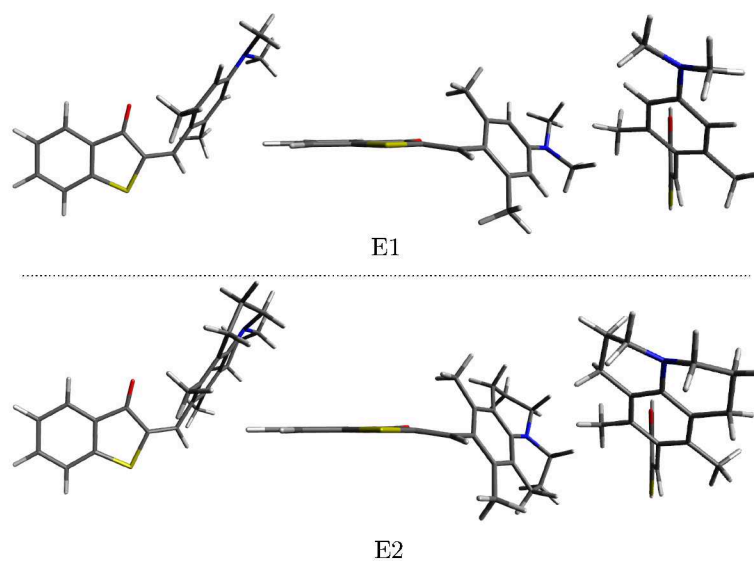


FIGURE C.5: Ground state equilibrium geometry of HTI E1 and E2 obtained at MP2/cc-pVDZ level of theory.

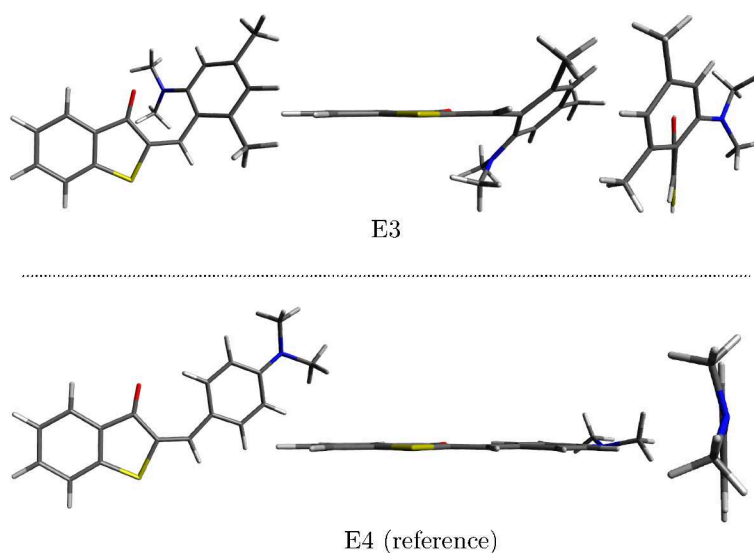


FIGURE C.6: Ground state equilibrium geometry of HTI E3 and E4 obtained at MP2/cc-pVDZ level of theory.

TABLE C.1: Comparison of the gas-phase vertical excitation energies and static dipole moments of the few lowest singlet states of HTI E1-E4 calculated at the FC geometry using different levels of theory. Orbital transitions ( $> 20\%$ )<sup>a</sup>, character of the transitions, vertical excitation energies  $\omega$  (in eV), oscillator strengths (in parenthesis) and relaxed static dipole moments  $\mu$  (in Debye) are given.

State	MOs	Character	ADC(2)		
			$\omega$	$\mu$	$\omega(\text{Z1})$
E1					
S <sub>1</sub>	H > L	$\pi\pi^*(\text{CT})$	2.79(0.18)	8.4	3.14(0.19)
	H-6 > L	$n\pi^*$			
S <sub>2</sub>	H-6 > L	$n\pi^*$	3.27(0.12)	3.3	3.33(0.14)
	H > L	$\pi\pi^*(\text{CT})$			
S <sub>3</sub>	H-1 > L	$\pi\pi^*(\text{Thioindigo})$	3.59(0.12)	5.6	
E2					
S <sub>1</sub>	H > L	$\pi\pi^*(\text{CT})$	2.69(0.16)	11.6	3.09(0.19)
	H-6 > L	$n\pi^*$			
S <sub>2</sub>	H-6 > L	$n\pi^*$	3.24(0.08)	5.9	3.33(0.10)
E3					
S <sub>1</sub>	H > L	$\pi\pi^*(\text{CT})$	2.56(0.15)	8.3	3.12(0.15)
S <sub>2</sub>	H-6 > L	$n\pi^*$	2.95(0.03)	2.14	3.26(0.10)
S <sub>3</sub>	H-1 > L	$\pi\pi^*(\text{CT}')$	3.38(0.06)	2.5	
	H-6 > L	$n\pi^*$			
S <sub>4</sub>	H-2 > L	$\pi\pi^*$	4.20(0.16)	5.0	4.31(0.21)
E4					
S <sub>1</sub>	H > L	$\pi\pi^*$	3.85(0.51)	7.9	3.10(0.64)
S <sub>3</sub>	H-1 > L	$\pi\pi^*$	3.68(0.34)	6.8	3.86(0.22)

<sup>a</sup> For the sake of compactness only the two leading configurations are given.

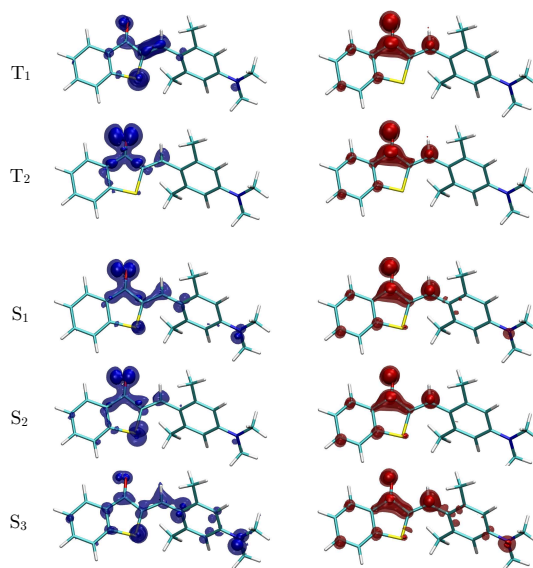


FIGURE C.7: Attachment (red) and detachment (blue) density plots for the lowest excited singlet and triplet states of HTI Z1 obtained at ADC(2)/cc-pVDZ level of theory (Isovalue 0.014)

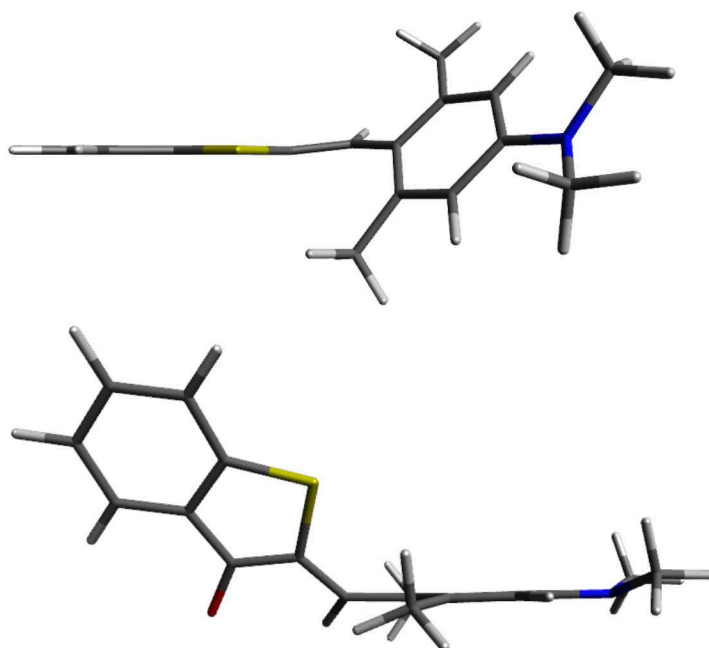


FIGURE C.8: Stationary structure of the  $S_1$  state ( $S_{1N_{\text{pyr}}}$ ) of HTI Z1 obtained at LR-CC2/cc-pVDZ level of theory upon full geometry optimization at the constrained-optimized geometry with  $\beta=90^\circ$  obtained at TD-CAM-B3LYP/cc-pVDZ level of theory.

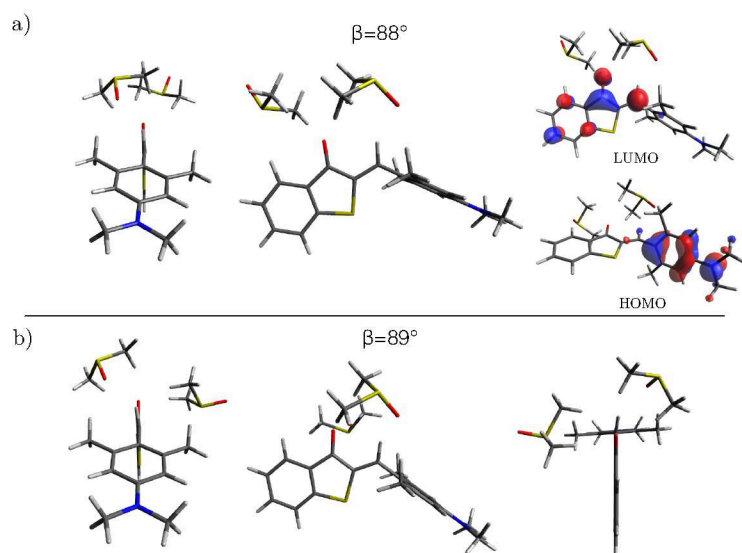


FIGURE C.9: Stationary structures of the  $S_1$  state of HTI Z1 DMSO clusters obtained at TD-CAM-B3LYP/6-31G\* level of theory.

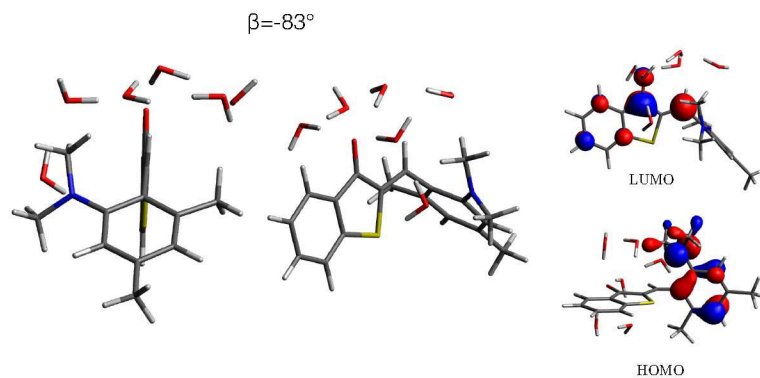


FIGURE C.10: Stationary structure of the  $S_1$  state of a HTI Z3  $H_2O$  cluster obtained at TD-CAM-B3LYP/6-31G\* level of theory.

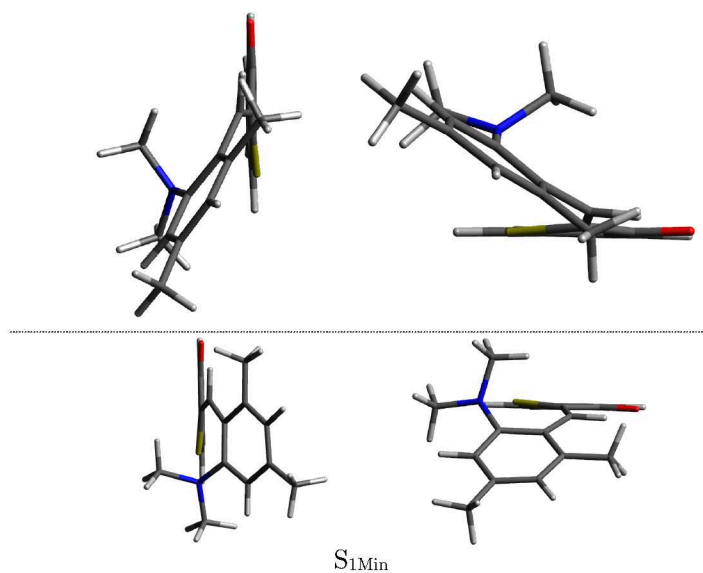


FIGURE C.11: Top: Two views of the geometry of HTI Z3 obtained upon geometry optimization of the  $S_1$  state starting with a  $\beta = -90^\circ$  twisted geometry, performed at LR-CC2/cc-pVDZ level of theory in which  $S_1$  and  $S_0$  states are almost degenerate. For comparison the local  $S_1$  state minimum  $S_{1Min}$  obtained at LR-CC2/cc-pVDZ level of theory is given at the bottom.

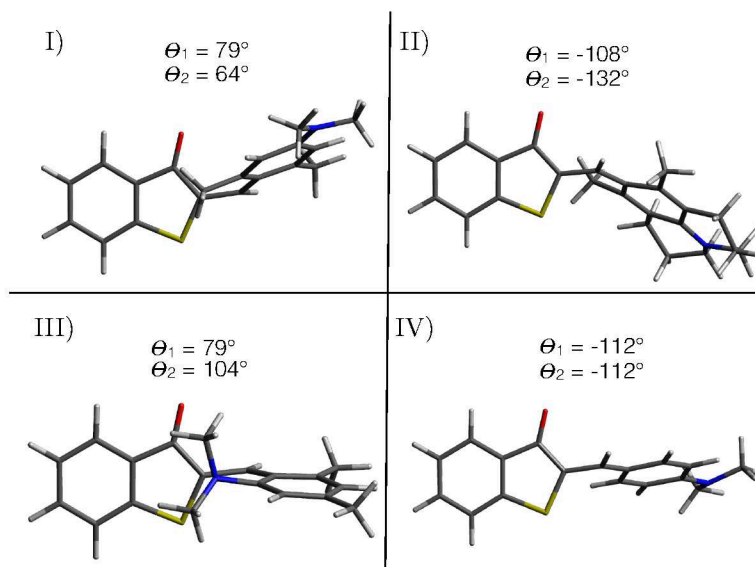


FIGURE C.12: Approximate  $T_1$ - $S_0$  conical intersection geometries of HTIs I) Z1 II) Z2 III) Z3 and IV) Z4 obtained at LR-CC2/cc-pVDZ level of theory.

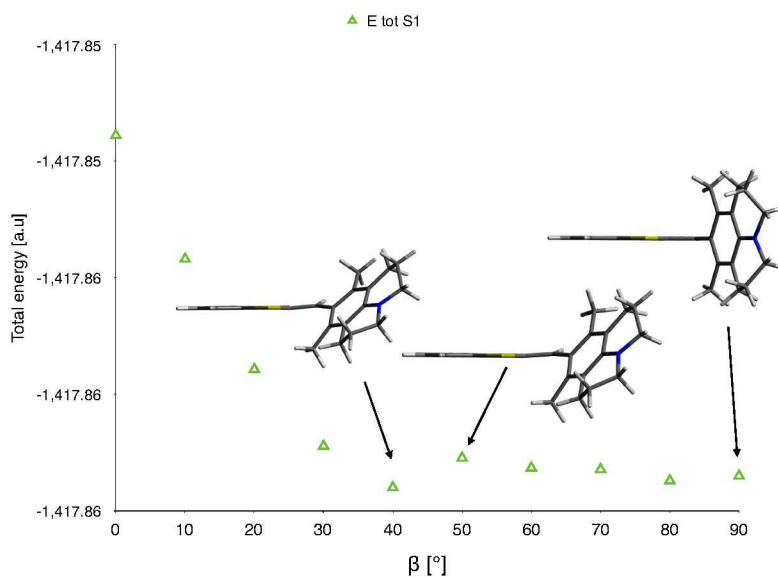


FIGURE C.13: Relaxed  $S_1$  PES scan of HTI Z2 along  $\beta$  obtained at TD-CAM-B3LYP/6-31G\*//TD-CAM-B3LYP/cc-pVDZ level of theory. Total energies of the  $S_1$  state are shown. At  $\beta=40^\circ$  a discontinuity occurs.

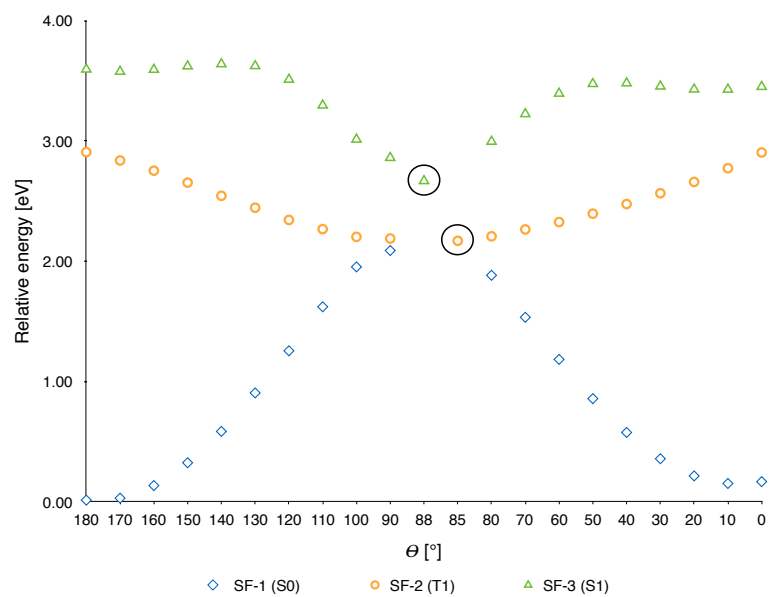


FIGURE C.14: Relaxed scan of the  $S_0$  PES of HTI 1 for the Z/E isomerization obtained at SF-B5050LYP/6-31G\* level of theory. Energies are relative to the  $S_0$  equilibrium energy.

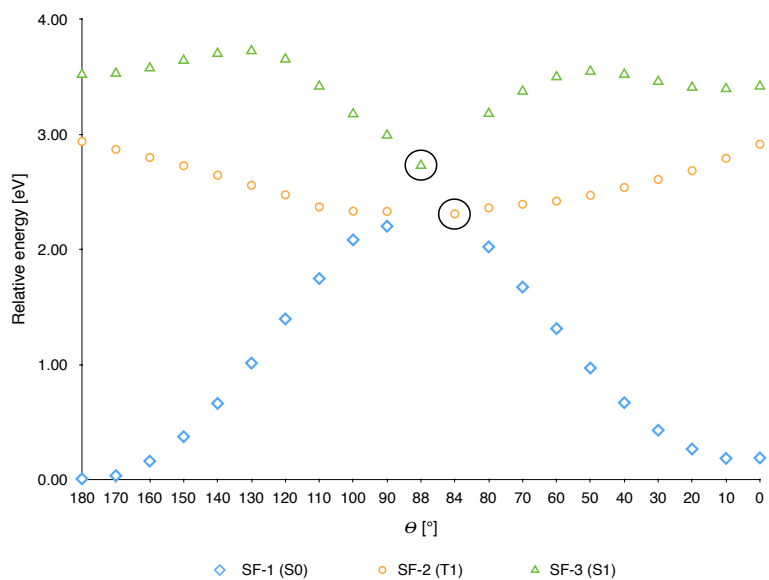


FIGURE C.15: Relaxed scan of the  $S_0$  PES of HTI 2 for the Z/E isomerization obtained at SF-B5050LYP/6-31G\* level of theory. Energies are relative to the  $S_0$  equilibrium energy.

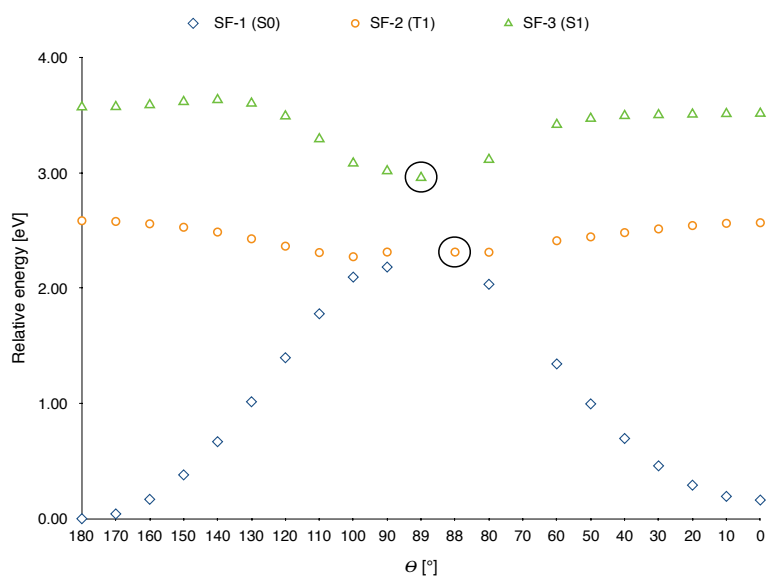


FIGURE C.16: Relaxed scan of the  $S_0$  PES of HTI 4 for the Z/E isomerization obtained at SF-B5050LYP/6-31G\* level of theory. Energies are relative to the  $S_0$  equilibrium energy.

## APPENDIX FOR CHAPTER 8

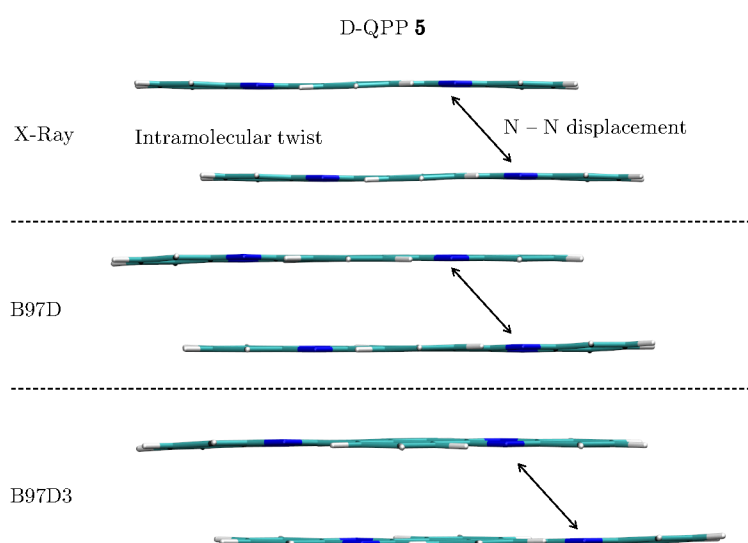
**D.1 INTERMOLECULAR INTERACTIONS IN  
QUINOXALINOPHENANTHROPHENAZINE (QPP) DIMERS**

FIGURE D.1: Structures of D-QPP **5** (with view along the y-axis) represented using the wireframe model. Top: Crystal structure (X-Ray). Middle: B97D/cc-pVDZ optimized geometry. Bottom: B97D3/cc-pVDZ optimized geometry.

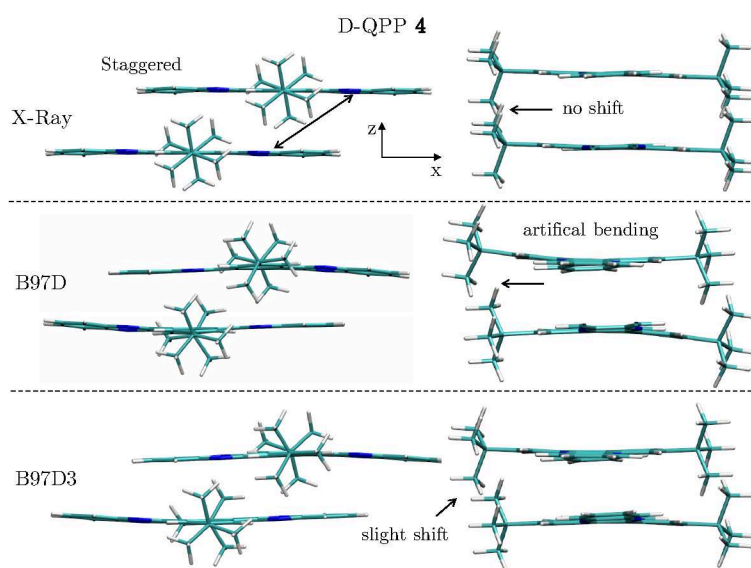


FIGURE D.2: Structures of D-QPP 4 from two different perspectives (with view along y- and along x-axis) represented using the wireframe model. Top: Crystal structure (CS). Middle: B97D/cc-pVDZ optimized geometry. Bottom: B97D3/cc-pVDZ optimized geometry.

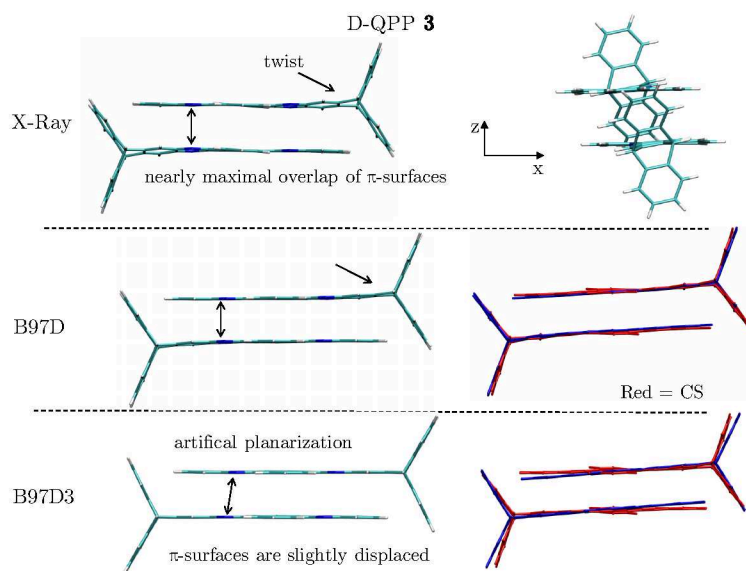


FIGURE D.3: Structures of D-QPP 3 represented using the wireframe model. Top: Crystal structure (X-Ray) (with view along y- and along x-axis). Middle: B97D/cc-pVDZ optimized geometry and superposition of the CS and B97D optimized geometry. Bottom: B97D3/cc-pVDZ optimized geometry.

---

## BIBLIOGRAPHY

---

- [1] Schrödinger, E. Quantisierung Als Eigenwertproblem. *Annalen der Physik* **1926**, *385*, 437–490.
- [2] Schrödinger, E. *Gesammelte Abhandlungen*; Friedr. Vieweg & Sohn, 1984.
- [3] Heitler, W.; London, F. Wechselwirkung Neutraler Atome Und Homöopolare Bindung Nach Der Quantenmechanik. *Zeitschrift für Physik A Hadrons and Nuclei* **1927**, *44*, 455–472.
- [4] Whitmarsh, J.; Singhal, G.; Renger, G.; Sopory, S.; Irrgang, K.; Govindjee, G. Concepts in Photobiology: Photosynthesis and Photomorphogenesis. 1999.
- [5] Ritz, T.; Damjanović, A.; Schulten, K. The Quantum Physics of Photosynthesis. *Chemical Physics and Physical Chemistry* **2002**, *3*, 243–248.
- [6] Fleming, G. R.; Scholes, G. D. Physical Chemistry: Quantum Mechanics for Plants. *Nature* **2004**, *431*, 256–257.
- [7] Dreuw, A. Quantum Chemical Methods for the Investigation of Photoinitiated Processes in Biological Systems: Theory and Applications. *Chemical Physics and Physical Chemistry* **2006**, *7*, 2259–2274.
- [8] Lee, H.; Cheng, Y.-C.; Fleming, G. R. Coherence Dynamics in Photosynthesis: Protein Protection of Excitonic Coherence. *Science* **2007**, *316*, 1462–1465.
- [9] Voityuk, A. A.; Michel-Beyerle, M.-E.; Rösch, N. A Quantum Chemical Study of Photoinduced DNA Repair: On the Splitting of Pyrimidine Model Dimers Initiated by Electron Transfer. *Journal of the American Chemical Society* **1996**, *118*, 9750–9758.
- [10] Hall, D. B.; Holmlin, R. E.; Barton, J. K. Oxidative DNA Damage Through Long-Range Electron Transfer. *Nature* **1996**, *382*, 731.
- [11] Sinha, R. P.; Häder, D.-P. UV-Induced DNA Damage and Repair: A Review. *Photochemical & Photobiological Sciences* **2002**, *1*, 225–236.
- [12] Faraji, S.; Dreuw, A. Physicochemical Mechanism of Light-Driven DNA Repair by (6-4) Photolyases. *Annual Review of Physical Chemistry* **2014**, *65*, 275–292.
- [13] Rosenfeld, T.; Honig, B.; Ottolenghi, M.; Hurley, J.; Ebrey, T. G. Cis-Trans Isomerization in the Photochemistry of Vision. *Pure and Applied Chemistry* **1977**, *49*, 341–351.

- [14] Green, B.; Monger, T.; Alfano, R.; Aton, B.; Callender, R. Cis–Trans Isomerisation in Rhodopsin Occurs in Picoseconds. *Nature* **1977**, *269*, 179–180.
- [15] Polli, D.; Altoè, P.; Weingart, O.; Spillane, K. M.; Manzoni, C.; Brida, D.; Tomasello, G.; Orlandi, G.; Kukura, P.; Mathies, R. A. Conical Intersection Dynamics of the Primary Photoisomerization Event in Vision. *Nature* **2010**, *467*, 440.
- [16] Kohler, A.; Dos Santos, D.; Beljonne, D.; Shuai, Z. Charge Separation in Localized and Delocalized Electronic States in Polymeric Semiconductors. *Nature* **1998**, *392*, 903.
- [17] Grätzel, M. Dye-Sensitized Solar Cells. *Journal of Photochemistry and Photobiology C: Photochemistry Reviews* **2003**, *4*, 145–153.
- [18] Coropceanu, V.; Cornil, J.; da Silva Filho, D. A.; Olivier, Y.; Silbey, R.; Brédas, J.-L. Charge Transport in Organic Semiconductors. *Chemical Reviews* **2007**, *107*, 926–952.
- [19] Brédas, J.-L.; Norton, J. E.; Cornil, J.; Coropceanu, V. Molecular Understanding of Organic Solar Cells: The Challenges. *Accounts of Chemical Research* **2009**, *42*, 1691–1699.
- [20] Jailaubekov, A. E.; Willard, A. P.; Tritsch, J. R.; Chan, W.-L.; Sai, N.; Gearba, R.; Kaake, L. G.; Williams, K. J.; Leung, K.; Rossky, P. J. Hot Charge-Transfer Excitons Set the Time Limit for Charge Separation at Donor/Acceptor Interfaces in Organic Photovoltaics. *Nature Materials* **2013**, *12*, 66.
- [21] Rohatgi-Mukherjee, K. *Fundamentals of Photochemistry*; New Age International, 1978.
- [22] Franck, J.; Dymond, E. Elementary Processes of Photochemical Reactions. *Transactions of the Faraday Society* **1926**, *21*, 536–542.
- [23] Condon, E. U. A Theory of Intensity Distribution in Band Systems. *Physical Review* **1926**, *28*, 1182.
- [24] Birge, R. T. The Band Spectra of Carbon Monoxide. *Physical Review* **1926**, *28*, 1157.
- [25] Jaffe, H.; Miller, A. L. The Fates of Electronic Excitation Energy. *Journal of Chemical Education* **1966**, *43*, 469.
- [26] Harris, D. C.; Bertolucci, M. D. *Symmetry and Spectroscopy: An Introduction to Vibrational and Electronic Spectroscopy*; Courier Corporation, 1978.
- [27] Marian, C. M. Spin-Orbit Coupling and Intersystem Crossing in Molecules. *Wiley Interdisciplinary Reviews: Computational Molecular Science* **2012**, *2*, 187–203.
- [28] Valeur, B.; Berberan-Santos, M. N. *Molecular Fluorescence: Principles and Applications*; John Wiley & Sons, 2012.
- [29] Kasha, M. Characterization of Electronic Transitions in Complex Molecules. *Discussions of the Faraday Society* **1950**, *9*, 14.
- [30] Suppan, P.; Ghoneim, N. *Solvatochromism*; Royal Society of Chemistry, 1997.
- [31] Frey, R. F.; Davidson, E. R. The von Neumann-Wigner and Jahn-Teller Theorems and Their Consequences. *Advances in Molecular Electronic Structure Theory* **1990**, *1*, 213–262.

- [32] Yarkony, D. R. Conical intersections: The New Conventional Wisdom. *The Journal of Physical Chemistry A* **2001**, *105*, 6277–6293.
- [33] Simon, J. *Ultrafast Dynamics of Chemical Systems*; Understanding Chemical Reactivity; Springer Netherlands, 2012.
- [34] Schrieber, C.; Lochbrunner, S.; Riedle, E.; Nesbitt, D. Ultrasensitive Ultraviolet-Visible 20 fs Absorption Spectroscopy of Low Vapor Pressure Molecules in the Gas Phase. *Review of Scientific Instruments* **2008**, *79*, 013107.
- [35] Berera, R.; van Grondelle, R.; Kennis, J. T. Ultrafast Transient Absorption Spectroscopy: Principles and Application to Photosynthetic Systems. *Photosynthesis Research* **2009**, *101*, 105–118.
- [36] Verhoeven, J. W. On the Role of Spin Correlation in the Formation, Decay, and Detection of Long-Lived, Intramolecular Charge-Transfer States. *Journal of Photochemistry and Photobiology C: Photochemistry Reviews* **2006**, *7*, 40–60.
- [37] González-Rodríguez, D.; Torres, T.; Olmstead, M. M.; Rivera, J.; Herranz, M. Á.; Echegoyen, L.; Castellanos, C. A.; Guldi, D. M. Photoinduced Charge-Transfer States in Subphthalocyanine- Ferrocene Dyads. *Journal of the American Chemical Society* **2006**, *128*, 10680–10681.
- [38] Ahn, T. K.; Avenson, T. J.; Ballottari, M.; Cheng, Y.-C.; Niyogi, K. K.; Bassi, R.; Fleming, G. R. Architecture of a Charge-Transfer State Regulating Light Harvesting in a Plant Antenna Protein. *Science* **2008**, *320*, 794–797.
- [39] Tucker, J. W.; Stephenson, C. R. Shining Light on Photoredox Catalysis: Theory and Synthetic Applications. *The Journal of Organic Chemistry* **2012**, *77*, 1617–1622.
- [40] Sasaki, S.; Drummen, G. P.; Konishi, G. Recent Advances in Twisted Intramolecular Charge Transfer (TICT) Fluorescence and Related Phenomena in Materials Chemistry. *Journal of Materials Chemistry C* **2016**, *4*, 2731–2743.
- [41] Blasse, G. The Influence of Charge-Transfer and Rydberg States on the Luminescence Properties of Lanthanides and Actinides. *Spectra and Chemical Interactions* **1976**, 43–79.
- [42] Renger, T. Theory of Optical Spectra Involving Charge Transfer States: Dynamic Localization Predicts a Temperature Dependent Optical Band Shift. *Physical Review Letters* **2004**, *93*, 188101.
- [43] Deibel, C.; Strobel, T.; Dyakonov, V. Role of the Charge Transfer State in Organic Donor–Acceptor Solar Cells. *Advanced Materials* **2010**, *22*, 4097–4111.
- [44] Margulies, E. A.; Miller, C. E.; Wu, Y.; Ma, L.; Schatz, G. C.; Young, R. M.; Wasielewski, M. R. Enabling Singlet Fission by Controlling Intramolecular Charge Transfer in  $\pi$ -Stacked Covalent Terrylene-diimide Dimers. *Nature Chemistry* **2016**, *8*, 1120–1125.
- [45] Hallermann, M.; Haneder, S.; Da Como, E. Charge-Transfer States in Conjugated Polymer/fullerene Blends: Below-Gap Weakly Bound Excitons for Polymer Photovoltaics. *Applied Physics Letters* **2008**, *93*, 290.

- [46] Beaujuge, P. M.; Amb, C. M.; Reynolds, J. R. Spectral Engineering in  $\pi$ -Conjugated Polymers with Intramolecular Donor- Acceptor Interactions. *Accounts of Chemical Research* **2010**, *43*, 1396–1407.
- [47] Lee, J.; Vandewal, K.; Yost, S. R.; Bahlke, M. E.; Goris, L.; Baldo, M. A.; Manca, J. V.; Voorhis, T. V. Charge Transfer State Versus Hot Exciton Dissociation in Polymer- Fullerene Blended Solar Cells. *Journal of the American Chemical Society* **2010**, *132*, 11878–11880.
- [48] Prier, C. K.; Rankic, D. A.; MacMillan, D. W. Visible Light Photoredox Catalysis with Transition Metal Complexes: Applications in Organic Synthesis. *Chemical Reviews* **2013**, *113*, 5322–5363.
- [49] Xi, Y.; Yi, H.; Lei, A. Synthetic Applications of Photoredox Catalysis with Visible Light. *Organic & Biomolecular Chemistry* **2013**, *11*, 2387–2403.
- [50] Grabowski, Z. R.; Dobkowski, J. Twisted Intramolecular Charge Transfer (TICT) Excited States: Energy and Molecular Structure. *Pure and Applied Chemistry* **1983**, *55*, 245–252.
- [51] Rettig, W. Charge Separation in Excited States of Decoupled Systems-TICT Compounds and Implications Regarding the Development of New Laser Dyes and the Primary Process of Vision and Photosynthesis. *Angewandte Chemie International Edition* **1986**, *25*, 971–988.
- [52] Ramamurthy, V.; Schanze, K. *Organic Molecular Photochemistry; Molecular and Supramolecular Photochemistry*; Taylor & Francis, 1999.
- [53] Hu, R.; Lager, E.; Aguilar-Aguilar, A.; Liu, J.; Lam, J. W. Y.; Sung, H. H. Y.; Williams, I. D.; Zhong, Y.; Wong, K. S.; Peña Cabrera, E.; Tang, B. Z. Twisted Intramolecular Charge Transfer and Aggregation-Induced Emission of BODIPY Derivatives. *The Journal of Physical Chemistry C* **2009**, *113*, 15845–15853.
- [54] Georgieva, I.; Aquino, A. J.; Plasser, F.; Trendafilova, N.; Köhn, A.; Lischka, H. Intramolecular Charge-Transfer Excited-State Processes in 4-(N, N-Dimethylamino) Benzonitrile: The Role of Twisting and the  $\pi\sigma^*$  State. *The Journal of Physical Chemistry A* **2015**, *119*, 6232–6243.
- [55] Cao, C.; Liu, X.; Qiao, Q.; Zhao, M.; Yin, W.; Mao, D.; Zhang, H.; Xu, Z. A Twisted-Intramolecular-Charge-Transfer (TICT) Based Ratiometric Fluorescent Thermometer with a Mega-Stokes Shift and a Positive Temperature Coefficient. *Chemical Communications* **2014**, *50*, 15811–15814.
- [56] Grabowski, Z. R.; Rotkiewicz, K.; Rettig, W. Structural Changes Accompanying Intramolecular Electron Transfer: Focus on Twisted Intramolecular Charge-Transfer States and Structures. *Chemical Reviews* **2003**, *103*, 3899–4032.
- [57] Alhassawi, F. M.; Corradini, M. G.; Rogers, M. A.; Ludescher, R. D. Potential Applications of Luminescent Molecular Rotors in Food Science and Engineering. *Critical Reviews in Food Science and Nutrition* **2017**, 1–15.
- [58] Demchenko, A. *Advanced Fluorescence Reporters in Chemistry and Biology I: Fundamentals and Molecular Design*; Springer Series on Fluorescence; Springer Berlin Heidelberg, 2010.

- [59] Launay, J.-P.; Sowinska, M.; Leydier, L.; Gourdon, A.; Amouyal, E.; Boillot, M.-L.; Heisel, F.; Miehé, J. A. Towards Molecular Switching: Photophysical Properties of N, N'-Bis (4-Cyanophenyl) Piperazine, a Bridging TICT Molecule. *Chemical Physics Letters* **1989**, *160*, 89–95.
- [60] Shen, P.; Xiao, S.; Zhan, X.; Zhang, W.; Chang, K.; Yang, C. A New PH Fluorescent Molecular Switch by Modulation of Twisted Intramolecular Charge Transfer with Protonation. *Journal of Physical Organic Chemistry* **2013**, *26*, 858–862.
- [61] Li, W.; Pan, Y.; Yao, L.; Liu, H.; Zhang, S.; Wang, C.; Shen, F.; Lu, P.; Yang, B.; Ma, Y. A Hybridized Local and Charge-Transfer Excited State for Highly Efficient Fluorescent Oleds: Molecular Design, Spectral Character, and Full Exciton Utilization. *Advanced Optical Materials* **2014**, *2*, 892–901.
- [62] Grabowski, Z. R.; Rotkiewicz, K.; Siemiarczuk, A. Dual Fluorescence of Donor-Acceptor Molecules and the Twisted Intramolecular Charge Transfer (TICT) States. *Journal of Luminescence* **1979**, *18*, 420–424.
- [63] Rettig, W.; Lippert, E. Twisting Relaxation and Dual Fluorescence of PN, N-Dialkylaminobenzonitriles. *Journal of Molecular Structure* **1980**, *61*, 17–22.
- [64] Mennucci, B.; Toniolo, A.; Tomasi, J. Ab Initio Study of the Electronic Excited States in 4-(N, N-Dimethylamino) Benzonitrile with Inclusion of Solvent Effects: The Internal Charge Transfer Process. *Journal of the American Chemical Society* **2000**, *122*, 10621–10630.
- [65] Ma, C.; Kwok, W.; Matousek, P.; Parker, A.; Phillips, D.; Toner, W.; Towrie, M. Excited States of 4-Aminobenzonitrile (ABN) and 4-Dimethylaminobenzonitrile (DMABN): Time-Resolved Resonance Raman, Transient Absorption, Fluorescence, and Ab Initio Calculations. *The Journal of Physical Chemistry A* **2002**, *106*, 3294–3305.
- [66] Zilberg, S.; Haas, Y. The Nature of the Intramolecular Charge Transfer Excited State in P-Pyrrolocyanobenzene (PBN) and Other Derivatives of Benzene Substituted by Electron Donor and Acceptor Groups. *The Journal of Physical Chemistry A* **2002**, *106*, 1–11.
- [67] Weigel, W.; Rettig, W.; Dekhtyar, M.; Modrakowski, C.; Beinhoff, M.; Schlüter, A. D. Dual Fluorescence of Phenyl and Biphenyl Substituted Pyrene Derivatives. *The Journal of Physical Chemistry A* **2003**, *107*, 5941–5947.
- [68] Murali, S.; Rettig, W. TICT Formation in Para- and Meta-Derivatives of N-Phenylpyrrole. *The Journal of Physical Chemistry A* **2006**, *110*, 28–37.
- [69] Lippert, E.; Lüder, W.; Moll, F.; Nägele, W.; Boos, H.; Prigge, H.; Seibold-Blankenstein, I. Umwandlung Von Elektronenanregungsenergie. *Angewandte Chemie* **73**, 695–706.
- [70] Lippert, E. Dipolmoment Und Elektronenstruktur Von Angeregten Molekülen. *Zeitschrift für Naturforschung A* **1955**, *10*, 541–545.
- [71] Lippert, E.; Lüder, W.; Boos, H.; Mangini, A. Advances in Molecular Spectroscopy. European Conference on Molecular Spectroscopy, Bologna, Italy, 1959-1962.
- [72] Kalcic, C. L.; Harris, D. A.; Dantus, M. Controlling the Excited State Charge Transfer in DMABN Using Shaped Femtosecond Pulses. Photonic Applications Systems Technologies Conference. 2007; p JWA61.

- [73] Zachariasse, K. A.; Druzhinin, S. I.; Kovalenko, S. A.; Senyushkina, T. Intramolecular Charge Transfer of 4-(dimethylamino) Benzonitrile Probed by Time-Resolved Fluorescence and Transient Absorption: No Evidence for Two ICT States and a  $\pi \sigma^*$  Reaction Intermediate. *The Journal of Chemical Physics* **2009**, *131*, 224313.
- [74] Nakashima, N.; Inoue, H.; Mataga, N.; Yamanaka, C. Time-Resolved Fluorescence Studies on the Dual Fluorescence Process of P-(Dimethylamino) Benzonitrile. *Bulletin of the Chemical Society of Japan* **1973**, *46*, 2288–2290.
- [75] Demeter, A.; Druzhinin, S.; George, M.; Haselbach, E.; Roulin, J.-L.; Zachariasse, K. A. Dual Fluorescence and Fast Intramolecular Charge Transfer with 4-(diisopropylamino) Benzonitrile in Alkane Solvents. *Chemical Physics Letters* **2000**, *323*, 351–360.
- [76] Cogan, S.; Zilberg, S.; Haas, Y. The Electronic Origin of the Dual Fluorescence in Donor-Acceptor Substituted Benzene Derivatives. *Journal of the American Chemical Society* **2006**, *128*, 3335–3345.
- [77] Druzhinin, S. I.; Ernstring, N. P.; Kovalenko, S. A.; Lustres, L. P.; Senyushkina, T. A.; Zachariasse, K. A. Dynamics of Ultrafast Intramolecular Charge Transfer with 4-(dimethylamino) Benzonitrile in Acetonitrile. *The Journal of Physical Chemistry A* **2006**, *110*, 2955–2969.
- [78] Coto, P. B.; Serrano-Andrés, L.; Gustavsson, T.; Fujiwara, T.; Lim, E. C. Intramolecular Charge Transfer and Dual Fluorescence of 4-(dimethylamino) Benzonitrile: Ultrafast Branching Followed by a Two-Fold Decay Mechanism. *Physical Chemistry Chemical Physics* **2011**, *13*, 15182–15188.
- [79] Park, M.; Kim, C. H.; Joo, T. Multifaceted Ultrafast Intramolecular Charge Transfer Dynamics of 4-(dimethylamino) Benzonitrile (DMABN). *The Journal of Physical Chemistry A* **2013**, *117*, 370–377.
- [80] Rotkiewicz, K.; Rechthaler, K.; Puchała, A.; Rasała, D.; Styrz, S.; Köhler, G. Dual Fluorescence and Intramolecular Charge Transfer in a Bulky Electron Donor-Acceptor System. N, N-Dimethylanilino-Bis-Pyrazolopyridine. *Journal of Photochemistry and Photobiology A: Chemistry* **1996**, *98*, 15–19.
- [81] Braun, D.; Rettig, W.; Delmond, S.; Letard, J.-F.; Lapouyade, a. R. Amide Derivatives of DMABN: A New Class of Dual Fluorescent Compounds. *The Journal of Physical Chemistry A* **1997**, *101*, 6836–6841.
- [82] Cornelissen-Gude, C.; Rettig, W. Dual Fluorescence and Multiple Charge Transfer Nature in Derivatives of N-Pyrrolobenzonitrile. *The Journal of Physical Chemistry A* **1998**, *102*, 7754–7760.
- [83] Parusel, A. B. A DFT/MRCI Study on the Excited State Charge Transfer States of N-Pyrrolobenzene, N-Pyrrolobenzonitrile and 4-N, N-Dimethylaminobenzonitrile. *Physical Chemistry Chemical Physics* **2000**, *2*, 5545–5552.
- [84] Pines, D.; Pines, E.; Rettig, W. Dual Fluorescence and Excited-State Structural Relaxations in Donor-Acceptor Stilbenes. *The Journal of Physical Chemistry A* **2003**, *107*, 236–242.
- [85] Zhao, Z.; Xing, Y.; Wang, Z.; Lu, P. Dual-Fluorescent Donor-Acceptor Dyad with Ter-carbazole Donor and Switchable Imide Acceptor: Promising Structure for an Integrated Logic Gate. *Organic Letters* **2007**, *9*, 547–550.

- [86] Collado, D.; Casado, J.; González, S. R.; Navarrete, J. T. L.; Suau, R.; Perez-Inestrosa, E.; Pappenfus, T.; Raposo, M. M. M. Enhanced Functionality for Donor–Acceptor Oligothiophenes by Means of Inclusion of BODIPY: Synthesis, Electrochemistry, Photophysics, and Model Chemistry. *Chemistry-A European Journal* **2011**, *17*, 498–507.
- [87] Grabowski, Z. R.; Rotkiewicz, K.; Siemiarczuk, A.; Cowley, D.; Baumann, W. Twisted Intra-Molecular Charge-Transfer States (TICT)-New Class of Excited-States with a Full Charge Separation. *Nouveau Journal De Chimie-New Journal of Chemistry* **1979**, *3*, 443–454.
- [88] Rettig, W. Topics in Current Chemistry. *Electron Transfer I, Springer, Berlin* **1994**, *169*, 253.
- [89] Heisel, F.; Miehé, J. P-Dimethylaminobenzonitrile in Polar Solution. Time-Resolved Solvatochromism of the TICT State Emission. *Chemical Physics Letters* **1986**, *128*, 323–329.
- [90] Zachariasse, K. A. Comment on “Pseudo-Jahn–Teller and TICT-Models: A Photophysical Comparison of Meta-and Para-DMABN Derivatives”[Chem. Phys. Lett. 305 (1999) 8]: The PICT Model for Dual Fluorescence of Aminobenzonitriles. *Chemical Physics Letters* **2000**, *320*, 8–13.
- [91] Jeziorski, B.; Moszynski, R.; Szalewicz, K. Perturbation Theory Approach to Intermolecular Potential Energy Surfaces of Van Der Waals Complexes. *Chemical Reviews* **1994**, *94*, 1887–1930.
- [92] Szalewicz, K.; Patkowski, K.; Jeziorski, B. In *Intermolecular Forces and Clusters II*; Wales, D., Ed.; Springer-Verlag, Berlin, 2005; pp 43–117.
- [93] Hohenstein, E. G.; Sherrill, C. D. Wavefunction Methods for Noncovalent Interactions. *Wiley Interdisciplinary Reviews: Computational Molecular Science* **2012**, *2*, 304–326.
- [94] Szalewicz, K. Symmetry-Adapted Perturbation Theory of Intermolecular Forces. *Wiley Interdisciplinary Reviews: Computational Molecular Science* **2012**, *2*, 254–272.
- [95] Jansen, G. Symmetry-Adapted Perturbation Theory Based on Density Functional Theory for Noncovalent Interactions. *Wiley Interdisciplinary Reviews: Computational Molecular Science* **2014**, *4*, 127–144.
- [96] Williams, H. L.; Chabalowski, C. F. Using Kohn–Sham Orbitals in Symmetry-Adapted Perturbation Theory to Investigate Intermolecular Interactions. *The Journal of Physical Chemistry A* **2001**, *105*, 646–659.
- [97] Lao, K. U.; Herbert, J. M. Accurate and Efficient Quantum Chemistry Calculations for Noncovalent Interactions in Many-Body Systems: The XSAPT Family of Methods. *The Journal of Physical Chemistry A* **2015**, *119*, 235–252.
- [98] Bohr, N. LXXIII. on the Constitution of Atoms and Molecules. *The London, Edinburgh, and Dublin Philosophical Magazine and Journal of Science* **1913**, *26*, 857–875.
- [99] Cramer, C. *Essentials of Computational Chemistry: Theories and Models*; John Wiley & Sons Inc, 2004.

- [100] Born, M.; Oppenheimer, R. Zur Quantentheorie der Molekeln. *Annalen der Physik* **1927**, *389*, 457–484.
- [101] Worth, G. A.; Cederbaum, L. S. Beyond Born-Oppenheimer: Molecular Dynamics Through a Conical Intersection. *Annual Review of Physical Chemistry* **2004**, *55*, 127–158.
- [102] Bernardi, F.; Olivucci, M.; Robb, M. A. Potential Energy Surface Crossings in Organic Photochemistry. *Chemical Society Reviews* **1996**, *25*, 321–328.
- [103] Franck, J.; Jordan, P. *Quanten*; Springer, 1926; pp 641–775.
- [104] Condon, E. U. Nuclear Motions Associated with Electron Transitions in Diatomic Molecules. *Physical Review* **1928**, *32*, 858.
- [105] Klán, P.; Wirz, J. *Photochemistry of Organic Compounds: From Concepts to Practice*; John Wiley & Sons, 2009.
- [106] Dirac, P. A. The Quantum Theory of the Emission and Absorption of Radiation. Proceedings of the Royal Society of London A: Mathematical, Physical and Engineering Sciences. 1927; pp 243–265.
- [107] Turro, N. J.; Ramamurthy, V.; Scaiano, J. C. *Principles of Molecular Photochemistry: An Introduction*; University science books, 2009.
- [108] Szabo, A.; Ostlund, N. S. *Modern Quantum Chemistry: Introduction to Advanced Electronic Structure Theory*; Courier Corporation, 2012.
- [109] Slater, J. C. The Theory of Complex Spectra. *Physical Review* **1929**, *34*, 1293.
- [110] Pauli, W. Über den Zusammenhang des Abschlusses der Elektronengruppen im Atom mit der Komplexstruktur der Spektren. *Zeitschrift für Physik A Hadrons and Nuclei* **1925**, *31*, 765–783.
- [111] Roothaan, C. C. J. New Developments in Molecular Orbital Theory. *Reviews of Modern Physics* **1951**, *23*, 69.
- [112] T., K. Ordering of Wave Functions and Eigenenergies to the Individual Electrons of an Atom. *Physica* **1933**, *1*, 104–113.
- [113] Veszprémi, T.; Fehér, M. *Quantum Chemistry: Fundamentals to Applications*; Springer US, 2012.
- [114] Janssen, C. L.; Nielsen, I. M. New Diagnostics for Coupled-Cluster and Møller–Plesset Perturbation Theory. *Chemical Physics Letters* **1998**, *290*, 423–430.
- [115] Kohn, W. Nobel Lecture: Electronic Structure of Matter-Wave Functions and Density Functionals. *Reviews of Modern Physics* **1999**, *71*, 1253.
- [116] Baggott, J. *Beyond Measure: Modern Physics, Philosophy, and the Meaning of Quantum Theory*; Oxford University Press, 2004.
- [117] Thomas, L. H. The Calculation of Atomic Fields. Mathematical Proceedings of the Cambridge Philosophical Society. 1927; pp 542–548.

- [118] Fermi, E. Application of Statistical Gas Methods to Electronic Systems. *Atti Della Accademia Nazionale Dei Lincei* **1927**, 6, 602–607.
- [119] Dirac, P. A. Note on Exchange Phenomena in the Thomas Atom. *Mathematical Proceedings of the Cambridge Philosophical Society*. 1930; pp 376–385.
- [120] Bloch, M. F. Bemerkung Zur Elektronentheorie des Ferromagnetismus und der Elektrischen Leitfähigkeit. *Zeitschrift für Physik A Hadrons and Nuclei* **1929**, 57, 545–555.
- [121] Slater, J. C. A Simplification of the Hartree-Fock Method. *Physical Review* **1951**, 81, 385.
- [122] Slater, J. C. Statistical Exchange-Correlation in the Self-Consistent Field. *Advances in Quantum Chemistry* **1972**, 6, 1–92.
- [123] Slater, J. C. *The Self-Consistent Field for Molecules and Solids*; McGraw-Hill New York, 1974; Vol. 4.
- [124] Hohenberg, P.; Kohn, W. Inhomogeneous Electron Gas. *Physical Review* **1964**, 136, B864.
- [125] Politzer, P.; Seminario, J. *Modern Density Functional Theory: A Tool for Chemistry*; Theoretical and Computational Chemistry; Elsevier Science, 1995.
- [126] Kohn, W.; Sham, L. J. Self-Consistent Equations Including Exchange and Correlation Effects. *Physical Review* **1965**, 140, A1133.
- [127] Becke, A. D. Becke's Three Parameter Hybrid Method Using the LYP Correlation Functional. *The Journal of Chemical Physics* **1993**, 98, 5648–5652.
- [128] Seminario, J. *Recent Developments and Applications of Modern Density Functional Theory*; Theoretical and Computational Chemistry; Elsevier Science, 1996.
- [129] Yanai, T.; Tew, D. P.; Handy, N. C. A New Hybrid Exchange–Correlation Functional Using the Coulomb-Attenuating Method (CAM-B3LYP). *Chemical Physics Letters* **2004**, 393, 51–57.
- [130] Baer, R.; Livshits, E.; Salzner, U. Tuned Range-Separated Hybrids in Density Functional Theory. *Annual Review of Physical Chemistry* **2010**, 61, 85–109.
- [131] Grimme, S. Semiempirical GGA-Type Density Functional Constructed with a Long-Range Dispersion Correction. *Journal of Computational Chemistry* **2006**, 27, 1787–1799.
- [132] Grimme, S.; Ehrlich, S.; Goerigk, L. Effect of the Damping Function in Dispersion Corrected Density Functional Theory. *Journal of Computational Chemistry* **2011**, 32, 1456–1465.
- [133] Møller, C.; Plesset, M. S. Note on an Approximation Treatment for Many-Electron Systems. *Physical Review* **1934**, 46, 618.
- [134] Jensen, F. *Introduction to Computational Chemistry*; Wiley, 2016.
- [135] Brillouin, L. Actualités Scientifiques et Industrielles. *Nos* **1934**, 71, 1933–1934.
- [136] Kendall, R. A.; Früchtl, H. A. The Impact of the Resolution of the Identity Approximate Integral Method on Modern Ab Initio Algorithm Development. *Theoretical Chemistry Accounts: Theory, Computation, and Modeling (Theoretica Chimica Acta)* **1997**, 97, 158–163.

- [137] Hellweg, A.; Hättig, C.; Höfener, S.; Klopper, W. Optimized Accurate Auxiliary Basis Sets for RI-MP2 and RI-CC2 Calculations for the Atoms Rb to Rn. *Theoretical Chemistry Accounts: Theory, Computation, and Modeling (Theoretica Chimica Acta)* **2007**, *117*, 587–597.
- [138] Christiansen, O.; Koch, H.; Jørgensen, P. The Second-Order Approximate Coupled Cluster Singles and Doubles Model CC2. *Chemical Physics Letters* **1995**, *243*, 409–418.
- [139] Hirata, S.; Nooijen, M.; Bartlett, R. J. High-Order Determinantal Equation-of-Motion Coupled-Cluster Calculations for Electronic Excited States. *Chemical Physics Letters* **2000**, *326*, 255–262.
- [140] Stanton, J. F.; Bartlett, R. J. The Equation of Motion Coupled-Cluster Method. A Systematic Biorthogonal Approach to Molecular Excitation Energies, Transition Probabilities, and Excited State Properties. *The Journal of Chemical Physics* **1993**, *98*, 7029–7039.
- [141] Watts, J. D. An Introduction to Equation-Of-Motion and Linear-Response Coupled-Cluster Methods for Electronically Excited States of Molecules. *Radiation Induced Molecular Phenomena in Nucleic Acids* **2008**, 65–92.
- [142] Dalgaard, E.; Monkhorst, H. J. Some Aspects of the Time-Dependent Coupled-Cluster Approach to Dynamic Response Functions. *Physical Review A* **1983**, *28*, 1217–1222.
- [143] Koch, H.; Jørgensen, P. Coupled Cluster Response Functions. *The Journal of Chemical Physics* **1990**, *93*, 3333–3344.
- [144] Coester, F.; Kümmel, H. Short-Range Correlations in Nuclear Wave Functions. *Nuclear Physics* **1960**, *17*, 477–485.
- [145] Čížek, J. On the Correlation Problem in Atomic and Molecular Systems. Calculation of Wavefunction Components in Ursell-Type Expansion Using Quantum-Field Theoretical Methods. *The Journal of Chemical Physics* **1966**, *45*, 4256–4266.
- [146] Bartlett, R. J.; Purvis, G. D. Many-Body Perturbation Theory, Coupled-Pair Many-Electron Theory, and the Importance of Quadruple Excitations for the Correlation Problem. *International Journal of Quantum Chemistry* **1978**, *14*, 561–581.
- [147] Bartlett, R. J. Coupled-Cluster Theory and Its Equation-Of-Motion Extensions. *Wiley Interdisciplinary Reviews: Computational Molecular Science* **2012**, *2*, 126–138.
- [148] Crawford, T. D.; Schäfer, H. F. An Introduction to Coupled Cluster Theory for Computational Chemists. *Reviews in Computational Chemistry* **2000**, *14*, 33–136.
- [149] Helgaker, T.; Jørgensen, P.; Olsen, J. *Molecular Electronic-Structure Theory*; John Wiley & Sons, 2014.
- [150] Christiansen, O.; Koch, H.; Jørgensen, P.; Helgaker, T. Integral Direct Calculation of CC2 Excitation Energies: Singlet Excited States of Benzene. *Chemical Physics Letters* **1996**, *263*, 530–539.
- [151] Hättig, C. Geometry Optimizations with the Coupled-Cluster Model CC2 Using the Resolution-Of-The-Identity Approximation. *The Journal of Chemical Physics* **2003**, *118*, 7751–7761.

- [152] Jensen, H.; Olsen, J. *Advances in Quantum Chemistry: Response Theory and Molecular Properties*; Advances in Quantum Chemistry; Elsevier Science, 2005.
- [153] Hättig, C.; Weigend, F. CC2 Excitation Energy Calculations on Large Molecules Using the Resolution of the Identity Approximation. *The Journal of Chemical Physics* **2000**, *113*, 5154–5161.
- [154] Dreuw, A.; Head-Gordon, M. Single-Reference Ab Initio Methods for the Calculation of Excited States of Large Molecules. *Chemical Reviews* **2005**, *105*, 4009–4037.
- [155] Grunenberg, J. *Computational Spectroscopy: Methods, Experiments and Applications*; Wiley, 2011.
- [156] Davidson, E. R. The Iterative Calculation of a Few of the Lowest Eigenvalues and Corresponding Eigenvectors of Large Real-Symmetric Matrices. *Journal of Computational Physics* **1975**, *17*, 87–94.
- [157] Head-Gordon, M.; Rico, R. J.; Oumi, M.; Lee, T. J. A Doubles Correction to Electronic Excited States from Configuration Interaction in the Space of Single Substitutions. *Chemical Physics Letters* **1994**, *219*, 21–29.
- [158] Head-Gordon, M.; Maurice, D.; Oumi, M. A Perturbative Correction to Restricted Open Shell Configuration Interaction with Single Substitutions for Excited States of Radicals. *Chemical Physics Letters* **1995**, *246*, 114–121.
- [159] Baudin, P.; Marín, J. S.; Cuesta, I. G.; Sánchez de Merás, A. M. Calculation of Excitation Energies from the CC2 Linear Response Theory Using Cholesky Decomposition. *The Journal of Chemical Physics* **2014**, *140*, 104111.
- [160] Császár, P.; Pulay, P. Geometry Optimization by Direct Inversion in the Iterative Subspace. *Journal of Molecular Structure* **1984**, *114*, 31–34.
- [161] Köhn, A.; Hättig, C. Analytic Gradients for Excited States in the Coupled-Cluster Model CC2 Employing the Resolution-Of-The-Identity Approximation. *The Journal of Chemical Physics* **2003**, *119*, 5021–5036.
- [162] Schirmer, J. Beyond the Random-Phase Approximation: A New Approximation Scheme for the Polarization Propagator. *Physical Review A* **1982**, *26*, 2395.
- [163] Trofimov, A.; Schirmer, J. An Efficient Polarization Propagator Approach to Valence Electron Excitation Spectra. *Journal of Physics B: Atomic, Molecular and Optical Physics* **1995**, *28*, 2299–2324.
- [164] Trofimov, A.; Stelter, G.; Schirmer, J. A Consistent Third-Order Propagator Method for Electronic Excitation. *The Journal of Chemical Physics* **1999**, *111*, 9982–9999.
- [165] Dreuw, A.; Wormit, M. The Algebraic Diagrammatic Construction Scheme for the Polarization Propagator for the Calculation of Excited States. *Wiley Interdisciplinary Reviews: Computational Molecular Science* **2015**, *5*, 82–95.
- [166] Harbach, P. H.; Wormit, M.; Dreuw, A. The Third-Order Algebraic Diagrammatic Construction Method (ADC (3)) for the Polarization Propagator for Closed-Shell Molecules: Efficient Implementation and Benchmarking A. *The Journal of Chemical Physics* **2014**, *141*, 064113.

- [167] Schirmer, J.; Trofimov, A. Intermediate State Representation Approach to Physical Properties of Electronically Excited Molecules. *The Journal of Chemical Physics* **2004**, *120*, 11449–11464.
- [168] Hättig, C. Structure Optimizations for Excited States with Correlated Second-Order Methods: CC2 and ADC (2). *Advances in Quantum Chemistry* **2005**, *50*, 37–60.
- [169] Laurent, A. D.; Jacquemin, D. TD-DFT Benchmarks: A Review. *International Journal of Quantum Chemistry* **2013**, *113*, 2019–2039.
- [170] Tussupbayev, S.; Govind, N.; Lopata, K.; Cramer, C. J. Comparison of Real-Time and Linear-Response Time-Dependent Density Functional Theories for Molecular Chromophores Ranging From Sparse to High Densities of States. *Journal of Chemical Theory and Computation* **2015**, *11*, 1102–1109.
- [171] Runge, E.; Gross, E. Time-Dependent Density Functional Theory. *Physical Review Letters* **1984**, *52*, 997.
- [172] Gross, E. W. Kohn In, *Density Functional Theory of Many-Fermion Systems*, Ed. by SB Trickey. *Advances in Quantum Chemistry* **1990**, *21*, 255.
- [173] Van Leeuwen, R. Causality and Symmetry in Time-Dependent Density-Functional Theory. *Physical Review Letters* **1998**, *80*, 1280.
- [174] Casida, M. E.; Huix-Rotllant, M. Progress in Time-Dependent Density-Functional Theory. *Annual Review of Physical Chemistry* **2012**, *63*, 287–323.
- [175] Casida, M. E. Response Theory for Molecules. *Recent Advances in Density Functional Methods:(Part I)* **1995**, *1*, 155.
- [176] van Leeuwen, R. Mapping from Densities to Potentials in Time-Dependent Density-Functional Theory. *Physical Review Letters* **1999**, *82*, 3863.
- [177] Van Leeuwen, R. Key Concepts in Time-Dependent Density-Functional Theory. *International Journal of Modern Physics B* **2001**, *15*, 1969–2023.
- [178] Gross, E. K.; Dobson, J.; Petersilka, M. *Density Functional Theory II*; Springer, 1996; pp 81–172.
- [179] Dreuw, A.; Head-Gordon, M. Failure of Time-Dependent Density Functional Theory for Long-Range Charge-Transfer Excited States: The Zincbacteriochlorin- Bacteriochlorin and Bacteriochlorophyll- Spheroidene Complexes. *Journal of the American Chemical Society* **2004**, *126*, 4007–4016.
- [180] Dreuw, A.; Weisman, J. L.; Head-Gordon, M. Long-Range Charge-Transfer Excited States in Time-Dependent Density Functional Theory Require Non-Local Exchange. *The Journal of Chemical Physics* **2003**, *119*, 2943–2946.
- [181] Salem, L.; Rowland, C. The Electronic Properties of Diradicals. *Angewandte Chemie International Edition* **1972**, *11*, 92–111.
- [182] Krylov, A. I. Spin-Flip Configuration Interaction: An Electronic Structure Model that is both Variational and Size-Consistent. *Chemical Physics Letters* **2001**, *350*, 522–530.

- [183] Krylov, A. I. Spin-Flip Equation-Of-Motion Coupled-Cluster Electronic Structure Method for a Description of Excited States, Bond Breaking, Diradicals, and Triradicals. *Accounts of chemical research* **2006**, *39*, 83–91.
- [184] Zhang, X.; Herbert, J. M. Analytic Derivative Couplings for Spin-Flip Configuration Interaction Singles and Spin-Flip Time-Dependent Density Functional Theory. *The Journal of Chemical Physics* **2014**, *141*, 064104.
- [185] Deglmann, P.; Schenk, S. Thermodynamics of Chemical Reactions with COSMO-RS: The Extreme Case of Charge Separation or Recombination. *Journal of Computational Chemistry* **2012**, *33*, 1304–1320.
- [186] Klamt, A.; Schüürmann, G. COSMO: A New Approach to Dielectric Screening in Solvents with Explicit Expressions for the Screening Energy and Its Gradient. *Journal of the Chemical Society, Perkin Transactions 2* **1993**, 799–805.
- [187] Klamt, A. Conductor-like Screening Model for Real Solvents: A New Approach to the Quantitative Calculation of Solvation Phenomena. *The Journal of Physical Chemistry* **1995**, *99*, 2224–2235.
- [188] Cossi, M.; Barone, V.; Cammi, R.; Tomasi, J. Ab Initio Study of Solvated Molecules: A New Implementation of the Polarizable Continuum Model. *Chemical Physics Letters* **1996**, *255*, 327–335.
- [189] Barone, V.; Cossi, M. Quantum Calculation of Molecular Energies and Energy Gradients in Solution by a Conductor Solvent Model. *The Journal of Physical Chemistry A* **1998**, *102*, 1995–2001.
- [190] Tomasi, J.; Mennucci, B.; Cammi, R. Quantum Mechanical Continuum Solvation Models. *Chemical Reviews* **2005**, *105*, 2999–3094.
- [191] Cramer, C. J.; Truhlar, D. G. Implicit Solvation Models: Equilibria, Structure, Spectra, and Dynamics. *Chemical Reviews* **1999**, *99*, 2161–2200.
- [192] Miertuš, S.; Scrocco, E.; Tomasi, J. Electrostatic Interaction of a Solute with a Continuum. a Direct Utilizaion of AB Initio Molecular Potentials for the Prevision of Solvent Effects. *Chemical Physics* **1981**, *55*, 117–129.
- [193] Bondi, A. Van Der Waals Volumes and Radii. *The Journal of Physical Chemistry* **1964**, *68*, 441–451.
- [194] Herbert, J. M.; Langea, A. W. In *Many-Body Effects and Electrostatics in Biomolecules*; Cui, Q., Pengyu, R., Meuwly, M., Eds.; Pan Stanford, 2016; Chapter 11, pp 363–416.
- [195] Fulay, P.; Lee, J.-K. *Electronic, Magnetic, and Optical Materials*; CRC Press, 2016.
- [196] Kirkwood, J. G. On the Theory of Strong Electrolyte Solutions. *The Journal of Chemical Physics* **1934**, *2*, 767–781.
- [197] Onsager, L. Electric Moments of Molecules in Liquids. *Journal of the American Chemical Society* **1936**, *58*, 1486–1493.
- [198] Cammi, R.; Tomasi, J. Analytical Derivatives for Molecular Solutes. I. Hartree–Fock Energy First Derivatives with Respect to External Parameters in the Polarizable Continuum Model. *The Journal of Chemical Physics* **1994**, *100*, 7495–7502.

- [199] Cramer, C. J.; Truhlar, D. G. A Universal Approach to Solvation Modeling. *Accounts of Chemical Research* **2008**, *41*, 760–768.
- [200] Klamt, A.; Mennucci, B.; Tomasi, J.; Barone, V.; Curutchet, C.; Orozco, M.; Luque, F. J. On the Performance of Continuum Solvation Methods. a Comment on “Universal Approaches to Solvation Modeling”. *Accounts of Chemical Research* **2009**, *42*, 489–492.
- [201] Pomogaeva, A.; Chipman, D. M. Hydration Energy from a Composite Method for Implicit Representation of Solvent. *Journal of Chemical Theory and Computation* **2013**, *10*, 211–219.
- [202] Pomogaeva, A.; Chipman, D. M. Composite Method for Implicit Representation of Solvent in Dimethyl Sulfoxide and Acetonitrile. *The Journal of Physical Chemistry A* **2014**, *119*, 5173–5180.
- [203] Cossi, M.; Barone, V. Time-Dependent Density Functional Theory for Molecules in Liquid Solutions. *The Journal of Chemical Physics* **2001**, *115*, 4708–4717.
- [204] Cammi, R.; Mennucci, B. Linear Response Theory for the Polarizable Continuum Model. *The Journal of Chemical Physics* **1999**, *110*, 9877–9886.
- [205] Cammi, R.; Corni, S.; Mennucci, B.; Tomasi, J. Electronic Excitation Energies of Molecules in Solution: State Specific and Linear Response Methods for Nonequilibrium Continuum Solvation Models. *The Journal of Chemical Physics* **2005**, *122*, 104513.
- [206] Scalmani, G.; Frisch, M. J.; Mennucci, B.; Tomasi, J.; Cammi, R.; Barone, V. Geometries and Properties of Excited States in the Gas Phase and in Solution: Theory and Application of a Time-Dependent Density Functional Theory Polarizable Continuum Model. *The Journal of Chemical Physics* **2006**, *124*, 094107.
- [207] Fukuda, R.; Ehara, M. Mechanisms for Solvatochromic Shifts of Free-Base Porphine Studied with Polarizable Continuum Models and Explicit Solute–Solvent Interactions. *Journal of Chemical Theory and Computation* **2012**, *9*, 470–480.
- [208] Kityk, A. V. Absorption and Fluorescence Spectra of Heterocyclic Isomers from Long-Range-Corrected Density Functional Theory in Polarizable Continuum Approach. *The Journal of Physical Chemistry A* **2012**, *116*, 3048–3055.
- [209] Gasiorski, P.; Danel, K.; Matusiewicz, M.; Uchacz, T.; Kuźnik, W.; Kityk, A. DFT/TDDFT Study on the Electronic Structure and Spectral Properties of Diphenyl Azafluoranthene Derivative. *Journal of Fluorescence* **2012**, *22*, 81–91.
- [210] Marques, M. In *Lecture Notes in Physics*; Ullrich, C. A., Nogueira, F., Rubio, A., Burke, K., Gross, E. K. U., Eds.; Springer Berlin Heidelberg, 2006; Vol. 706; p 555.
- [211] Improta, R.; Scalmani, G.; Frisch, M. J.; Barone, V. Toward Effective and Reliable Fluorescence Energies in Solution by a New State Specific Polarizable Continuum Model Time Dependent Density Functional Theory Approach. *The Journal of Chemical Physics* **2007**, *127*, 074504.
- [212] Lipparini, F.; Mennucci, B. Perspective: Polarizable Continuum Models for Quantum-Mechanical Descriptions. *The Journal of Chemical Physics* **2016**, *144*, 160901.

- [213] Pedone, A. Role of Solvent on Charge Transfer in 7-Aminocoumarin Dyes: New Hints from TD-CAM-B3LYP and State Specific PCM Calculations. *Journal of Chemical Theory and Computation* **2013**, *9*, 4087–4096.
- [214] Guido, C. A.; Jacquemin, D.; Adamo, C.; Mennucci, B. Electronic Excitations in Solution: The Interplay Between State Specific Approaches and a Time-Dependent Density Functional Theory Description. *Journal of Chemical Theory and Computation* **2015**, *11*, 5782–5790.
- [215] Caricato, M.; Mennucci, B.; Tomasi, J.; Ingrosso, F.; Cammi, R.; Corni, S.; Scalmani, G. Formation and Relaxation of Excited States in Solution: A New Time Dependent Polarizable Continuum Model Based on Time Dependent Density Functional Theory. *The Journal of Chemical Physics* **2006**, *124*, 124520.
- [216] Mewes, J.-M.; You, Z.-Q.; Wormit, M.; Kriesche, T.; Herbert, J. M.; Dreuw, A. Experimental Benchmark Data and Systematic Evaluation of Two a Posteriori, Polarizable-Continuum Corrections for Vertical Excitation Energies in Solution. *The Journal of Physical Chemistry A* **2015**, *119*, 5446–5464.
- [217] Mewes, J.-M.; Herbert, J. M.; Dreuw, A. On the Accuracy of the General, State-Specific Polarizable-Continuum Model for the Description of Correlated Ground-and Excited States in Solution. *Physical Chemistry Chemical Physics* **2017**, *19*, 1644–1654.
- [218] Yomosa, S. Theory of the Excited State of Molecular Complex in Solution. *Journal of the Physical Society of Japan* **1974**, *36*, 1655–1660.
- [219] Bonaccorsi, R.; Cimraglia, R.; Tomasi, J. Ab Initio Evaluation of Absorption and Emission Transitions for Molecular Solutes, Including Separate Consideration of Orientational and Inductive Solvent Effects. *Journal of Computational Chemistry* **1983**, *4*, 567–577.
- [220] Kim, H. J.; Hynes, J. T. Equilibrium and Nonequilibrium Solvation and Solute Electronic Structure. I. Formulation. *The Journal of Chemical Physics* **1990**, *93*, 5194–5210.
- [221] Klamt, A. Calculation of UV/Vis Spectra in Solution. *The Journal of Physical Chemistry* **1996**, *100*, 3349–3353.
- [222] Mennucci, B.; Cammi, R.; Tomasi, J. Excited States and Solvatochromic Shifts Within a Nonequilibrium Solvation Approach: A New Formulation of the Integral Equation Formalism Method at the Self-Consistent Field, Configuration Interaction, and Multiconfiguration Self-Consistent Field Level. *The Journal of Chemical Physics* **1998**, *109*, 2798–2807.
- [223] Jacobson, L. D.; Herbert, J. M. A Simple Algorithm for Determining Orthogonal, Self-Consistent Excited-State Wave Functions for a State-Specific Hamiltonian: Application to the Optical Spectrum of the Aqueous Electron. *Journal of Chemical Theory and Computation* **2011**, *7*, 2085–2093.
- [224] Lunkenheimer, B.; Köhn, A. Solvent Effects on Electronically Excited States Using the Conductor-like Screening Model and the Second-Order Correlated Method ADC (2). *Journal of Chemical Theory and Computation* **2012**, *9*, 977–994.
- [225] Marcus, R. A. Electrostatic Free Energy and Other Properties of States Having Nonequilibrium Polarization. I. *The Journal of Chemical Physics* **1956**, *24*, 979–989.

- [226] Marcus, R. A. On the Theory of Oxidation-Reduction Reactions Involving Electron Transfer. I. *The Journal of Chemical Physics* **1956**, *24*, 966–978.
- [227] Pekar, S. Research in Electron Theory of Crystals, Technical Report No. AEC-Tr-5575. **1963**,
- [228] Cossi, M.; Barone, V. Separation Between Fast and Slow Polarizations in Continuum Solvation Models. *The Journal of Physical Chemistry A* **2000**, *104*, 10614–10622.
- [229] Bayliss, N. S.; McRae, E. G. Solvent Effects in the Spectra of Acetone, Crotonaldehyde, Nitromethane and Nitrobenzene. *The Journal of Physical Chemistry* **1954**, *58*, 1006–1011.
- [230] Brady, J. E.; Carr, P. W. An Analysis of Dielectric Models of Solvatochromism. *The Journal of Physical Chemistry* **1985**, *89*, 5759–5766.
- [231] Frenkel, J. *Wave Mechanics: Advanced General Theory*; International series of monographs on physics; Clarendon Press, 1934.
- [232] Casida, M. E. Time-Dependent Density-Functional Theory for Molecules and Molecular Solids. *Journal of Molecular Structure: THEOCHEM* **2009**, *914*, 3–18.
- [233] You, Z.-Q.; Mewes, J.-M.; Dreuw, A.; Herbert, J. M. Comparison of the Marcus and Pekar Partitions in the Context of Non-Equilibrium, Polarizable-Continuum Solvation Models. *The Journal of Chemical Physics* **2015**, *143*, 204104.
- [234] Plasser, F.; Wormit, M.; Dreuw, A. New Tools for the Systematic Analysis and Visualization of Electronic Excitations. I. Formalism. *The Journal of Chemical Physics* **2014**, *141*, 024106.
- [235] Bohnwagner, M. V.; Burghardt, I.; Dreuw, A. Solvent Polarity Tunes the Barrier Height for Twisted Intramolecular Charge Transfer in N-Pyrrolobenzonitrile (PBN). *The Journal of Physical Chemistry A* **2015**, *120*, 14–27.
- [236] Belau, L.; Haas, Y.; Rettig, W. Dual Emission of 4-(1H-Pyrrol-1-yl)benzoni-trile Clusters with Acetonitrile in a Supersonic Jet and Its Absence in Phenylpyrrole Clusters. *The Journal of Physical Chemistry A* **2004**, *108*, 3916–3925.
- [237] Schweke, D.; Baumgarten, H.; Haas, Y.; Rettig, W.; Dick, B. Charge-Transfer-Type Fluorescence of 4-(1H-Pyrrol-1-yl)benzoni-trile (PBN) and N-Phenylpyrrole (PP) in Cryogenic Matrixes: Evidence for Direct Excitation of the CT Band. *The Journal of Physical Chemistry A* **2005**, *109*, 576–585.
- [238] Roznowska, A.; Tomin, V.; Fisz, J.; Hubisz, K. Dual Fluorescence of N-Pyrrolobenzonitrile in Extended Polyvinyl Alcohol Films. *Optics and Spectroscopy* **2011**, *111*, 66.
- [239] Haidekker, M.; Brady, T.; Lichlyter, D.; Theodorakis, E. Effects of Solvent Polarity and Solvent Viscosity on the Fluorescent Properties of Molecular Rotors and Related Probes. *Bioorganic chemistry* **2005**, *33*, 415–425.
- [240] Sarkar, A.; Chakravorti, S. A Study on the Spectroscopy and Photophysics of N-Phenyl Pyrrole and N-Phenyl Pyrazole. *Chemical Physics Letters* **1995**, *235*, 195–201.
- [241] Yoshihara, T.; Galievsky, V.; Druzhinin, S.; Saha, S.; Zachariasse, K. N-Phenylpyrroles and 4-(dimethylamino) Benzoni-trile from Solvatochromic and Thermo-chromic Spectral Shifts. *Photochemical & Photobiological Sciences* **2003**, *2*, 342–353.

- [242] Murali, S.; Rettig, W. Meta-Positioning Effect in Sterically Hindered N-Phenyl-Pyrroles: A Photophysical Study. *Chemical Physics Letters* **2005**, *412*, 135–140.
- [243] Sung, J.; Kim, P.; Lee, Y.; Kim, J.; Kim, D. Characterization of Ultrafast Intramolecular Charge Transfer Dynamics in Pyrenyl Derivatives: Systematic Change of the Number of Peripheral N, N-Dimethylaniline Substituents. *The Journal of Physical Chemistry Letters* **2011**, *2*, 818–823.
- [244] Zakharov, M.; Krauss, O.; Nosenko, Y.; Brutschy, B.; Dreuw, A. Specific Microsolvation Triggers Dissociation-Mediated Anomalous Red-Shifted Fluorescence in the Gas Phase. *Journal of the American Chemical Society* **2009**, *131*, 461–469.
- [245] Wiedbrauk, S.; Maerz, B.; Samoylova, E.; Reiner, A.; Trommer, F.; Mayer, P.; Zinth, W.; Dube, H. Twisted Hemithioindigo Photoswitches: Solvent Polarity Determines the Type of Light-Induced Rotations. *Journal of the American Chemical Society* **2016**, *138*, 12219–12227.
- [246] Willock, D. *Molecular Symmetry*; John Wiley & Sons, 2009.
- [247] Rettig, W.; Marschner, F. Molecular Conformation and Biradicaloid Charge Transfer States in Substituted N-Phenyl-Pyrroles. *New Journal of Chemistry* **1990**, *14*, 819.
- [248] Cornelissen-Gude, C.; Rettig, W. Dual Fluorescence and Multiple Charge Transfer Nature in Derivatives of N-Pyrrolobenzonitrile. *The Journal of Physical Chemistry A* **1998**, *102*, 7754–7760.
- [249] Belau, L.; Haas, Y.; Rettig, W. Jet Cooled Spectra of Pyrrolobenzene and of Pyrrolobenzonitrile: The Nature of the Excited States. *Chemical Physics Letters* **2002**, *364*, 157–163.
- [250] Zilberg, S.; Haas, Y. The Nature of the Intramolecular Charge Transfer Excited State in P-Pyrrolocyanobenzene (PBN) and Other Derivatives of Benzene Substituted by Electron Donor and Acceptor Groups. *The Journal of Physical Chemistry A* **2002**, *106*, 1–11.
- [251] Fuß, W.; Rettig, W.; Schmid, W.; Trushin, S.; Yatsushashi, T. Ultrafast Temporary Charge Transfer in Pyrrolidinyl–Benzonitrile and Pyrrolyl–Benzonitrile in the Gas Phase. *Faraday Discussion* **2004**, *127*, 23–33.
- [252] Schweke, D.; Haas, Y.; Dick, B. Photophysics of Phenylpyrrole Derivatives and Their Acetonitrile Clusters in the Gas Phase and in Argon Matrixes: Simulations of Structure and Reactivity. *The Journal of Physical Chemistry A* **2005**, *109*, 3830–3842, PMID: 16833699.
- [253] Druzhinin, S. I.; Kovalenko, S. A.; Senyushkina, T. A.; Demeter, A.; Machinek, R.; Noltemeyer, M.; Zachariasse, K. A. Intramolecular Charge Transfer with the Planarized 4-Cyanofluorazene and Its Flexible Counterpart 4-Cyano-N-Phenylpyrrole. Picosecond Fluorescence Decays and Femtosecond Excited-State Absorption. *The Journal of Physical Chemistry A* **2008**, *112*, 8238–8253.
- [254] Minezawa, N. State-Specific Solvation Effect on the Intramolecular Charge Transfer Reaction in Solution: A Linear-Response Free Energy TDDFT Method. *Chemical Physics Letters* **2014**, *608*, 140–144.
- [255] Kleven, H. B.; Platt, J. R. Geometry and Spectra of Substituted Anilines. *Journal of the American Chemical Society* **1949**, *71*, 1714–1720.

- [256] Rettig, W. Application of a Simplified Microstructural Solvent Interaction Model to the Solvatochromism of Twisted Intramolecular Charge Transfer (TICT) States. *Journal of Molecular Structure* **1982**, *84*, 303–327.
- [257] Murali, S.; Changuenet-Barret, P.; Ley, C.; Plaza, P.; Rettig, W.; Martin, M.; Lapouyade, R. Photophysical Properties of Pyrrolobenzenes with Different Linking and Substitution Pattern: The Transition Between Charge Transfer States with Large (MICT) and Small (TICT) Resonance Interaction. *Chemical Physics Letters* **2005**, *411*, 192 – 197.
- [258] Grotendorst, J. Modern Methods and Algorithms of Quantum Chemistry. *John von Neumann Institute for Computing* **2000**,
- [259] Kirkwood, J. G. Theory of Solutions of Molecules Containing Widely Separated Charges with Special Application to Zwitterions. *The Journal of Chemical Physics* **1934**, *2*, 351–361.
- [260] Kirkwood, J. G. The Dielectric Polarization of Polar Liquids. *The Journal of Chemical Physics* **1939**, *7*, 911–919.
- [261] Dunning Jr, T. Gaussian Basis Sets for Use in Correlated Molecular Calculations. I. the Atoms Boron Through Neon and Hydrogen. *The Journal of Chemical Physics* **1989**, *90*, 1007–1023.
- [262] Kendall, R.; Dunning Jr, T.; Harrison, R. Electron Affinities of the First-Row Atoms Revisited. Systematic Basis Sets and Wave Functions. *The Journal of Chemical Physics* **1992**, *96*, 6796.
- [263] Woon, D.; Dunning Jr, T. Gaussian Basis Sets for Use in Correlated Molecular Calculations. III. the Atoms Aluminum Through Argon. *The Journal of Chemical Physics* **1993**, *98*, 1358.
- [264] Weigend, F. A Fully Direct RI-HF Algorithm: Implementation, Optimised Auxiliary Basis Sets, Demonstration of Accuracy and Efficiency. *Physical Chemistry Chemical Physics* **2002**, *4*, 4285–4291.
- [265] Becke, A. *The Journal of Chemical Physics* **1993**, *98*, 1372.
- [266] Lee, C.; Yang, W.; Parr., R. G. Development of the Colle-Salvetti Correlation-Energy Formula into a Functional of the Electron Density. *Physical Review B* **1988**, *37(2)*, 785–789.
- [267] Shao, Y.; Gan, Z.; Epifanovsky, E.; Gilbert, A. T. B.; Wormit, M.; Kussmann, J.; Lange, A. W.; Behn, A.; Deng, J.; Feng, X.; Ghosh, D.; Goldey, M.; Horn, P. R.; Jacobson, L. D.; Kaliman, I.; Khaliullin, R. Z.; Kus, T.; Landau, A.; Liu, J.; Proynov, E. I.; Rhee, Y. M.; Richard, R. M.; Rohrdanz, M. A.; Steele, R. P.; Sundstrom, E. J.; III, H. L. W.; Zimmerman, P. M.; Zuev, D.; Albrecht, B.; Alguire, E.; Austin, B.; Beran, G. J. O.; Bernard, Y. A.; Berquist, E.; Brandhorst, K.; Bravaya, K. B.; Brown, S. T.; Casanova, D.; Chang, C.-M.; Chen, Y.; Chien, S. H.; Closser, K. D.; Crittenden, D. L.; Diedenhofen, M.; Jr., R. A. D.; Do, H.; Dutoi, A. D.; Edgar, R. G.; Fatehi, S.; Fusti-Molnar, L.; Ghysels, A.; Golubeva-Zadorozhnaya, A.; Gomes, J.; Hanson-Heine, M. W. D.; Harbach, P. H. P.; Hauser, A. W.; Hohenstein, E. G.; Holden, Z. C.; Jagau, T.-C.; Ji, H.; Kaduk, B.; Khistyayev, K.; Kim, J.; Kim, J.; King, R. A.; Klunzinger, P.; Kosenkov, D.; Kowalczyk, T.; Krauter, C. M.; Lao, K. U.; Laurent, A.; Lawler, K. V.; Levchenko, S. V.; Lin, C. Y.;

- Liu, F.; Livshits, E.; Lochan, R. C.; Luenser, A.; Manohar, P.; Manzer, S. F.; Mao, S.-P.; Mardirossian, N.; Marenich, A. V.; Maurer, S. A.; Mayhall, N. J.; Oana, C. M.; Olivares-Amaya, R.; O'Neill, D. P.; Parkhill, J. A.; Perrine, T. M.; Peverati, R.; Pieniazek, P. A.; Prociuk, A.; Rehn, D. R.; Rosta, E.; Russ, N. J.; Sergueev, N.; Sharada, S. M.; Sharma, S.; Small, D. W.; Sodt, A.; Stein, T.; Stuck, D.; Su, Y.-C.; Thom, A. J. W.; Tsuchimochi, T.; Vogt, L.; Vydrov, O.; Wang, T.; Watson, M. A.; Wenzel, J.; White, A.; Williams, C. F.; Vanovschi, V.; Yeganeh, S.; Yost, S. R.; You, Z.-Q.; Zhang, I. Y.; Zhang, X.; Zhao, Y.; Brooks, B. R.; Chan, G. K. L.; Chipman, D. M.; Cramer, C. J.; III, W. A. G.; Gordon, M. S.; Hehre, W. J.; Klamt, A.; III, H. F. S.; Schmidt, M. W.; Sherrill, C. D.; Truhlar, D. G.; Warshel, A.; Xu, X.; Aspuru-Guzik, A.; Baer, R.; Bell, A. T.; Besley, N. A.; Chai, J.-D.; Dreuw, A.; Dunietz, B. D.; Furlani, T. R.; Gwaltney, S. R.; Hsu, C.-P.; Jung, Y.; Kong, J.; Lambrecht, D. S.; Liang, W.; Ochsenfeld, C.; Rassolov, V. A.; Slipchenko, L. V.; Subotnik, J. E.; Voorhis, T. V.; Herbert, J. M.; Krylov, A. I.; Gill, P. M. W.; Head-Gordon, M. *Molecular Physics* **2015**, *113*, 184–215.
- [268] Krylov, A. I.; Gill, P. M. Q-Chem: An Engine for Innovation. *Wiley Interdisciplinary Reviews: Computational Molecular Science* **2013**, *3*, 317–326.
- [269] Furche, F.; Ahlrichs, R.; Hättig, C.; Klopper, W.; Sierka, M.; Weigend, F. Turbomole. *Wiley Interdisciplinary Reviews: Computational Molecular Science* **2014**, *4*, 91–100.
- [270] Neese, F. The ORCA Program System. *Wiley Interdisciplinary Reviews: Computational Molecular Science* **2012**, *2*, 73–78.
- [271] TURBOMOLE V6.3.1 2011, a Development of University of Karlsruhe and Forschungszentrum Karlsruhe GmbH, 1989-2007, TURBOMOLE GmbH, Since 2007; Available from <http://www.turbomole.com> 12/13/2017.
- [272] Shao, Y.; Molnar, L. F.; Jung, Y.; Kussmann, J.; Ochsenfeld, C.; Brown, S. T.; Gilbert, A. T.; Slipchenko, L. V.; Levchenko, S. V.; O'Neill, D. P.; DiStasio Jr, R. A.; Lochan, R. C.; Wang, T.; Beran, G. J.; Besley, N. A.; Herbert, J. M.; Yeh Lin, C.; Van Voorhis, T.; Hung Chien, S.; Sodt, A.; Steele, R. P.; Rassolov, V. A.; Maslen, P. E.; Korambath, P. P.; Adamson, R. D.; Austin, B.; Baker, J.; Byrd, E. F. C.; Dachsel, H.; Doerksen, R. J.; Dreuw, A.; Dunietz, B. D.; Dutoi, A. D.; Furlani, T. R.; Gwaltney, S. R.; Heyden, A.; Hirata, S.; Hsu, C.-P.; Kedziora, G.; Khalliulin, R. Z.; Klunzinger, P.; Lee, A. M.; Lee, M. S.; Liang, W.; Lotan, I.; Nair, N.; Peters, B.; Proynov, E. I.; Pieniazek, P. A.; Min Rhee, Y.; Ritchie, J.; Rosta, E.; David Sherrill, C.; Simmonett, A. C.; Subotnik, J. E.; Lee Woodcock III, H.; Zhang, W.; Bell, A. T.; Chakraborty, A. K.; Chipman, D. M.; Keil, F. J.; Warshel, A.; Hehre, W. J.; Schaefer III, H. F.; Kong, J.; Krylov, A. I.; Gill, P. M. W.; Head-Gordon, M. Advances in Methods and Algorithms in a Modern Quantum Chemistry Program Package. *Phys. Chem. Chem. Phys.* **2006**, *8*, 3172–3191.
- [273] Frisch, M. J.; Trucks, G. W.; Schlegel, H. B.; Scuseria, G. E.; Robb, M. A.; Cheeseman, J. R.; Scalmani, G.; Barone, V.; Mennucci, B.; Petersson, G. A.; Nakatsuji, H.; Caricato, M.; Li, X.; Hratchian, H. P.; Izmaylov, A. F.; Bloino, J.; Zheng, G.; Sonnenberg, J. L.; Hada, M.; Ehara, M.; Toyota, K.; Fukuda, R.; Hasegawa, J.; Ishida, M.; Nakajima, T.; Honda, Y.; Kitao, O.; Nakai, H.; Vreven, T.; Montgomery, J. J. A.; Peralta, J. E.; Ogliaro, F.; Bearpark, M.; Heyd, J. J.; Brothers, E.; Kudin, K. N.; Staroverov, V. N.; Kobayashi, R.; Normand, J.; Raghavachari, K.; Rendell, A.; Burant, J. C.; Iyengar, S. S.; Tomasi, J.; Cossi, M.; Rega, N.; Millam, N. J.; Klene, M.; Knox, J. E.; Cross, J. B.; Bakken, V.;

- Adamo, C.; Jaramillo, J.; Gomperts, R.; Stratmann, R. E.; Yazyev, O.; Austin, A. J.; Cammi, R.; Pomelli, C.; Ochterski, J. W.; Martin, R. L.; Morokuma, K.; Zakrzewski, V. G.; Voth, G. A.; Salvador, P.; Dannenberg, J. J.; Dapprich, S.; Daniels, A. D.; Farkas, Ö.; Foresman, J. B.; Ortiz, J. V.; Cioslowski, J.; Fox, D. J. Gaussian 09, Revision D.01. 2013.
- [274] Pauling, L.; Brockway, L. O.; Beach, J. The Dependence of Interatomic Distance on Single Bond-Double Bond Resonance. *Journal of the American Chemical Society* **1935**, *57*, 2705–2709.
- [275] Pauling, L. *The Nature of the Chemical Bond: And the Structure of Molecules and Crystals : An Introduction to Modern Structural Chemistry*, 3rd ed.; The George Fisher Baker non-resident lectureship in chemistry at Cornell university; Cornell University Press: Ithaca and N.Y, op. 1960.
- [276] Yanai, T.; Tew, D. P.; Handy, N. C. A New Hybrid Exchange–Correlation Functional Using the Coulomb-Attenuating Method (CAM-B3LYP). *Chemical Physics Letters* **2004**, *393*, 51 – 57.
- [277] Lipkowitz, K. B., Boyd, D. B., Eds. *Reviews in Computational Chemistry*; Wiley-VCH: New York and N.Y, 1999; Vol. 13.
- [278] Pacchioni, G.; Frigoli, F.; Ricci, D.; Weil, J. A. Theoretical Description of Hole Localization in a Quartz al Center: The Importance of Exact Electron Exchange. *Physical Review B* **2000**, *63*, 054102.
- [279] Lambert, C.; Risko, C.; Coropceanu, V.; Schelter, J.; Amthor, S.; Gruhn, N. E.; Durivage, J. C.; Brédas, J.-L. Electronic Coupling in Tetraanisylarylenediamine Mixed-Valence Systems: The Interplay Between Bridge Energy and Geometric Factors. *Journal of the American Chemical Society* **2005**, *127*, 8508–8516.
- [280] Sala, M. *Quantum Dynamics and Laser Control for Photochemistry*; Springer Theses; Springer International Publishing, 2016.
- [281] von Neumann, J.; Wigner, E. On Some Peculiar Discrete Eigenvalues. *Physikalische Zeitschrift* **1929**, 465.
- [282] Hund, F. Z. Physik 40, 742 (1927); RS Mulliken. *Physical Review* **1928**, *32*, 186.
- [283] Plötner, J.; Dreuw, A. Pigment Yellow 101: A Showcase for Photo-Initiated Processes in Medium-Sized Molecules. *Chemical Physics* **2008**, *347*, 472–482.
- [284] Brabec, C. J.; Sariciftci, N. S.; Hummelen, J. C. Plastic Solar Cells. *Advanced Functional Materials* **2001**, *11*, 15–26.
- [285] Colladet, K.; Fourier, S.; Cleij, T. J.; Lutsen, L.; Gelan, J.; Vanderzande, D.; Huong Nguyen, L.; Neugebauer, H.; Sariciftci, S.; Aguirre, A.; Janssen, G.; Goovaerts, E. Low Band Gap Donor-Acceptor Conjugated Polymers Toward Organic Solar Cells Applications. *Macromolecules* **2007**, *40*, 65–72.
- [286] Huang, F.; Chen, K.-S.; Yip, H.-L.; Hau, S. K.; Acton, O.; Zhang, Y.; Luo, J.; Jen, A. K.-Y. Development of New Conjugated Polymers with Donor-  $\pi$ -Bridge- Acceptor Side Chains for High Performance Solar Cells. *Journal of the American Chemical Society* **2009**, *131*, 13886–13887.

- [287] Jenekhe, S.; Lu, L.; Alam, M. New Conjugated Polymers with Donor-Acceptor Architectures: Synthesis and Photophysics of Carbazole-Quinoline and Phenothiazine-Quinoline Copolymers and Oligomers Exhibiting Large Intramolecular Charge Transfer. *Macromolecules* **2001**, *34*, 7315–7324.
- [288] Zhu, Y.; Champion, R. D.; Jenekhe, S. A. Conjugated Donor-Acceptor Copolymer Semiconductors with Large Intramolecular Charge Transfer: Synthesis, Optical Properties, Electrochemistry, and Field Effect Carrier Mobility of Thienopyrazine-Based Copolymers. *Macromolecules* **2006**, *39*, 8712–8719.
- [289] Kim, J.-H.; Lee, S.; Kang, I.-N.; Park, M.-J.; Hwang, D.-H. Photovoltaic Devices Using Semiconducting Polymers Containing Head-to-Tail-Structured Bithiophene, Pyrene, and Benzothiadiazole Derivatives. *Journal of Polymer Science Part B: Polymer Chemistry* **2012**, *50*, 3415–3424.
- [290] Liu, J.; Zhang, H.; Dong, H.; Meng, L.; Jiang, L.; Jiang, L.; Wang, Y.; Yu, J.; Sun, Y.; Hu, W. High Mobility Emissive Organic Semiconductor. *Nature Communications* **2015**, *6*, 10032.
- [291] Mushrush, M.; Facchetti, A.; Lefenfeld, M.; Katz, H. E.; Marks, T. J. Easily Processable Phenylene-Thiophene-Based Organic Field-Effect Transistors and Solution-Fabricated Nonvolatile Transistor Memory Elements. *Journal of the American Chemical Society* **2003**, *125*, 9414–9423.
- [292] Justin Thomas, K.; Hsu, Y.-C.; Lin, J. T.; Lee, K.-M.; Ho, K.-C.; Lai, C.-H.; Cheng, Y.-M.; Chou, P.-T. 2, 3-Disubstituted Thiophene-Based Organic Dyes for Solar Cells. *Chemistry of Materials* **2008**, *20*, 1830–1840.
- [293] Champion, R. D.; Cheng, K.-F.; Pai, C.-L.; Chen, W.-C.; Jenekhe, S. A. Electronic Properties and Field-Effect Transistors of Thiophene-Based Donor-Acceptor Conjugated Copolymers. *Macromolecular Rapid Communications* **2005**, *26*, 1835–1840.
- [294] Perepichka, I. F.; Perepichka, D. F. *Handbook of Thiophene-Based Materials: Applications in Organic Electronics and Photonics*; Wiley Online Library, 2009.
- [295] Zhang, F.; Wu, D.; Xu, Y.; Feng, X. Thiophene-Based Conjugated Oligomers for Organic Solar Cells. *Journal of Materials Chemistry* **2011**, *21*, 17590–17600.
- [296] Casado, J.; Ortiz, R. P.; Navarrete, J. T. L. Quinoidal Oligothiophenes: New Properties Behind an Unconventional Electronic Structure. *Chemical Society Reviews* **2012**, *41*, 5672–5686.
- [297] Li, X.-C.; Sirringhaus, H.; Garnier, F.; Holmes, A. B.; Moratti, S. C.; Feeder, N.; Clegg, W.; Teat, S. J.; Friend, R. H. A Highly  $\pi$ -Stacked Organic Semiconductor for Thin Film Transistors Based on Fused Thiophenes. *Journal of the American Chemical Society* **1998**, *120*, 2206–2207.
- [298] Xiao, K.; Liu, Y.; Qi, T.; Zhang, W.; Wang, F.; Gao, J.; Qiu, W.; Ma, Y.; Cui, G.; Chen, S.; Zhan, X.; Yu, G.; Qin, J.; Hu, W.; Zhu, D. A Highly  $\pi$ -Stacked Organic Semiconductor for Field-Effect Transistors Based on Linearly Condensed Pentathienoacene. *Journal of the American Chemical Society* **2005**, *127*, 13281–13286, PMID: 16173758.

- [299] D'Auria, M. Ab Initio Study of the Photochemical Isomerization of Thiophene Derivatives. *Journal of Photochemistry and Photobiology A: Chemistry* **2002**, *149*, 31–37.
- [300] Karsten, B. P.; Bijleveld, J. C.; Viani, L.; Cornil, J.; Gierschner, J.; Janssen, R. A. Electronic Structure of Small Band Gap Oligomers Based on Cyclopentadithiophenes and Acceptor Units. *Journal of Materials Chemistry* **2009**, *19*, 5343–5350.
- [301] Estrada, L. A.; Montes, V. A.; Zyryanov, G.; Anzenbacher, P. Triplet Energy Studies of Thiophene and Para-Phenylene Based Oligomers. *The Journal of Physical Chemistry B* **2007**, *111*, 6983–6986.
- [302] Ji, S.; Ge, J.; Escudero, D.; Wang, Z.; Zhao, J.; Jacquemin, D. Molecular Structure–Intersystem Crossing Relationship of Heavy-Atom-Free BODIPY Triplet Photosensitizers. *The Journal of Organic Chemistry* **2015**, *80*, 5958–5963.
- [303] Rohrdanz, M. A.; Martins, K. M.; Herbert, J. M. A Long-Range-Corrected Density Functional That Performs Well for Both Ground-State Properties and Time-Dependent Density Functional Theory Excitation Energies, Including Charge-Transfer Excited States. *The Journal of Chemical Physics* **2009**, *130*, 054112.
- [304] Heß, B. A.; Marian, C. M.; Wahlgren, U.; Gropen, O. A Mean-Field Spin-Orbit Method Applicable to Correlated Wavefunctions. *Chemical Physics Letters* **1996**, *251*, 365–371.
- [305] Schimmelpfennig, B.; Maron, L.; Wahlgren, U.; Teichteil, C.; Fagerli, H.; Gropen, O. On the Combination of ECP-Based CI Calculations with All-Electron Spin-Orbit Mean-Field Integrals. *Chemical Physics Letters* **1998**, *286*, 267–271.
- [306] Schimmelpfennig, B. AMFI, an Atomic Mean-Field Spin-Orbit Integral Program. 1996; University of Stockholm.
- [307] Steffen, C.; Thomas, K.; Huniar, U.; Hellweg, A.; Rubner, O.; Schroer, A. TmoleX – Graphical User Interface for TURBOMOLE. *Journal of Computational Chemistry* **2010**, *31*, 2967–2970.
- [308] Humphrey, W.; Dalke, A.; Schulten, K. VMD: Visual Molecular Dynamics. *Journal of Molecular Graphics* **1996**, *14*, 33–38.
- [309] Katritzky, A. R.; Ramsden, C. A.; Joule, J. A.; Zhdankin, V. V. *Handbook of Heterocyclic Chemistry*; Elsevier, 2010.
- [310] Kleinschmidt, M.; Tatchen, J.; Marian, C. M. Spin-Orbit Coupling of DFT/MRCI Wavefunctions: Method, Test Calculations, and Application to Thiophene. *Journal of Computational Chemistry* **2002**, *23*, 824–833.
- [311] Gavrilov, N.; Salzmann, S.; Marian, C. M. Deactivation Via Ring Opening: A Quantum Chemical Study of the Excited States of Furan and Comparison to Thiophene. *Chemical Physics* **2008**, *349*, 269–277.
- [312] Stenrup, M. Theoretical Study of the Radiationless Deactivation Mechanisms of Photo-Excited Thiophene. *Chemical Physics* **2012**, *397*, 18–25.
- [313] Head-Gordon, M.; Grana, A. M.; Maurice, D.; White, C. A. Analysis of Electronic Transitions As the Difference of Electron Attachment and Detachment Densities. *The Journal of Physical Chemistry* **1995**, *99*, 14261–14270.

- [314] Becker, R. S.; Seixas de Melo, J.; Macanita, A. L.; Elisei, F. Comprehensive Evaluation of the Absorption, Photophysical, Energy Transfer, Structural, and Theoretical Properties of  $\alpha$ -Oligothiophenes with One to Seven Rings. *The Journal of Physical Chemistry* **1996**, *100*, 18683–18695.
- [315] Weinkauff, R.; Lehr, L.; Schlag, E.; Salzmann, S.; Marian, C. Ultrafast Dynamics in Thiophene Investigated by Femtosecond Pump Probe Photoelectron Spectroscopy and Theory. *Physical Chemistry Chemical Physics* **2008**, *10*, 393–404.
- [316] Köppel, H.; Gromov, E.; Trofimov, A. Multi-Mode–Multi-State Quantum Dynamics of Key Five-Membered Heterocycles: Spectroscopy and Ultrafast Internal Conversion. *Chemical Physics* **2004**, *304*, 35–49.
- [317] Holland, D.; Trofimov, A.; Seddon, E.; Gromov, E.; Korona, T.; de Oliveira, N.; Archer, L.; Joyeux, D.; Nahon, L. Excited Electronic States of Thiophene: High Resolution Photoabsorption Fourier Transform Spectroscopy and Ab Initio Calculations. *Physical Chemistry Chemical Physics* **2014**, *16*, 21629–21644.
- [318] Kleinschmidt, M.; Tatchen, J.; Marian, C. M. Spin-Orbit Coupling of DFT/MRCI Wavefunctions: Method, Test Calculations, and Application to Thiophene. *Journal of Computational Chemistry* **2002**, *23*, 824–833.
- [319] Marian, C. M. Spin-Orbit Coupling and Intersystem Crossing in Molecules. *Wiley Interdisciplinary Reviews: Computational Molecular Science* **2012**, *2*, 187–203.
- [320] Wayne, R. P. *Principles and Applications of Photochemistry*; Oxford University Press, 1988.
- [321] Englman, R.; Jortner, J. The Energy Gap Law for Radiationless Transitions in Large Molecules. *Molecular Physics* **1970**, *18*, 145–164.
- [322] Salzmann, S.; Kleinschmidt, M.; Tatchen, J.; Weinkauff, R.; Marian, C. M. Excited States of Thiophene: Ring Opening as Deactivation Mechanism. *Physical Chemistry Chemical Physics* **2008**, *10*, 380–392.
- [323] Cui, G.; Fang, W. Ab Initio Trajectory Surface-Hopping Study on Ultrafast Deactivation Process of Thiophene. *The Journal of Physical Chemistry A* **2011**, *115*, 11544–11550.
- [324] Handy, N. C.; Cohen, A. J. Left-Right Correlation Energy. *Molecular Physics* **2001**, *99*, 403–412.
- [325] Levine, B. G.; Ko, C.; Quenneville, J.; Martínez, T. J. Conical Intersections and Double Excitations in Time-Dependent Density Functional Theory. *Molecular Physics* **2006**, *104*, 1039–1051.
- [326] Zakharov, M.; Krauss, O.; Nosenko, Y.; Brutschy, B.; Dreuw, A. Specific Microsolvation Triggers Dissociation-Mediated Anomalous Red-Shifted Fluorescence in the Gas Phase. *Journal of the American Chemical Society* **2008**, *131*, 461–469.
- [327] Bohnwagner, M. V.; Dreuw, A. Regular Fluorescence of 4-Fluoro-N, N-Dimethylaniline: No Charge Transfer and No Twisting. *The Journal of Physical Chemistry A* **2017**, *121*, 5834–5841.

- [328] Zachariasse, K. A.; Demeter, A.; Druzhinin, S. I. Absence of Intramolecular Charge Transfer with 4-Fluoro-N, N-Dimethylaniline (DMA4F), Contrary to an Experimental Report Supported by Computations. *Journal of Physical Chemistry A* **2017**, *121*, 1223–1232.
- [329] Fujiwara, T.; Reichardt, C.; Vogt, R. A.; Crespo-Hernández, C. E.; Zgierski, M. Z.; Lim, E. C. Electronic Spectra and Excited-State Dynamics of 4-Fluoro-N, N-Dimethylaniline. *Chemical Physics Letters* **2013**, *586*, 70–75.
- [330] Koutek, B.; Musil, L.; Velek, J.; Souček, M. Fluorescence Behaviour of Some 4-Substituted Halobenzenes. *Collection of Czechoslovak Chemical Communications* **1985**, *50*, 1753–1763.
- [331] Zachariasse, K. A.; Von Der Haar, T.; Hebecker, A.; Leinhos, U.; Kuehnle, W. Intramolecular Charge Transfer in Aminobenzonitriles: Requirements for Dual Fluorescence. *Pure and Applied Chemistry* **1993**, *65*, 1745–1750.
- [332] Zachariasse, K.; Grobys, M.; Von der Haar, T.; Hebecker, A.; Il'ichev, Y. V.; Morawski, O.; Rückert, I.; Kühnle, W. Photo-Induced Intramolecular Charge Transfer and Internal Conversion in Molecules with a Small Energy Gap Between S1 and S2. Dynamics and Structure. *Journal of Photochemistry and Photobiology A: Chemistry* **1997**, *105*, 373–383.
- [333] Zachariasse, K. A.; Druzhinin, S. I.; Galievsky, V. A.; Demeter, A.; Allonas, X.; Kovalenko, S. A.; Senyushkina, T. A. Pentacyano-N, N-Dimethylaniline in the Excited State. Only Locally Excited State Emission, in Spite of the Large Electron Affinity of the Pentacyanobenzene Subgroup. *The Journal of Physical Chemistry A* **2010**, *114*, 13031–13039.
- [334] Druzhinin, S. I.; Kovalenko, S. A.; Senyushkina, T.; Zachariasse, K. A. Dynamics of Ultrafast Intramolecular Charge Transfer with 1-Tert-Butyl-6-Cyano-1,2,3,4-Tetrahydroquinoline (NTC6) in N-Hexane and Acetonitrile. *The Journal of Physical Chemistry A* **2007**, *111*, 12878–12890.
- [335] Druzhinin, S. I.; Mayer, P.; Stalke, D.; von Bülow, R.; Noltemeyer, M.; Zachariasse, K. A. Intramolecular Charge Transfer with 1-Tert-Butyl-6-Cyano-1,2,3,4-Tetrahydroquinoline (NTC6) and Other Aminobenzonitriles. A Comparison of Experimental Vapor Phase Spectra and Crystal Structures with Calculations. *Journal of the American Chemical Society* **2010**, *132*, 7730–7744.
- [336] Krauß, O.; Lommatzsch, U.; Lahmann, C.; Brutschy, B.; Rettig, W.; Herbich, J. Fluorescence of Solvent-Complexed Aminobenzonitriles in a Supersonic Jet. *Physical Chemistry Chemical Physics* **2001**, *3*, 74–79.
- [337] Druzhinin, S. I.; Kovalenko, S. A.; Senyushkina, T. A.; Demeter, A.; Machinek, R.; Noltemeyer, M.; Zachariasse, K. A. Intramolecular Charge Transfer with the Planarized 4-Cyanofluorazene and Its Flexible Counterpart 4-Cyano-N-Phenylpyrrole. Picosecond Fluorescence Decays and Femtosecond Excited-State Absorption. *The Journal of Physical Chemistry A* **2008**, *112*, 8238–8253.
- [338] Xu, X.; Cao, Z.; Zhang, Q. Computational Characterization of Low-Lying States and Intramolecular Charge Transfers in N-Phenylpyrrole and the Planar-Rigidized Fluorazene. *Journal of Physical Chemistry A* **2006**, *110*, 1740–1748.

- [339] Schuddeboom, W.; Jonker, S. A.; Warman, J. M.; Leinhos, U.; Kuehnle, W.; Zachariasse, K. A. Excited-State Dipole Moments of Dual Fluorescent 4-(dialkylamino) Benzoni- triles. Influence of Alkyl Chain Length and Effective Solvent Polarity. *Journal of Physical Chemistry* **1992**, *96*, 10809–10819.
- [340] Krauter, C. M.; Schimmelpfennig, B.; Pernpointner, M.; Dreuw, A. Algebraic Diagram- matic Construction for the Polarization Propagator with Spin-Orbit Coupling. *Chemical Physics* **2017**, 286–293.
- [341] Shao, Y.; Gan, Z.; Epifanovsky, E.; Gilbert, A. T.; Wormit, M.; Kussmann, J.; Lange, A. W.; Behn, A.; Deng, J.; Feng, X. Advances in Molecular Quantum Chemistry Contained in the Q-Chem 4 Program Package. *Molecular Physics* **2015**, *113*, 184–215.
- [342] Hanwell, M. D.; Curtis, D. E.; Lonie, D. C.; Vandermeersch, T.; Zurek, E.; Hutchison, G. R. Avogadro: An Advanced Semantic Chemical Editor, Visualization, and Analysis Platform. *Journal of Cheminformatics* **2012**, *4*, 17.
- [343] Barbatti, M.; Lan, Z.; Crespo-Otero, R.; Szymczak, J. J.; Lischka, H.; Thiel, W. Critical Appraisal of Excited State Nonadiabatic Dynamics Simulations of 9 H-Adenine A. *The Journal of Chemical Physics* **2012**, *137*, 22A503.
- [344] Wiggins, P.; Williams, J. G.; Tozer, D. J. Excited State Surfaces in Density Functional Theory: A New Twist on an Old Problem. 2009.
- [345] Plötner, J.; Tozer, D. J.; Dreuw, A. Dependence of Excited State Potential Energy Surfaces on the Spatial Overlap of the Kohn-Sham Orbitals and the Amount of Nonlocal Hartree- Fock Exchange in Time-Dependent Density Functional Theory. *Journal of Chemical Theory and Computation* **2010**, *6*, 2315–2324.
- [346] Zhang, H.; Jiang, X.; Wu, W.; Mo, Y. Electron Conjugation Versus  $\pi$ - $\pi$  Repulsion in Substituted Benzenes: Why the Carbon–Nitrogen Bond in Nitrobenzene is Longer Than in Aniline. *Physical Chemistry Chemical Physics* **2016**, *18*, 11821–11828.
- [347] Siebrand, W.; Zgierski, M. Z. Non-Condon Effects on Radiationless Triplet Decay in Benzene and Naphthalene. *Chemical Physics Letters* **1980**, *72*, 411–415.
- [348] Scharf, B. Qualitative Considerations of the T1-S0 Intersystem Crossing in Benzene. *Chemical Physics Letters* **1979**, *68*, 242–244.
- [349] Minns, R.; Parker, D.; Penfold, T.; Worth, G.; Fielding, H. Competing Ultrafast Intersys- tem Crossing and Internal Conversion in the “channel 3” Region of Benzene. *Physical Chemistry Chemical Physics* **2010**, *12*, 15607–15615.
- [350] Cogan, S.; Haas, Y.; Zilberg, S. Intersystem Crossing at Singlet Conical Intersections. *Journal of Photochemistry and Photobiology A: Chemistry* **2007**, *190*, 200–206.
- [351] Penfold, T.; Worth, G. The Effect of Molecular Distortions on Spin-Orbit Coupling in Simple Hydrocarbons. *Chemical Physics* **2010**, *375*, 58–66.
- [352] Simons, J.; Smith, A. Radiationless Decay Processes in Benzene; an External Deuterium Isotope Effect. *Chemical Physics Letters* **1972**, *16*, 536–541.
- [353] Anderson, E.; Kistiakowsky, G. Fluorescence and Intersystem Crossing of Benzene-h<sub>6</sub>-d<sub>6</sub>, and -1,4-d<sub>2</sub>. *The Journal of Chemical Physics* **1969**, *51*, 182–188.

- [354] Wright, M.; Frosch, R.; Robinson, G. Phosphorescence Lifetime of Benzene. An Intermolecular Heavy-Atom Effect, a Deuterium Effect, and a Temperature Effect. *The Journal of Chemical Physics* **1960**, *33*, 934–935.
- [355] Parker, D.; Minns, R.; Penfold, T.; Worth, G.; Fielding, H. Ultrafast Dynamics of the S1 Excited State of Benzene. *Chemical Physics Letters* **2009**, *469*, 43–47.
- [356] Lumb, M.; Braga, C. L.; Pereira, L. Emission Spectra and Phosphorescence Lifetime of Benzene Solutions at 77 K, As a Function of Concentration and Excitation Wavelength. *Transactions of the Faraday Society* **1969**, *65*, 1992–1999.
- [357] Wiedbrauk, S.; Maerz, B.; Samoylova, E.; Mayer, P.; Zinth, W.; Dube, H. Ingredients to TICT Formation in Donor Substituted Hemithioindigo. *The Journal of Physical Chemistry Letters* **2017**, *8*, 1585–1592.
- [358] Waldeck, D. H. Photoisomerization Dynamics of Stilbenes. *Chemical Reviews* **1991**, *91*, 415–436.
- [359] Tian, H.; Zhang, J. *Photochromic Materials: Preparation, Properties and Applications*; Wiley, 2016.
- [360] Lennartson, A.; Roffey, A.; Moth-Poulsen, K. Designing Photoswitches for Molecular Solar Thermal Energy Storage. *Tetrahedron Letters* **2015**, *56*, 1457–1465.
- [361] Wiedbrauk, S.; Dube, H. Hemithioindigo-an Emerging Photoswitch. *Tetrahedron Letters* **2015**, *56*, 4266–4274.
- [362] Kitzig, S.; Thilemann, M.; Cordes, T.; Rück-Braun, K. Light-Switchable Peptides with a Hemithioindigo Unit: Peptide Design, Photochromism, and Optical Spectroscopy. *ChemPhysChem* **2016**, *17*, 1252–1263.
- [363] Kink, F.; Collado, M. P.; Wiedbrauk, S.; Mayer, P.; Dube, H. Bistable Photoswitching of Hemithioindigo with Green and Red Light: Entry Point to Advanced Molecular Digital Information Processing. *Chemistry-A European Journal* **2017**, *23*, 6237–6243.
- [364] Seki, T.; Tamaki, T.; Yamaguchi, T.; Ichimura, K. Photochromism of Hemithioindigo Derivatives. II. Photochromic Behaviors in Bilayer Membranes and Related Systems. *Bulletin of the Chemical Society of Japan* **1992**, *65*, 657–663.
- [365] Lougheed, T.; Borisenko, V.; Hennig, T.; Rück-Braun, K.; Woolley, G. A. Photomodulation of Ionic Current Through Hemithioindigo-Modified Gramicidin Channels. *Organic & Biomolecular Chemistry* **2004**, *2*, 2798–2801.
- [366] Tanaka, K.; Kohayakawa, K.; Iwata, S.; Irie, T. Application of 2-Pyridyl-Substituted Hemithioindigo as a Molecular Switch in Hydrogen-Bonded Porphyrins. *The Journal of Organic Chemistry* **2008**, *73*, 3768–3774.
- [367] Dube, H.; Rebek, J. Selective Guest Exchange in Encapsulation Complexes Using Light of Different Wavelengths. *Angewandte Chemie International Edition* **2012**, *51*, 3207–3210.
- [368] Cordes, T.; Schadendorf, T.; Rück-Braun, K.; Zinth, W. Chemical Control of Hemithioindigo-Photoisomerization-Substituent-effects on Different Molecular Parts. *Chemical Physics Letters* **2008**, *455*, 197–201.

- [369] Herre, S.; Steinle, W.; Rück-Braun, K. Synthesis of Photoswitchable Hemithioindigo-Based  $\omega$ -Amino Acids and Application in Boc-Based Peptide Assembly. *Synthesis* **2005**, *2005*, 3297–3300.
- [370] Cordes, T.; Riesselmann, K.; Herre, S.; Rück-Braun, K.; Zinth, W. A New Class of Ultrafast Photoswitchable Chromopeptides. International Conference on Ultrafast Phenomena. 2006; p ThE3.
- [371] Schadendorf, T.; Hoppmann, C.; Rück-Braun, K. Synthesis of Rigid Photoswitchable Hemithioindigo  $\omega$ -Amino Acids. *Tetrahedron Letters* **2007**, *48*, 9044–9047.
- [372] Regner, N.; Herzog, T. T.; Haiser, K.; Hoppmann, C.; Beyermann, M.; Sauermann, J.; Engelhard, M.; Cordes, T.; Rück-Braun, K.; Zinth, W. Light-Switchable Hemithioindigo–Hemistilbene-Containing Peptides: Ultrafast Spectroscopy of the Z→E Isomerization of the Chromophore and the Structural Dynamics of the Peptide Moiety. *The Journal of Physical Chemistry B* **2012**, *116*, 4181–4191.
- [373] Cordes, T.; Elsner, C.; Herzog, T. T.; Hoppmann, C.; Schadendorf, T.; Summerer, W.; Rück-Braun, K.; Zinth, W. Ultrafast Hemithioindigo-Based Peptide-Switches. *Chemical Physics* **2009**, *358*, 103–110.
- [374] Cordes, T.; Weinrich, D.; Kempa, S.; Riesselmann, K.; Herre, S.; Hoppmann, C.; Rück-Braun, K.; Zinth, W. Hemithioindigo-Based Photoswitches as Ultrafast Light Trigger in Chromopeptides. *Chemical Physics Letters* **2006**, *428*, 167–173.
- [375] Nenov, A.; Cordes, T.; Herzog, T. T.; Zinth, W.; de Vivie-Riedle, R. Molecular Driving Forces for Z/E Isomerization Mediated by Heteroatoms: The Example Hemithioindigo. *The Journal of Physical Chemistry A* **2010**, *114*, 13016–13030.
- [376] Maerz, B.; Wiedbrauk, S.; Oesterling, S.; Samoylova, E.; Nenov, A.; Mayer, P.; de Vivie-Riedle, R.; Zinth, W.; Dube, H. Making Fast Photoswitches Faster-Using Hammett Analysis to Understand the Limit of Donor-Acceptor Approaches for Faster Hemithioindigo Photoswitches. *Chemistry-A European Journal* **2014**, *20*, 13984–13992.
- [377] Yang, M.; Huo, C.; Li, A.; Lei, Y.; Yu, L.; Zhu, C. Excited-State E→Z Photoisomerization Mechanism Unveiled by ab Initio Nonadiabatic Molecular Dynamics Simulation for Hemithioindigo-Hemistilbene. *Physical Chemistry Chemical Physics* **2017**, *19*, 12185–12198.
- [378] Pløtner, J.; Dreuw, A. Molecular Mechanism of the Z/E-Photoisomerization of Hemithioindigo Hemistilbene. *The Journal of Physical Chemistry A* **2009**, *113*, 11882–11887.
- [379] Samoylova, E.; Maerz, B.; Wiedbrauk, S.; Oesterling, S.; Nenov, A.; Dube, H.; de Vivie-Riedle, R.; Zinth, W. *Ultrafast Phenomena XIX*; Springer, 2015; pp 391–394.
- [380] Crabb, J. *Techniques in Protein Chemistry*; Techniques in Protein Chemistry Bd. 6; Elsevier Science, 1995.
- [381] Shao, Y.; Head-Gordon, M.; Krylov, A. I. The Spin-Flip Approach Within Time-Dependent Density Functional Theory: Theory and Applications to Diradicals. *The Journal of Chemical Physics* **2003**, *118*, 4807–4818.

- [382] Hargittai, M.; Hargittai, I. *Advances in Molecular Structure Research*; Advances in Molecular Structure Research Bd. 4; Elsevier Science, 1998.
- [383] Engle, J. M.; Lakshminarayanan, P.; Carroll, C. N.; Zakharov, L. N.; Haley, M. M.; Johnson, D. W. Molecular Self-Assembly: Solvent Guests Tune the Conformation of a Series of 2, 6-Bis (2-anilinoethynyl) Pyridine-Based Ureas. *Crystal growth & design* **2011**, *11*, 5144–5152.
- [384] Zhou, Y.; Deng, G.; Zheng, Y.-Z.; Xu, J.; Ashraf, H.; Yu, Z.-W. Evidences for Cooperative Resonance-Assisted Hydrogen Bonds in Protein Secondary Structure Analogs. *Scientific Reports* **2016**, *6*, 36932.
- [385] Kohl, B.; Bohnwagner, M. V.; Rominger, F.; Wadepohl, H.; Dreuw, A.; Mastalerz, M. Attractive Dispersion Interactions Versus Steric Repulsion of Tert-Butyl Groups in the Crystal Packing of a D<sub>3h</sub>-Symmetric Tris (quinoxalinophenanthrophenazine). *Chemistry-A European Journal* **2016**, *22*, 646–655.
- [386] Kohl, B. Auf Triptycenen Basierende Pyren-Fusionierte Pyrazaacene-Eine Kombination aus Porosität Und Optoelektronischen Eigenschaften. Ph.D. thesis, 2017.
- [387] Kohl, B.; Rominger, F.; Mastalerz, M. Rigid  $\pi$ -Extended Triptycenes Via a Hexaketone Precursor. *Organic letters* **2014**, *16*, 704–707.
- [388] Kumar, K. V.; Preuss, K.; Titirici, M.-M.; Rodríguez-Reinoso, F. Nanoporous Materials for the Onboard Storage of Natural Gas. *Chemical Reviews* **2017**, *117*, 1796–1825.
- [389] Zhu, G.; Ren, H. *Porous Organic Frameworks: Design, Synthesis and Their Advanced Applications*; Springer Berlin Heidelberg: Berlin, Heidelberg, 2015; pp 1–11.
- [390] Davis, M. E. Ordered Porous Materials for Emerging Applications. *Nature* **2002**, *417*, 813–821.
- [391] Klenkler, R.; Perepichka, D.; Taerum, T.; Ahmida, M.; Shuai, C.; Eichhorn, S.; Demenev, A.; Kayal, H.; Grozema, F. C.; Patwardhan, S. A Combined Study of Mesomorphism, Optical, and Electronic Properties of Donor-Acceptor Columnar Liquid Crystals. *Proceedings of SPIE, 2011 vol. 8114* **2011**,
- [392] Makowski, T.; Moustafa, R. M.; Uznanski, P.; Zajackowski, W.; Pisula, W.; Tracz, A.; Kaafarani, B. R. Structural, Thermo-Optical, and Photophysical Properties of Highly Oriented Thin Films of Quinoxalinophenanthrophenazine Derivative. *The Journal of Physical Chemistry C* **2014**, *118*, 18736–18745.
- [393] Wex, B.; Ala'á, O.; Vanvooren, A.; Zschieschang, U.; Klauk, H.; Krause, J. A.; Cornil, J.; Kaafarani, B. R. Crystalline TQPP as p-Type Semiconductor: X-Ray Crystallographic Investigation, OTFT Device, and Computational Analysis of Transport Properties. *Journal of Molecular Structure* **2015**, *1093*, 144–149.
- [394] Siegel, J.; Wu, Y. *Polyarenes I*; Topics in Current Chemistry; Springer Berlin Heidelberg, 2014.
- [395] Kanters, J.; Schouten, A.; Steinwender, E.; van der Maas, J.; Groenen, L.; Reinhoudt, D. Spectroscopic and Crystallographic Study of 27,28-Diethoxy-p-tert-butylcalix [4]arenes. *Journal of molecular structure* **1992**, *269*, 49–64.

- [396] Kohl, B.; Rominger, F.; Mastalerz, M. Ein Pyren-Fusioniertes N-Heteroacen Mit Elf Linear Anellierten Aromatischen Ringen. *Angewandte Chemie* **2015**, *127*, 6149–6154.
- [397] Kohl, B.; Rominger, F.; Mastalerz, M. A Pyrene-Fused N-Heteroacene with Eleven Rectilinearly Annulated Aromatic Rings. *Angewandte Chemie International Edition* **2015**, *54*, 6051–6056.
- [398] Becke, A. D. Density-Functional Thermochemistry. V. Systematic Optimization of Exchange-Correlation Functionals. *The Journal of Chemical Physics* **1997**, *107*, 8554–8560.
- [399] Schmider, H. L.; Becke, A. D. Optimized Density Functionals from the Extended G2 Test Set. *The Journal of Chemical Physics* **1998**, *108*, 9624–9631.
- [400] Liu, B.; McLean, A. Accurate Calculation of the Attractive Interaction of Two Ground State Helium Atoms. *The Journal of Chemical Physics* **1973**, *59*, 4557–4558.
- [401] Lao, K. U.; Herbert, J. M. Accurate and Efficient Quantum Chemistry Calculations for Noncovalent Interactions in Many-Body Systems: The XSAPT Family of Methods. *The Journal of Physical Chemistry A* **2014**, *119*, 235–252.
- [402] Jacobson, L. D.; Richard, R. M.; Lao, K. U.; Herbert, J. M. Efficient Monomer-Based Quantum Chemistry Methods for Molecular and Ionic Clusters. *Annual Reports in Computational Chemistry* **2013**, *9*, 25–56.
- [403] Lao, K. U.; Herbert, J. M. Symmetry-Adapted Perturbation Theory with Kohn-Sham Orbitals Using Non-Empirically Tuned, Long-Range-Corrected Density Functionals. *The Journal of Chemical Physics* **2014**, *140*, 044108.
- [404] Misquitta, A. J.; Szalewicz, K. Intermolecular Forces from Asymptotically Corrected Density Functional Description of Monomers. *Chemical Physics Letters* **2002**, *357*, 301–306.
- [405] Rohrdanz, M. A.; Herbert, J. M. Simultaneous Benchmarking of Ground-and Excited-State Properties with Long-Range-Corrected Density Functional Theory. *The Journal of Chemical Physics* **2008**, *129*, 034107.
- [406] Hehre, W. J.; Ditchfield, R.; Pople, J. A. Self-consistent Molecular Orbital Methods. XII. Further Extensions of Gaussian-Type Basis Sets for Use in Molecular Orbital Studies of Organic Molecules. *The Journal of Chemical Physics* **1972**, *56*, 2257–2261.
- [407] Ditchfield, R.; Hehre, W. J.; Pople, J. A. Self-Consistent Molecular-Orbital Methods. IX. an Extended Gaussian-Type Basis for Molecular-Orbital Studies of Organic Molecules. *The Journal of Chemical Physics* **1971**, *54*, 724–728.
- [408] Hariharan, P. C.; Pople, J. A. The Influence of Polarization Functions on Molecular Orbital Hydrogenation Energies. *Theoretical Chemistry Accounts: Theory, Computation, and Modeling (Theoretica Chimica Acta)* **1973**, *28*, 213–222.
- [409] Hariharan, P.; Pople, J. Accuracy of AH<sub>n</sub> Equilibrium Geometries by Single Determinant Molecular Orbital Theory. *Molecular Physics* **1974**, *27*, 209–214.
- [410] Gordon, M. S. The Isomers of Silacyclopropane. *Chemical Physics Letters* **1980**, *76*, 163–168.

- [411] Binning, R.; Curtiss, L. Compact Contracted Basis Sets for Third-Row Atoms: Ga–Kr. *Journal of Computational Chemistry* **1990**, *11*, 1206–1216.
- [412] Yuan, Y.; Giri, G.; Ayzner, A. L.; Zoombelt, A. P.; Mannsfeld, S. C.; Chen, J.; Nordlund, D.; Toney, M. F.; Huang, J.; Bao, Z. Ultra-High Mobility Transparent Organic Thin Film Transistors Grown by an Off-Centre Spin-Coating Method. *Nature Communications* **2014**, *5*, 1–9.
- [413] Qiao, Y.; Wei, Z.; Risko, C.; Li, H.; Brédas, J.-L.; Xu, W.; Zhu, D. Synthesis, Experimental and Theoretical Characterization, and Field-Effect Transistor Properties of a New Class of Dibenzothiophene Derivatives: From Linear to Cyclic Architectures. *Journal of Materials Chemistry* **2012**, *22*, 1313–1325.
- [414] Diao, Y.; Lenn, K. M.; Lee, W.-Y.; Blood-Forsythe, M. A.; Xu, J.; Mao, Y.; Kim, Y.; Reinspach, J. A.; Park, S.; Aspuru-Guzik, A. Understanding Polymorphism in Organic Semiconductor Thin Films Through Nanoconfinement. *Journal of the American Chemical Society* **2014**, *136*, 17046–17057.
- [415] Payne, M. M.; Parkin, S. R.; Anthony, J. E.; Kuo, C.-C.; Jackson, T. N. Organic Field-Effect Transistors from Solution-Deposited Functionalized Acenes with Mobilities as High as  $1 \text{ Cm}^2/\text{V}\cdot\text{s}$ . *Journal of the American Chemical Society* **2005**, *127*, 4986–4987.
- [416] Brédas, J.-L.; Calbert, J. P.; da Silva Filho, D.; Cornil, J. Organic Semiconductors: A Theoretical Characterization of the Basic Parameters Governing Charge Transport. *Proceedings of the National Academy of Sciences* **2002**, *99*, 5804–5809.
- [417] Ayzner, A. L.; Nordlund, D.; Kim, D.-H.; Bao, Z.; Toney, M. F. Ultrafast Electron Transfer at Organic Semiconductor Interfaces: Importance of Molecular Orientation. *The Journal of Physical Chemistry Letters* **2014**, *6*, 6–12.

---

PUBLICATION LIST

---

- 2017 **Regular Fluorescence of 4-Fluoro-N,N-dimethylaniline: No Charge Transfer and No Twisting**, Bohnwagner MV, Dreuw A, *Journal of Physical Chemistry A*, **2017**, *121*(31), pages 5834-5841
- 2017 **Regular and red-shifted fluorescence of the donor-acceptor compound 5-(1H-pyrrole-1-yl)thiophenecarbonitrile (TCN) is efficiently quenched by internal modes of thiophene**, Bohnwagner MV, Burghardt I, Dreuw A, *Physical Chemistry Chemical Physics*, **2017**, *19*(21), pages 13951-13959
- 2016 **Attractive Dispersion Interactions Versus Steric Repulsion of tert-Butyl groups in the Crystal Packing of a  $D_{3h}$ -Symmetric Tris(quinoxalinophenanthrophenazine)** Kohl B, Bohnwagner MV, Rominger F, Wadepohl H, Dreuw A, Mastalerz M, *Chemistry-A European Journal*, **2016**, *22*, pages 646-655.
- 2016 **Solvent Polarity Tunes the Barrier Height for Twisted Intramolecular Charge Transfer in N-pyrrolobenzonitrile (PBN)**, Bohnwagner MV, Burghardt I, Dreuw A, *Journal of Physical Chemistry A*, **2016**, *120*(1), pages 14-27.



---

LIST OF FIGURES

---

1.1	Jablonski-diagram illustrating possible decay processes occurring after vertical excitation at the Franck-Condon geometry . . . . .	4
2.1	Schematic illustration of the energetically lowest intramolecular charge-transfer state of the donor- (D) acceptor (A) molecule N-pyrrolobenzonitrile (PBN) at its ground state equilibrium (or Franck-Condon) geometry. The surface plots correspond to molecular orbitals. . . . .	8
2.2	a) Sketch of experimental absorption and emission spectra of the TICT compound DMABN in polar acetonitrile solution. The emission spectrum shows dual fluorescence. (The spectra are adapted from refs <sup>[72,73]</sup> ) b) Schematic illustration of the TICT mechanism. After vertical excitation two minima on the $S_1$ state PES may be populated. The almost planar LE state minimum and the TICT state minimum. . . . .	9
3.1	Schematic representation of two different one-dimensional potential energy surfaces of an arbitrary polyatomic molecule as a function of the reaction coordinate. Furthermore, a conical intersection of the two potential energy surfaces is shown.	17
3.2	Illustration of the Franck-Condon principle. . . . .	18
3.3	Schematic representation of the basic idea of the HF approximation. Electron correlation (left) is treated in an average way by introducing an effective potential called HF potential (right). . . . .	24
3.4	Schematic representation of the Hartree Fock reference determinant $\Phi^{\text{HF}}$ , three possible single excitations resulting in three different singly excited determinants $\Phi^S$ and three possible double excitations resulting in three different doubly excited determinants $\Phi^D$ . . . . .	37
3.5	Graphical representation of the structures of the ADC matrix in the first order ADC(1), strict and extended second-order ADC(2)-s and ADC(2)-x, as well as the third-order scheme ADC(3) . . . . .	50
3.6	Schematic illustration of the electronic structure of a diradical. Six Slater determinants that can be generated by distributing two electrons in two molecular orbitals ( $\phi$ ) are shown. From these three singlet $\Psi^S$ and three triplet states $\Psi^T$ can be composed. . . . .	56
4.1	Schematic illustration showing the effect of solvent polarity on the potential energy curve of $S_1$ state and the energy of the TICT state. . . . .	73
4.2	Structures of of 4-(Dimethylamino)benzonitrile (DMABN) (left), 4-(1H-pyrrol-1-yl)benzonitrile (PBN) (right) . . . . .	74

4.3	Structure of PBN and numbering of the relevant atoms. Additionally the twisting coordinate $\beta$ (in red) and the twofold symmetry axis $C_2$ are shown. . . . .	81
4.4	HF molecular orbitals obtained at LR-CC2/cc-pVTZ level of theory at the $S_0$ equilibrium geometry (isovalue of 0.05). DFT/BHLYP and DFT/CAM-B3LYP orbitals are practically identical. . . . .	82
4.5	Schematic representation of the bond length pattern in the equilibrium geometries of ground ( $S_0$ ), 1B (LE), bright 2A ( $\pi\pi^*$ ) and 2B (CT) states obtained at LR-CC2/cc-pVTZ level of theory and corresponding geometries. . . . .	88
4.6	Top: Equilibrium geometry of the ground ( $S_0$ ) state, Bottom: approximate $S_2$ - $S_1$ intersection geometry obtained at LR-CC2/cc-pVTZ level of theory. One of the main coordinates leading to the $S_2$ - $S_1$ (2A-1B) CI is the pyramidalization of the C1 atom. . . . .	90
4.7	2B transitions state (TS) structure of PBN obtained at LR-CC2/cc-pVTZ level of theory. . . . .	92
4.8	Relaxed scan of the PESs of the 2A state (green solid line) and 2B state (red dashed line) along the twisting coordinate $\beta$ at LR-CC2/cc-pVTZ level of theory. Energies are relative to the FC geometry. The black arrow displays vertical excitation at the FC geometry. . . . .	95
4.9	HF molecular orbitals obtained at LR-CC2/cc-pVTZ level of theory: HOMO, HOMO-1, HOMO-2, HOMO-3, LUMO and LUMO+1 at $\beta = 63^\circ$ (isovalue = 0.05). . . . .	96
4.10	Particle and hole NTO pairs of the 1B and 2B states of PBN at the geometry with $\beta = 50^\circ$ obtained at ADC(2)/cc-pVTZ level of theory (isovalue = 0.05). . . . .	97
4.11	Particle and hole NTO pairs of the 1B and 2B states of PBN at the geometry with $\beta = 70^\circ$ obtained at ADC(2)/cc-pVTZ level of theory (isovalue = 0.05). . . . .	97
4.12	Relaxed scan of the 2A PES (light green) along the twisting coordinate $\beta$ at TD-CAM-B3LYP/cc-pVTZ level of theory. As input geometries, LR-CC2/cc-pVTZ optimized 2A state geometries have been used. Energies are relative to the FC geometry. . . . .	98
4.13	Relaxed PES scan of the 2A state (solid lines) and 2B state (dashed lines) along the twisting coordinate $\beta$ at the ADC(2)/cc-pVTZ level of theory using SS-COSMO.100	
4.14	Schemes of the photochemical reaction of PBN in the gas phase and polar solution. In weakly polar solvents both pathways are possible and likely to occur. 102	
5.1	Structures of the two investigated isomers of TCN: 5-(1H-pyrrole-1-yl)thiophenecarbonitrile (2-TCN) (left) and 5-(1H-pyrrole-1-yl)thiophenecarbonitrile (3-TCN) (right) and numbering of the relevant atoms. The twisting coordinate $\beta$ is indicated in red. 106	
5.2	a) HOMO-1, HOMO, LUMO and LUMO+1 of 2-TCN b) HOMO-1, HOMO, LUMO and LUMO+1 of 3-TCN (bottom) computed at ADC(2)/cc-pVTZ level of theory at the FC geometry (isovalues = 0.05). Kohn-Sham MOs are practical identical . . . . .	111
5.3	Electron detachment (blue) and attachment (red) density plots for the $S_1$ , $S_2$ , $T_1$ and $T_2$ states of 2-TCN obtained at the ADC(2)/cc-pVTZ level of theory at the CC2 $S_0$ equilibrium geometry. TD-BHLYP and TD-CAM-B3LYP electron detachment and attachment densities are practically identical.(Isovalues = 0.009 and 0.00225) . . . . .	112

5.4	Electron detachment (blue) and attachment (red) density plots for the $S_1$ , $S_2$ , $T_1$ and $T_2$ states of 3-TCN obtained at the ADC(2)/cc-pVTZ level of theory at the CC2 $S_0$ equilibrium geometry. TD-BHLYP and TD-CAM-B3LYP electron detachment and attachment densities are practically identical. (Isovalues = 0.009 and 0.00225) . . . . .	112
5.5	Schematic representation of the nonradiative decay of the bright $S(\pi\pi^*)$ state of 2- and 3-TCN in the gas phase. Vertical excitation energies $\omega$ of the bright $S(\pi\pi^*)$ state and total energies $E_{(\text{approx. CI})}$ of the approximate conical intersection geometries (relative to the $S_0$ equilibrium energy) are given in the table. . . . .	114
5.6	$S_1$ $S(\pi\pi^*)$ state equilibrium geometries of 2-TCN a) and 3-TCN b) obtained at TD-CAM-B3LYP/cc-pVTZ and TD-BHLYP/cc-pVTZ levels of theory. . . . .	116
5.7	Schematic representation of the deactivation pathway of the $S(\text{CT})$ ( $S_2$ ) state of 2-TCN and 3-TCN obtained at LR-CC2/cc-pVTZ level of theory in the gas phase. Vertical excitation energies $\omega$ of the $S(\pi\pi^*)$ state and total energies of the approximate conical intersection (relative to the $S_0$ equilibrium energy) and the $S(\text{CT})$ (TICT) minimum geometries of both isomers are given in the table. In parenthesis values obtained at ADC(2)/cc-pVTZ level of theory are given. . . . .	117
5.8	Schematic representation of the deactivation pathway of the $S(\pi\pi^*)$ ( $S_1$ ) state of TCN simulating ACN solution. Vertical excitation energies $\omega$ of $S(\pi\pi^*)$ and $S(\text{CT})$ states and total energies of the approximate conical intersection geometries (relative to the $S_0$ equilibrium energy) obtained at ADC(2)/cc-pVTZ/SS-COSMO level of theory are given in the table. . . . .	120
5.9	Schematic representation of the deactivation pathway of the $S(\pi\pi^*)$ ( $S_1$ ) state of TCN simulating ACN solution. Vertical excitation energies $\omega$ of $S(\pi\pi^*)$ and $S(\text{CT})$ states and total energies of the approximate conical intersection geometries (relative to the $S_0$ equilibrium energy) obtained at ADC(2)/cc-pVTZ/SS-COSMO level of theory are given in the table. . . . .	121
6.1	Schematic illustration of the deactivation mechanism of FDMA obtained at LR-CC2 level of theory. . . . .	124
6.2	Structure of FDMA and numbering of the relevant atoms. The twisting coordinate $\beta$ is shown in red. . . . .	125
6.3	Relaxed PES scan of the ground state along the twisting coordinate $\beta$ obtained at MP2//TD-CAM-B3LYP/cc-pVDZ level of theory. Vertical excitation energies of the first six lowest excited states considering singlet and triplets states have been computed at each ground state geometry along the PES scan. . . . .	129
6.4	Rigid PES scan of the $S_1$ state along the twisting coordinate $\beta$ obtained TD-B3LYP/cc-pVDZ level of theory. As starting geometry, the $1A''$ planar ( $\beta = 0^\circ$ ) equilibrium geometry has been used. . . . .	130
6.5	Rigid PES scan of the $S_1$ state along the twisting coordinate $\beta$ obtained ADC(2)/cc-pVDZ level of theory. As starting geometry, the $1A''$ planar ( $\beta = 0^\circ$ ) equilibrium geometry computed at the TD-B3LYP/cc-pVDZ level of theory has been used. . . . .	130
6.6	$S_1$ state equilibrium geometries of FDMA a) $S_{1\text{twisted}}$ and b) $1A''_{\text{planar}}$ obtained at TD-B3LYP/cc-pVDZ level of theory. $1A''_{\text{planar}}$ is predicted to be a transition state ( $\nu = 100.4 \text{ cm}^{-1}$ ) at TD-CAM-B3LYP/cc-pVDZ level of theory. The $S_{1\text{twisted}}$ geometry is not found at CAM-B3LYP and LR-CC2 levels of theory. . . . .	131

6.7	ADC(2)/cc-pVTZ electron detachment (blue) and attachment (red) density plots for the $S_1$ (1A") and $S_2$ (1A") states of FDMA calculated at the MP2 $S_0$ equilibrium geometry. . . . .	132
6.8	a) planar ( $S_{1\text{planar}}$ ) and b) twisted (and pyramidalized) ( $S_{1\text{pyr}}$ ) $S_1$ state minima of FDMA obtained at the TD-CAM-B3LYP/cc-pVDZ level of theory. . . . .	134
6.9	a) Approximate $S_2$ - $S_1$ conical intersection geometry obtained with and without applying $C_s$ symmetry constraints and b) approximate $S_1$ - $S_0$ conical intersection geometry both obtained at the TD-CAM-B3LYP/cc-pVDZ level of theory. . . .	135
6.10	Schematic illustration of the suggested deactivation mechanism of FDMA: After photoexcitation to the bright $S_2$ ( $\pi\pi^*$ ) state, FDMA may either relax to an almost planar $S_1$ state minimum $S_{1\text{planar}}$ and fluoresce or it may decay nonradiatively to the ground state via a $S_1$ - $S_0$ conical intersection. . . . .	139
7.1	Structures of Z and E isomers of hemithioindio (HTI) and the Z/E isomerization about the double bond (indicated in orange) induced by visible light. . . . .	142
7.2	Schematic representation of two possible excited-state decay pathways of photoexcited HTIs Z1-Z3. In polar solvents mainly single-bond rotation occurs while in apolar solvents primarily Z/E photoisomerization of the double bond takes place. <sup>[245]</sup> . . . . .	143
7.3	Skeleton structures of Z isomers of HTIs I-IV. The Z/E photoisomerization coordinate $\theta$ is indicated in orange. . . . .	145
7.4	Skeleton structure of the HTI core and numbering of the atoms. . . . .	147
7.5	Local ground state minima nearest to the initial structures of HTIs Z1-Z4 obtained at MP2/cc-pVDZ level of theory. The twisting coordinate $\beta$ is indicated in red. For Z4 it is assumed that no single-bond rotation resulting in TICT formation occurs, hence, this coordinate is not considered. . . . .	149
7.6	Valence molecular orbitals of HTI Z1 computed at ADC(2)/cc-pVDZ level of theory (Isovalue = 0.05). . . . .	151
7.7	Valence molecular orbitals of HTI Z2 computed at ADC(2)/cc-pVDZ level of theory (Isovalue = 0.05). . . . .	151
7.8	Valence molecular orbitals of HTI Z3 computed at ADC(2)/cc-pVDZ level of theory (Isovalue = 0.05). . . . .	152
7.9	Valence molecular orbitals of HTI Z4 computed at ADC(2)/cc-pVDZ level of theory (Isovalue = 0.05). . . . .	152
7.10	Local $S_1$ state minimum geometries of HTI Z1 obtained at LR-CC2/cc-pVDZ and TD-CAM-B3LYP/cc-pVDZ levels of theory, respectively (shown from two different views). . . . .	156
7.11	Local $S_1$ state minimum geometries of HTI Z1 obtained at LR-CC2/cc-pVDZ and TD-CAM-B3LYP/cc-pVDZ levels of theory, respectively (shown from two different views). The TD-CAM-B3LYP structure, in contrast to the LR-CC2 one, has a planar benzene ring and the out-of-plane bending of the central double bond out of the thioindigo plane is $8^\circ$ smaller. . . . .	156
7.12	Local $S_1$ state minimum geometries of HTI Z3 obtained at LR-CC2/cc-pVDZ and TD-CAM-B3LYP/cc-pVDZ levels of theory, respectively (shown from two different views). . . . .	157
7.13	Local $S_1$ state minimum geometries of HTI Z4 obtained at LR-CC2/cc-pVDZ and TD-CAM-B3LYP/cc-pVDZ levels of theory, respectively (shown from two different views). . . . .	157

7.14	Relaxed scan of the $S_1$ PES of HTI 4 for the Z/E isomerization obtained at SF-B5050LYP/6-31G* level of theory. Energies are relative to the $S_0$ equilibrium energy at $\theta=180^\circ$ . . . . .	160
7.15	Relaxed scan of the $S_1$ PES of HTI 1 for the Z/E isomerization obtained at SF-B5050LYP/6-31G* level of theory. Energies are relative to the $S_0$ equilibrium energy at $\theta=180^\circ$ . . . . .	161
7.16	Relaxed scan of the $S_1$ PES of HTI 2 for the Z/E isomerization obtained at SF-B5050LYP/6-31G* level of theory. Energies are relative to the $S_0$ equilibrium energy at $\theta=180^\circ$ . . . . .	162
7.17	Relaxed scan of the $S_1$ PES of HTI 3 for the Z/E isomerization obtained at SF-B5050LYP/6-31G* level of theory. Energies are relative to the $S_0$ equilibrium energy at $\theta=180^\circ$ . . . . .	163
7.18	Relaxed $S_1$ PES scan of HTI Z1 along $\beta$ obtained at TD-CAM-B3LYP/6-31G**/TD-CAM-B3LYP/cc-pVDZ level of theory. Energies are relative to the ground state minimum at $\beta=50^\circ$ . . . . .	165
7.19	Relaxed $S_1$ PES scan of HTI Z2 along $\beta$ obtained at TD-CAM-B3LYP/6-31G**/TD-CAM-B3LYP/cc-pVDZ level of theory. Energies are relative to the ground state minimum at $\beta=50^\circ$ . . . . .	166
7.20	Relaxed $S_1$ PES scan of HTI Z3 along $\beta$ obtained at TD-CAM-B3LYP/6-31G**/TD-CAM-B3LYP/cc-pVDZ level of theory. Energies are relative to the ground state minimum at $\beta=-40^\circ$ . . . . .	166
8.1	Structure of the Quinoxalinophenanthrophenazines (QPP) core. R stands for an organic substituent e.g. H, <i>tert</i> -butyl or triptycene. . . . .	172
8.2	Structure of a $D_{3h}$ symmetric tris(quinoxalinophenanthrophenazines) (tQPP) molecule. . . . .	172
8.3	Schematic representation of the observed particular honeycomb crystal packing motif. . . . .	173
8.4	Skeletal formula of the monomers QPP 2-5 and wireframe model of the crystal structures of the investigated dimers D-QPP 2-5 (top view). . . . .	173
8.5	Wireframe models of the crystal structure (X-Ray) and the B97D, B97D3 and B98 optimized geometries of D-QPP 5. Distances between the monomers are shown in dashed lines. The values are taken from Ref. [385]. . . . .	176
8.6	Wireframe models of the crystal structure (X-Ray) and the B97D, B97D3 and B98 optimized geometries of D-QPP 4. Distances between the monomers are shown in dashed lines. The values are taken from Ref. [385]. . . . .	177
8.7	Wireframe models of the crystal structure (X-Ray) and the B97D, B97D3 and B98 optimized geometries of D-QPP 3. Distances between the monomers are shown in dashed lines. The values are taken from Ref. [385]. . . . .	178
8.8	Wireframe models of the crystal structure (X-Ray) and the B97D, B97D3 and B98 optimized geometries of D-QPP 2. Distances between the monomers are shown in dashed lines. The values are taken from Ref. [385]. . . . .	179
B.1	Ground state equilibrium geometry obtained at MP2/cc-pVDZ level with two <i>n</i> -hexane molecules added. No reoptimization has been performed . . . . .	195
B.2	Ground state equilibrium geometry obtained at MP2/cc-pVDZ level with two ACN molecules added. No reoptimization has been performed . . . . .	196

B.3	Relaxed PES scan of the ground state along the twisting coordinate $\beta$ obtained at MP2//TD-B3LYP/cc-pVDZ level of theory. . . . .	196
B.4	Rigid PES scans of the $S_1$ ( $1A''$ ) state along the twisting coordinate $\beta$ obtained at TD-CAM-B3LYP/cc-pVDZ level of theory. As starting geometry, the $1A''$ planar ( $\beta = 0^\circ$ ) equilibrium geometry computed at TD-B3LYP/cc-pVDZ level of theory has been used. . . . .	197
B.5	$C_s$ symmetric ground state equilibrium geometry obtained at MP2/cc-pVTZ level of theory. . . . .	197
B.6	HF valence MOs obtained at ADC(2)/cc-pVTZ level of theory at the MP2 ground state equilibrium geometry (Isovalue = 0.05). . . . .	198
B.7	KS valence MOs obtained at TD-CAM-B3LYP/cc-pVTZ level of theory at the MP2 ground state equilibrium geometry (Isovalue = 0.05). . . . .	198
B.8	KS MOs obtained at TD-CAM-B3LYP/cc-pVTZ level of theory at the MP2 ground state equilibrium geometry with two <i>n</i> -hexane molecules added (Isovalue = 0.05). Without reoptimization of the FDMA- <i>n</i> -hexane cluster. . . . .	199
B.9	KS MOs obtained at TD-CAM-B3LYP/cc-pVTZ level of theory at the MP2 ground state equilibrium geometry with two acetonitrile (ACN) molecules added (Isovalue = 0.05). Without reoptimization of the FDMA-ACN cluster. . . . .	199
B.10	Approximate $S_2$ - $S_1$ conical intersection geometry obtained at LR-CC2/cc-pVDZ level of theory without applying symmetry constraints during geometry optimization	200
B.11	Approximate $S_1$ - $S_0$ conical intersection geometries obtained at LR-CC2/cc-pVDZ (left), TD-CAM-B3LYP (middle) and TD-B3LYP/cc-pVDZ (right) levels of theory without applying symmetry constraints during geometry optimization	200
B.12	$T_1$ equilibrium geometry obtained at CAM-B3LYP/cc-pVDZ level of theory. . . . .	200
C.1	$S_0$ equilibrium geometry of HTI Z1 obtained at MP2/cc-pVDZ level of theory. . . . .	201
C.2	$S_0$ equilibrium geometry of HTI Z2 obtained at MP2/cc-pVDZ level of theory. . . . .	201
C.3	$S_0$ equilibrium geometry of HTI Z3 obtained at MP2/cc-pVDZ level of theory. . . . .	201
C.4	$S_0$ equilibrium geometry of HTI Z4 obtained at MP2/cc-pVDZ level of theory. . . . .	201
C.5	Ground state equilibrium geometry of HTI E1 and E2 obtained at MP2/cc-pVDZ level of theory. . . . .	202
C.6	Ground state equilibrium geometry of HTI E3 and E4 obtained at MP2/cc-pVDZ level of theory. . . . .	202
C.7	Attachment (red) and detachment (blue) density plots for the lowest excited singlet and triplet states of HTI Z1 obtained at ADC(2)/cc-pVDZ level of theory (Isovalue 0.014) . . . . .	203
C.8	Stationary structure of the $S_1$ state ( $S_{1N_{pyr}}$ ) of HTI Z1 obtained at LR-CC2/cc-pVDZ level of theory upon full geometry optimization at the constrained-optimized geometry with $\beta=90^\circ$ obtained at TD-CAM-B3LYP/cc-pVDZ level of theory. . . . .	204
C.9	Stationary structures of the $S_1$ state of HTI Z1 DMSO clusters obtained at TD-CAM-B3LYP/6-31G* level of theory. . . . .	204
C.10	Stationary structure of the $S_1$ state of a HTI Z3 $H_2O$ cluster obtained at TD-CAM-B3LYP/6-31G* level of theory. . . . .	205

- C.11 Top: Two views of the geometry of HTI Z3 obtained upon geometry optimization of the  $S_1$  state starting with a  $\beta=-90^\circ$  twisted geometry, performed at LR-CC2/cc-pVDZ level of theory in which  $S_1$  and  $S_0$  states are almost degenerate. For comparison the local  $S_1$  state minimum  $S_{1\text{Min}}$  obtained at LR-CC2/cc-pVDZ level of theory is given at the bottom. . . . . 205
- C.12 Approximate  $T_1$ - $S_0$  conical intersection geometries of HTIs I) Z1 II) Z2 III) Z3 and IV) Z4 obtained at LR-CC2/cc-pVDZ level of theory. . . . . 206
- C.13 Relaxed  $S_1$  PES scan of HTI Z2 along  $\beta$  obtained at TD-CAM-B3LYP/6-31G\*\*/TD-CAM-B3LYP/cc-pVDZ level of theory. Total energies of the  $S_1$  state are shown. At  $\beta=40^\circ$  a discontinuity occurs. . . . . 206
- C.14 Relaxed scan of the  $S_0$  PES of HTI 1 for the Z/E isomerization obtained at SF-B5050LYP/6-31G\* level of theory. Energies are relative to the  $S_0$  equilibrium energy. . . . . 207
- C.15 Relaxed scan of the  $S_0$  PES of HTI 2 for the Z/E isomerization obtained at SF-B5050LYP/6-31G\* level of theory. Energies are relative to the  $S_0$  equilibrium energy. . . . . 207
- C.16 Relaxed scan of the  $S_0$  PES of HTI 4 for the Z/E isomerization obtained at SF-B5050LYP/6-31G\* level of theory. Energies are relative to the  $S_0$  equilibrium energy. . . . . 208
- D.1 Structures of D-QPP 5 (with view along the y-axis) represented using the wireframe model. Top: Crystal structure (X-Ray). Middle: B97D/cc-pVDZ optimized geometry. Bottom: B97D3/cc-pVDZ optimized geometry. . . . . 209
- D.2 Structures of D-QPP 4 from two different perspectives (with view along y- and along x-axis) represented using the wireframe model. Top: Crystal structure (CS). Middle: B97D/cc-pVDZ optimized geometry. Bottom: B97D3/cc-pVDZ optimized geometry. . . . . 210
- D.3 Structures of D-QPP 3 represented using the wireframe model. Top: Crystal structure (X-Ray) (with view along y- and along x-axis). Middle: B97D/cc-pVDZ optimized geometry and superposition of the CS and B97D optimized geometry. Bottom: B97D3/cc-pVDZ optimized geometry. . . . . 210



---

LIST OF TABLES

---

4.1	PBN Gas Phase Excitation Energies . . . . .	83
4.2	PBN Excitation Energies obtained using COSMO and ptSS-PCM and the parameters of ACN . . . . .	87
4.3	Dominant MO contributions <sup>a</sup> , character, vertical excitation energies $\omega$ (in eV), oscillator strengths (in parenthesis), total excited state energies <sup>b</sup> (in eV) and static dipole moments $\mu$ (in Debye) of the four lowest excited states at the 1B <sub>Min</sub> geometry obtained at LR-CC2/cc-pVTZ level of theory are given. . . . .	89
4.5	Dominant MO contributions <sup>a</sup> , character, vertical excitation energies $\omega$ (in eV), oscillator strengths (in parenthesis), total excited state energies <sup>b</sup> (in eV) and static dipole moments $\mu$ (in Debye) of the four lowest excited states at the 2A <sub>Min</sub> geometry obtained at LR-CC2/cc-pVTZ level of theory are given. . . . .	91
4.7	Dominant MO contributions <sup>a</sup> , character, corresponding irreducible representation (in C <sub>2</sub> symmetry) vertical excitation energies $\omega$ (in eV), oscillator strengths (in parenthesis), total excited state energies <sup>b</sup> (in eV) and static dipole moments $\mu$ (in Debye) of the three lowest excited states at the 2B <sub>Min</sub> geometry obtained at LR-CC2/cc-pVTZ level of theory are given. . . . .	94
5.1	Relevant bond lengths (Å) in the S <sub>0</sub> equilibrium geometries of 2- and 3-TCN obtained at CC2/cc-pVTZ level of theory and the corresponding ones in pyrrole <sup>[309]</sup> and thiophene <sup>[309]</sup> . For numbering of atoms see Figure 5.1. . . . .	109
5.2	Comparison of gas-phase vertical excitation energies and static dipole moments of 2- and 3-TCN . . . . .	110
5.3	Comparison of vertical excitation energies of 2- and 3-TCN obtained at ADC(2)/cc-pVTZ and ADC(2)/cc-pVTZ/ptSS-PCM levels of theory . . . . .	118
6.1	Comparison of gas-phase vertical excitation energies and static dipole moments of the first lowest singlet and triplet excited states of FDMA . . . . .	131
6.2	Comparison of vertical excitation energies of the first lowest excited singlet states of FDMA obtained at ADC(2)/cc-pVTZ and ADC(2)/cc-pVTZ/ptSS-PCM levels of theory . . . . .	133
7.1	Solvent parameters used for the solvent model . . . . .	146
7.2	Characterization of the excited states of HTIs Z1-Z4 computed at the FC geometry in gas phase. . . . .	150
7.3	Comparison of computed absorption energies with experimental absorption spectra of HTIs Z1-Z4 . . . . .	153

---

8.1	Total interaction energy ( $E_{int}$ ) and relevant energy components of the total interaction energy calculated at the X-ray single crystal structures of D-QPPs <b>2-5</b> as provide by B. Kohl and modified versions of the crystal structure of D-QPP <b>2</b> obtained at the XSAPT(KS)-D3/wPBE/6-31G level of theory. . . . .	180
A.1	Cartesian coordinates of the ground state equilibrium geometry of 2-TCN obtained at RI-MP2/cc-pVTZ level of theory . . . . .	191
A.2	Cartesian coordinates of the ground state equilibrium geometry of 2-TCN obtained at RI-CC2/cc-pVTZ level of theory . . . . .	192
A.3	Cartesian coordinates of the ground state equilibrium geometry of 3-TCN obtained at RI-MP2/cc-pVTZ level of theory . . . . .	192
A.4	Cartesian coordinates of the ground state equilibrium geometry of 3-TCN obtained at RI-CC2/cc-pVTZ level of theory . . . . .	193
A.5	Comparison of vertical excitation energies and static dipole moments of the first four lowest excited states of 2- and 3-TCN obtained at ADC(2)/cc-pVTZ and ADC(2)/cc-pVTZ/SS-COSMO levels of theory at the gas phase ground state equilibrium geometry using the parameter of <i>n</i> -hexane, acetonitrile and water for the solvent model. Vertical excitation energies in gas phase $\omega$ (in eV), solvent-corrected vertical excitation energies $\omega_{sol}$ (in eV) and solvent shifts $\Delta\omega_{gas}^a$ and $\Delta\Delta\omega_{sol}$ (in eV) and relaxed static dipole moments (in Debye) are given. . . . .	194
C.1	Characterization of the excited states of HTIs E1-E4 in the gas phase. . . . .	203

# Danksagung

An dieser Stelle möchte ich all denjenigen danken, die mich während der Promotion fachlich, moralisch und emotional unterstützt haben und für mich da waren.

Ein besonderes Wort des Dankes möchte ich an meinen Doktorvater Herr Prof. Dr. Andreas Dreuw richten. Andreas habe ich im Bachelor Studium an der Goethe Universität Frankfurt, in der "Mathematik für Naturwissenschaftler 1" Vorlesung kennengelernt.

Spätestens nach meinem ersten Praktikum in der *Theoretical and Computational Chemistry* im Arbeitskreis von Andreas, das im Rahmen des Bachelor Studiums ablief, und noch bevor ich meine Bachelorarbeit bei ihm geschrieben hatte, hat sich in mir der große Wunsch entwickelt, bei Andreas meine Doktorarbeit zu schreiben. Dies hatte mehrere Gründe. Ich war nicht nur von seiner fachlichen Kompetenz tief beeindruckt, sondern auch von seiner Persönlichkeit. Ich hatte das intuitive Gefühl, dass mich eine Doktorarbeit unter seiner Betreuung nicht nur wissenschaftlich weiterbringen würde, sondern dass Andreas gute Bedingungen schaffen und mir Möglichkeiten geben würde mich auch persönlich weiter zu entwickeln. Und im Nachhinein kann ich sagen, dass sich meine Intuition bewahrheitet hat.

Ich bin Andreas sehr dankbar dafür, dass er immer das richtige Maß an Betreuung gefunden hat. Er hat mir viel Freiheit gelassen, aber in den richtigen Moment auch Druck ausgeübt, der mich motiviert und angetrieben hat. Er hat es geschafft mich meine eigenen Stärken und Schwächen erkennen zu lassen und mich mit sehr viel Geduld darin unterstützt, die Stärken weiter auszubauen und an den Schwächen zu arbeiten. Insbesondere bin ich auch sehr dankbar dafür, dass er mich in der Zeit mit den Augenproblemen unterstützt hat. Vielen Dank Andreas, dass du mir die Möglichkeit gegeben hast bei dir zu promovieren. Die Promotion war nicht immer leicht für mich, aber sie hat mich über meine Grenzen hinauswachsen lassen und war alles in allem eine gute und wichtige Erfahrung.

Herr Prof. Dr. Peter Comba danke ich vielmals für die Zweitkorrektur meiner Doktorarbeit.

Ein herzlicher Dank gilt auch meinen Eltern Gerda und Knut, meinem Bruder Reto und meiner Oma Heidi. Danke, dass ihr immer für mich da wart und mich unterstützt habt.

Darüber hinaus möchte ich mich vielmals bei meinen Freundinnen und Freunden Martina, Maja, Carolina, Linn, Katie, Cornelia, Maria, Sabrina, Johanna, Stefan, Mirko, Peter, Florian, Sebastian, Youssef und Christian bedanken. Ich wusste, dass ihr immer, zu jeder Tages- und Uhrzeit für mich da seid und dass ich mich egal mit welchem Problem an euch wenden kann. Vor allem wenn ich mal von Selbstzweifel geplagt oder in einem Tief gefangen war, wart ihr diejenigen die mir den Kopf zurecht gerückt habt. Vielen vielen tausend dank dafür, dass ihr da wart und mich moralisch und emotional unterstützt habt, vor allem in der schwierigen Zeit zwischen und nach den OPs. Ich bin sehr glücklich und dankbar euch in meinem Leben zu haben!

Dr. Jan Mewes, Dr. Felix Plasser und Dr. Daria Brisker-Klaiman danke ich für anregenden und hilfreiche wissenschaftliche Diskussionen.

Hereby, a special thank you goes to Daria. Thank you Daria for meeting up with me after the first eye surgery and convincing me to come back to the office and talk to my colleagues. I was very insecure and ashamed of needing help, but thank to you and our conversations, I made the step and went to the office. This was a very important step because I experienced that all colleagues

were very interested and extremely supportive.

Ausserdem möchte ich mich bei meinem Arbeitskreis bedanken. Ich bin außerordentlich glücklich und dankbar dafür, dass ich während der Promotion von wunderbareren, einzigartigen, lustigen, liebevollen und hilfsbereiten Arbeitskollegen umgeben war. Ihr seid ein grossartiger Arbeitskreis! Ansonsten möchte ich noch unserem Systemadministrator Manfred Trunk bedanken. Danke Manfred, dass du einige meiner Rechnungen, z.T auch am Wochenende, vor dem sicheren "walltime exceeded" Tod gerettet hast.

A special thank you goes to my colleague Jie Han. Jie took care about me and did the medical treatment when I was not able to do it by myself in the weeks after the surgeries. He also kept me informed about events and other things related to our working group. Thank you very much for everything Jie!

**Eidesstattliche Versicherung gemäß § 8 der Promotionsordnung der  
Naturwissenschaftlich-Mathematischen Gesamtfakultät der Universität Heidelberg**

- 1 Bei der eingereichten Dissertation zu dem Thema  
**“Intramolecular Charge Transfer in Solvated Organic Molecules: A Quantum Chemical Study”**  
handelt es sich um meine eigenständig erbrachte Leistung.
- 2 Ich habe nur die angegebenen Quellen und Hilfsmittel benutzt und mich keiner unzulässigen Hilfe Dritter bedient. Insbesondere habe ich wörtlich oder sinngemäß aus anderen Werken übernommene Inhalte als solche kenntlich gemacht.
- 3 Die Arbeit oder Teile davon habe ich bislang nicht an einer Hochschule des In- oder Auslands als Bestandteil einer Prüfungs- oder Qualifikationsleistung vorgelegt.
- 4 Die Richtigkeit der vorstehenden Erklärungen bestätige ich.
- 5 Die Bedeutung der eidesstattlichen Versicherung und die strafrechtlichen Folgen einer unrichtigen oder unvollständigen eidesstattlichen Versicherung sind mir bekannt.

Ich versichere an Eides statt, dass ich nach bestem Wissen die reine Wahrheit erklärt und nichts verschwiegen habe.

---

Ort/Datum

---

Unterschrift